

Dusty discs around evolved stars

A thesis submitted to the University of Manchester
for the degree of Doctor of Philosophy
in the Faculty of Engineering and Physical Sciences

2013

Foteini Lykou
School of Physics and Astronomy

Contents

Abstract	15
Declaration	16
Copyright Statement	17
Acknowledgements	18
Dedication	20
The Author	21
1 Introduction	23
1.1 Evolution of a single star	25
1.1.1 Main Sequence and beyond	25
1.1.2 AGB	26
1.1.2.1 Chemistry and the stellar core	27

1.1.3	Post-AGB	28
1.1.4	Planetary nebula	29
1.1.5	Very late thermal pulse	30
1.2	Evolution of a binary	31
1.2.1	Fate of binary systems	32
1.3	Mass loss	33
1.3.1	Asymmetries	34
1.4	Shaping mechanisms	36
1.5	Dusty structures	37
1.5.1	Forming such structures	38
1.5.2	Detecting the structures	40
1.6	This work	42
2	Interferometric techniques	43
2.1	Atmospheric contribution	44
2.2	Single telescope	45
2.3	Interferometer	46
2.3.1	Monochromatic, polychromatic and extended sources . .	48
2.3.2	Visibility	51
2.3.3	Aperture synthesis	51
2.3.4	Bispectrum analysis	52
2.4	Image reconstruction	54
2.5	Interferometry with the VLTI	56
2.5.1	MIDI	58
2.5.1.1	Observing sequence	60
2.5.1.2	Data reduction	60
2.6	Single telescope interferometry	62
2.6.1	Aperture masking	63

2.6.1.1	SAM	63
2.6.1.1.1	Data reduction	67
2.7	Fitting the data	67
3	Radiative transfer modelling	69
3.1	The theory in short	69
3.2	Dust	71
3.3	MC3D	73
3.3.1	Inputs	76
3.3.2	Estimation of the temperature distribution	78
3.3.2.1	Dependencies	79
3.3.3	Outputs	83
4	A dusty structure around Sakurai's Object	85
4.1	A reborn star	85
4.2	Observations	88
4.2.1	VLTI	89
4.2.2	SPITZER	91
4.2.3	Infrared photometry	94
4.3	Model fitting	94
4.3.1	MC3D models	96
4.3.1.1	Dust composition	97
4.3.1.2	Parameter selection	99
4.3.2	Fitting accuracy	101
4.4	Sakurai's planetary nebula	108
4.5	Discussion	109
5	The young nebula M2-9	115
5.1	The nebula	115

5.1.1	Orbital period	116
5.1.2	Distance of M2-9	116
5.1.3	Mass of the ejecta	117
5.2	Observational data	118
5.2.1	VLTI	118
5.2.2	NACO	119
5.2.3	ISO	120
5.2.3.1	ISOCAM	120
5.2.3.2	SWS	121
5.2.4	SPITZER	121
5.2.5	AKARI	122
5.3	Observational results	124
5.3.1	Spectral Energy Distribution	124
5.3.1.1	Short-High	124
5.3.1.2	Long-High	125
5.3.2	Interferometry	126
5.3.2.1	Correction to Lykou et al. (2011)	128
5.4	Physical parameters of the disc	128
5.4.1	Dust composition	128
5.4.2	Parametric study	130
5.4.3	Large grains and different grain size distributions	131
5.4.4	Fitting results	132
5.5	Where is the companion relative to the dust source?	136
5.5.1	The inner dusty disc	137
5.5.2	The exterior torus	138
5.6	The mass of the components and an accretion disc	139
5.7	Remarks	141

6	V Hya, a variable carbon star	145
6.1	History of V Hya	145
6.1.1	Asymmetries	149
6.1.2	A suspected companion	151
6.2	Observations	152
6.3	Stellar diameter	154
6.3.1	Physical sizes	158
6.4	Near-infrared interferometric imaging	159
6.4.1	NACO/VLT	159
6.4.2	Keck	163
6.5	An evolving dusty structure	165
6.5.1	What lies within the structure	166
6.5.2	Similarities with other stars	168
7	Conclusions	173
7.1	Results	173
7.1.1	A disc-like structure in Sakurai's Object	174
7.1.2	The disc in M2-9	174
7.1.2.1	Comparison to the disc in Mz3	175
7.1.3	An evolving structure around V Hya	176
7.2	Past research on dusty structures	178
7.3	Evolution of dusty structures	179
7.4	Conclusions	182
7.5	Future work	186
7.5.1	The future of V Hya	186
7.5.1.1	Visual to near-infrared	186
7.5.1.2	Far-infrared to millimetre	187
7.5.2	The current evolution of Sakurai's Object	187

7.5.3 Other sources	188
A Evolved stars with dusty structures	191
B MIDI data reduction	201
Bibliography	209
Final wordcount~40,000 words	

List of Figures

1.1	Hertzsprung-Russel diagram	27
1.2	The post-AGB stars Red Rectangle and Calabash nebula	29
1.3	Examples of bipolar and multipolar nebulae.	30
1.4	Schematic representation of an AGB star.	35
1.5	The case of IRC+10216	36
1.6	An image of the Bug Nebula	38
1.7	Formation of a disc and a bipolar outflow	39
1.8	Formation of a spiral structure	41
2.1	Fringe patterns recorded by a single-dish telescope and an interferometer with two apertures.	45
2.2	Resolution capabilities of the a single UT and the VLTI. . . .	46
2.3	Sketch of a two-element interferometric array	47
2.4	The Very Large Telescope of the European Southern Observatory in Chile.	57
2.5	Sketch of the MIDI cold box.	59

2.6	MIDI interferometric instrument in a nutshell	59
2.7	Example of MIDI <i>uv</i> coverage.	61
2.8	SAM/NACO masks	64
2.9	Calibration frames for NACO	65
2.10	SAM/NACO interferograms	66
3.1	Illustration of a photon's random walk through an abstract model space.	76
3.2	MC3D grid	77
3.3	Temperature distribution of amorphous carbon dust within a disc.	80
3.4	Radial profile of a disc demonstrating the significance of increas- ing flaring	81
3.5	Absorption and scattering coefficients for amorphous silicates.	82
3.6	Absorption and scattering coefficients for different grain size distributions.	82
4.1	Light curve of V4334 Sgr from 01/06/1996 to 01/01/2000.	86
4.2	IRAS and MSX maps of Sakurai's Object	87
4.3	Projected VLTI baselines for Sakurai's Object observations.	89
4.4	Spectral energy distribution of V4334 Sgr.	90
4.5	Gaussian fits to the MIDI visibilities for Sakurai's Object.	92
4.6	Differential phases of Sakurai's Object.	93
4.7	Gaussian fits for selected wavelengths.	96
4.8	Uniform disc fits for selected wavelengths.	97
4.9	Circular uniform ring fits for selected wavelengths.	98
4.10	Cartoon of a disc model	98
4.11	Comparison of different radiative transfer models to the MIDI visibilities.	101

4.12	Comparison of different radiative transfer models to the MIDI spectrum.	102
4.13	Best fit visibilities of a disc around V4334 Sgr	103
4.14	Sakurai's Object modelled disc images	105
4.15	Model spectrum with amorphous and graphitic carbon dust. . .	106
4.16	Model visibilities with amorphous graphitic carbon dust. . . .	107
4.17	Sakurai's Object planetary nebula	108
4.18	Sakurai's Object nebula in $H\alpha$	110
4.19	Optimal selection of position angle	112
5.1	The symbiotic nebula M2-9 from 1989 till 2007.	117
5.2	HST/STIS and NACO/VLT imaging of M2-9	119
5.3	Positioning of the Spitzer/IRS slits over an HST image of M2-9	122
5.4	High-resolution spectra of the northern lobe of M2-9 by SPITZER.	123
5.5	Interstellar extinction by Savage & Mathis (1979).	125
5.6	Correlated flux of M2-9	127
5.7	Gaussian size distribution of the dusty structure in M2-9	129
5.8	The ansae of M2-9	130
5.9	M2-9 spectral energy distribution	134
5.10	MIDI visibilities compared with the best model	135
5.11	Modelled images of discs in M2-9 and Mz3	143
6.1	V Hya light curve from April 1990 to April 2013	146
6.2	Mid-infrared spectra of C-rich red giants.	147
6.3	V Hya spectral energy distribution	148
6.4	V Hya torus and disc	151
6.5	Example of "bad" quality data	153
6.6	Gaussian model fits for SAM data at 3.74 and $4.05\mu\text{m}$ azimuthally-averaged data	155

6.7	The circumstellar environment of V Hya at 3.74 and 4.05 μ m as seen by SAM/NACO on 29/06/2010	161
6.8	The circumstellar environment of V Hya at 3.74 and 4.05 μ m as seen by SAM/NACO on 30/06/2010	162
6.9	Comparing NACO/VLT and SAM/NACO imaging	162
6.10	Keck aperture masking over four epochs from December 1997 until January 2000 at 3.08 μ m.	164
6.11	Keck aperture masking in April 2004 at 4.67 μ m.	165
6.12	Model of a spiral	168
6.13	Comparison of estimated angular sizes (Gaussian) for V Hya by interferometric observations in the near- and mid-infrared	170
7.1	Continuum subtracted spectrum of Mz3.	177
7.2	V Hya angular size variations	179
7.3	PIONIER/VLTI <i>uv</i> coverage and V^2 amplitude in H band for V Hya	184
7.4	AMBER/VLTI <i>uv</i> coverage and V^2 amplitude in H and K bands for V Hya	185
7.5	AFGL2688 at 2.15 μ m imaged by the HST.	188
B.1	Application of a mask for PRISM in MIA	204
B.2	MIDI Interactive Analysis flowchart.	205
B.3	Example of MIDI photometry	206
B.4	MIA graphical user interface	207
B.5	Good and bad powerspectra	208
B.6	Instrumental visibility	209
B.7	Calibrated visibility	210
B.8	Calibrated spectrum	210

List of Tables

1.1	Types of white dwarfs and their fate in close binary systems (cf. Section 1.2.1)	32
2.1	Angular resolution of SAM/NACO	63
2.2	SAM/NACO masks	64
3.1	MC3D parameters for a disc	77
3.2	Example of parameters required for the modelling of a disc in MC3D	81
4.1	MIDI observing log for V4334 Sgr.	91
4.2	Spitzer Space Telescope IRS slits.	92
4.3	Broadband photometry by AKARI and WISE	94
4.4	MC3D model parameters of an amorphous carbon disc.	99
5.1	VLTI observing log for M2-9	118
5.2	ISOCAM photometry	121

5.3	M2-9 photometry	126
5.4	Grain size distributions	132
5.5	Parameters of the best fitted model for M2-9. Our trial and error estimates of the parameters' uncertainties do not significantly alter the quality of the fit.	132
5.6	Dust sublimation radii	137
5.7	Binary orbital diameters	138
5.8	Accretion luminosities	141
6.1	V Hya photometry	149
6.2	NACO filters	152
6.3	Diameters of V Hya from interferometric observations in the literature.	156
6.4	Diameters of V Hya by SAM/NACO	157
6.5	Physical stellar radii of V Hya	158
6.6	Image reconstruction parameters for SAM data.	160
6.7	Dusty envelope sizes for V Hya	163
6.8	V Hya binary orbital semimajor axis estimations	166
6.9	Angular sizes (Gaussian) in mas from the Keck aperture masking experiment.	171
6.10	Observation log of V Hya	172
7.1	Dusty structures at different evolutionary stages	180
A.1	Evolved stars with discs	190
A.2	MIDI data reduction	190
B.1	An example for a science target and a calibrator	202

Abstract

From the main sequence onwards, stars of intermediate masses ($1\text{--}8M_{\odot}$) eject a large portion of their mass with rates as high as $10^{-4}M_{\odot}\text{yr}^{-1}$ during their transition through the Asymptotical Giant Branch (AGB) stage. The outflows are shaped by the same mechanisms that shape the ejecta, which in turn appear to depart from spherical symmetry as early as the AGB stage. The ejecta are then evolving into asymmetrical structures. Stars like that are giant factories of dust, responsible for the enrichment of their surrounding Galactic medium in metals heavier than helium. Depending on their abundances during the AGB stage, the stars are either oxygen-rich or carbon-rich, and as such, the dust produced in their atmospheres is either O-rich or C-rich. The chemical composition of the ejecta, indicates the stellar chemistry at the moment of ejection. The disruption of the spherical symmetry of the mass loss can be caused by fast rotation, stellar magnetic fields or binarity, the latter being the most efficient and favourable mechanism. Such mechanisms can lead to the creation of circumstellar, equatorial, dusty structures, like discs, torii or spirals. Due to their small relative sizes, compared to their surrounding nebulae, they can be studied at best with the use of infrared interferometric techniques.

We report the discovery of three such structures in sources at three different evolutionary stages, respectively, with the use of single- and multi-aperture interferometry. In the C-rich AGB star V Hya we imaged via aperture masking in the near-infrared, a complex and possibly orbiting structure, which is embedded within the star's molecular torus. Our MIDI observations in the mid-infrared have revealed, a silicate disc within the symbiotic nebula M2-9 that is currently being shaped by the central binary system within its core, and a C-rich disc-like structure in the born-again star Sakurai's Object, that is also aligned to an asymmetry found in its surrounding planetary nebula.

Finally, we compare the properties of the structures found here with those found in the literature in order to establish a relation between late stellar evolution and the existence of dusty structures.

Declaration

No portion of the work referred to in the dissertation has been submitted in support of an application for another degree or qualification of this or any other university or other institute of learning.

Supporting publications:

A dense disc of dust around the born-again Sajurai's object

Chesneau O., Clayton G.C., Lykou F., de Marco O., Hummel C.A., Kerber F., Lagadec E., Nordhaus J., Zijlstra A.A., and Evans A. (2009) *A&A* *493* L17

A disc inside the bipolar planetary nebula M2-9

Lykou F., Chesneau O., Zijlstra A.A., Castro-Carrizo A., Lagadec E., Balick B., and Smith N. (2011) *A&A* *527* A105

A close halo of large transparent grains around extreme red giant stars

Norris B.R.M., Tuthill P.G., Ireland M.J., Lacour S., Zijlstra A.A., Lykou F., Evans T.M., Stewart P., and Bedding T.R. (2012) *Nature* *484* 220

Copyright Statement

- i. The author of this thesis (including any appendices and/or schedules to this thesis) owns certain copyright or related rights in it (the “Copyright”) and s/he has given The University of Manchester certain rights to use such Copyright, including for administrative purposes.
- ii. Copies of this thesis, either in full or in extracts and whether in hard or electronic copy, may be made **only** in accordance with the Copyright, Designs and Patents Act 1988 (as amended) and regulations issued under it or, where appropriate, in accordance with licensing agreements which the University has from time to time. This page must form part of any such copies made.
- iii. The ownership of certain Copyrights, patents, designs, trade marks and other intellectual property (the “Intellectual Property”) and any reproductions of copyright works in the thesis, for example graphs and tables (“Reproductions”), which may be described in the thesis, may not be owned by the author and may be owned by third parties. Such Intellectual Property and Reproductions cannot and must not be made available for use without the prior written permission of the owner(s) of the relevant Intellectual Property and/or Reproductions.
- iv. Further information on the conditions under which disclosure, publication and commercialisation of this thesis, the Copyright and any Intellectual Property and/or Reproductions described in it may take place is available in the University IP Policy (see <http://www.campus.manchester.ac.uk/medialibrary/policies/intellectual-property.pdf>), in any relevant Thesis restriction declarations deposited in the University Library, The University Library’s regulations (see <http://www.manchester.ac.uk/library/aboutus/regulations>) and in The University’s policy on presentation of Theses.

Acknowledgements

It's been five years since I started this work and in all this time and in all the places that I've been, there have been many people that influenced me.

This project wouldn't have started unless a certain person believed that I had some potential in the first place. Albert, I thank you for your trust and support, for allowing me to become a better scientist by figuring out the answers to my own questions (yes, the Socratic method does work), for helping me when I needed it, and for introducing me to Oddsocks! I will keep all your advice in my future career.

There's a lot to be said about my co-supervisor, Olivier. We've spent nearly six years spinning (sometimes crazy) theories, fitting thousands of models, arguing about science, all that while enjoying some good wine and cuisine in Côte d'Azur. All I can say Chef is thanks for being there.

Eric, mon PCDM, is the very first person I met in this University when I came here six years ago. He left the country the very next morning (for his observing run in Chile). Thanks for showing me the tricks of the job, allowing me to ask you the stupid questions I was too scared to ask the supervisors, engaging in legendary kicking matches (where I will always win by the way!) and being a friend.

I'd like to thank my good friend David for all his support and for good relaxing times over pint(s) and a game of pool. Ana and Marta, zee portuguese, started their PhD with me. We've become close friends ever since and have been through thick and thin. Thanks for being there with me girls. Stefania, has helped me a lot while I was lost in translation with all the polarisation jargon. And there's no better partner in crime when it comes to cooking and photographic expeditions. Liz "the Mexican menace" and Czarek my partners in crime for so many years. A big thank you goes out to Dave who has lent an ear in difficult times and managed to keep my spirits up. I'd also like to thank all the people that I've met in the office – Bruno, Tijl, Kerry, Peter, Nico, Lyshia, Nadya, Roisin, Danny – for accepting me as one of their own, having

some great fun when our work was just too much, and being my friends.

I'd like to thank the people at the OCA Grasse for welcoming me each time I went to work there. And let me thank the Australians, Peter and Barny, for helping me learn the secrets of aperture masking.

Last but not least, are my sister, who always pushed me forward (sometimes quite literally) and my parents. After all, without them nothing would have started. My family's love and support allowed me to be a scientist and I hope I made them proud.

Dedication

Στους γονείς μου

Ντίνα και Θανάση

χωρίς τους οποίους δε θα έφθانا ποτέ ως εδώ.

The Author

has received a BSc in Physics from the University of Crete, Greece, and a MSc by Research in Astrophysics from the University of Manchester. The contents of that MSc thesis were published in a scientific journal (Chesneau et al., 2007, A&A, [473](#), L29). The author has received two European Initiative Fizeau visitor scholarships to work with her co-supervisor Olivier Chesneau at the Observatoire de la Côte d’Azur in Grasse, France, for a period of four months in total. Another visitor grant allowed her to train in aperture masking at the University of Sydney. Two publications have been based on the contents of this thesis (Chesneau et al. 2009, A&A, [493](#), L17 and Lykou et al. 2011, A&A, [527](#), A105), and three more are in preparation. Data from the last observing run at VLT/ESO have been presented in *Nature* by Norris et al. 2012, *Nature*, [484](#), 220. In late 2010, the author edited the Asymmetric Planetary Nebulae V conference proceedings.

CHAPTER 1

Introduction

Αστέρες ουράνιοι, Νυκτός φίλα τέκνα μελαίνης
εγκυκλίοις δίναιοι περιθρόνια κυκλέοντες
ανταυγείς, πυρόεντες, αει γενέτηρες απάντων,
μοιρίδιοι, πάσης μοίρης σημάντορες όντες...

Celestial stars, Night kisses [its] dark children
following endless circles
bright, flashing, giving birth to all
myriads, rulers of fate...

Orfic Hymn to the Stars

For millennia man has been looking at the stars in an attempt to find what lies beyond his reach. Being unable to understand the heavens, an early solution

was to attribute their presence to gods and deities and name them accordingly. The names of the brightest stars, planets and constellations were known as early as the Bronze Age and the Babylonian astronomers. As societies evolved so did the scientific conception seen in the advances of civilisations such as the Ancient Egyptians, Greeks and Romans. The Antikythera Mechanism, an ancient form of a computer that worked as an almanac and a calendar by calculating the exact movements of the Sun, the Moon and some of the known planets, is an example of such progress (Freeth et al. 2006, 2008).

Of course the ancient civilisations left us with some misconceptions as well, like the Ptolemaic view of the ἀπλανείς αστέρες (meaning “immovable stars”) placed at a fixed distance around the Earth, over the circles that defined the positions of the known planets. It took centuries for people to accept Copernicus’ idea that the Earth is orbiting the Sun and only after the progress made by Brahe, Kepler and Newton on celestial mechanics, and the use of a telescope for astronomical observations by Galileo, to reach the level of knowledge we have today. Even though we have advanced significantly technologically speaking and we can say that we comprehend in general what ancient peoples assumed to be the mysteries of the Universe, there are still many questions that remain open, such as the one about stellar evolution. For the Ancient Greeks, the term “immovable stars” meant that they were not supposed either to move or evolve. Yet we now know that neither of those traits is true, and we are able to observe the evolution of stars within less than a century’s timeframe (e.g. Sakurai’s Object, V838 Monocerotis).

Stellar evolution in the Universe is a recycling process. Every star is born through the “ashes” of previous stars and dies only to produce similar ashes and replenish its surroundings. Those ashes are of gaseous and dusty form and they are produced at its late evolutionary stages. Stars with an initial mass between 0.8 and 8 Solar masses, are considered as low and intermediate mass stars. These stars will follow, similar to the Sun, an evolution that is described below.

1.1 Evolution of a single star

1.1.1 Main Sequence and beyond

Low and intermediate mass stars mature for a few billions of years¹ on the Main Sequence (MS). Depending on their initial mass, two different nuclear-burning helium-producing sequences may occur. Stars more massive than $1.5 M_{\odot}$, burn their hydrogen resources via the *CNO cycle*. These stars contain a convective core and a radiative envelope. In stars with masses less than $1.5 M_{\odot}$ the *proton-proton reaction* is dominant and the core is radiative while the envelope is convective (Karttunen et al. 2007).

Nuclear burning in the core ceases when hydrogen is exhausted, leaving behind a helium-rich core. That signifies the end of the main sequence era. Gravitational forces prevail over radiation pressure and the core contracts. Hydrogen is still burning in a shell above the core and an increase in luminosity is observed (Fig. 1.1). To enable the outwards transportation of the increasing luminosity, the radiative envelope is converted into a convective one (Applegate 1988). The envelope is expanding and thus cooling², as seen in the Hertzsprung-Russel (H-R) diagram, and the star is now ascending the Red Giant Branch (RGB, Figure 1.1) and it will remain there for $\sim 10^8$ years. For a short period of time, the convective hydrogen envelope may penetrate the helium core allowing heavier material³ (helium, carbon, oxygen and nitrogen) to be carried towards the stellar surface. This process is called a “dredge-up” event. Due to convective mixing the nitrogen abundance is increased while the carbon abundance on the surface is reduced and oxygen levels remain the same⁴.

For low-mass stars, core contraction produces a degenerate helium-rich sphere. Further contraction of the surrounding shells is stopped by the core’s degenerate electron gas pressure. Once the core contracts enough for its temperature to rise to ~ 350 million degrees, helium is violently ignited in the

¹The time spent by a star in each evolutionary stage is highly dependent on its mass at the beginning of the Main Sequence.

²The star approaches the Hayashi track where the effective temperature is nearly constant (Hayashi 1966).

³Elements heavier than helium are also known as “metals” in astrophysics.

⁴The conversion of ^{14}N to ^{15}O is slow and allows the accumulation of nitrogen.

core lifting the degeneracy of the solid-like core. This process is known as a “helium flash” and helium is now converted into carbon by the “triple-alpha” reaction. For intermediate-mass stars helium burns into carbon and oxygen, producing a degenerate carbon-oxygen rich core⁵.

With the helium flash comes the end of the RGB and both low- and intermediate-mass stars can now move towards the Horizontal Branch (HB) where helium burns quiescently in the core. When that ceases, a degenerate carbon and oxygen core is left surrounded by helium and hydrogen convective shells and a larger idle hydrogen-rich envelope.

1.1.2 AGB

The contraction of the core, and the re-ignition of hydrogen at the shell boundaries, allows a second dredge-up to occur and the star is now ascending the Asymptotic Giant Branch (AGB). Oxygen is again the most abundant element, thus the star is called “oxygen-rich” (O-rich). This stage of ascent is called early-AGB (E-AGB). The stellar envelope expands while the stellar core contracts and the increase in temperature between the core and the helium shell leads again to thermonuclear burning of helium. The phenomenon is called a “thermal pulse” after which the second AGB stage is named (thermally-pulsing AGB, TP-AGB). Pulsations are responsible for the variability in stellar luminosity, which is detected by constant photometric monitoring of the star.

Thermal pulses allow material to escape from the star, until the stellar envelope is reduced to less than $0.05 M_{\odot}$ in mass (Bloeker 1995; Schonberger & Blocker 1993). A star can stay for approximately 10^6 years on the AGB. It is assumed that mass loss ceases (Section 1.3) when the envelope mass is decreased to $0.001 M_{\odot}$ (Schonberger & Blocker 1993; Schönberger & Blöcker 1996). This signifies the end of the AGB and the star will now slowly evolve bluewards on the HR diagram (Figure 1.1).

⁵For future reference, carbon-oxygen chemistry will be designated with a ‘CO-’ prefix, not to be confused with carbon monoxide.

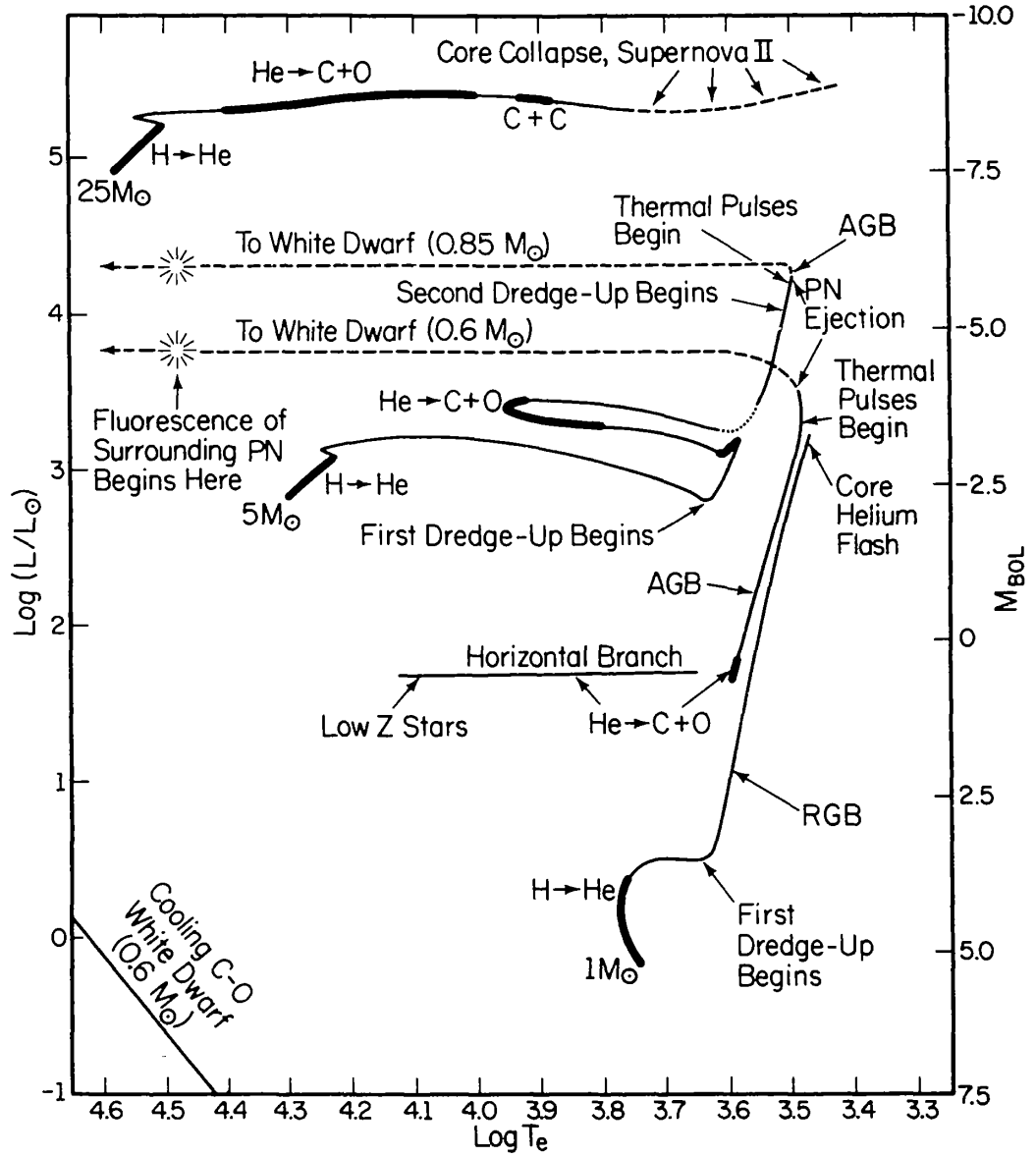


Figure 1.1 – A Hertzsprung-Russell diagram showing the evolution tracks of stars of low- to intermediate-mass stars. The massive $25 M_{\odot}$ star isochrone is for reference only. *Reproduction from Iben (1985).*

1.1.2.1 Chemistry and the stellar core

AGB evolution is highly dependent on the initial stellar mass. Stars with masses $0.8\text{--}1.8 M_{\odot}$ experience a helium-flash at the tip of the RGB while those with masses $1.8\text{--}10 M_{\odot}$ burn helium quiescently in the core from the RGB to

the AGB. The initial mass predefines the chemical composition of the AGB star and its final chemical composition as a white dwarf (Herwig 2005).

If a star is less massive than $4 M_{\odot}$, the first thermal pulse engages a third dredge-up which now enriches the envelope with carbon, thus turning the AGB star into a “carbon-rich” (C-rich) star. All subsequent thermal pulses allow slow neutron capture reactions (s-process) in the stellar interior that build elements with atomic mass numbers as high as those in the group of actinoids. For more massive stars ($4\text{--}10 M_{\odot}$) the intermixture of the convective envelope with the top of the hydrogen shell, enriches with heavier fuel its hydrogen-burning counterpart and this thermonuclear process is known as “hot-bottom burning” (HBB). Hot-bottom burning converts carbon into nitrogen. For this reason all massive AGB stars are O-rich (Herwig 2005).

Stars with masses less than $8 M_{\odot}$ develop a degenerate carbon-oxygen core which leads them to become C-O white dwarfs (CO-WD). Carbon-oxygen white dwarfs masses vary between $0.5\text{--}1 M_{\odot}$. More massive stars ($8\text{--}10 M_{\odot}$) experience both carbon-burning and hot-bottom burning during the AGB (Herwig 2005). This lifts the degeneracy from a carbon-oxygen core allowing further thermonuclear processing until the core becomes oxygen-neon rich and leading to heavier white dwarfs ($1\text{--}1.4 M_{\odot}$, ONe-WD).

1.1.3 Post-AGB

Right after the AGB phase, stars pass through the post-AGB era. At that point, the ejected stellar envelope will form a nebula around the star, which on the other hand is not hot enough to ionise the nebula. The core will contract as it is unable to sustain large sizes due to the reduction of the H-rich shell ($<10^{-3} M_{\odot}$). This shrinkage raises the effective temperature from approximately 2000 K to tens of thousands degrees within a few thousand years.

The chemical composition of post-AGB stars is defined by the abundance of the dominant elements in the AGB envelope. If oxygen is more abundant by number than carbon then the object is O-rich and if carbon is more abundant then it is C-rich.

In most cases the surrounding nebulae are not spherically symmetric. Fig-

ure 1.2 exhibits two striking examples: the Red Rectangle with a peculiar bipolar nebula (Cohen et al. 2004; Waelkens et al. 1996) and a gaseous torus (Bujarbal et al. 2003, 2005) and the Calabash nebula which possesses an equatorial overdensity (Etoka et al. 2008; Matsuura et al. 2006; Sánchez Contreras et al. 2004; Gómez & Rodríguez 2001). An interesting commonality is that they engulf binaries.

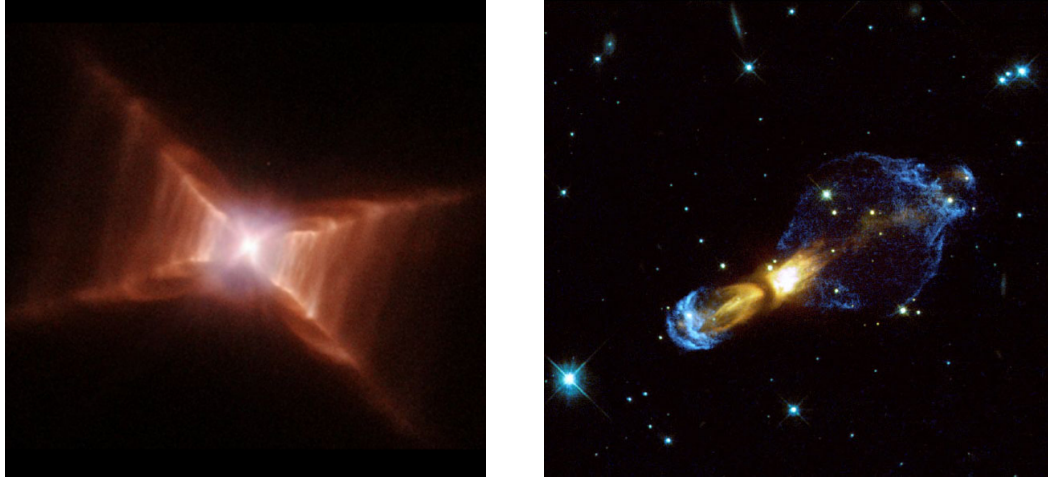


Figure 1.2 – The post-AGB stars Red Rectangle (left, Cohen et al. 2004) and Calabash nebula (right, Hubble Space Telescope NASA).

1.1.4 Planetary nebula

The effective temperature of a post-AGB star increases gradually due to the reduction of the envelope’s mass, while the luminosity remains stable (Fig. 1.1). When the effective temperature approaches 20,000 K, ionisation of the ejected envelope is initiated and the object is now a planetary nebula (PN, Herschel 1785). Nuclear burning continues and the central star can reach temperatures as high as 200,000 K. The stellar luminosity will drop rapidly once nuclear burning ceases and the star will enter the pre-white dwarf track. A typical planetary nebula core has a mass of $0.6 M_{\odot}$ and a nuclear burning rate about $6 \times 10^{-8} M_{\odot} \text{ yr}^{-1}$. A nebula created by an envelope of mass of $0.001 M_{\odot}$ (cf. Section 1.1.2) has a lifetime of $\leq 20,000$ years (H. J. Habing & H. Olofsson 2003).

Planetary nebula shapes can be either spherical, elliptical, bipolar, multipolar or irregular depending on the initial shaping conditions and viewing angle. Many exhibit even more riveting structures such as jets and ansae⁶ (Figure 1.3).

The PN shells are predominantly composed of ionised hydrogen, oxygen, nitrogen and sulphur. Planetary nebulae lifetimes are short (a few tens of thousands years) compared to the total lifespan of a star, since due to their high expansion velocities of 20 to 500 km s⁻¹, they are dispersed in the ISM.

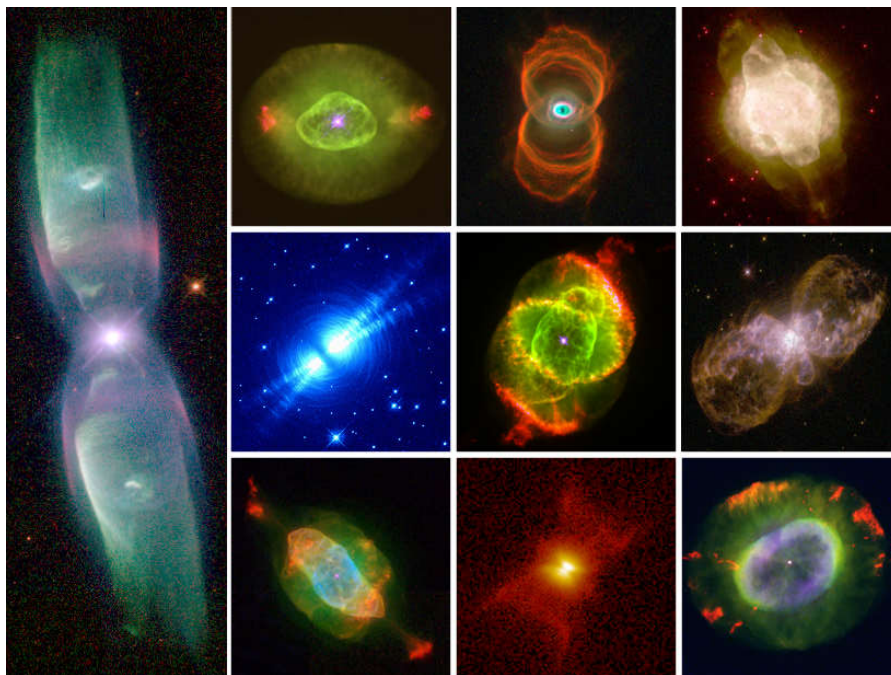


Figure 1.3 – Examples of bipolar and multipolar nebulae. Ansae are seen in the top and bottom PNe of the second column from the left. *Reproduction by Balick & Frank (2002).*

1.1.5 Very late thermal pulse

The final stages before the death of low- and intermediate-mass stars are thought to be very well known: the star will become a white dwarf and as all nuclear burning will have already stopped, its temperature will drop as it follows the WD cooling track (Figure 1.1). Nevertheless, the probability of a

⁶Knots usually extending on a symmetry axis at the farthest distances from the illuminating source.

different evolutionary track has been proposed (Iben 1985). It seems that a significant number of stars (15–20%) might pass through the stage of a “very late thermal pulse” (VLTP, Herwig 2005).

Due to the increase in pressure while the dormant star has already started descending the white dwarf cooling track in the HR diagram, nuclear burning might start again between the hydrogen and helium shell, until the temperature reaches a critical value to allow the ignition of helium (Iben 1985). Their initial nebulae may still be present (e.g. Sakurai’s Object, Chesneau et al. (2009)), although they are quite old and faint with a life expectancy about 10^4 years until they are dissociated into the interstellar medium.

During the VLTP, the helium shell is re-ignited and the star re-traces the post-AGB track. This procedure lasts a few tens of years and can be repeated within some hundreds of years. During the very late thermal pulse, new carbonaceous dust is created and as it is transferred outside, new⁷ dusty circumstellar shells are created.

1.2 Evolution of a binary

Stellar birth is not restricted to single stars only. Many stars belong in binary, or multiple, systems and their evolution depends strongly on the separation of the stars, their initial masses, and the eccentricity of their orbit (Soker 1999, 2006; de Ruyter et al. 2006; Miszalski et al. 2011c, and references therein).

The more massive companion is the one that evolves faster. As an expanding red giant, it is expected to fill its Roche lobe⁸, if it is a close binary, and its ejecta will be accreted by the companion star through the first Lagrangian point (L1). The companion is thus enriched with metals (e.g. carbon, nitrogen, lithium, neon, magnesium), which should affect its own evolutionary timescale. Part of the ejecta can also spread in the surrounding ISM via stellar winds and tidal interactions between the companions.

This series of events can occur more than once: when the primordial primary

⁷As opposed to the circumstellar shells in the initial AGB phase.

⁸An equipotential surface, defined by the orbit and masses of the binary companions, within which the mass-losing star is gravitationally bound.

refills its Roche envelope during the AGB phase or when the companion has already evolved into a red giant as well. The sequence should stop when both companions have reached the white dwarf stage.

For systems with orbits smaller than 5 AU and mass ratios $1.2 \leq M_1/M_2 \leq 1.8$ with $M_1 \geq 2M_\odot$ (Soker & Livio 1994), during the envelope expansion of the primary, the companion spirals in and is eventually engulfed within the primary’s envelope, leading to what is called a “common envelope” evolution (CE, Livio & Soker 1988). Such close binaries have orbital periods of a few hours to hundreds of days.

Wide binaries have orbital separations larger than 100 AU and orbital periods of decades to thousands of years. For example the Stingray Nebula’s binary separation is ~ 2200 AU (Soker 1999). Such long distances allow the binary components to evolve as single stars without being affected by their companion.

Table 1.1 – Types of white dwarfs and their fate in close binary systems (cf. Section 1.2.1)

Mass ¹ [M_\odot]	Type	Binary mergers ²
0.2 – 0.6	He-WD	$\xRightarrow{2\times}$ sdO star
		\searrow CO-WD swallows He-WD
0.6 – 1.0	CO-WD	$\xRightarrow{2\times}$ Type I SN
1.0 – 1.4	ONe-WD	———

¹Remnant baryonic mass by Iben & Tutukov (1986)

²Webbink (1984)

1.2.1 Fate of binary systems

The zero-age-main-sequence (ZAMS) mass defines the fate of single and binary stars. The most probable end for an intermediate mass star is for it to evolve into a CO white dwarf with the second most common scenario a He white dwarf (He-WD, Table 1.1). Oxygen-neon white dwarfs have a low production probability (see Fig. 1, Iben & Tutukov 1986).

If a close binary consists of two white dwarfs (Table 1.1), the evolution as described by Webbink (1984) is the following: (i) two He-WDs will merge into a He-burning O-type subdwarf (sdO star, Heber 1998); (ii) a CO-WD would accrete a He-WD’s helium, expand and eventually swallow its companion, and (iii) two CO-WDs would merge into a star that exceeds $1.4 M_{\odot}$ in mass, thus explode as a Type I supernova. Meng & Yang (2010) stipulate that the combination of a CO-WD and a main sequence (MS) star will end in a Type Ia supernova, as well.

There have been many detections of binary systems within planetary nebulae. Most of them were made from radial velocity observations and/or photometric variability. A small sample of such sources available in the current literature is presented in Table A.1.

1.3 Mass loss

As stated previously, an AGB star has a carbon-oxygen core, a helium and a hydrogen shell and a convective envelope. This envelope is composed mainly of hydrogen and molecules can be found on the envelope’s surface. Most of the carbon and the oxygen atoms in the envelope are locked in CO due to the stability of that molecular bond. Any excess carbon or oxygen is processed into more complex molecules, such as SiO, TiO and H₂O, and HCN, CN and poly-aromatic hydrocarbons (PAHs) in O-rich and C-rich stars respectively (see “molecule formation” region in Figure 1.4). Maser emission is detected mainly in O-rich stars (SiO originating within the atmosphere, H₂O in the circumstellar envelope and OH at larger distances), although water emission has been detected in some C-rich stars as well (e.g. IRC+10216, Decin et al. 2010).

Further processing of molecules and heavier metals allows the creation of dust in the envelope. AGB stars are assumed to be the main dust factories in the current Universe (Habing 1996; Höfner 2009; Olofsson 2008; Speck 2012). Dust created in O-rich environments will be mainly silicate-rich, such as amorphous silicates, crystallines, olivines and pyroxenes, while in C-rich environments dust will contain carbides, hydrocarbons and sulphides. In some cases, a mixing of

both dust types is possible.

Dust species condense at different radii depending on their chemistry. Amorphous carbon and forsterite (Mg_2SiO_4) dust condenses between 2–3 stellar radii, while iron-rich dust, such as olivine (MgFeSiO_4), condenses at distances longer than 10 stellar radii. At radii smaller than the ones mentioned here, dust grains are evaporated by stellar radiation, or destroyed by sputtering or grain-grain collisions. Micron-sized iron-free silicate grains are responsible for scattering and they help initiate the radiative pressure wind (Norris et al. 2012; Höfner 2008b).

AGB stars undergo extreme mass loss ($\leq 10^{-4} M_\odot$) which is enhanced during the visual minimum of a pulsation cycle in these red giants (Habing 1996; Iben & Renzini 1983; Iben 1985). Pulsation and radiation driven winds propel dust outside the stellar atmosphere. As a consequence, dust particles (grain radii larger than $1\mu\text{m}$) sweep gas due to their larger cross section. AGB wind velocities range from 5 to 20 km s^{-1} with corresponding mass-loss rates of 10^{-7} to $10^{-4} M_\odot \text{ yr}^{-1}$ (Höfner 2008a).

1.3.1 Asymmetries

One would expect the ejecta to be expanding symmetrically from the mass-losing star. This is not the case as seen in many evolved stars accompanied by asymmetric⁹ dust and gaseous nebulae. Approximately 80% of all planetary nebulae are aspherical (Parker et al. 2006). The creation of such non-spherical nebulae is quite puzzling. A study of asymmetric nebulae can only reveal information on the spatial distribution and velocity fields. In order to explain the origin of those asymmetries, one should look for them in the vicinity of the stellar cores as early as in the AGB.

S Ori is a pulsating O-rich AGB red giant. Interferometric observations in near-infrared, mid-infrared and radio during different pulsation phases have shown the radial expansion of the star (Wittkowski et al. 2007, 2008). The spatial distribution of the water and carbon monoxide molecular shells have been found to change along with the pulsating photosphere. In addition SiO

⁹Not spherically symmetric.

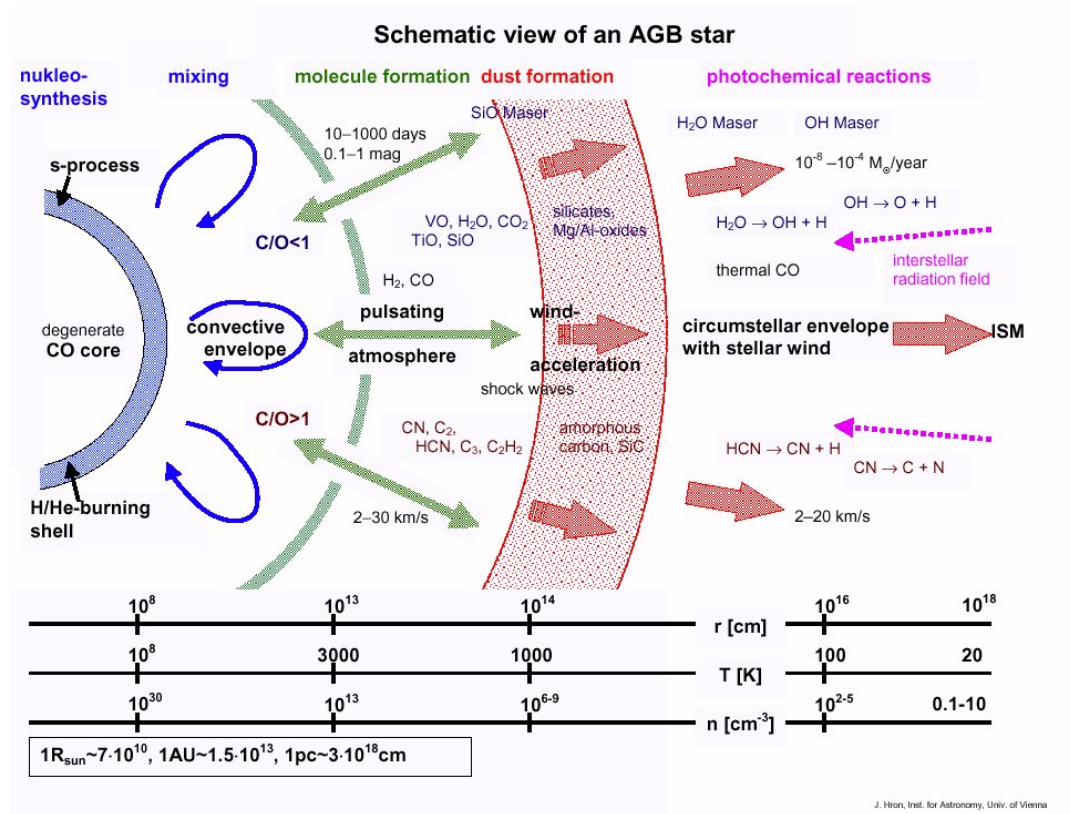


Figure 1.4 – Schematic representation of an AGB star. The top part of the image shows the products of an O-rich star, from the pulsating atmosphere toward the ISM, and the lower part those of a C-rich. *Cartoon by J. Hron*
<http://www.univie.ac.at/agb/agbdetail.htm>.

maser emission varies in phase with the expansion of an Al_2O_3 dust shell that engulfs the star (Wittkowski et al. 2007). All layers seem to expand radially without any prominent deviation from axisymmetry.

On the other hand, the carbon star IRC+10216 is a vibrant example of said asymmetries. Although the star is surrounded by an approximately 24 arcmin halo that is interacting with the ISM (Sahai & Chronopoulos 2010) and there are multiple circular dust shells forming its envelope (Mauron & Huggins 2000; Leão et al. 2006), recent interferometric observations have revealed a clumpy structure near the star that is certainly not circular as seen in Figure 1.5 (Haniff & Buscher 1998; Weigelt et al. 1998; Tuthill et al. 2000). Probable causes for the formation of such nebulae are described below.

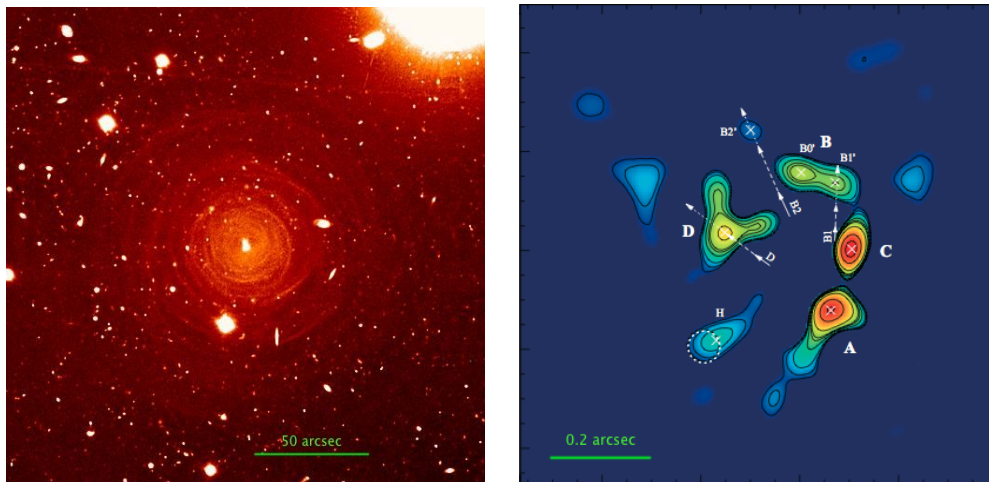


Figure 1.5 – IRC+10216. *Left*: the circumstellar dust shells in the optical by FORS1/VLT (*image credit: I. Leão*). *Right*: the core’s clumpy structure observed with aperture masking interferometry by Tuthill et al. (2000) (*Reproduction from Leão et al. 2006*).

1.4 Shaping mechanisms

The mechanisms that shape the ejecta into bipolar, multipolar or irregular nebulae are of particular interest. For example a dense structure could allow the ejecta to travel faster along the polar axis (the outflow is parallel to the polar axis, i.e. collimated outflow) of the mass-losing star.

Stellar rotation would be expected to be the main cause of such formations, but a mass-losing star is losing orbital angular momentum during the mass loss events. Thus rotation alone is not the cause of polar or equatorial ejections (Soker & Rappaport 2001; Soker 2004). Magnetic fields could also trap ejecta on the equatorial plane and there have been detections of relatively strong fields from SiO, H₂O and OH maser observations (0.1mG–3G Vlemmings 2011; Amiri 2011). Nevertheless, a magnetic field’s drag in a slowly rotating mass-losing star, that is also losing angular momentum, should eventually break the dynamo (Soker 2002, 2006). Hence, a magnetic field cannot be the sole shaping mechanism either. Collimating jets can also be responsible for nebulae shaping by driving ejecta ballistically from the star (García-Segura et al. 2005). A single star though is not capable of spinning fast enough or creating collimating jets, thus another shaping factor is needed.

The most widely accepted shaping mechanism thus far is the interactions of a binary system, such as CE evolution for binaries with small orbits, disruption of mass outflows by companions with large orbits and shifting of the centre-of-mass (Zijlstra 2007; de Marco 2009). The orbital motions of a companion will enhance the orbital angular momentum of the mass-losing star and can also shred the ejecta equatorially (as described in the following Section). The efficiency of this mechanism is highly dependent on many variables, such as the mass of the stellar companion, the separation and eccentricity of the orbits and the evolutionary stage of the companion. Close companions directly affect the mass loss of the primary star, while wide companions affect the morphology of the primary's ejected envelope (Soker 1999). There are many examples of wide binaries with orbital periods of thousands of years and asymmetric planetary nebulae. For a detailed description the author suggests the study of Soker (1999).

Planetary jovian-sized companions could play a role in shaping as well via tidal capture, though in order to survive through the Red Giant Branch phase they should orbit at distances larger than the expanded envelope of the red giant. The orbits are highly dependent on the primary's stellar mass and the onset of mass loss, e.g. 1.5 AU for a $1 M_{\odot}$ star (Madappatt et al. 2011) and 1.2 AU for a $2 M_{\odot}$ star (Kunitomo et al. 2011). Even though the planets can be absorbed by the star, they can still induce instabilities on the stellar surface and modify the stellar outflow (although mass-loss rates at this stage are low $\sim 10^{-9} M_{\odot} \text{ yr}^{-1}$).

1.5 Dusty structures

Most asymmetric nebulae are accompanied by equatorial, dusty structures, such as the one seen in the Bug nebula in Figure 1.6. These are either accretion discs, circumbinary discs, torii or spirals. They are remnants of the nebulae shaping mechanisms and are believed to be mainly associated with binary interactions in the cores of those nebulae.



Figure 1.6 – The Bug Nebula; a bipolar planetary nebula with a tight waist and a large, dusty, equatorial torus that obstructs our view to the central illuminating source. (*Image credit: NASA, ESA, Hubble SM4 ERO team*)

1.5.1 Forming such structures

Mastrodemos & Morris (1999) performed a number of simulations of binary systems of different mass ratios and separations and showed that in almost all of them, a dusty *disc* was formed. For the example shown in Figure 1.7, a companion of $0.5M_{\odot}$ orbits a three times more massive red giant at approximately 4 AU. The companion manages to spin-up the mass-losing star and increases its angular momentum. A dense dusty structure is created for a mass-loss rate of $\sim 10^{-5} M_{\odot}\text{yr}^{-1}$ and a slow wind (10 km s^{-1}). The size of the more dense part of the disc shown here is approximately 47 AU, although the disc can

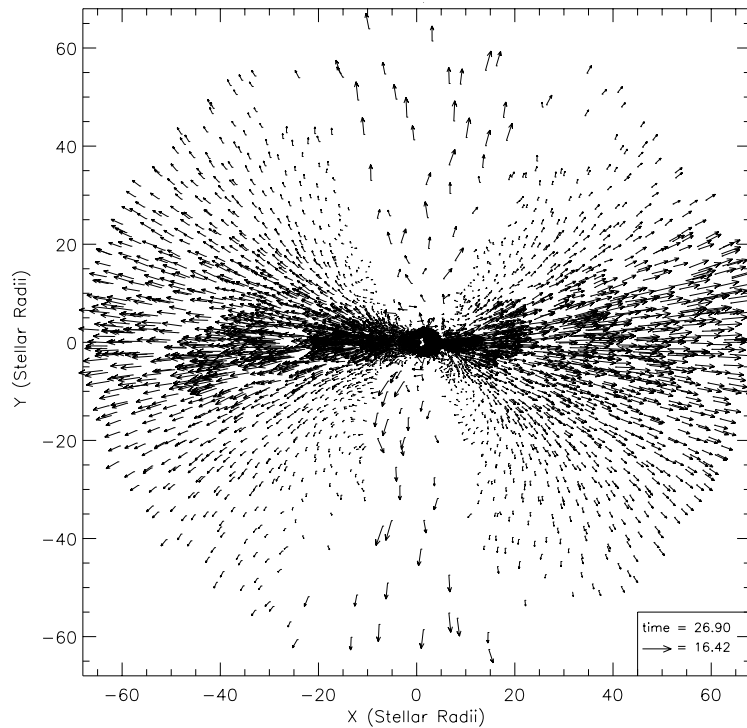


Figure 1.7 – Velocity field of the mass-loss wind from a red giant (radius \sim 1.2 AU) towards and around its companion (view edge-on to the orbital plane). The majority of the material settles in an equatorial disc, while a small part is ejected into a bipolar outflow that is seen rising from the structure. *Reproduction from Mastrodemos & Morris (1999).*

extend at larger distances and higher latitudes ($\sim 70^\circ$). The stellar wind will now encounter a dense barrier in the equatorial plane and a wide gap in the polar direction, thus the ejecta escape along the polar axis.

In a different occasion, the companion may channel the primary’s partial Roche lobe overflow onto a *spiral* structure (e.g. R Scl; Maercker et al. 2012). While the intermediate space between the binary components is cleared, the spiral might condense in order to form a large *torus* (Frankowski & Jorissen 2007). Spirals can also be formed by substellar companions as seen in the work of Nordhaus & Blackman (2006, and Figure 1.8).

In cases where the primary manages to fully fill its Roche lobe, the escaping material is gravitationally driven toward the companion creating a bridge between the stars and eventually forms an *accretion disc* around the

companion (Mastrodemos & Morris 1998). Nevertheless, dusty structures are not necessarily created only during common-envelope evolution (Soker & Livio 1994).

There have been plenty of detections of dusty structures around evolved stars in the past, from the AGB, such as AFGL3068 (Raga et al. 2011; Maunon & Huggins 2006; Morris et al. 2006), till the planetary nebula phase: Mz3 (Chesneau et al. 2007), CPD-56°8032 (Chesneau et al. 2006), OH231.8+4.2 (Matsuura et al. 2006), Hen 2-113 (Lagadec et al. 2006) and the Red Rectangle (Bujarrabal et al. 2005).

Assuming now that binarity is the main shaping mechanism of dusty structures, there are still some unanswered questions concerning their evolution:

- Do the structures stabilise after their creation or do they evolve along with their originating source?
- What is their lifetime? Could they survive the ascension from the start of the AGB to PN considering it lasts approximately a million years?

These are questions we are hoping to answer within this work and they are one of the reasons we decided to select sources from the AGB until the VLTP stage, so that a comparison can be made for structures on an evolutionary sequence.

1.5.2 Detecting the structures

Observing the dusty structures in the infrared (dust particles absorb and scatter stellar radiation which is then re-emitted in the infrared) gives information about the geometry of the structures and the chemical composition of the stars. Information about the expansion of the nebula, the directions and the velocities of the stellar wind can be derived after monitoring the atomic and molecular gas motions in the nebula.

Circumbinary discs are formed by dust from the mass-losing star that settles around the binary and outside its orbit. Silicates seem to be the dominant component (Chesneau et al. 2007; Deroo et al. 2006). Indicative radial sizes of those discs are a few $\times 10^2$ – 10^3 astronomical units. The discs are stratified. That

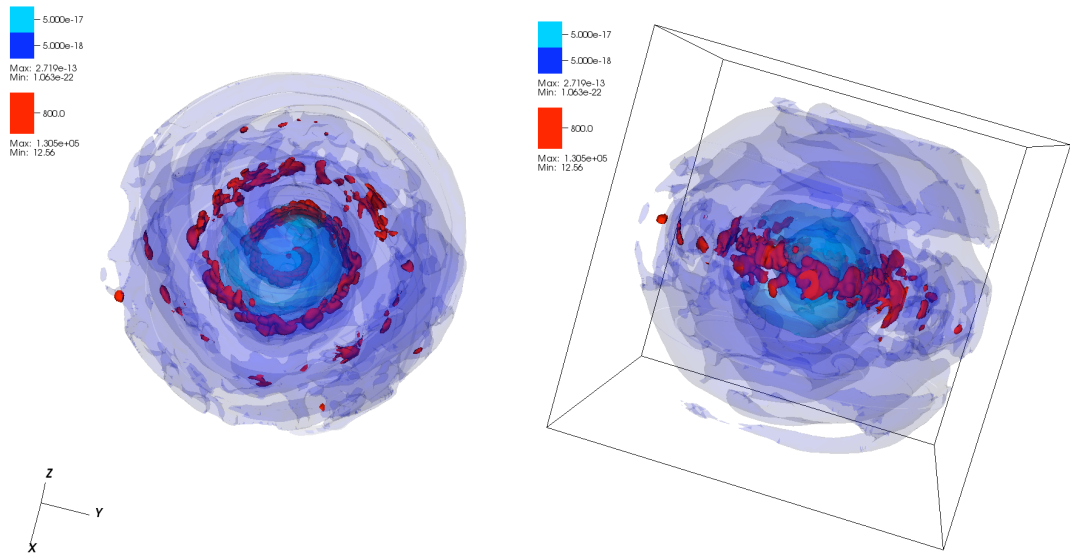


Figure 1.8 – 3D rendering of the interaction of a $0.25 M_{\odot}$ companion with the ejecta of a late-AGB primary. Binary separation is 10 AU. The temperature distribution is coloured red (800 K) and the density distributions in blue differ by an order of magnitude (dark blue $5 \times 10^{-18} \text{ g cm}^{-3}$; cyan blue $5 \times 10^{-17} \text{ g cm}^{-3}$). Pole-on view on the left and an inclined version on the right; each side of the box is 250 AU. A spiral can be clearly seen in the orbital plane of the system, as well as a bulge of material within the first two spiral arms. The overall distribution of the ejecta is spherical, but asymmetries are spread within it (Jason Nordhaus, private communication; Edgar et al. 2008).

is older, colder dust resides in the mid-plane and new material is embedded on the surface. The radii of their inner rims are dependent on their proximity to the more luminous of the stars (usually the mass-losing primary) since dust particles are evaporated by strong stellar radiation fields. Even though discs are dense and their radii can extend to a few hundred astronomical units, thus their inner parts are protected from cosmic and stellar radiation, through the course of time they are expected to be dispersed in the ISM (M2-29, Gesicki et al. 2010) and replenish it with heavier elements.

The structure of the observed target, the nebula or its jets, can be misleading about the actual shape of the discs. Nebulae with equatorial waists seen pole-on in our line-of-sight are easy to characterise (a disc or spiral structure will be obvious). That cannot be said about those nebulae perpendicular to our line-of-sight, whose equatorial waists are edge-on. The orientation will make it difficult to identify them, such as the one of the right panel of Figure 1.8.

Due to the small sizes of those dusty structures (usually 1/1000 of the surrounding nebula) single optical and infrared telescopes are not able to resolve neither the structures nor the stars engulfed in them. A solution to that problem is presented by the use of infrared interferometric techniques. Those offer resolutions as high as a few milliarcseconds and following recent advancements in the field with the combined use of more than three telescopes, images can be now recovered via these techniques.

1.6 This work

Two interferometric techniques have been employed to observe dusty structures in the vicinity of stars and these are described in the next chapter. Chapter 3 presents the basics of radiative transfer and the simulation software used in this work. Although a star evolves from the AGB to the VLTP, we present our findings in a reverse order; one that follows the sequence in which the results have been published in scientific journals. As such, we report the presence of dusty structures around three different sources: (i) Sakurai's Object, a star currently re-tracing the post-AGB track (Chapter 4); (ii) M2-9, a symbiotic star with an elongated, bipolar nebula (Chapter 5) and (iii) V Hya, a semi-regular AGB star (Chapter 6). Concluding remarks to this work and suggestions for future work can be found in the last chapter. Appendix A presents an extensive list of evolved stars that contain disc-like structures and/or other asymmetries and appendix B is a summary of data reduction process followed for MIDI data.

CHAPTER 2

Interferometric techniques

In the science field of astrophysics there is one main rhetorical question

Where would astronomers be without light ?

It would be impossible to study the stars if they were not emitting light. Although mankind has always looked at the stars, observations were limited by the use of the original visual instrument: the eye. Later on the telescope became the main observing tool at hand. In simple terms, in a reflective telescope (Newtonian) light is collected by the mirror and is guided off a secondary mirror, and optionally through lenses, on a recording device and the observer can look at the final image. Only in the last century has it been possible to advance enough technologically in order to study the Universe in the full electromagnetic spectrum.

2.1 Atmospheric contribution

The only thing that protects us from dangerous solar and cosmic radiation is our planet's atmosphere and magnetosphere¹. Unfortunately for astronomers the atmosphere is also the main reason they cannot observe the Universe properly. Much of the electromagnetic spectrum is absorbed and scattered so that only a small portion of it is able to reach the surface of the Earth. As well as this reduction in transparency, the atmosphere also distorts the light. This distortion is called *atmospheric seeing* and it is caused by variations in the refractive index of the Earth's atmosphere along different lines of sight, which introduce a phase shift to the original signal. Seeing is a main contribution to the deterioration of the efficiency of optical and infrared telescopes since optical and infrared electromagnetic waves are affected more strongly by atmospheric seeing than other wavelengths.

The size of the distortions in the phase fronts of incoming electromagnetic waves are described by *Fried's parameter*, r_0 . This is defined as the size of aperture over which the root-mean-square variation of the traversing wave's phase is one radian (Fried 1965, 1982). If the diameter of a telescope is less than r_0 , then we can recover diffraction-limited images from it, whereas if the diameter is larger than r_0 , we are limited by seeing. In this case, one possibility is to analyse large sequences of short exposures. To achieve diffraction-limited imaging in this way the signals should be recorded on detectors faster than the atmospheric temporal fluctuation time (*coherence time*, t_0). This scales linearly with the Fried's parameter: $t_0 = 0.314 \cdot r_0 / v_{wind}$, where v_{wind} is the wind speed above the telescope. In this case, if the integration time is shorter than t_0 we may assume that we have 'frozen' the atmospheric fluctuations and we can record a signal that contains diffraction limited information. Average values at the European Southern Observatory Cerro Paranal site in Chile are $r_0 = 60$ and 400 cm and $t_0 = 60$ and 400 milliseconds, for 2.2 and $10\mu\text{m}$ respectively (Ratzka 2005).

¹The Earth's magnetosphere repels high energy particles.

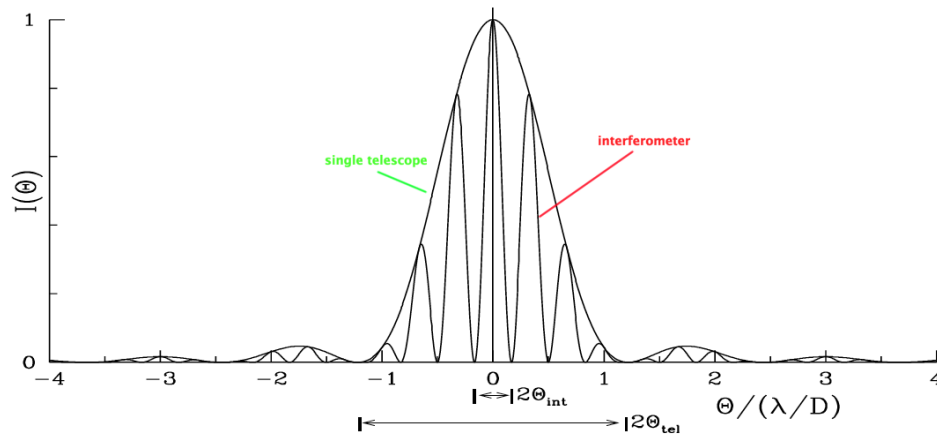


Figure 2.1 – Fringe patterns recorded by a single-dish telescope and an interferometer with two apertures. The first null of each normalised intensity distribution indicates the type of angular resolution that can be obtained with each instrument. For the single-dish telescope that is $1.22 \lambda/D$ and for the interferometer it is $0.5 \lambda/D$. For a further explanation see main text. *Reproduction from Traub (2000)*

2.2 Single telescope

A telescope’s diameter defines its ability to distinguish objects. As it was posited by Young (1802), light that passes through a small aperture is diffracted. The diffraction pattern recorded by the detector is called a *fringe*. A circular aperture, like a telescope, creates such an interference pattern whose maximum is contained within a circle known as an *Airy disc*. The size of an Airy disc is the resolution of a telescope. This is defined by the Rayleigh criterion $\sin \theta = 1.22 \lambda/D$, where for a very small angle θ (i.e. resolution), $\sin \theta \approx \theta$; λ is the wavelength at which the telescope operates and D is the telescope’s diameter (Figure 2.1). Evidently the larger the diameter of the primary mirror, the better the resolution.

The largest telescopes at the moment are the Keck twin telescopes in U.S.A. (10-m), the Gran Canarias in Spain (10.4-m), the South African Large Telescope² in South Africa (11-m) and the VLT (8.2-m). The resolution of a 10-m telescope in the K band ($2.2\mu\text{m}$) is ~ 55 milliarcseconds (mas). Any stars or structures with sizes smaller than that can not be resolved. A solution to the

²This telescope has not been optimised for imaging.

problem of maximising a telescope's diameter is the use of an interferometer.

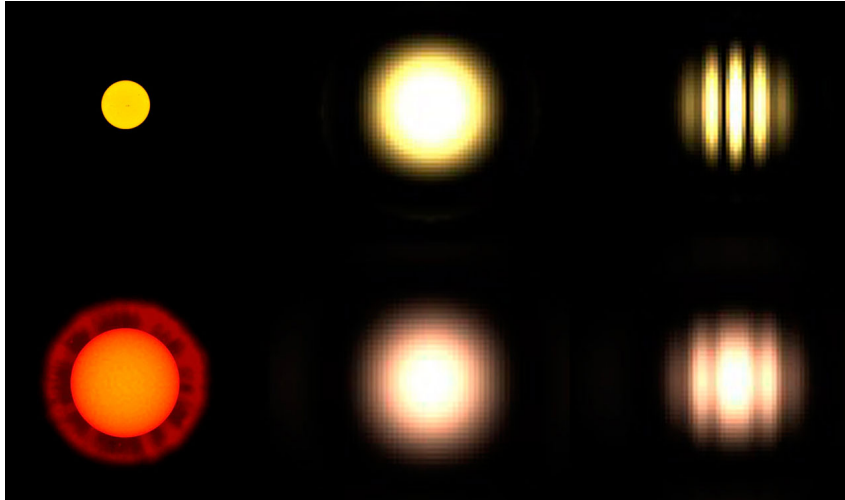


Figure 2.2 – Resolution capabilities of a single UT and the VLTI. On the top row is a star (point source) and on the bottom row a red giant with an expanding envelope. As seen in the middle column, the difference in size can not be distinguished by a single-dish telescope. An interferometer (right column) would be able to differentiate the stars. The detected fringe patterns differ and the fringe contrast of the smaller object is higher (Image by ESO)

2.3 Interferometer

An interferometer is a composite telescope. It combines light detected by each of the individual apertures, whose relative distance (baselines) determine its resolving power. Unlike single-dish telescopes that measure the intensity of the stellar light in a focal plane, interferometers measure the contrast of the fringes in the interference pattern from two or more light beams. In principle this is not so different from Young's double slit experiment, where light was allowed to pass through a sheet with two identical slits resulting in a certain diffraction pattern similar to that shown in the right column of Fig. 2.2.

A typical two-element interferometric array is shown in Fig. 2.3. Light from a distant source reaches first telescope A on the right and then telescope B on the left, since the two are separated by a distance $\vec{B} = \vec{x}_B - \vec{x}_A$ (the baseline) and the source is not located at the zenith. The extra distance covered by plane waves to reach B is indicated as $\vec{s} \cdot \vec{B}$. To compensate for this optical

delay, light collected at A is delayed by the same amount before being mixed with light from B at the detector. The two waves will then create a fringe pattern (interferogram) on the detector.

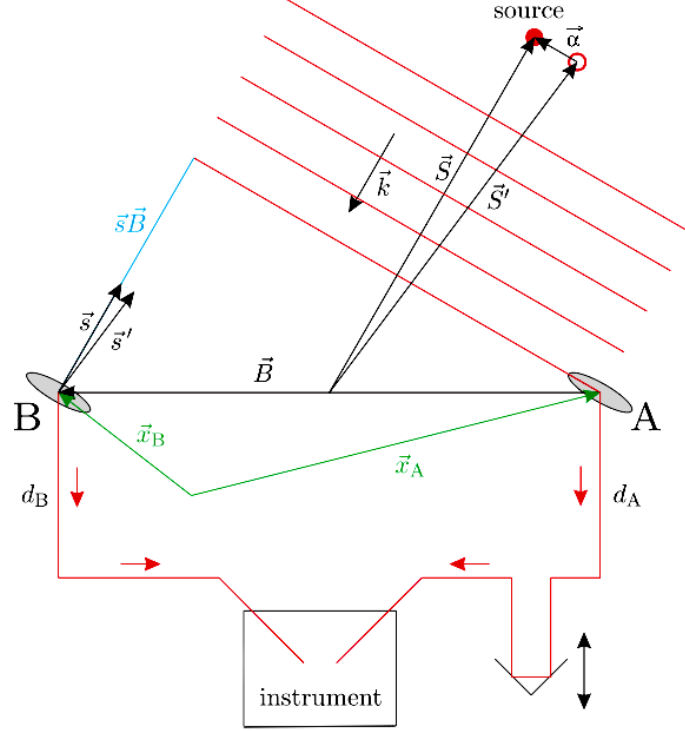


Figure 2.3 – Sketch of a two-element interferometric array from Tristram (2007). The unit vectors \vec{s} and \vec{B} of the distance to the source and the telescope separation, respectively, are clearly indicated. Their scalar product equals the geometric delay added to the signal received at the telescope closest to the source.

The waves, \vec{E}_A and \vec{E}_B , arriving at the detector have a sinusoidal pattern with the difference that signal A is modulated by the phase shift introduced from the delay line A, d_A , and signal B is modulated by the phase shift introduced by the delay line B, d_B , and the optical delay $\vec{s} \cdot \vec{B}$:

$$\vec{E}_A = \vec{E}_{A,0} \exp(-i\omega t) \exp(ikd_A), \quad (2.1)$$

$$\vec{E}_B = \vec{E}_{B,0} \exp(-i\omega t) \exp(ikd_B) \exp(-ik\vec{s} \cdot \vec{B}), \quad (2.2)$$

where k is the wavenumber and it is equal to $2\pi/\lambda$. We may now define the variable $D = d_A - d_B + \vec{s} \cdot \vec{B}$ as the optical path difference (OPD).

To be able to resolve (i.e. apply the Rayleigh criterion; Section 2.2) a second

source at \vec{S}' (Fig. 2.3), the peak of the fringe pattern of the source at \vec{S} should fall within the first minimum of the second source's fringe pattern. Thus the two fringe patterns have a phase shift of $\lambda/2$ (or π radians):

$$\begin{aligned} kD &= kD' + \pi \\ k(d_A - d_B + \vec{s} \cdot \vec{B}) &= k(d_A - d_B + \vec{s}' \cdot \vec{B}) + \pi, \end{aligned} \quad (2.3)$$

which by substituting the wavenumber $k = 2\pi/\lambda$ simplifies to

$$(\vec{s} - \vec{s}') \cdot \vec{B} = \frac{\lambda}{2}, \quad (2.4)$$

and by projecting the baseline vector on the separation $\vec{\theta} = \vec{s} - \vec{s}'$ one finds the interferometer's resolution to be equal to

$$\theta = \frac{\lambda}{2B_{\text{projected}}}, \quad (2.5)$$

as seen also in Figure 2.1.

2.3.1 Monochromatic, polychromatic and extended sources

The intensities of the waves exiting telescopes A and B will be equal to the squared modulus of the respective electric fields, which in turn are equal to the source's intensity I_{src} modified by each telescope by a factor³ $f_{\text{A or B}}$, i.e. $I_A = |\vec{E}_A|^2 = f_A I_{\text{src}}$ and $I_B = |\vec{E}_B|^2 = f_B I_{\text{src}}$, respectively. In the case of a Michelson interferometer (e.g. MIDI/VLTI), the signals (electric fields) from telescopes A and B, pass through a beam combiner. The respective waves, \vec{E}_A and \vec{E}_B , will be modified by the reflection and transmission efficiencies (\mathcal{R} and \mathcal{T}) of the beam combiner as well as an additional phase shift of $\pi/2$ due to the reflection of the beam combiner's mirror. The two recorded fields, \vec{E}_1 and \vec{E}_2 are

$$\vec{E}_1 = \sqrt{\mathcal{T}} \vec{E}_A + \sqrt{\mathcal{R}} \vec{E}_B \exp\left(i\frac{\pi}{2}\right), \quad (2.6)$$

$$\vec{E}_2 = \sqrt{\mathcal{R}} \vec{E}_A \exp\left(i\frac{\pi}{2}\right) + \sqrt{\mathcal{T}} \vec{E}_B, \quad (2.7)$$

³It depends on the optical elements' characteristics.

and the recorded time-averaged beam intensities⁴ can be evaluated as

$$I_1 = \mathcal{T}I_A + \mathcal{R}I_B + 2\sqrt{\mathcal{T}I_A\mathcal{R}I_B} \sin kD, \quad (2.8)$$

$$I_2 = \mathcal{R}I_A + \mathcal{T}I_B - 2\sqrt{\mathcal{R}I_A\mathcal{T}I_B} \sin kD. \quad (2.9)$$

Subtracting one beam intensity from another (since they have the opposite phase) we get

$$\begin{aligned} I_1 - I_2 &= (\mathcal{R} - \mathcal{T})(I_A - I_B) + 4\sqrt{\mathcal{R}\mathcal{T}I_AI_B} \sin kD \\ &= I_{\text{src}} \left[(\mathcal{R} - \mathcal{T})(f_A - f_B) + 4\sqrt{\mathcal{R}\mathcal{T}f_Af_B} \sin kD \right]. \end{aligned} \quad (2.10)$$

Ideally there should be no attenuation by the telescopes' optical elements, thus $f_A = f_B = 1$, and the beam splitter should allow 50% of the light to be transmitted and 50% to be reflected, so $\mathcal{R} = \mathcal{T} = 0.5$. Now, from Eq.[2.10] we can define the interferometric intensity to be

$$I_{\text{int}} = I_1 - I_2 = 4 I_{\text{src}} \sqrt{\mathcal{R}\mathcal{T}f_Af_B} \sin kD = 2 I_{\text{src}} \sin kD. \quad (2.11)$$

The above is true for monochromatic sources. In reality stars emit a wide range of wavelengths, thus we should integrate Eq.[2.11] over all wavelengths, λ (or else wave numbers $k = 2\pi/\lambda$),

$$I_{\text{int}} = \int 2 I_{\text{src}}(\lambda) \eta(\lambda) \sin kD d\lambda, \quad (2.12)$$

where we had to multiply with a spectral filter function, $\eta(\lambda)$, that describes the configuration used (bandpass, atmospheric window). For an ideal interferometer, the spectral filter function has the form of a top hat function⁵ centred at λ_0 and with a width $\Delta\lambda$

$$\eta(\lambda) = \begin{cases} \eta_0, & \text{if } \lambda_0 - \Delta\lambda/2 < \lambda < \lambda_0 + \Delta\lambda/2; \\ 0, & \text{else.} \end{cases} \quad (2.13)$$

⁴Remember that $I = (\vec{E}_A + \vec{E}_B)(\vec{E}_A^* + \vec{E}_B^*)$, where $*$ stands for complex conjugate.

⁵A good approximation of the N-band atmospheric transmission.

Integrating within the width $\Delta\lambda$ yields

$$I_{\text{int}} = 2 I(\lambda_0) \Delta\lambda \eta_0 \frac{\sin(\pi \Delta\lambda / \lambda_0^2 D)}{\pi \Delta\lambda / \lambda_0^2 D} \sin k_0 D \quad (2.14)$$

$$= 2 I(\lambda_0) \Delta\lambda \eta_0 \text{sinc}(\pi \Delta\lambda / \lambda_0^2 D) \sin k_0 D. \quad (2.15)$$

The sinc function is simply the Fourier transform of the spectral filter function $\eta(\lambda)$. The quantity $\lambda_0^2 / \Delta\lambda$ is known as the coherence length, Λ_{coh} . The sinc function becomes small for $|\pi D| > \Lambda_{\text{coh}}$, thus fringes can be observed only if the optical path difference, $D < \Lambda_{\text{coh}}$. The coherence length over the whole N -band ($8\text{--}13\mu\text{m}$) at $\lambda_0 = 10.5\mu\text{m}$ is approximately $22\mu\text{m}$.

Astronomical sources are not necessarily point sources. They may emit incoherent photons from an extended surface described by a number of emerging coherent point sources along a direction $\vec{\alpha}$ (Fig. 2.3). Introducing a weighting factor, \mathfrak{w} , equal to the fraction of light received by each telescope and integrating Eq.[2.11] over the surface of the target, we estimate the intensity of the extended source:

$$I_{\text{int}} = 2\mathfrak{w} \int_{\text{source}} I(\vec{\alpha}) \sin \left[k \left(D + \vec{\alpha} \cdot \vec{B} \right) \right] d\Omega \quad (2.16)$$

$$= \mathfrak{w} \left[\frac{1}{i} e^{ikD} \int I(\vec{\alpha}) e^{ik\vec{\alpha} \cdot \vec{B}} d\Omega - \frac{1}{i} e^{-ikD} \int I(\vec{\alpha}) e^{-ik\vec{\alpha} \cdot \vec{B}} d\Omega \right]. \quad (2.17)$$

The two integrals on the right-hand side are the Fourier transforms of the intensity and can be expressed ⁶ in terms of the projected baseline, B_λ (Eq.[2.5]), and the phase, $\phi = k\vec{\alpha} \cdot \vec{B}$, as:

$$\int_{\text{source}} I(\vec{\alpha}) e^{i\frac{2\pi}{\lambda} \vec{\alpha} \cdot \vec{B}} d\Omega = |\tilde{I}(B_\lambda)| e^{i\phi(B_\lambda)} = \tilde{I}(+B_\lambda), \quad (2.18)$$

$$\int_{\text{source}} I(\vec{\alpha}) e^{-i\frac{2\pi}{\lambda} \vec{\alpha} \cdot \vec{B}} d\Omega = |\tilde{I}(B_\lambda)| e^{-i\phi(B_\lambda)} = \tilde{I}(-B_\lambda), \quad (2.19)$$

and by substituting these in Eq.2.17:

$$I_{\text{int}} = \mathfrak{w} |\tilde{I}(B_\lambda)| \frac{1}{i} \left[e^{i[kD + \phi(B_\lambda)]} - e^{-i[kD + \phi(B_\lambda)]} \right] \quad (2.20)$$

$$= 2\mathfrak{w} |\tilde{I}(B_\lambda)| \sin[kD + \phi(B_\lambda)]. \quad (2.21)$$

⁶From Fourier analysis we know that the Fourier transform $\mathcal{F}(\vec{v})$ of a real function $f(\vec{x})$, i.e. $f(\vec{x}) = f^*(\vec{x})$, is Hermitian. That is, $\mathcal{F}(-\vec{v}) = |\mathcal{F}(-\vec{v})| e^{i\phi(-\vec{v})} = |\mathcal{F}(\vec{v})| e^{-i\phi(\vec{v})} = \mathcal{F}^*(\vec{v})$

2.3.2 Visibility

Unlike typical optical and infrared telescopes, an interferometer measures the contrast of the fringes, e.g. Eq.[2.21], created by the interfering beams. For a two beam interferometer this can be expressed as the time-averaged product of the intensities⁷ of the individual beams, I_m and I_n ,

$$V_{m,n} = \langle I_m(t) I_n^*(t + \tau) \rangle, \quad (2.22)$$

for an adjustable time delay τ between the two beams; the result of Eq.[2.22] is a complex quantity and it is known as *visibility*.

As shown by the van Cittert-Zernike theorem, the visibility is proportional to the Fourier transform of the brightness distribution:

$$V_{m,n} \propto \iint I(\vec{s}) \exp\left(-2\pi i \frac{\vec{s} \cdot \vec{B}_{m,n}}{\lambda}\right) d\Omega, \quad (2.23)$$

where $I(\vec{s})$ is the intensity of the signal, at a wavelength λ , in direction \vec{s} , and $\vec{B}_{m,n}$ is the vector separation of the two telescopes (see Fig. 2.3). The reader will notice that the visibility does not differ much from the quantities in Eqs.[2.18–2.19]. The result is a complex quantity

$$V_{m,n} = |V_{m,n}| \exp(i\phi_{m,n}). \quad (2.24)$$

The normalised visibility is calculated using Eq.[2.21] and knowing that for a zero baseline $\tilde{I}(0) = I_{\text{src}}$

$$V(B_\lambda) = \frac{|\tilde{I}(B_\lambda)|}{|\tilde{I}(0)|} = \frac{|I_{\text{int}}|}{2\pi I_{\text{src}}}. \quad (2.25)$$

2.3.3 Aperture synthesis

An interferometer samples the Fourier space⁸. This is a conversion between the actual coordinates of the object observed and their projection on the

⁷Or else, the time-averaged electric fields of the detected photons.

⁸A 2-element interferometer usually samples only a single point of the Fourier space.

interferometer itself. The coordinates of the Fourier plane u and v are given in spatial frequencies

$$u = \frac{B_x}{\lambda}, \quad v = \frac{B_y}{\lambda}. \quad (2.26)$$

Their orientation is along the direction of the right ascension and declination, for u and v respectively.

Theoretically in order to recover an image from Eq.[2.23], the full Fourier – or else uv -space – should be covered by the projected baselines on the sky to synthesise a full aperture. That would require a large number of ground stations, which is not currently feasible in the infrared regime since even the world’s two largest infrared interferometers, VLTI and CHARA, have only 4 and 6 stations, respectively. In principle the next generation of near-infrared arrays may be able to use larger numbers of ground-stations, but that will have to wait to be seen.

A cheap way to go around this problem is to use the Earth’s rotation during an observation. For a general interferometer, the orientation and length of the projected baselines on the sky will change for any source as it moves relative to the interferometer during the night. Nevertheless this is still time consuming and in most cases the movement of the celestial sphere and the average length of an observing night do not allow full aperture synthesis. Selecting telescope configurations with ground baselines (nearly) perpendicular to each other and spending a few hours on each target would at least allow us to identify whether the object is spherically symmetric or not (Ratzka et al. 2007). Such an object would have the same visibility at all projected baselines of the same length. Any deviation would indicate that the object is more complex in nature.

2.3.4 Bispectrum analysis

Bispectrum analysis or triple correlation is a mathematical method that allows the recovery of phase in interferometric configurations with three baselines forming a triangular pattern (Lohmann et al. 1983; Bartelt et al. 1984; Roddier 1986). For this the time-averaged third-order moment of the signal, or else the

bispectrum (\mathfrak{T}), is evaluated as:

$$\mathfrak{T} \equiv \langle \tilde{I}^3(f) \rangle \equiv \langle \tilde{I}(f_1)\tilde{I}(f_2)\tilde{I}^*(f_1+f_2) \rangle \equiv \langle \tilde{I}(f_1)\tilde{I}(f_2)\tilde{I}^*(f_3) \rangle, \quad (2.27)$$

which in essence is

$$\mathfrak{T} = \tilde{O}(f_1)\tilde{O}(f_2)\tilde{O}^*(f_3) \langle \tilde{P}(f_1)\tilde{P}(f_2)\tilde{P}^*(f_3) \rangle, \quad (2.28)$$

where the terms $\tilde{O}(f_i)$ and $\tilde{P}(f_i)$ are the Fourier transforms (FT) of the object's brightness distribution and the point spread function, respectively. f_i ($i=1,2,3$) refers to the spatial frequency of each baseline B_i and the asterisk $*$ denotes the complex conjugate.

A further clarification is needed though. This technique allows the recovery of the *closure phase*, not the actual phase of the signal detected by each baseline, which is corrupted by the atmosphere.

In more detail, let ϵ_{ϕ_1} , ϵ_{ϕ_2} and ϵ_{ϕ_3} be the phase errors for each telescope; each phase error corresponds the phase delay added by the atmospheric fluctuations above each telescope. The phase signals corresponding to each baseline, that is the phase of the complex visibility detected to each baseline, are ϕ_{12} , ϕ_{23} and ϕ_{13} . By taking the argument of the bispectrum one can estimate the closure phase. The phase signal can be included by expanding Eq.[2.27]:

$$\begin{aligned} \mathfrak{T} &= |\tilde{I}(f_1)| |\tilde{I}(f_2)| |\tilde{I}^*(f_3)| e^{-i(\phi_{12}+\epsilon_{\phi_1}-\epsilon_{\phi_2})} e^{-i(\phi_{23}+\epsilon_{\phi_2}-\epsilon_{\phi_3})} e^{-i(\phi_{13}+\epsilon_{\phi_3}-\epsilon_{\phi_1})} \\ &= |\tilde{I}(f_1)| |\tilde{I}(f_2)| |\tilde{I}^*(f_3)| e^{-i(\phi_{12}+\phi_{23}+\phi_{13})} \\ &= |\tilde{I}(f_1)| |\tilde{I}(f_2)| |\tilde{I}^*(f_3)| [\cos(\phi_{12} + \phi_{23} + \phi_{13}) - i \sin(\phi_{12} + \phi_{23} + \phi_{13})] \\ &= |\mathcal{V}(f_1)| |\mathcal{V}(f_2)| |\mathcal{V}^*(f_3)| [\cos(\phi_{12} + \phi_{23} + \phi_{13}) - i \sin(\phi_{12} + \phi_{23} + \phi_{13})], \quad (2.29) \end{aligned}$$

in which case all the phase errors are cancelled and we are left with a phase-like quantity that is the sum of all the individual phase signals. Note that here we have assumed that the phase of the average bispectrum transfer function (this is the term in the angled brackets that appears at the end of Eq.[2.28]) is zero, and we have substituted the FTs of the intensities with the corresponding visibilities \mathcal{V} of the target.

The closure phase β_{123} is then defined as the argument of the bispectrum, \mathfrak{I} ,

$$\beta_{123} \equiv \arg \mathfrak{I} = \arctan \left(\frac{\text{Im} \mathfrak{I}}{\text{Re} \mathfrak{I}} \right) = \phi_{12} + \phi_{23} + \phi_{13}. \quad (2.30)$$

This product is highly efficient for image reconstruction.

2.4 Image reconstruction

Imaging in interferometry requires the intensity distribution to be determined as a function of position on the sky. While some details of the type of source can be recovered from the visibility amplitudes, as we have previously shown, to find the exact morphology of the source (and thus not depend on model fitting; Section 2.7) one needs also to recover the phase information (Eq.[2.24]).

Assuming that one has used the aperture synthesis technique to fill in as much of the Fourier space as possible, and/or a telescope configuration that allows the recovery of closure phases, further steps are needed for images to be recovered from the data. The closure phases alone would not yield information about the absolute strength and position of the target, since their inverse Fourier transform would not return the target’s intensity distribution. These quantities can be extracted only by taking the inverse Fourier transform of the calibrated complex visibilities:

$$I'(x, y) = \iint V(u, v) \exp[2i\pi(ux + vy)] du dv. \quad (2.31)$$

Summing measurements from different uv points will give an estimate of the sky brightness, also known as a “dirty map”, which in turn is the convolution⁹ of the original brightness with a transfer function (“dirty beam”)

$$I'(x, y) = I(x, y) \otimes P(x, y). \quad (2.32)$$

The above is a linear solution that does not provide good results due to artefacts in the reconstructed data created by the assumption that a visibility

⁹Noted as ‘ \otimes ’ in Eq.[2.32]

measurement in any unsampled uv space is zero. In non-linear reconstruction there exist algorithms that are able to fill in the unsampled spatial frequencies. These algorithms will use the prior knowledge about the source and will readjust the calculations according to the statistics of the previous measurements. The produced maps will always have brightness values above zero (i.e. realistic values).

In radio interferometry the widely employed algorithm for image reconstruction is the CLEAN algorithm (Pearson & Readhead 1984, and references therein). CLEAN will deconvolve the dirty map through iterative removal of the point spread function from the point in the map with the highest intensity (Eq.[2.32]), until it reproduces a map within the expected noise level limits. The elements removed from the procedure can be convolved with a “clean beam”, i.e. an elliptical Gaussian with a FWHM similar to that of the core of the “dirty beam”, and then added to the reconstructed map. The result will be a “clean map”.

Another image reconstructive method is the *maximum entropy method* (MEM; Bryan & Skilling 1980; Buscher 1994). In this method, the generated map must have positive values in every pixel and must be the most “logical” representation of prior information. For each map, w , an “entropy” $S(w)$ is defined as

$$S(w) = - \sum_n w_n \log w_n, \quad (2.33)$$

where the index n is an identified referring to each pixel in the map. Compared to the CLEAN algorithm, where the output is composed of weighted δ -function superpositions, MEM is better suited to imaging smoothly varying intensity distributions.

The algorithm in principle creates images that are compatible with the observed data, with the inclusion of certain limiting parameters, such as the map pixel size, an image window size, and any prior information on the type (e.g. a uniform or a Gaussian disc) and angular size of the expected brightness distribution. At each iteration of the reconstruction process a new map is chosen in order to maximise the entropy and on the condition that its χ^2 will be equal or smaller than the number of sampled spatial frequencies. Here,

the χ^2 value quantifies the difference between the predicted and the observed visibility and/or closure phase measurements. The process is repeated with as many iterations needed to reproduce the original data within errors.

In this work, I have used the BiSpectrum Maximum Entropy Method software (BSMEM; Buscher 1994), which utilises the MEMSYS library (Maximum Entropy Data Consultants of Cambridge, UK). BSMEM uses the Gull-Skilling regularisation for entropy

$$S = \sum_n (I_n - M_n - I_n \log(I_n/M_n)), \quad (2.34)$$

where I_n and M_n represent the current source brightness estimate and the prior image respectively, each of which has a total number n pixels. The prior image can be a δ -function, a uniform disc or a Gaussian. This algorithm has been used to reconstruct images from the aperture masking data in Chapter 6.

2.5 Interferometry with the VLTI

The Very Large Telescope Interferometer (VLTI; Fig. 2.4) is currently the largest infrared interferometer in the Southern Hemisphere. Located in the desert on Cerro Paranal in Chile at an altitude of 2600 metres, it is composed by eight telescopes, four of which are 8.2 metres (Unit Telescope, UT) in diameter and the other four 1.8 metres (Auxiliary Telescope, AT). It has two instruments, one in the near infrared, the Astronomical Multi-BEam combineR¹⁰ (AMBER, Petrov & The AMBER Consortium 2003), which combines light from three different telescopes in the wavelength range 1–2.4 μ m, and one in the mid infrared, the MID-infrared Interferometric instrument¹¹ (MIDI, Leinert et al. 2003), which combines light from only two telescopes in the N band (8–13.5 μ m).

¹⁰<http://www.eso.org/sci/facilities/paranal/instruments/amber/>

¹¹<http://www.eso.org/sci/facilities/paranal/instruments/midi/>

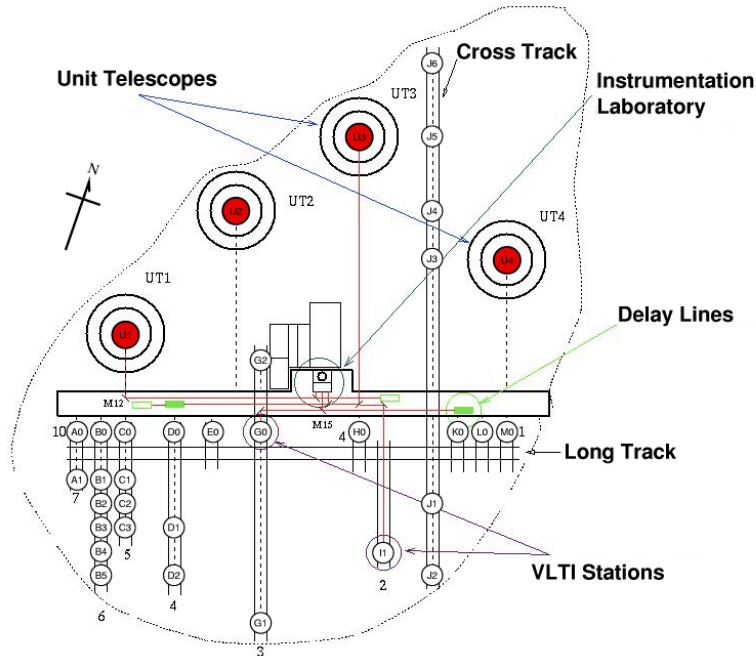
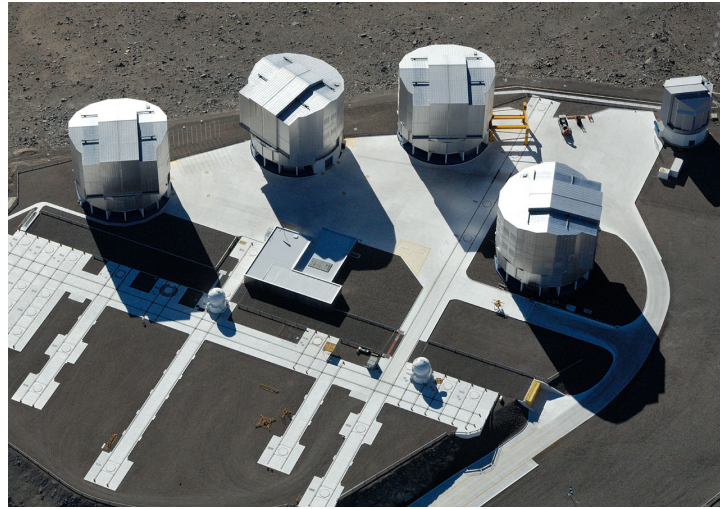


Figure 2.4 – The Very Large Telescope of the European Southern Observatory in Chile. The four 8.2m Unit Telescopes (UTs) are the dominant figures. Two of the 1.8m Auxiliary Telescopes (ATs) are shown here (there are currently four). VISTA is the telescope seen in the upper-right side of the image. The rail tracks seen on the telescope’s platform (also annotated on the sketch below), beneath which lie the interferometric delay tracks, are used to change the position of the ATs, thus change the baseline configurations of the VLTI. The building in the middle is the VLTI station. (Images by ESO © G. Hüdepohl)

2.5.1 MIDI

For this project our team has used MIDI to study in detail the central cores of nebulae and any underlying asymmetries. The MIDI instrument operates in a similar way to a classical Michelson interferometer by combining light from two Unit Telescopes or two Auxiliary Telescopes. The interferometer's best resolution is ~ 10 mas at $10\mu\text{m}$ using the longest baseline (200 metres with the ATs).

The detector is 320×240 pixels with a $50\mu\text{m}$ pixel scale that corresponds to $0.516''$ on the sky. The interferometric field of view (FOV) for the MIDI instrument¹² is $2''$ (i.e. 4 pixels; von der L  he & Ageorges 1997). The full-width-half-maximum of the Airy disc is 3 pixels per λ/D , which translates to $0.28''$ and $1.15''$ for the UTs and ATs, respectively.

In MIDI light from the two telescopes, after successfully passing through the delay lines, enters a cold box (Fig. 2.5). Each beam can be split into a photometric and an interferometric one by a photometric beam splitter. This allows 30% of the light to be used for photometry while simultaneously recording the interference pattern on the detector. This is the ‘‘science-photometry’’ (SCI-PHOT) mode. For the ‘‘high-sense’’ (HIGH-SENS) mode, the beam splitters are not included in the path and all light is directed to the beam combiner. In this mode photometry is recorded afterwards.

The beam combiner holds a ZnSe plate covered with a 50:50 coating¹³ on the bottom half of one side. The exiting interferometric beam have the opposite phase ($\Delta\phi = \pi$) and the signals are the same as those in Eqs.[2.8] and [2.9] (Fig. 2.6).

All beams pass through a filter and/or a dispersive unit before reaching the detector. Two dispersive units are available: a low-resolution prism ($R = \lambda/\Delta\lambda \sim 30$) and a moderate-resolution grism ($R \sim 230$). These offer the benefit of recording spectrally dispersed visibilities, that is one visibility is recorded per wavelength (i.e. per spatial frequency B/λ , where the baseline length B is stable and λ varies within the N band; see Fig. 2.7). MIDI offers also the

¹²<http://www.eso.org/sci/facilities/paranal/instruments/midi/doc/>

¹³50% of the beam is transmitted and 50% reflected.

acquisition of direct images at $8.7\mu\text{m}$ and of a spectrum in the N band.

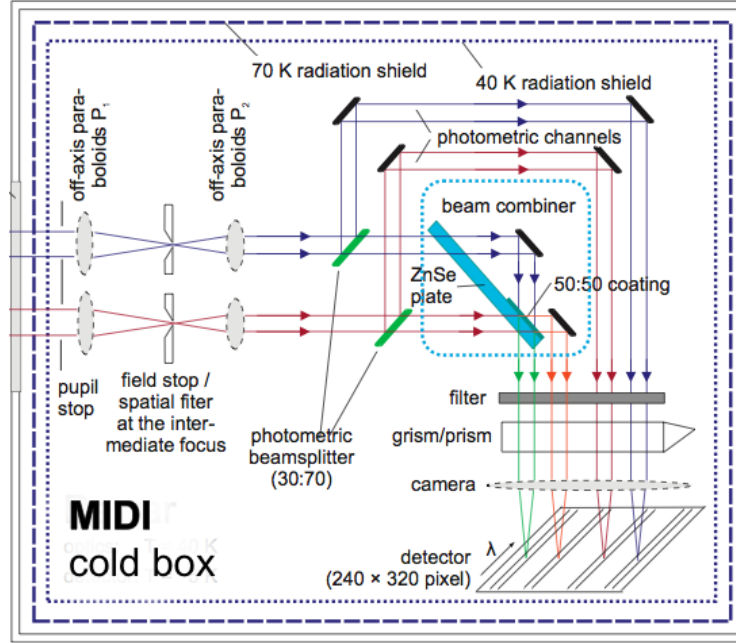


Figure 2.5 – Sketch of the MIDI cold box. The beams of the two telescopes, A in blue and B in red, can be split into two photometric and two interferometric beams by the photometric beamsplitter (green). The interferometric beams pass from the beam combiner (turquoise). All beams will then pass through a filter and a prism/grism before reaching the detector. *Adapted from Tristram (2007)*

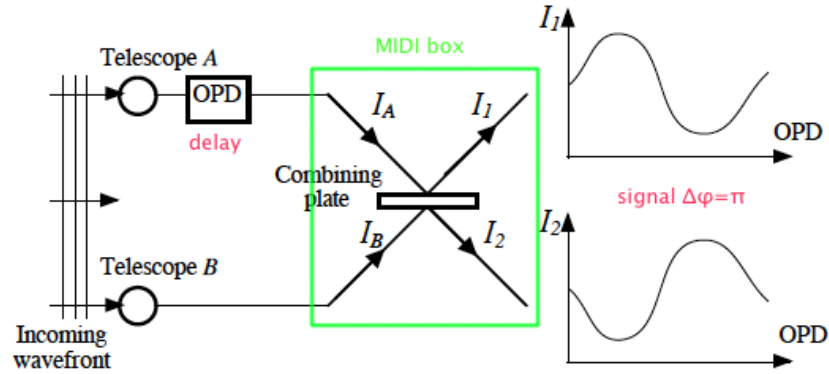


Figure 2.6 – MIDI interferometric instrument in a nutshell. Light beams from the two telescopes I_A (delayed beam) and I_B are combined within the MIDI box and the intensities of the two output channels are recorded (I_1 and I_2). The latter are phase shifted by π (cf. Eqs.[2.8] and [2.9]). *Adapted from the MIDI manual.*

2.5.1.1 Observing sequence

Initially, acquisition images are recorded from one station, with implemented chopping¹⁴ for background subtraction, to allow the good centering of the target on the detector. The procedure ceases when the two beams are aligned within one detector pixel. In the next step, the dispersive element is included in the path. The instrument will search for the fringe signal by moving the delay lines to scan the OPD within a few millimetres from an expected position¹⁵. A moving fringe pattern is recorded while MIDI's piezo-driven mirrors continue scanning in a sawtooth pattern. Fringes are usually found within an OPD range equal to the coherence length of the dispersive element. As an example, the coherence length, $\Lambda_{\text{coh}} = \lambda_0^2 / \Delta\lambda = R\lambda_0$, at $\lambda_0 = 10.5\mu\text{m}$ for the grism is $\sim 2.4\text{mm}$ and for the prism $\sim 0.3\text{mm}$. After fringes are found, the process will continue with fringe tracking during which multiple scans will be made near what is now zero OPD and the fringes are recorded on the detector. The instrumental delay is constantly monitored, which enables the re-adjustment of the delay lines to compensate for the phase shifts added. As a final step, photometry is performed, either during or after the fringe tracking, for each of the telescopes with implemented chopping. The process will be repeated for the target and all calibrators. The total observing time for a target and its calibrator for one baseline is approximately one hour.

2.5.1.2 Data reduction

Two data reduction packages can be used to analyse the data. These are the MIDI Interactive Analysis (MIA) and the Expert Work Station (EWS) packages¹⁶. Both reduction packages use the same procedures to estimate the photometry and to subtract the background¹⁷ from the recorded fringes; the latter includes the application of Gaussian masks that allow the subtraction of

¹⁴Alternating observations by tilting the telescope's secondary mirror between the science target and a nearby reference star for sky subtraction.

¹⁵Estimated from an experiential model

¹⁶For the novice reader, we suggest the use of the MIDI data reduction manual, where each data reduction step is fully explained <http://home.strw.leidenuniv.nl/~jaffe/ews/MIA+EWS-Manual/index.html>

¹⁷Thermal noise from the instrument.

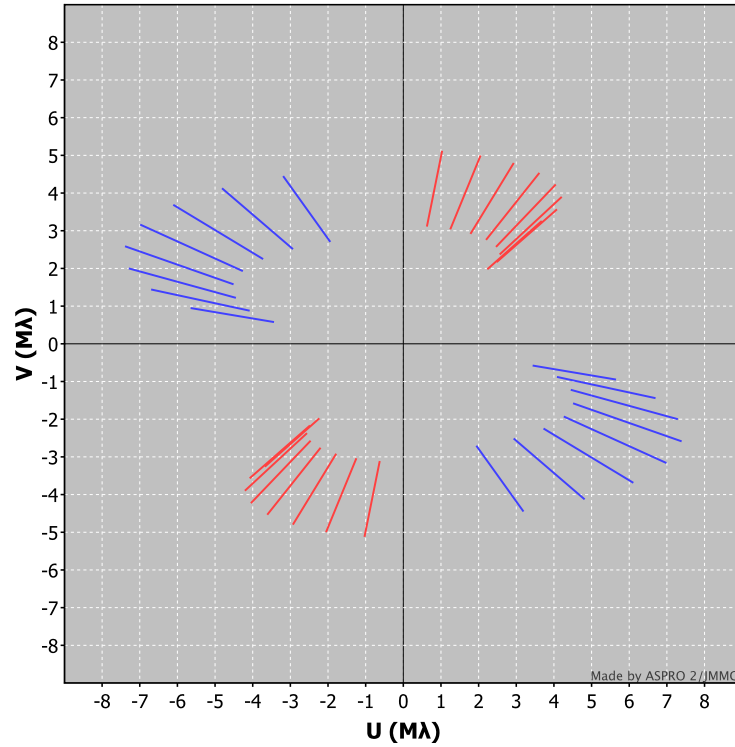


Figure 2.7 – MIDI uv coverage with telescopes UT2-UT3 (red, 47-m) and UT3-UT4 (blue, 62-m) for 8 hours of observation. One visibility is recorded per hour. The spread is due to spectral dispersion within the N band, that is one visibility is recorded per wavelength within the band, i.e. per spatial frequency $Baseline/\lambda$. One may notice that it is impossible to fill the uv plane with MIDI even within one night of observing time (~ 10 hours).

the background prior to extracting the visibilities. In theory, both packages should produce similar results. The two reduction processes are summarised below.

MIA employs power spectrum (or incoherent) analysis to calculate the object's normalised correlated flux, i.e. visibility, in the same process described in Sections 2.3.1 and 2.3.2 for polychromatic sources. A summary of the process¹⁸ is presented in Appendix B.

As opposed to MIA, the Expert Work Station package (EWS) uses coherent analysis. After the application of a mask, the signal is collapsed (integrated) in the direction perpendicular to that of the spectral dispersion, the two beams

¹⁸The notation here is similar to that presented in Section 2.3.1

(Eq.[2.10]) are subtracted from each other and then a high-pass filter is applied to remove residual noise. EWS works in very narrow bandwidths and as such Eq.[2.21] can be rewritten as:

$$I_{\text{int}} = 2\mathfrak{w}|\tilde{I}(B/\lambda)|\Delta k \sin(kD + \phi). \quad (2.35)$$

The software introduces the delay term to the signal, by multiplying it with the phase factor $\exp(-ikD)$:

$$I'_{\text{int}} = 2\mathfrak{w}|\tilde{I}(B/\lambda)|\Delta k \sin(kD + \phi) \cdot \exp(-ikD). \quad (2.36)$$

By expanding the sine using De Moivre theorem and re-evaluating the delay, D , to be the sum of the instrumental delay and the atmospheric delay, D_{atm} , we get:

$$I'_{\text{int}} = \mathfrak{w}|\tilde{I}(B/\lambda)|\Delta k \frac{1}{i} [\exp(i\phi) - \exp(-i(2kD + \phi))]. \quad (2.37)$$

Averaging the signal over time will remove the last term from Eq.[2.37], i.e. $\exp(-i(2kD + \phi))$. We now have a coherent signal that is

$$I_{\text{coh}} = \mathfrak{w} I_{\text{src}} V(B_{\lambda}) e^{i\phi_{\text{diff}}}, \quad (2.38)$$

where the phase deduced from Eq.[2.37] is called the *differential phase*.

2.6 Single telescope interferometry

Although interferometry has been widely used in the radio regime, the technique was re-established in the optical by Labeyrie in the 1970s (Labeyrie 1970, 1974; Labeyrie et al. 1974). Labeyrie introduced *speckle imaging* with a single-dish telescope. In this technique a series of exposures with integration times ideally smaller than coherence time are taken. Instead of images, speckle patterns are recorded and all information is obtained through Fourier analysis of those patterns. A similar development known as *speckle masking* was pioneered later by Weigelt (1977). One of the methods used to extract information from the speckle images is bispectrum analysis.

2.6.1 Aperture masking

Aperture masking is a revolutionary technique that converts a single-dish telescope into an interferometer. As stated by its name, the telescope’s pupil, either the mirror itself or the re-imaged beam at the pupil plane, is covered by a non-redundant¹⁹ mask whose holes act as new apertures and form an interferometer with excellent uv coverage (Haniff & Buscher 1992; Buscher & Haniff 1993; Tuthill 1994; Tuthill et al. 2010). The technique allows the recovery of diffraction-limited images from single-dish telescopes, if the apertures are smaller than r_0 at the wavelength of operation. Most telescopes offer a resolution larger than $1.22 \lambda/B$ due to atmospheric distortions. But this technique can offer high dynamic range imaging with resolutions as good as $0.5 \lambda/B$ (Tuthill et al. (2010) and here, Table 2.1).

The first imaging capabilities of this technique were introduced by Haniff et al. (1987). Diffraction-limited imaging allows the estimation of stellar sizes and the detection of faint companions. It has been tested successfully on different facilities around the world with many interesting results, especially from the twin 10-metre Keck telescopes where masks were used to cover the secondary mirror (Tuthill et al. 1998, 2000, 2006; Woodruff et al. 2008, 2009).

Table 2.1 – Angular resolution of SAM/NACO (aperture masking) in the near-infrared in mas. The diffraction-limit values, as defined in NACO specifications, are given by λ/B .

Baseline	λ [μm]	$0.5 \lambda/B$ [mas]	λ/B [mas]	$1.22 \lambda/B$ [mas]
	1.24	15.98	31.97	39.0
SAM	1.64	21.14	42.28	51.58
VLT	2.24	28.87	57.75	70.46
8-m	3.74	48.21	96.42	117.64
	4.05	52.21	104.42	127.39

2.6.1.1 SAM

At the moment, the Very Large Telescope offers the Sparse Aperture Masking (SAM) mode. It utilises the near-infrared camera CONICA of UT4 with the

¹⁹That is, each baseline configuration is unique.

Table 2.2 – SAM/NACO masks

Mask	Hole size	Throughput	Filters	# baselines	# CPs
18-1_hole	0.37 mm	3.9%	NB,IB	136	680
9_hole	0.92 mm	12.1%	NB,IB	36	84
BB9_hole	0.78 mm	12.1%	BB	36	84
7_hole	1.20 mm	16%	BB	21	35

NB : narrow band, IB : intermediate band, BB : broad band

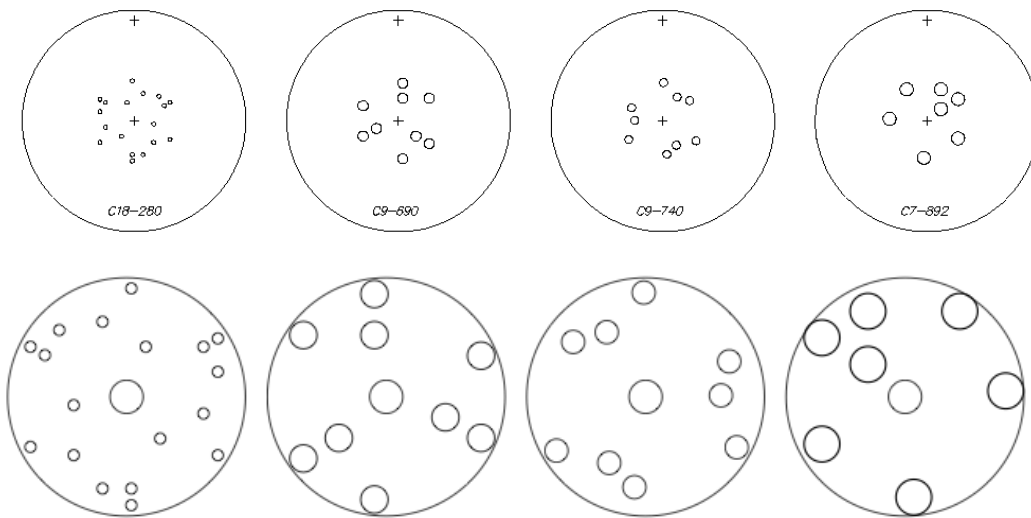


Figure 2.8 – The top row shows mechanical sketch of pupil masks (left-to-right: 18, 9, BB9 and 7 hole masks; actual diameter is 2-cm) compared to the respective apodised pupils after the insertion of masks (bottom row). The hole in the middle denotes the shadowing by the secondary mirror. © P. G. Tuthill

inclusion of the adaptive optics system NAOS (NACO/UT4). This mode differs from the one available on Keck telescope in respect to the position of the mask. A 2-cm diameter steel mask is positioned at the pupil plane, thus masking the light beam exiting the telescope (Tuthill et al. 2010). The resolution capability of UT4 increases significantly with the inclusion of SAM (Table 2.1), since for simple imaging the angular resolution is at best $1.22\lambda/D$, while for an interferometer it can drop below the diffraction limit of λ/D (see also Figure 2.1).

Four masks (Figure 2.8) are available offering a variety of uv coverages with the 18-1_hole mask being obviously the best option. Table 2.2 states

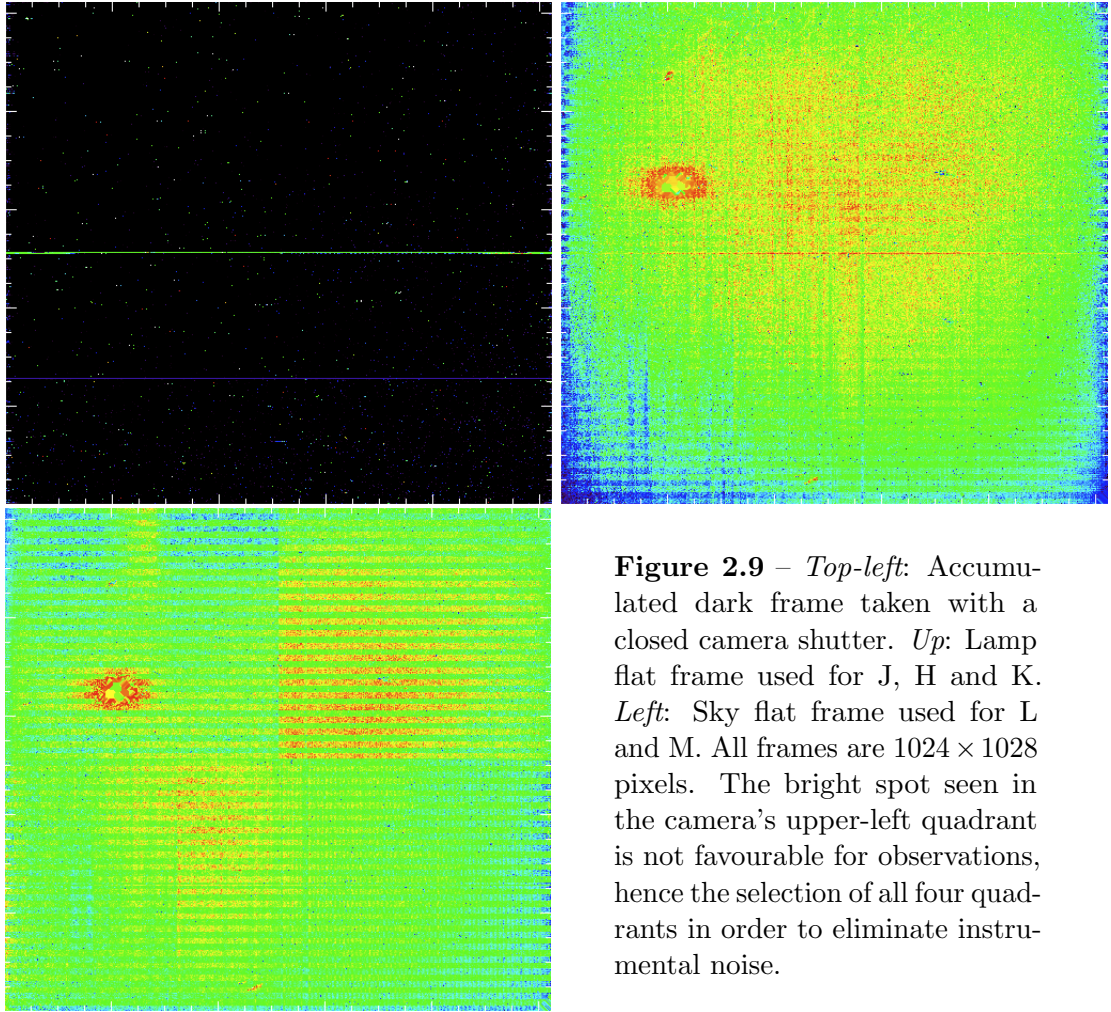


Figure 2.9 – *Top-left*: Accumulated dark frame taken with a closed camera shutter. *Up*: Lamp flat frame used for J, H and K. *Left*: Sky flat frame used for L and M. All frames are 1024×1028 pixels. The bright spot seen in the camera’s upper-left quadrant is not favourable for observations, hence the selection of all four quadrants in order to eliminate instrumental noise.

information about each mask including the number of baselines ($N(N-1)/2$) and closure phases ($N(N-1)(N-2)/6$) produced by the respective number of holes, N , for each mask.

Narrow- and intermediate-band filters can be used only for `18-1_hole` and the `9_hole` masks, while the `BB9_hole` and the `7_hole` masks accept broad-band filters only. This is mainly due to bandwidth smearing in the `18-1_hole` and the `9_hole` masks. This is further explained by the type of sources each mask should be used for observations. Bright targets must be observed either with the `18-1_hole` or the `9_hole` masks to avoid saturation with the broad-band filters. The exact selection depends on the coherence time and required amount of counts for a definitive detection. The opposite stands for fainter targets.

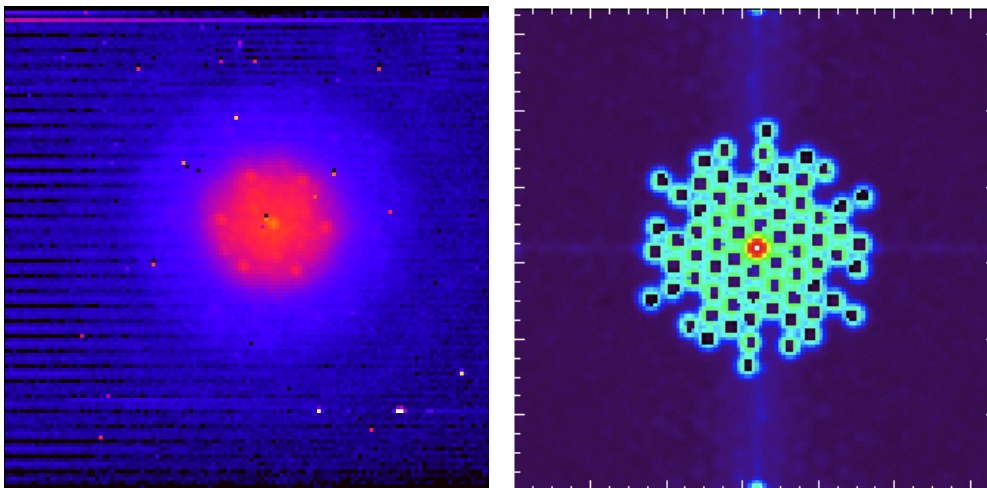


Figure 2.10 – *Left*: Raw interferogram with the 9_hole mask. Bad camera pixels can be seen within the window (size is 256×256 pixels and pixel scale is 27.05 mas). *Right*: Mean power spectrum of 600 speckle exposures cross-referenced with the MTF of the 9_hole mask (rectangular-like dark points) at $3.74\mu\text{m}$.

Furthermore for fainter targets or if the 7_hole mask is used, it is advisable to use Earth’s rotation to fill in Fourier space and to reduce further calibration errors.

To avoid concealing of the holes during observations, SAM invokes the *pupil tracking* mode of NACO. That is, the telescope’s pupil and detector are locked into the same orientation, allowing only the sky to rotate during the observing run. Hence the telescope spiders will never cover the mask holes.

Image recovery is based on bispectrum analysis, meaning the extraction of closure phases from the recorded series of interferograms. A long set of rapid exposures is taken to allow final signal enhancing, preferably faster than atmospheric coherence time (Figure 2.10).

Since observing in the optical and infrared is limited by photon and thermal backgrounds in the detectors – dark currents, photon noise and readout noise – the acquisition of a series of calibrating frames is also needed. Bias frames for each integration time and camera and flats for each filter and camera, both instrument and sky flats. A PSF must be observed as well to complete the calibration of the science target in terms of flux and angular size.

2.6.1.1.1 Data reduction The pipeline²⁰ processes the data of both the science target and the calibrator as follows:

1. Correction for instrument effects: Camera biases and flats are subtracted (Figure 2.9), then bad pixel removal is performed and at last the sky background is subtracted.
2. The modulation transfer function (MTF²¹) of each combination of mask-filter-camera is calculated (Figure 2.10) and the complex visibilities of each baseline is estimated by the FFT of each exposure.
3. Bispectra are then calculated in the manner described in Section 2.3.4; that is by multiplying the complex visibilities of each baseline in a closed triangle.
4. Finally the science target is calibrated by fitting the power spectra and closure phases of the calibrator with a polynomial function and then dividing them from their respective science target outputs.

The final results, as well as observational information from the original data, are saved in Optical Interferometry FITS (OIFITS) format, which is commonly accepted by many image reconstruction and radiative transfer codes.

2.7 Fitting the data

In the absence of direct imaging with any infrared interferometric technique, one must employ other means to interpret the observations. Radiative transfer and image reconstruction algorithms are some of those tools.

Since interferometry offers the best resolving power in modern astronomy, one may measure the angular extensions of stars and thus estimate their radii assuming that their distance is known. Sources detected by interferometers can be described with simple intensity distributions, such as a Uniform disc (UD)

²⁰Developed at the University of Sydney. The novice reader could refer to Monnier (1999) for a full explanation, even though that treatise presents an older version of the code.

²¹That is the autocorrelation of the pupil's transfer function.

for a stellar surface and a Gaussian disc (GD) for a stellar envelope or a dust shell, or a Circular Uniform Ring, respectively,

$$I(r) = \begin{cases} I_0 (4/\pi\theta^2) & , r \leq \theta/2 \\ 0 & , \text{else} , \end{cases} \quad (2.39)$$

$$I(r) = I_0 \exp \left[-\frac{4 \ln 2 r^2}{\theta^2} \right] , \quad (2.40)$$

$$I(r) = \begin{cases} I_0 (4/\pi)(\theta_2^2 - \theta_1^2)^{-1} & , \theta_1/2 \leq r \leq \theta_2/2 \\ 0 & , \text{else} , \end{cases} \quad (2.41)$$

where any θ parameter corresponds to the angular size, r is the radius in polar coordinates and I_0 is a constant. By taking the Fourier transform of the above equations, the visibility is estimated. The relation between the visibility, the spatial frequency and the angular size as shown in Michelson (1891) and Michelson & Pease (1921) can be easily described by, respectively,

$$V\left(\frac{B}{\lambda}\right) = \frac{2J_1(\pi\theta\frac{B}{\lambda})}{\pi\theta\frac{B}{\lambda}} , \quad (2.42)$$

$$V\left(\frac{B}{\lambda}\right) = \exp \left[-\frac{(\pi\theta\frac{B}{\lambda})^2}{4 \ln 2} \right] , \quad (2.43)$$

$$V\left(\frac{B}{\lambda}\right) = \frac{2}{\theta_2^2 - \theta_1^2} \left(\theta_2^2 \frac{J_1(\pi\theta_2\frac{B}{\lambda})}{\pi\theta_2\frac{B}{\lambda}} - \theta_1^2 \frac{J_1(\pi\theta_1\frac{B}{\lambda})}{\pi\theta_1\frac{B}{\lambda}} \right) , \quad (2.44)$$

where V stands for visibility, J_1 is a Bessel function of the 1st order and B/λ is the spatial frequency.

These are the models that have been used in this work for the purpose of angular size fitting. There are numerous other combinations that can approximate the complexity of stellar environments; for a list of such models we refer to the literature, e.g. Zhao-Geisler (2010).

Radiative transfer modelling

In order to relate the observed visibilities to the detected structure in the infrared, models are employed. To ensure these models are consistent representations of thermal, circumstellar environments, radiative transfer is needed.

3.1 The theory in short

The propagation of radiation through a medium is described by radiative transfer¹. Depending on its physical and chemical properties, the medium of a density ρ will change the intensity of radiation along a specific direction, I_ν , by an amount dI_ν over a distance dr described by

$$dI_\nu = j_\nu \rho dr - \kappa_\nu \rho I_\nu dr, \quad (3.1)$$

¹The discussion on radiative transfer follows the treatises of Rutten (2003, 1995); Peraiah (2001); Galvez (2005).

where $j_\nu \rho dr$ is the amount of energy emitted by the medium and $\kappa_\nu \rho I_\nu dr$ is the amount lost with κ_ν being the *absorption coefficient*. The specific intensity I_ν has units $\text{Wm}^{-2}\text{Hz}^{-1}\text{sterad}^{-1}$ while the units of j_ν and κ_ν are $\text{Wkg}^{-1}\text{Hz}^{-1}\text{sterad}^{-1}$ and kg^{-1}m^2 , respectively.

The quantity $-\kappa_\nu \rho dr$ is known as the increment of *optical depth*, $d\tau_\nu$, and it describes the medium's opacity over the distance dr the direction of travel

$$d\tau_\nu = -\kappa_\nu \rho dr \Rightarrow \tau_\nu = -\int_0^r \kappa_\nu \rho dr. \quad (3.2)$$

Substituting Eq.[3.2] in the equation of radiative transfer (Eq.[3.1])² we get:

$$\frac{dI_\nu}{d\tau_\nu} = I_\nu - \frac{j_\nu}{\kappa_\nu} = I_\nu - S_\nu(\tau_\nu), \quad (3.3)$$

where S_ν is the *source function*. Multiplying Eq.[3.3] by a factor $e^{-\tau_\nu}$ yields

$$\begin{aligned} e^{-\tau_\nu} \frac{dI_\nu}{d\tau_\nu} - e^{-\tau_\nu} I_\nu(\tau_\nu) &= -e^{-\tau_\nu} S_\nu(\tau_\nu) \Rightarrow \\ \frac{d(I_\nu e^{-\tau_\nu})}{d\tau_\nu} &= -e^{-\tau_\nu} S_\nu(\tau_\nu), \end{aligned} \quad (3.4)$$

which, by integrating from high optical depth to zero, will result in

$$I_\nu = I_0 e^{-\tau_\nu} - \int_\tau^0 S_\nu e^{-\tau_\nu} d\tau, \quad (3.5)$$

where S_ν and I_ν are interdependent and I_0 is the specific intensity at the location with optical depth τ_ν .

In local thermodynamic equilibrium the medium emits as a blackbody at a temperature T , and

$$S_\nu = B_\nu(T) = \frac{2h\nu^3}{c^2} \frac{1}{e^{h\nu/kT} - 1}. \quad (3.6)$$

Assuming that S_ν is independent of τ_ν (and so independent of position),

²This is for monochromatic emission; integration over all frequencies yields the original emission.

equation 3.5 becomes

$$I_\nu = I_0 e^{-\tau_\nu} + S_0(1 - e^{-\tau_\nu}). \quad (3.7)$$

In our case, we are interested in the anisotropic dusty medium near stars and so need to consider radiative transfer in three dimensions. The three-dimensional transport equation of radiation³ along a direction \vec{n} is

$$\begin{aligned} \vec{n} \nabla I(\lambda, \vec{n}) = & -\kappa_{\text{ext}}(\lambda) I(\lambda, \vec{n}) && , \text{extinction by dust particles} \\ & + \kappa_{\text{abs}}(\lambda) B(\lambda, T) && , \text{re-emission by dust particles} \\ & + \frac{\kappa_{\text{sca}}(\lambda)}{4\pi} \oint \mathbf{p}(\lambda, \vec{n}, \vec{n}') I(\lambda, \vec{n}') \cdot \vec{n}', && \text{scattering by dust in direction } \vec{n}' \end{aligned} \quad (3.8)$$

where κ_{ext} , κ_{abs} and κ_{sca} , stand for the extinction, absorption and scattering coefficients of dust, respectively. The function $\mathbf{p}(\lambda, \vec{n}, \vec{n}') I(\lambda, \vec{n}')$ is known as the *phase function* and describes the distribution of scattered photons.

The non-local coupling between the radiation field and the matter in radiative transfer problems means that typically significant computational power is required to solve the three-dimensional equation of radiative transfer (Eq.[3.8]), which is why it is common to solve it in one dimension only. However, there are methods to circumvent this problem and these will be explained further in Section 3.3.

3.2 Dust

The attenuation of radiation by a dusty medium is given by the *extinction efficiency*, Q_{ext} , of the grains, which is the sum of the *absorption*, Q_{abs} , and *scattering*, Q_{sca} , efficiencies. The extinction efficiency depends on: (a) the wavelength of observation; (b) the grain size and shape, and (c) the grain's optical properties, i.e. the refractive index $m = n - ik$ (where k gives rise to absorption as opposed to scattering).

³For continuum radiation, not line emission/absorption.

The efficiencies can be expressed as a function of the variable, $x = 2\pi a/\lambda$, that combines both the grain size a and the wavelength λ . For a dusty environment with a grain density, n_g , and a grain cross section⁴ $\sigma_g = \pi a^2$, the attenuation term in Eq.[3.3] can be rewritten as:

$$\begin{aligned} I_\nu &= I_0 \exp(-\tau_\nu) \\ &= I_0 \exp(-n_g \pi a^2 Q_{\text{ext}} \ell) \end{aligned} \quad (3.9)$$

$$= I_0 \exp(-n_g C_{\text{ext}} \ell), \quad (3.10)$$

where ℓ is the path length of the medium in the observer's line of sight, and $C_{\text{ext}} = \sigma_g Q_{\text{ext}}$ is the *extinction coefficient*. From the above it is clear that the optical depth, or opacity, depends on the dust grain properties

$$\tau_\nu = -n_g C_{\text{ext}} \ell. \quad (3.11)$$

For a single dust species, and thus constant coefficients, it is the size of grains that affects the propagation of light. The energy re-emitted following an absorption does not contain information about the origin of the emission, but gives information about the absorptive medium itself. The implications of physical and chemical processes that alter the grains themselves, even though they play a role in the life of dust, will not be considered here since the main question is the estimation of the grain temperature after its interaction with a photon.

Circumstellar and interstellar clouds are expected to have a wide range of grain sizes from a few nanometers to many micrometers. This is taken into account by selecting grain size distributions

$$n(a) \sim a^{-n}, \quad (3.12)$$

for a given power law index n with a minimum and a maximum size (Weingartner & Draine 2001; Mathis et al. 1977).

Grains scatter light, in which case the information of the original wave

⁴In this work, we assume that grains are homogeneous spheres of radius a , although they may have irregular shapes.

packet is not lost but it only changes direction of propagation. This phenomenon explains the diffuse light halos around dust-embedded stars. For large grains⁵, Mie scattering⁶ theory is employed to solve Maxwell's equations for the propagation of light, where the estimated dust efficiencies are co-dependent on the complex refractive properties of the grains.

3.3 MC3D

To solve the radiative transfer problem in dusty discs, we use a simulator program based on the Monte Carlo method, called MC3D (Wolf et al. 1999; Wolf 2003; Wolf & Hillenbrand 2003), which calculates the temperature distribution of dust particles within a disc and can produce spectral energy distributions and images. The code has been successfully used for the simulation of discs around young stars and Herbig Ae/Be objects (see Wolf & Hillenbrand 2003, and references therein) and can be applied to disc-like structures around evolved stars as well. We have successfully used a modified version of MC3D for the case of one young planetary nebula (Mz3; Chesneau et al. 2007; Lykou 2008).

There are other publicly available radiative transfer codes. A well known 1-D radiative transfer code is DUSTY (Ivezic & Elitzur 1997; Ivezic et al. 1999). So far, it has been widely used to model dusty environments in evolved stars (for example Lagadec et al. 2012, 2009; Blöcker et al. 2001; Zubko & Elitzur 2000). It simulates spectral energy distributions and intensity radial profiles using a repository of the optical properties of various dust species. However, this code assumes spherical symmetry, e.g. a circumstellar shell, and as such the solution of the equation of radiative transfer is computed only in one direction. Although DUSTY has the option of multiple black body emitters, it does not take into account their separation but considers them as a single point source (Ivezic et al. 1999). A pseudo-3D radiative transfer code used for spectral synthesis and simulation of photoionisation in gaseous environments is CLOUDY_3D (Morisset 2006; Ferland et al. 2013; Baldwin et al. 1991). The code includes ionisation and dust (graphites and silicates). It

⁵As an example, silicate-rich dust grains larger than $1\mu\text{m}$ (Norris et al. 2012; Höfner 2008b,a)

⁶Rayleigh scattering efficiency (small grains) is proportional to λ^{-4}

solves the radiative transfer equation in one dimension and then interpolates the results in a 3D structure. As such, this code assumes a local isotropic radiation field which does not account for variations in intensity over different directions.

MC3D is a better tool than the above radiative transfer codes as it is fully 3-D. A major advantage is the implementation of the Monte Carlo method which is much faster to calculate than full 3-D radiative transfer (although still much slower than the previous methods). The caveats of this method are the insufficient amount of photon interactions if the structure is far away from the illuminating source, and the significant computational time required for very optically thick media (e.g. eight-core 2.4GHz processor with 2GB RAM could require 4 days to process an MC3D model of a very dense disc). In this case, a point like star (of a certain luminosity L_*) will emit stochastically a number of “photon packets” in random directions within a predefined model space (Fig. 3.1). The code employs raytracing in order to follow every interaction of the photon packet with the medium enclosed within the model space, i.e. dust grains, and solves the equation of radiative transfer for each interaction.

The model space is divided into “energy cells” – according to the required geometric configuration and density gradient – in which the energy and thus the temperature after each interaction is calculated. The temperature is assumed constant over each cell.

In the case of a circumstellar disc (Fig. 3.2), stochastic emission in spherical coordinates, θ_{em} and ϕ_{em} , is given by

$$\cos \theta_{\text{em}} = (-1 + 2Z_1) \cdot \sin(\xi), \quad \phi_{\text{em}} = 2\pi Z_2, \quad (3.13)$$

where Z_1 and Z_2 are two random numbers within $[0,1]$, and ξ is the opening angle (scale height, Fig. 3.2). The energy cells closer to the illuminating source are smaller in size to allow for the steep temperature gradient calculations (Wolf 2003). The division of the grid (Fig. 3.2) into 3-D energy cells, i , is

computed by

$$r = [Z_3(r_{i+1}^3 - r_i^3) + r_i^3]^{1/3}, \quad R_{\text{in}} \leq r \leq R_{\text{out}} \quad (3.14)$$

$$\cos \theta = \cos \theta_{i+1} + Z_4(\cos \theta_i - \cos \theta_{i+1}), \quad \xi \leq \theta \leq 180^\circ - \xi \quad (3.15)$$

$$\phi = 2\pi Z_5, \quad 0^\circ \leq \phi < 360^\circ \quad (3.16)$$

where the numbers Z_3, Z_4, Z_5 also take uniform values within $[0,1]$. *Monte Carlo essentially allows three-dimensional simulations.*

Each photon is required to be scattered at least once within the grid, assuming that it will encounter at least one dust grain (τ_0) in its random walk. The free path length, ℓ , is proportional to the medium's optical depth (Eq.[3.11]) which can be evaluated to

$$\tau_{\text{ext}} = \sum_i \left[\sum_j^{n_g} \rho_{g,j}(\vec{r}_{l,i}) \cdot C_{\text{ext},j} \right] \cdot \Delta \ell_i = -\ln(1 - Z_6[1 - e^{\tau_0}]), \quad (3.17)$$

where random number $Z_6 \in [0,1]$, τ_{ext} and C_{ext} are the optical depth and coefficient of extinction, respectively, n_g is the number of different dust species j , $\rho_{g,j}$ is the density of said dust species and $\vec{r}_{l,i}$ is the direction of the photon packet for each interaction along ℓ . The random number ensures that ℓ will be in an arbitrary direction $\vec{r}_{l,i}$ within the energy cell. The step width $\Delta \ell_i$ cannot be larger than the size of an energy cell. This allows all energy cells to be used at least once.

For each point of interaction, the code will calculate the probability of the photon packet either being scattered (in a random direction based on the phase function, Eq.[3.8]) or absorbed. In the latter case, the energy within the energy cell is increased breaking the local thermodynamic equilibrium. The excess energy will be released through a new photon packet with a new frequency. This packet's transit will be also traced through the grid. The process converges once all photon packets have exited the grid.

More similar 3D codes utilising the Monte Carlo method have been developed since this work started, e.g. MCMMax (Min et al. 2009), MCFOST (Pinte et al. 2006) and HYPERION (Robitaille 2011), but benchmarking is beyond the scope of this work.

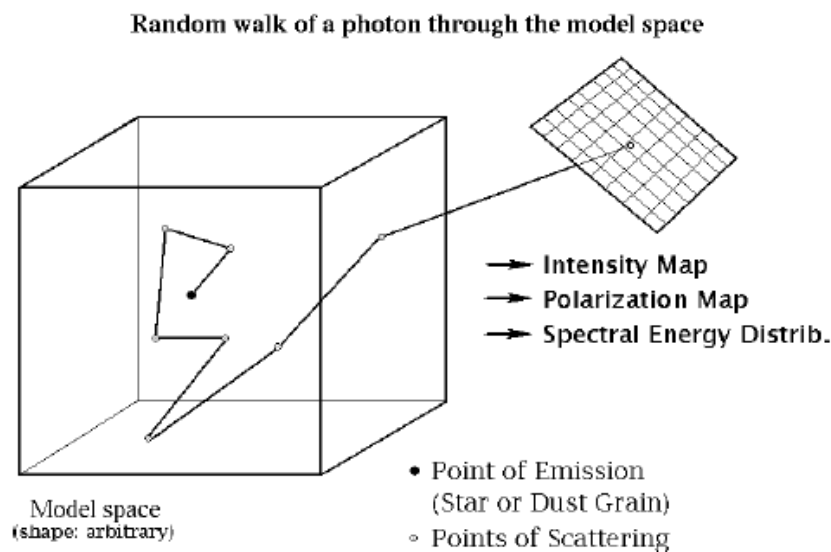


Figure 3.1 – Illustration of a photon’s random walk through an arbitrary model space. The starting point (black) can be either the star or re-emission from a dust grain. Possible points of further scattering are marked as open circles. Upon its exit from the model space, the photon’s Stokes vector is projected on an “observation plane” and the products are intensity and polarisation maps and stellar energy distributions. *Reproduction from Wolf et al. (1999)*

3.3.1 Inputs

To study the radiative transfer within a dusty environment, certain spatial and physical parameters must be defined in advance, a model of the disc geometry and density distribution, the properties of the dust compound in use, i.e. grain size, chemical composition and the illumination. The boundaries can be defined by a comparison to observations and/or theoretical approaches. For example, interferometric observations would give limits for the spatial extent of a dusty structure, while previous knowledge on the source’s spectrum would give a hint on the main chemical features hidden in the structure, e.g. silicates, carbonaceous material, oxides and others.

MC3D extracts the dust compounds optical properties from laboratory measurements of the dust refractive indices of the Heidelberg-Jena consortium⁷. The code will calculate the extinction, absorption and scattering efficiencies and coefficients for the given dust mixtures, grain sizes and requested wavelengths

⁷HJPD0C catalogue www.mpia-hd.mpg.de/HJPD0C/

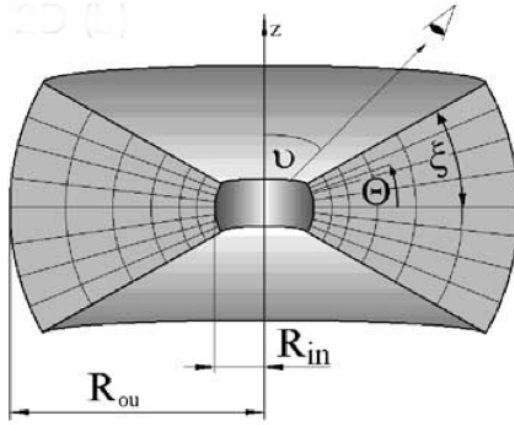


Figure 3.2 – A two-dimensional grid configuration of a disc in MC3D. Energy cells are created in both the vertical and radial directions for the given spatial limits. The user can select the sizes of the inner and outer radii, R_{in} and R_{out} , the scale height ξ as well as the inclination v in our line of sight. Adapted from Wolf (2003)

of observation. It will use a scattering matrix⁸ based on Mie theory in order to estimate the modification of propagating light, that is the photons' Stokes vectors, by dust grains.

Table 3.1 – MC3D parameters for a disc

Name	Description
R_{in}	Inner rim radius
R_{out}	Outer rim radius
M_{dust}	Mass of dust enclosed within
α	Power law index for density in the midplane
β	Flaring
h_{100AU}	Scale height at 100 AU from R_{in}
T_{eff}	Temperature of the heating source
L	Luminosity of the heating source
i	Inclination of the structure
ρ_{grain}	Dust grain density

The spatial density distribution is defined by a density law depending on both the radial and vertical extent of the disc and the geometric boundaries of the disc: inner and outer radii, flaring and scale height (Table 3.1). A two-dimensional grid (Fig. 3.2) will be defined by those parameters and it will be split into finite *energy cells*⁹ in which the radiative transfer problem is solved. Eq.[3.2] yields the optical depth and mean free path length for each

⁸The scattering matrix describes the change of the photon's Stokes vectors upon impact with a grain.

⁹Each cell contains the absorbed, within its volume, energy of the radiation field.

energy cell. The latter must be smaller than the size of the cell itself. MC3D enforces scattering in each simulation, which guarantees that each photon will be scattered at least once within the cell before escaping.

The density law used in this code is based on the best approximation of a flared disc geometry around a young stellar object (Bjorkman & Wood 2001; Wood et al. 2002), which is an adaptation of an accretion disc in a binary system with a black hole (Shakura & Syunyaev 1973). The equation of the density distribution is

$$\rho(r, z) = \rho_0 \left(\frac{R_\star}{r} \right)^\alpha \exp \left(-\frac{1}{2} \left[\frac{z}{h(r)} \right]^2 \right), \quad (3.18)$$

with

$$h(r) = h_0 \left(\frac{r}{R_\star} \right)^\beta, \quad (3.19)$$

where z is the disc vertical height, r is the radial distance in the disc midplane, R_\star is the stellar radius, β is the vertical density parameter (flaring), α is the density parameter in the midplane and h_0 is the scale height at a given distance from the star.

Intergrating over height z one obtains the surface density of the disc,

$$\Sigma(r) = \frac{\rho_0 \sqrt{2\pi}}{2h_0} \left(\frac{R_\star}{r} \right)^{\alpha-\beta}. \quad (3.20)$$

A point-like star with a known effective temperature and luminosity is defined as the radiation source (black body). The monochromatic luminosity and Stokes parameters of the emitted photons will be estimated for the required range of wavelengths (e.g. from near-infrared to millimetre). These are modified and recalculated after an interaction with a dust particle, until the photon escapes from the grid.

3.3.2 Estimation of the temperature distribution

Conservation of energy requires that the luminosity of the radiative source ($L_\star = 4\pi R_\star^2 \pi B_\lambda(T_{\text{eff}})$) should equal the luminosity absorbed and re-emitted

by dust, and that of the photons escaping directly from the grid. MC3D will solve this radiative transfer¹⁰ problem within each energy cell to estimate the grain temperature. Following the expressions of Wolf & Hillenbrand (2003), the luminosity absorbed by a dust grain, when there is no absorption between the dust grain and the star, is

$$L_{\lambda,g}^{\text{abs}} = 4\pi R_{\star}^2 \pi B_{\lambda}(T_{\text{eff}}) Q_{\lambda}^{\text{abs}} \frac{\pi a^2}{4\pi d^2}, \quad (3.21)$$

where R_{\star} and T_{eff} are the stellar radius and effective temperature, respectively; Q_{λ}^{abs} is the absorption efficiency of the grain; a is the grain size; d is the distance from the star. The re-emitted luminosity is

$$L_{\lambda,g}^{\text{emi}} = 4\pi a^2 Q_{\lambda}^{\text{abs}} \pi B_{\lambda}(T_g), \quad (3.22)$$

where T_g is the grain temperature. Integrating both equations for all wavelengths and equating to satisfy thermodynamic equilibrium, the dust temperature distribution is found:

$$d(T_g) = \frac{R_{\star}}{2} \left[\frac{\int_0^{\infty} d\lambda Q_{\lambda}^{\text{abs}}(a) B_{\lambda}(T_{\text{eff}})}{\int_0^{\infty} d\lambda Q_{\lambda}^{\text{abs}}(a) B_{\lambda}(T_g)} \right]^{1/2}. \quad (3.23)$$

3.3.2.1 Dependencies

The distribution of grain temperatures within the disc's structure depends on the disc's geometry and the properties of the dust. Such an example of a MC3D model for a dense disc (Table 3.2) for four amorphous carbon components at temperatures of 400, 600, 800 and 1000°C with respective densities at 1.44, 1.67, 1.84 and 1.99 g cm⁻³, is illustrated in Figure 3.3. All four dust components were populated by the same grain size distribution (index: $n = 3.5$; sizes: $0.005 \leq a \leq 5\mu\text{m}$).

In Figure 3.3, it is evident that the disc temperature drops with increasing grain density and increasing disc radius. The lower limits in the four plots

¹⁰Returning to the equation of radiative transfer (Eq.[3.1]), the emission and absorption coefficients per unit volume for a number of grains, n_g , will be $j_{\nu}\rho = \frac{1}{4\pi}n_g4\pi a^2\pi Q_{\nu}B_{\nu}(T) = n_g\pi a^2Q_{\nu}B_{\nu}(T)$ and $\kappa_{\nu}\rho = \frac{n_g\frac{4}{3}\pi a^3\rho_g}{n_g\frac{4}{3}\pi a^3\rho_g} = \frac{3Q_{\nu}}{4a\rho_g}$.

correspond to grain temperatures within the disc's midplane, while the higher limits correspond to those on the disc's surface. This indicates that grains residing within an opaque structure and far from the radiative source have lower temperature. Zero temperatures indicate grains that did not interact with photons.

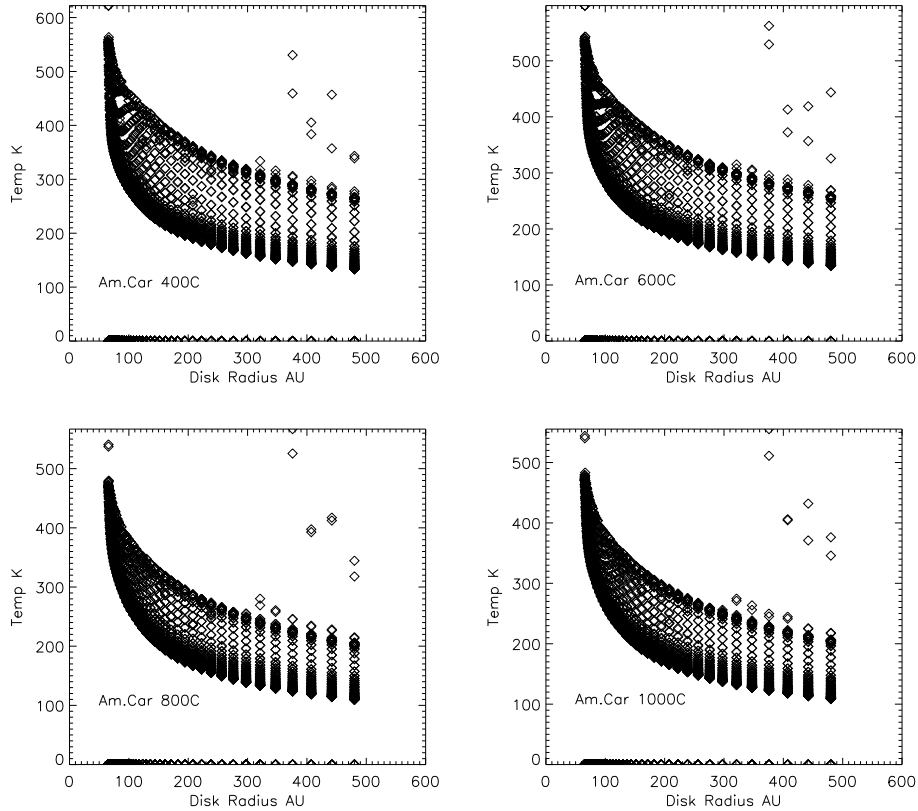


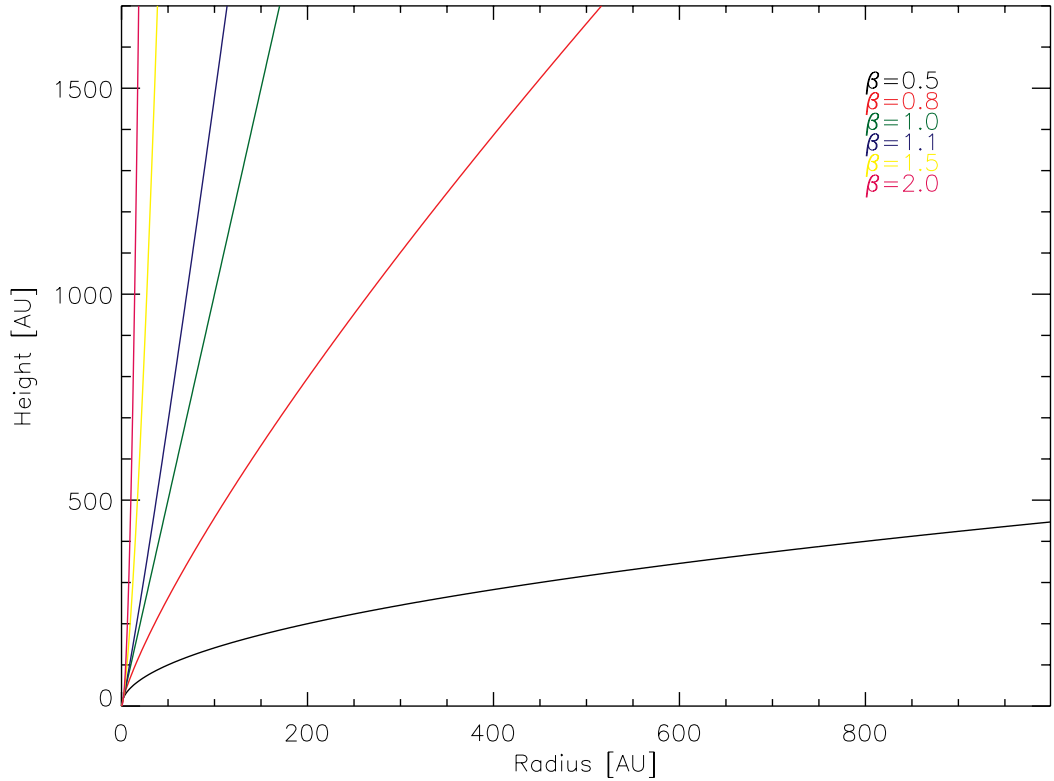
Figure 3.3 – An example of temperature distribution radial profiles for four amorphous carbon dust species (namely, 400, 600, 800 and 1000°C) of different densities (1.44, 1.67, 1.84 and 1.99 g cm⁻³, respectively). The disc's parameters are given in Table 3.2. The disc's radius is binned in 50 cells within it's size range with an increment equal to 1.1.

Assuming that all other parameters are kept constant, an increase in disc radius – inner, outer or even both – will decrease the mean dust temperature and subsequently the net infrared flux of the object. By placing the disc further from the radiation source, the amount of warm dust in the disc is reduced.

Table 3.2 – Example of parameters required for the modelling of a disc in MC3D

disc size	65 – 500 AU
M_{dust}	$6 \times 10^{-5} M_{\odot}$
α, β, h_{100AU}	2.2, 1.0, 50
T_{eff}, L_{\star}	12,000 K, 5000 L_{\odot}
i	76°

Further on, and keeping the same assumption, an increase in flaring creates a dust wall near the disc’s inner rim, since the scale height is a power law with flaring as the index. An example is shown in Fig. 3.4, where a radial profile of a disc is given for different values of flaring. The parameters h_0 and R_{\star} (Eq.[3.19]) are kept constant at 20 and 2 AU, respectively.

**Figure 3.4** – Radial profile of a disc demonstrating the significance of increasing flaring, β , in creating a wall of dust near the inner rim of a disc. The total amount of dust in the disc remains constant.

A more steep power law (grain size) distribution, i.e. -3.5 (Mathis et al. 1977), will allow the smaller grains to contribute more in absorption and

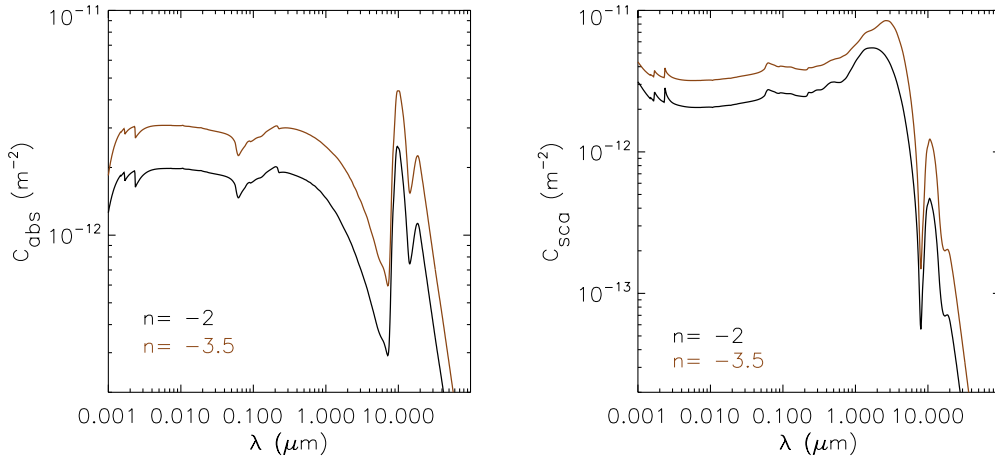


Figure 3.5 – Absorption and scattering coefficients for an amorphous silicate compound of the MC3D dust database. The grain size range is the same for both distributions ($0.01\text{--}1\mu\text{m}$) but the power law indices differ. The distribution with the larger index (-3.5 ; brown) is more effective by a factor of 1.5. The total amount of dust in the disc remains constant.

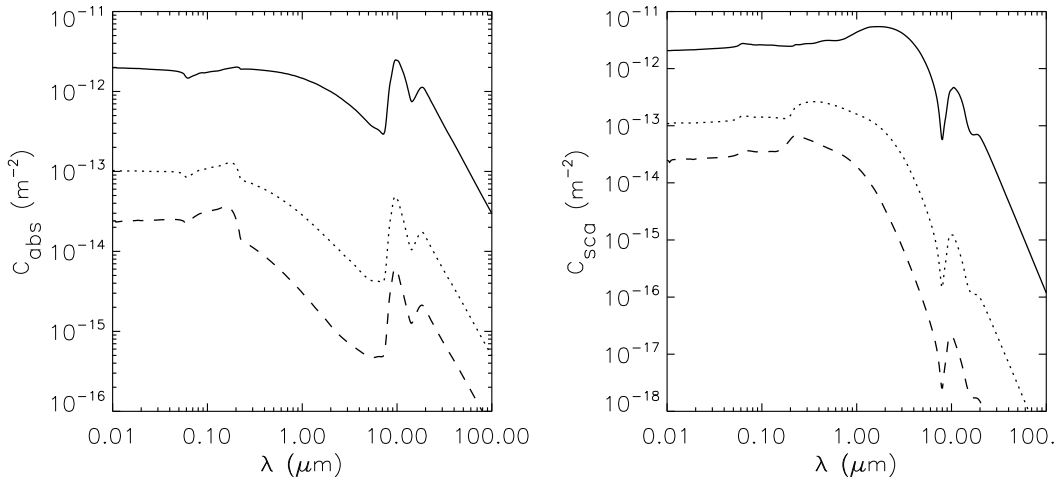


Figure 3.6 – Absorption and scattering coefficients for different grain size distributions. All dust compounds are amorphous silicates and have the same index (-3.5). The grain size ranges in both panels for the lines from *top to bottom* are: $0.5\text{--}5\mu\text{m}$ (bold), $0.05\text{--}2\mu\text{m}$ (dotted) and $0.005\text{--}1\mu\text{m}$ (dashed). The total amount of dust in the disc remains constant.

scattering. An example is shown in Figure 3.5. The absorption and scattering coefficients of the same amorphous silicate compound¹¹ are shown for two different power law indices in the grain size distribution ($0.01\mu\text{m} \leq r_{\text{grain}} \leq 1\mu\text{m}$). If the power law index is fixed but the grain sizes vary, the compounds that contain larger grains are more efficient absorbers and scatterers of light due to the larger grain cross sections (Fig. 3.6).

3.3.3 Outputs

MC3D can produce spectral energy distributions and images using the following simple routes.

All photons are collected on an observing plane upon exiting the environment. The plane is subdivided in pixels on which the wavelength, monochromatic luminosity and Stokes vector of each exiting photon is recorded and can be used to reproduce an image of the disc.

The photons escaping this radiating area σ_A will be combined within a solid angle Ω and by summing their monochromatic luminosities, one finds the intensity of the disc

$$I_\lambda = \frac{L_{\lambda,\Omega}}{\Omega\sigma_A}, \quad (3.24)$$

which for a known distance to the object d will give the spectral energy distribution

$$S_\lambda = \frac{\sigma_A}{d^2} I_\lambda = \frac{L_{\lambda,\Omega}}{\Omega d^2}. \quad (3.25)$$

For the purpose of this project, those images had to be transposed into visibility signals to allow comparison with observations. To achieve that¹² the images were (i) rotated according to the projected position angle of observation, then (ii) integrated along the projected baseline direction (x-axis) and (iii) Fourier transformed. Then, (iv) the normalised visibility amplitude is calculated and (v) interpolated to the observed spatial frequencies within the N band.

In the next two chapters, I present comparisons of the MIDI observational data to modelled spectral energy distributions, images and visibilities created

¹¹Model as shown in Table 3.2.

¹²Routine written by O.Chesneau and S.Wolf.

with MC3D.

A dusty structure around Sakurai's Object

A portion of the contents of this chapter were used in Chesneau et al. (2009).

4.1 A reborn star

V4334 Sgr (PN-010+04.2), also known as Sakurai's object in favour of I. Sakurai, an amateur astronomer who detected it first in February 1996, is an evolved star that is already passing for the second time through the asymptotic giant branch stage. Sakurai's Object used to be a hydrogen-deficient white dwarf that had already ejected and illuminated a planetary nebula about 17,000 years ago, with an expansion velocity of $\sim 25 \text{ km s}^{-1}$ (Duerbeck & Benetti 1996). The

nebula is $\sim 41''$ in diameter (Hajduk et al. 2005) and has a circular shape.

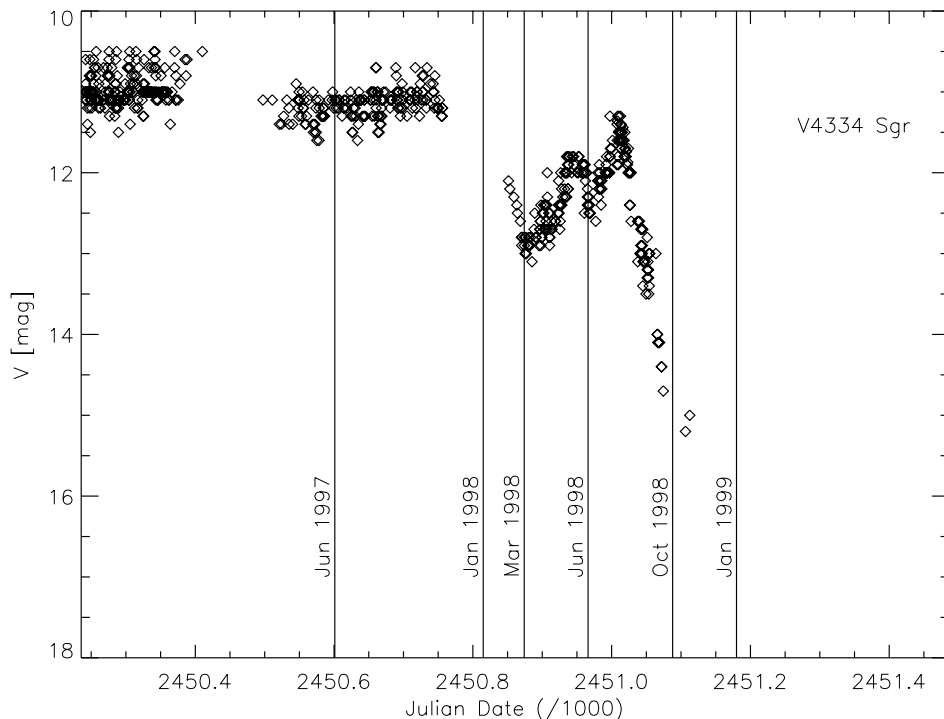


Figure 4.1 – Light curve of V4334 Sgr from 01/06/1996 to 01/01/2000. The vertical lines correspond to the dates assigned to them. The onset of dust creation was in late 1997 (first visual dip). V4334 Sgr is not visible since 1999. Data by AAVSO.

In 1996 the star became suddenly bright – although some increase in brightness had already been recorded in 1995 (Duerbeck & Benetti 1996) – as a helium burning flash occurred (a very late thermal pulse, after which the star re-traced the post-AGB track; see Figure 1.1), and it remained as such for two more years. In less than two years its magnitude decreased from 11 to 13 in V and by 2000 it has dropped below 17 mag (Figure 4.1). The extreme decrease in the visual, and subsequent increase in the infrared, was due to dust formation. No warm dust¹ has been detected before 1996/1997 near Sakurai’s Object (non-detections by IRAS² and MSX³; Figure 4.2). The stellar spectrum has been monitored ever since (Eyres et al. 1999; Kerber et al. 1999b; Tyne

¹In the mid-infrared; $T_{\text{dust}} = 200 - 350$ K.

²InfraRed Satellite

³Mid-infrared Space

et al. 2002; Käufl et al. 2003; Eyres et al. 2004; Evans et al. 2006; Worters et al. 2009).

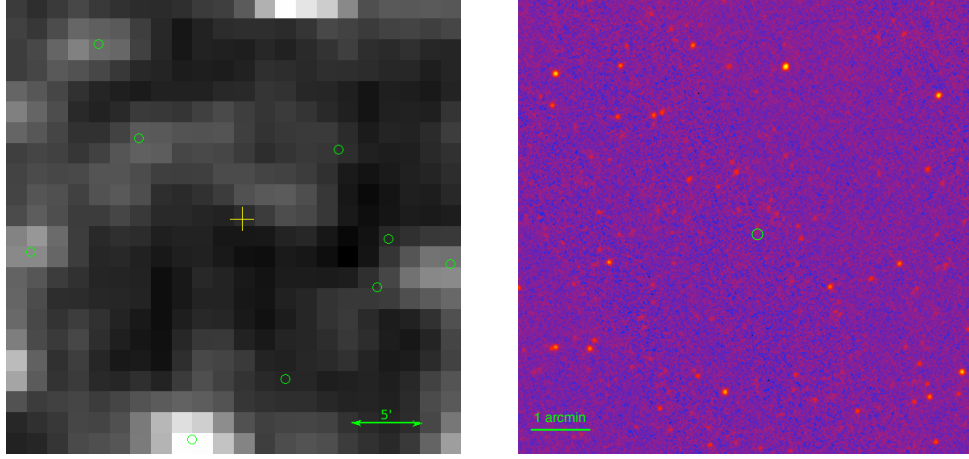


Figure 4.2 – *Left*: A map of the region around Sakurai’s Object (cross) at $12\mu\text{m}$ as seen by IRAS space telescope in 1992. As indicated clearly by the detected infrared sources in the region (circles), there was no emission from Sakurai’s Object in the mid-infrared at that epoch. *Right*: An $8.28\mu\text{m}$ map of Sakurai’s Object (circle) taken by MSX space telescope between 1996 and 1997. Although the late thermal pulse occurred just before the MSX observation, no dust has been detected.

Sakurai’s Object is one of the two stars with rapid evolution (approximately 16 years to this date since the eruption) after a VLTP event. V605 Aql is the other one, whose last eruption was in 1917 (Clayton & De Marco 1997). It is also surrounded by a round planetary nebula (A30). A slower evolution was expected for VLTP events, such as the one of FG Sge of ~ 120 years (Lawlor & MacDonald 2003; Iben 1984; Herbig & Boyarchuk 1968). Thus, the fast evolution of Sakurai’s Object allows us to study VLTP eruptions in real time.

After the flash occurred, the initial assumption was that this belonged to a “nova-like event”. Novae are known to produce ionised ejecta, whose thermal emission can be detected in radio wavelengths. Eyres et al. (1998b) observed V4334 Sgr with the Very Large Array (VLA) radio interferometer at 4.86 GHz in order to detect such ejecta, as well as the old planetary nebula previously found by Duerbeck & Benetti (1996). They estimated a statistical distance for the nebula at 3.8 ± 0.6 kpc and a flux equal to 2.0 ± 0.2 mJy. The same group improved the sampling in their VLA observations in 2002 (Eyres 2002)

and re-estimated the flux at $2.7 \pm 0.1 \text{ mJy}$. In both cases, the mass of the total ionised gas in the planetary nebula was 0.15 M_{\odot} . It is worth mentioning that Eyres (2002) observed V4334 Sgr with other facilities too. CO gas observations with the James Clerk Maxwell Telescope (JCMT) were used for the estimation of the mass of CO: $10^{-6} \text{ M}_{\odot}$ for a distance $D = 3.5 \text{ kpc}$. Their high-angular resolution observations with the Multi-element Radio-linked Interferometer Network (MERLIN) at $\sim 6 \text{ cm}$ did not reveal anything, neither did the Australia Telescope Compact Array (ATCA) observations (no OH maser emission was detected). Strong emission lines seen in novae events are absent from the spectrum of Sakurai's Object, so the ionised ejecta detected by Eyres et al. (1998b); Eyres (2002) were not produced by such an event.

Worters et al. (2009) reported a $^{12}\text{C}/^{13}\text{C}$ ratio of 3.5 and $2.5 \times 10^{-6} \text{ M}_{\odot}$ on average for CO gas. The star is carbon-rich and such a $^{12}\text{C}/^{13}\text{C}$ ratio confirms that the carbonaceous material was created after the VLTP event (Pavlenko et al. 2004). Eyres et al. (1998a) found increasing absorption features of carbonaceous material from the near-infrared observations shortly after the flash and within a year after the first observation with an additional shift of the spectrum towards lower temperatures. This indicated the presence of a dense medium, most probably a dust shell.

Hajduk et al. (2005), presenting the latest observations of V4334 Sgr with VLA and the VLT between 2004 and 2006, attribute the increasing radio flux (from $0.13 \text{ } \mu\text{Jy}$ (detection limit Eyres 2002) to $100 \text{ } \mu\text{Jy}$ at 8.6 GHz) and the diminishing optical line emissions to a fast shock initiated probably before 2001. Even though some gaseous emission and absorption lines are visible until the present day, the star itself remains hidden behind a dusty bulge. The bulge was assumed to have a spherical shape and carbonaceous composition.

4.2 Observations

Considering the shift of Sakurai's Object spectrum toward longer wavelengths (Figure 4.4) since 2000 (UKIRT spectroscopy, Geballe et al. 2002) the source should be detected in the near- and mid-infrared (Eyres et al. 1998a; Kerber et al. 1999a; Evans et al. 2004). Suggestions have been made to observe the

star with 8–10-m telescopes (Tyne et al. 2002). Although the dusty envelope with an approximate size of 85 mas has not been resolved (Evans et al. 2006; van Hoof et al. 2007), high angular resolution observations should be able to pick up the structure.

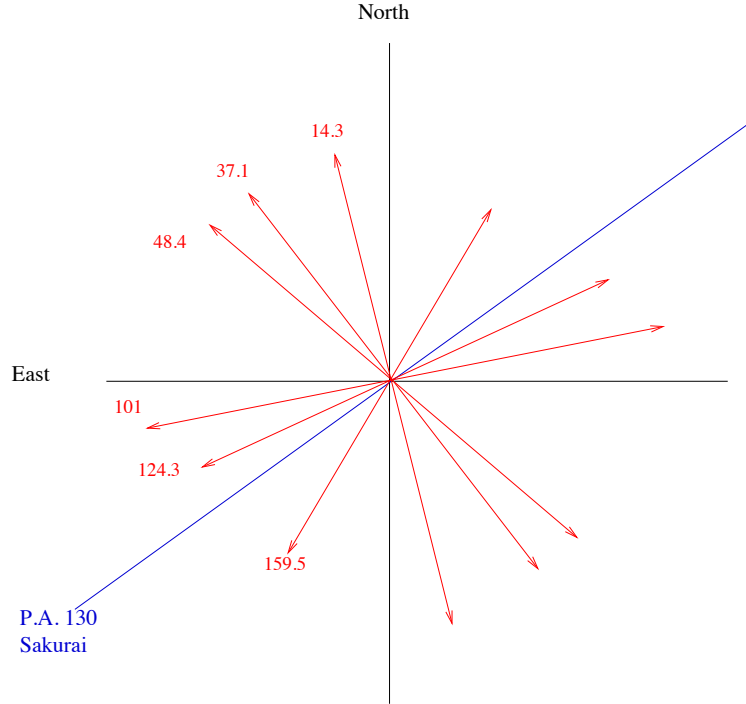


Figure 4.3 – Projected VLTI baselines for Sakurai’s Object observations. Baseline lengths not in scale. The significance of the position angle (blue) is discussed in a following section.

4.2.1 VLTI

Sakurai’s object was observed in the mid-infrared in June 2007 by MIDI in *High.Sens* mode with Unit Telescopes 2, 3 and 4 (Table 4.1). Using Earth’s rotation, the projected baselines were placed at consecutive position angles in a anti-clockwise direction (North to East), in order to provide sufficient Fourier space coverage (Figure 4.3). To prove the existence of a disc-like structure, the Fourier amplitudes had to diminish with an increasing projected position angle. That is, the closer the projected baseline was to the equatorial plane⁴ of the

⁴Assuming that the orientation of the equatorial plane is known.

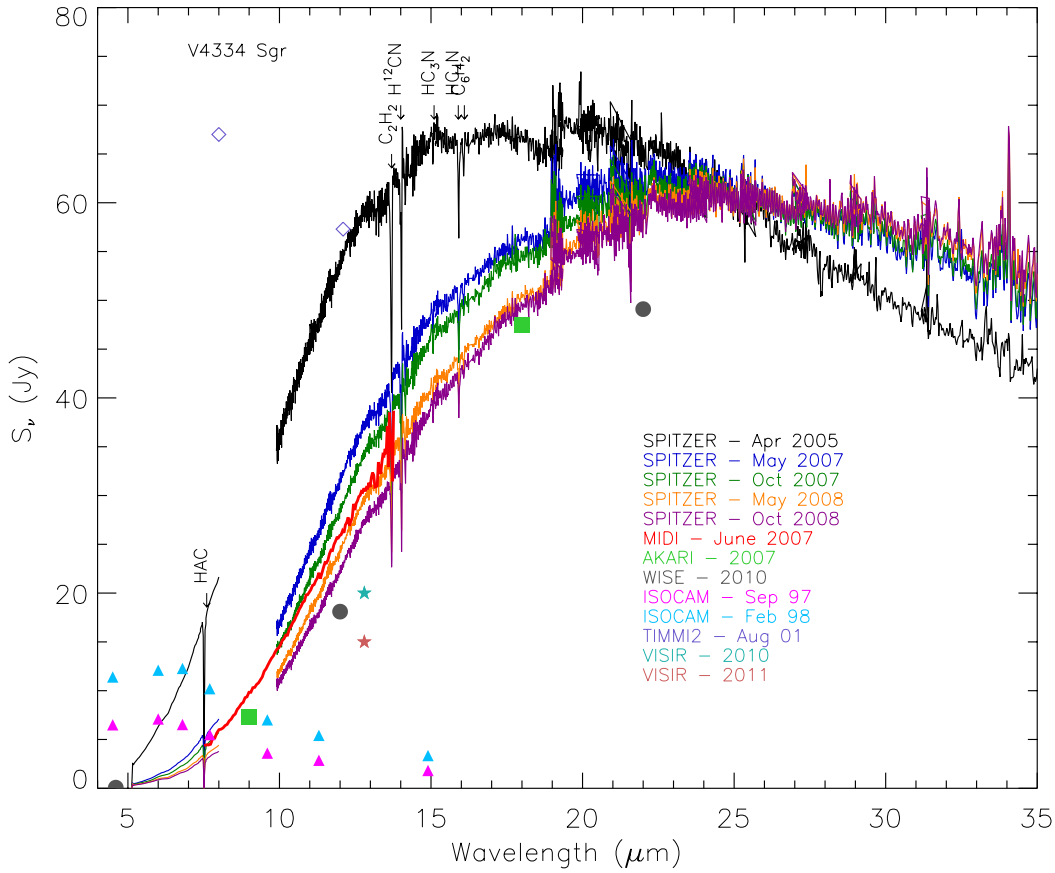


Figure 4.4 – Spectral energy distribution of V4334 Sgr. Both IRS/SPITZER high-resolution ($9.5\text{--}37.5\mu\text{m}$) and low-resolution ($5.5\text{--}8\mu\text{m}$) modes are plotted here. Steep absorption features are evident in all IRS spectra and they are attributed to hydrocarbons (species identified on the plot). MIDI spectrum, ISOCAM photometry by Kerber et al. (1999a), VISIR (P. van Hoof, private communication) and AKARI and WISE photometry is presented for comparison.

structure, the lower would the visibility be, as the object there would be more resolved than in any other direction (or else larger in size).

A low spectral resolution spectrum, acquisition images at $8.7\mu\text{m}$ (angular resolution ~ 250 mas) and six spectrally dispersed visibilities have been recorded with visibility errors between 8 and 15%. The absolute flux was calibrated to $\leq 10\%$. The data were reduced with both MIA and EWS (for a description see Section 2.5.1) by Dr. O. Chesneau⁵.

⁵The author reduced the data as well using MIA and the results are consistent with Chesneau et al. (2009).

The acquisition images by the 8.2-m telescope revealed just a point source, which was nevertheless resolved by MIDI as shown by the very low levels of the visibility spectra ($0.0 \lesssim V^2 \lesssim 0.2$) with approximate sizes given by Gaussian fits of 25–40 mas at $8\mu\text{m}$ and 50–60 mas at $13.5\mu\text{m}$ (Figure 4.5). Although circular Gaussian intensity distributions are a rather simplified fitting, all projected baselines show a similar linear growth apart from **Saku_6** (Table 4.1). We were also able to recover⁶ differential phases with a $\pm 10 - 20^\circ$ range indicating asymmetries, except for baselines **Saku_4** and **Saku_5** with almost null phases.

Table 4.1 – MIDI observing log for V4334 Sgr.

OB	Date	Base	Projected baseline	
			Length [m]	PA [degrees]
Saku_1	2007-06-29T01:06:07	UT2–UT3	41.9	14.6
Saku_2	2007-06-29T02:35:28	UT2–UT3	45.9	37.1
Saku_3	2007-06-29T06:24:21	UT2–UT3	44.4	48.4
Saku_4	2007-06-30T01:21:09	UT3–UT4	51.3	101.0
Saku_5	2007-06-30T06:07:29	UT3–UT4	54.7	124.3
Saku_6	2007-06-30T08:32:44	UT3–UT4	39.2	159.5

Calibrators: HD 152334 K4III $3.99 \pm 0.07\text{mas}$, HD 163376 M0III
 $3.79 \pm 0.12\text{mas}$, HD 169916 K1III $3.75 \pm 0.04\text{mas}$,
 HD177716 K1III $3.72 \pm 0.07\text{mas}$
 Calibrator sizes given in milliarcseconds (mas).

4.2.2 SPITZER

The Spitzer space telescope⁷ Infrared Spectrograph (IRS, Houck et al. 2004) has been used to observe Sakurai’s Object from 2005 to 2009. The post-calibrated spectroscopic data presented here (Figure 4.4) were retrieved from the telescope’s archive (P.I. Aneurin Evans; Evans et al. (2006); also Evans et al., in preparation). Both low- and high-resolution modes were used with all four slits (Table 4.2), although the saturated Long-Low data are not shown in Figure 4.4. A further discussion on the data presented here follows in Section 4.5.

⁶O. Chesneau using the EWs software.

⁷<http://ssc.spitzer.caltech.edu/>

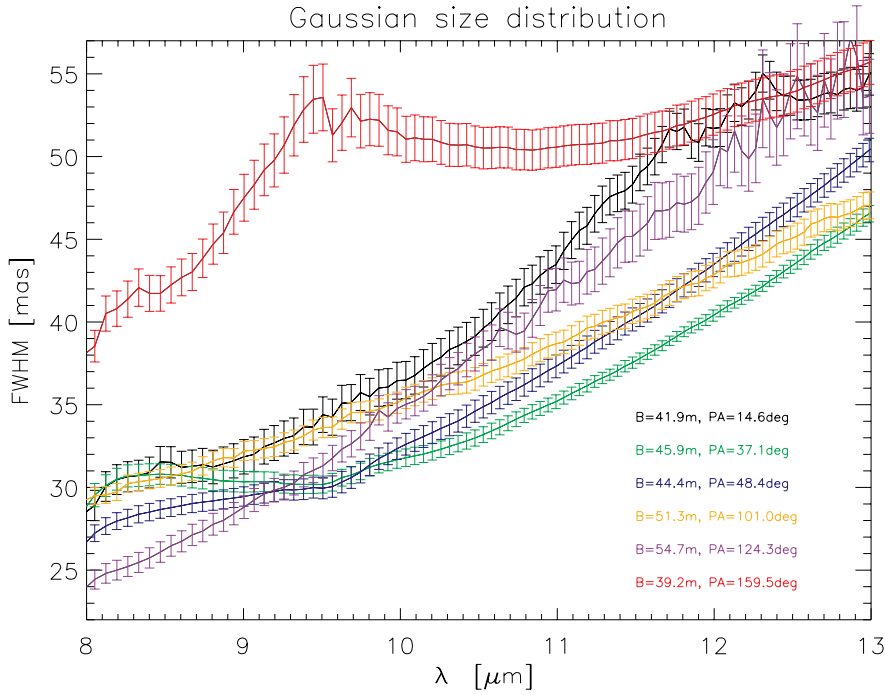


Figure 4.5 – Gaussian fits to the MIDI visibilities for Sakurai’s Object. All projected baselines (Table 4.1) show a similar growth, apart from the deviation seen in Saku_6 (PA=159.5°).

Absorption features are evident in all spectra. Most of them have been identified by Evans et al. (2006): polynes (C_2H_2 , $13.7\mu\text{m}$; C_6H_2 , $16.1\mu\text{m}$) and hydrocyanide isotopes (H^{12}CN , $14\mu\text{m}$; H^{13}CN , $14.1\mu\text{m}$; HC_3N , $15.1\mu\text{m}$; HC_4N , $15.9\mu\text{m}$; HC_6N , $16.1\mu\text{m}$). An HeI emission line at $34\mu\text{m}$ has risen just after April 2005.

Table 4.2 – Spitzer Space Telescope IRS slits.

Name	$\Delta\lambda$ [μm]	Resolution	Size
Short-Low	7.4–14.5	1.8''/pixel, R~60–127	3.7'' \times 57''
	5.2–7.7	"	3.6'' \times 57''
Long-Low	19.5–38.0	5.1''/pixel, R~57–126	10.7'' \times 168''
	14.0–21.3	"	10.5'' \times 168''
Short-High	9.9–19.6	2.3''/pixel, R~600	4.7'' \times 11.3''
Long-High	18.7–37.2	4.5''/pixel, R~600	11.1'' \times 22.3''

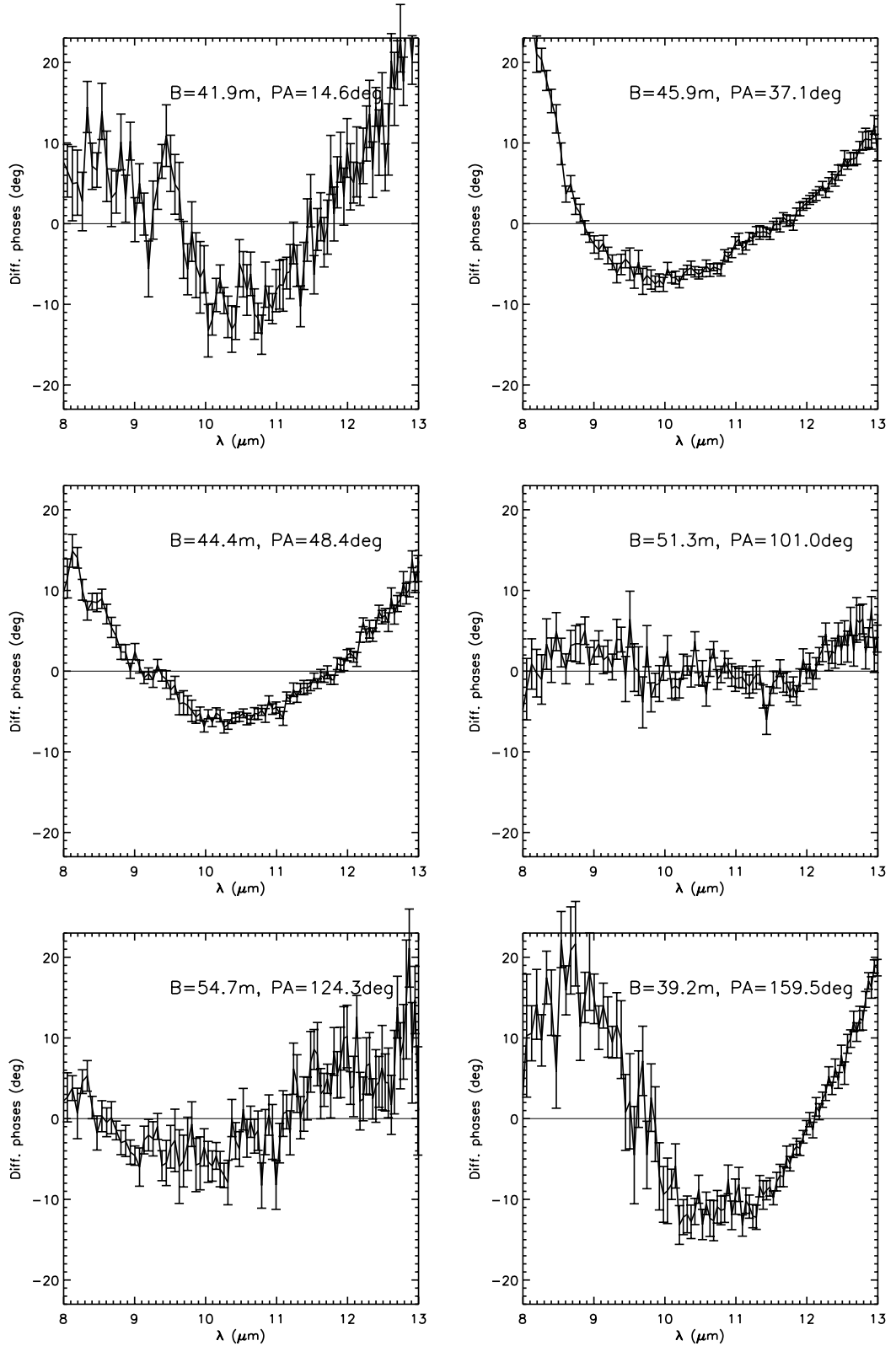


Figure 4.6 – Differential phases of Sakurai's Object. A small deviation from point symmetry (zero phases) is evident in most of the projected baselines, except for baselines Saku_4 and Saku_5 (Table 4.1).

4.2.3 Infrared photometry

Sakurai’s Object has been included in the list of targets of two infrared photometric catalogues by AKARI⁸ (Murakami et al. 2007; Ishihara et al. 2010) and WISE⁹ (Wright et al. 2010) space telescopes in the near- and mid-infrared. AKARI observations occurred at an unspecified month in 2007 and WISE observations occurred between January and April 2010. ISOCAM¹⁰ (Cesarsky et al. 1996) observations from February 1997 to February 1998 have been already published by Kerber et al. (1999a). We present this archived photometric data (Table 4.3) in Figure 4.4 for comparison to the MIDI and Spitzer spectra.

Table 4.3 – Broadband photometry by AKARI and WISE

Telescope	λ_c [μm]	Bandwidth [μm]	S_λ [Jy]
AKARI	9	4.9	13.26
...	18	11.7	53.01
WISE	3.4	0.66	5.5×10^{-3}
...	4.6	1.04	0.12
...	12	5.5	25.34
...	22	4.1	48.37

4.3 Model fitting

Earlier studies assumed that Sakurai’s Object was engulfed in a spherical, expanding dust shell (Eyres et al. 1999; Kerber et al. 1999b; Tyne et al. 2002; Käufl et al. 2003; Eyres et al. 2004; Evans et al. 2006; van Hoof et al. 2007; Worters et al. 2009). The differential phase signal in baselines nearly perpendicular to the structure’s main axis (Figure 4.6) with marginally non-zero deviation from point symmetry (phase $\leq 10^\circ$ in some cases), suggest that the dust shell is not spherically symmetric¹¹. The visibility pattern appears to be that of the second or third lobe of a spatial distribution that would present a null, i.e. not a smooth distribution but one with an edge, such as a uniform

⁸<http://www.ir.isas.jaxa.jp/AKARI/>

⁹Wide-field Infrared Explorer; <http://wise2.ipac.caltech.edu/>

¹⁰Infrared Space Observatory’s (ISO) infrared camera

¹¹A spherically symmetric shell like a Gaussian would have zero phase

disc or uniform circular ring. Christian Hummel (priv. communication) had attempted to fit the visibilities with elliptical ring models and found better fits for position angles of the major axis near 120° ¹² but could never reproduce the secondary lobes seen in the data.

To further test these assumptions, we plotted the visibility vs. spatial frequency at three different wavelengths and attempted to fit simpler distributions, that is (a) a Gaussian distribution, (b) a Uniform disc, and (c) a Uniform ring (Eqs.[2.43–2.44]). We explored values from 10 to 100 mas with increments of 5 mas and the best fits are shown in Figures 4.7 to 4.9.

We find angular sizes similar to those presented in Figure 4.5 when fitting Gaussian distributions to MIDI data for three wavelengths (8, 10 and $13\mu\text{m}$), although these distributions do not fit the data except for a better approximation at $13\mu\text{m}$. The application of a uniform disc did not fare better. As seen in Figure 4.8, a uniform disc model clearly does not fit the data at $13\mu\text{m}$ and first nulls at 8 and $10\mu\text{m}$ are located at shorter spatial frequencies than the actual data. In the case of a circular uniform ring, it appears the model curve fits the level and shape of the data (Fig. 4.9). Nevertheless, the structure appears to have a consistent inner ring size (also with respect to the values given in the uniform disc fits), while the outer ring increases in dimension with respective increase in wavelength. This was something already seen in Figure 4.5 and even though all these fits are just approximations, they lead us to believe that the size of the detected structure increases at longer wavelengths.

We recognise that an even more complex (dusty) structure is required in order to fit the data. Due to the incomplete Fourier space coverage of V4334 Sgr and thus the lack of imaging, we attempt to reconstruct the detected structure with the means of a radiative transfer model for a passive disc (MC3D, Section 3.3). In the following sections, we will present disc models in our attempt to reach a good fit for both the MIDI spectrum and the MIDI visibilities. Although, the size of the apertures for the spectrum and the visibilities differ, we chose the images created by MC3D to have the same aperture as MIDI and then we Fourier-transform them into spectrally dispersed visibilities.

¹²The importance of this will be discussed in a following section

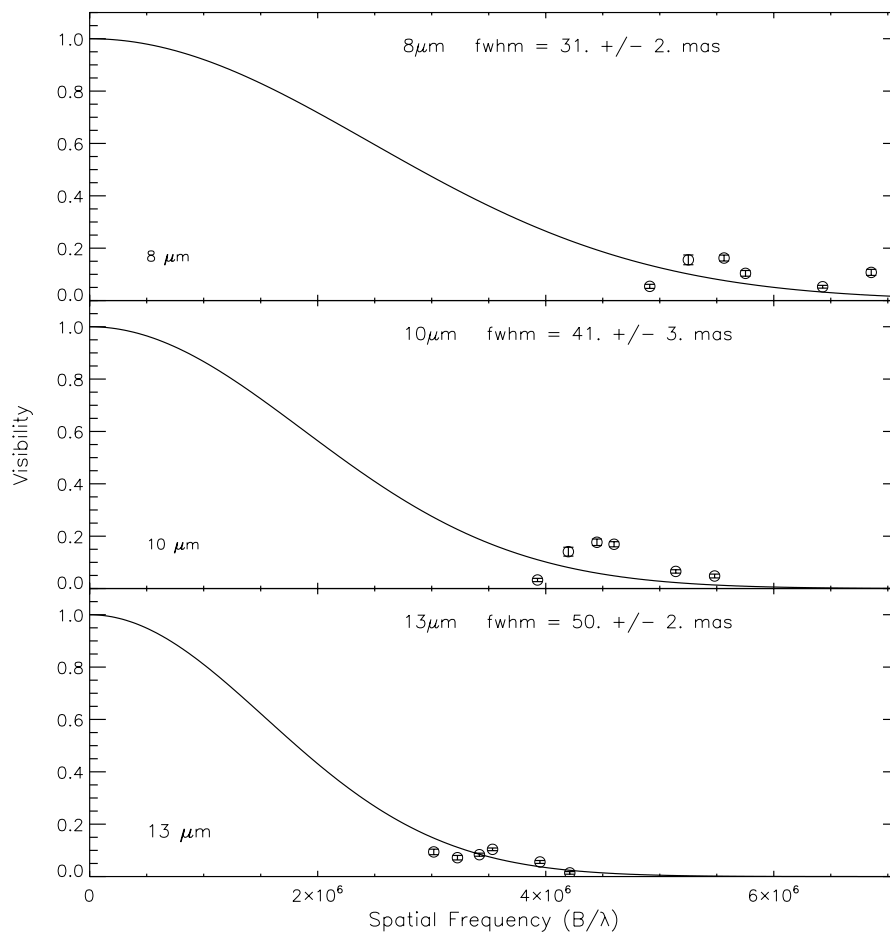


Figure 4.7 – Gaussian fits for 8, 10 and 13 μm from top to bottom for all six baselines. Longer spatial frequencies have sampled the warmer component, and vice versa for the colder component. It is clear that circular Gaussian distributions do not fit the interferometric data at 8 and 10 μm , but might fit the visibilities at 13 μm . Nevertheless, the values estimated from the fits, 31 ± 2 , 41 ± 3 and 50 ± 2 mas for the respective wavelengths, do not differ that much from the values given in Figure 4.5

4.3.1 MC3D models

The density law for the modelled disc is described in Eq.[3.18] and [3.19]. An example of the model at hand is shown in Figure 4.10: the inner edge of the disc is heated by stellar radiation and acts like a barrier for the midplane layers located at larger radii. For a further description we refer to Section 3.3.

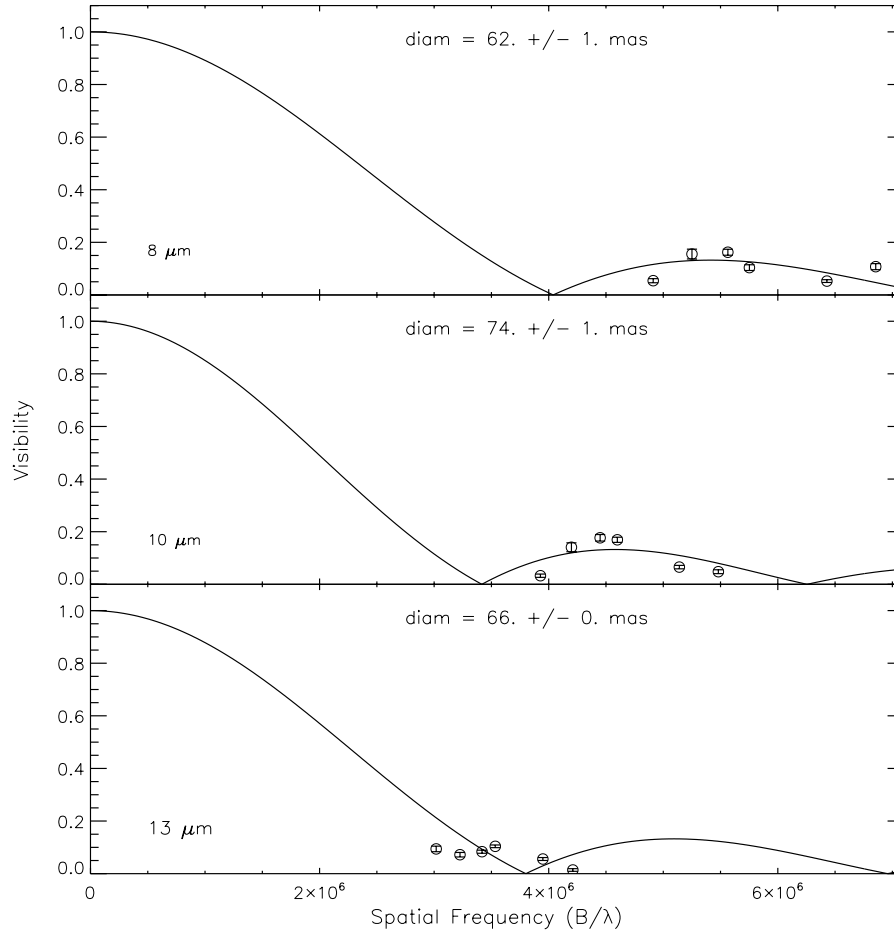


Figure 4.8 – Uniform disc fits for 8, 10 and 13 μ m from top to bottom for all six baselines. Initial assumption for the diameter was 65 mas. A uniform disc seems to fit the interferometric data at 8 and 10 μ m better than circular Gaussian distributions (Fig. 4.5).

4.3.1.1 Dust composition

An object that has re-ascended the AGB track such as Sakurai’s Object, is expected to have an overabundance of carbon leading to the formation of a surplus of carbonaceous dust. The spectral energy distribution, apart from the hydrocarbon absorption lines, is featureless (Figure 4.4). Models with *graphites* have been tested, but they could reproduce neither the shape of the MIDI spectrum nor the visibility patterns. We present an example here for comparison (see Figures 4.15 and 4.16) although it is not optimised. The best results were given by *amorphous carbon* dust.

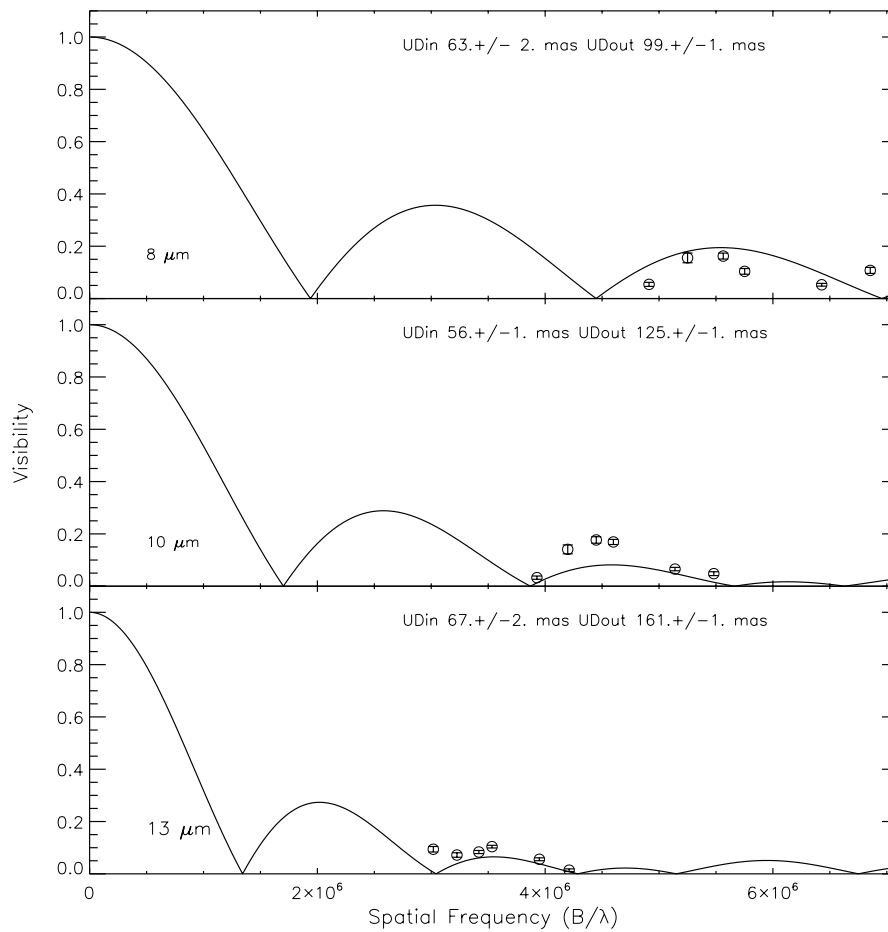


Figure 4.9 – Circular uniform ring fits for 8, 10 and 13 μm from top to bottom for all six baselines. Initial assumption for the ring’s inner and outer diameters was 45 and 100 mas, respectively. Uniform rings appear to fit better the visibilities than uniform discs or Gaussians. The sizes are consistent, and in accordance with those in Fig. 4.8, and the outer ring size increases with respective wavelength.



Figure 4.10 – Cartoon of a disc model. The inner rim of the disc forms a wall that shields the interior of the disc, but the top and bottom surfaces of the disc expand in height with respect to the increasing disc radius. The cartoon is not in scale.

Table 4.4 – MC3D model parameters of an amorphous carbon disc. ‘Cetal2009’ stands for Chesneau et al. (2009).

Parameters	model_A	model_B	model_C	model_D	model_F
Luminosity (L_{\odot})	4000	5000	5000	10000	5000
Inner radius (AU)	65	65	65	65	60
Outer radius (AU)	500	500	500	500	500
Inclination ($^{\circ}$)	74	75	75	75	74
α	2.2	2.2	2.2	2.0	2.2
β	1.05	1.0	1.0	1.0	1.0
$h_{100\text{AU}}$ (AU)	50	50	50	47	50
Dust mass [♣]	7	6.5	8.5	6.5	8.5
Parameters	model_G	model_H	model_I	model_J	Cetal2009
Luminosity (L_{\odot})	3000	5000	5000	7000	7500 \pm 2500
Inner radius (AU)	60	55	65	55	65 \pm 10
Outer radius (AU)	500	500	500	500	500
Inclination ($^{\circ}$)	74	76	76	76	75 \pm 3
α	2.2	2.2	2.2	2.2	2.0 \pm 0.1
β	1.0	1.0	1.0	1.0	1.0 \pm 0.1
$h_{100\text{AU}}$ (AU)	50	50	50	50	47 \pm 7
Dust mass [♣]	9.5	6.5	5	5	6 \pm 3
T_{eff} (K)					12 000
Distance (kpc)					3.5
PA angle ($^{\circ}$)					132 \pm 3

[♣] Units are $\times 10^{-5} M_{\odot}$.

4.3.1.2 Parameter selection

Many models have been tested and their characteristics slowly evolved, since some initial decisions on the parameters appeared to be misleading (such as a size of 85 mas by Evans et al. 2006). We were able to narrow down all the fitting parameters to the set presented in Table 4.4. The “best fit” published in Chesneau et al. (2009) is a representation of the mean value of each parameter from the nine other models. Chesneau et al. (2009) attempted to include different parameters for their *best fit* as opposed to the best model presented here.

In the range of distances explored (1–4 kpc), the inner rim radius was selected by the conversion, in physical units, of the Gaussian uniform discs on

the visibilities (approximately 40–120 AU). With increments of 0.5 AU and assuming a *distance* of 3.5 kpc, the visibilities provide a tight upper limit of the *inner rim*, that cannot be beyond 52.5–70 AU. The exact distance of V4334 Sgr is not known (see range above). We achieve better fits at a distance of 3.5 kpc, but this could be disproved in the future.

In the initial range of distances explored (1–4 kpc), the SED for an *inclination* with respect to our line of sight lower than 60° is systemically too hot, that is the flux levels are significantly higher than the SED observed. We explored larger inclinations with 1° increments.

One must keep in mind that the temperature used in our models for the best fitting of the SED was lower than the one estimated so far for V4334 Sgr. The estimation of the stellar temperature, according to the evolutionary model of Hajduk et al. (2005), for the period of our observations in July 2007 was $\sim 15,000$ K. In our models the *effective temperature* is lower than that (12,000 K). The stellar *luminosity* is not known and we selected values between 3,000 and $10,000 L_\odot$.

An opaque disc was required to fit the observational data. As such, we chose a compact geometry with *outer radii* approximately a factor of magnitude larger than the inner radius (500–600 AU). From the SED fitting we found that discs with outer radii less than 450 AU were too optically thick and gave null visibilities, while for values larger than 700 AU the disc was too optically thin.

We selected a *scale height* of similar size to the inner radius (45–55 AU) and a moderate density gradient in the *midplane* of r^{-2} . The disc's *flaring* was set to one so that the increase in scaleheight from the inner rim outwards is directly proportional to the radius.

To further increase the disc's opacity, we gradually increase the mass of dust from 10^{-5} to $10^{-4} M_\odot$. Modelled discs are highly sensitive to the enclosed amount of dust and the stellar luminosity, or else the dust opacity and the amount of photons emitted by the central illuminating source. Thus, we narrowed our search within the values stated in Table 4.4.

We selected a *position angle* with respect to North for the disc between 114 – 140° following a priori information on visibility model fits as stated before

(C.Hummel, priv. communication). The importance of the position angle is discussed further in Section 4.5.

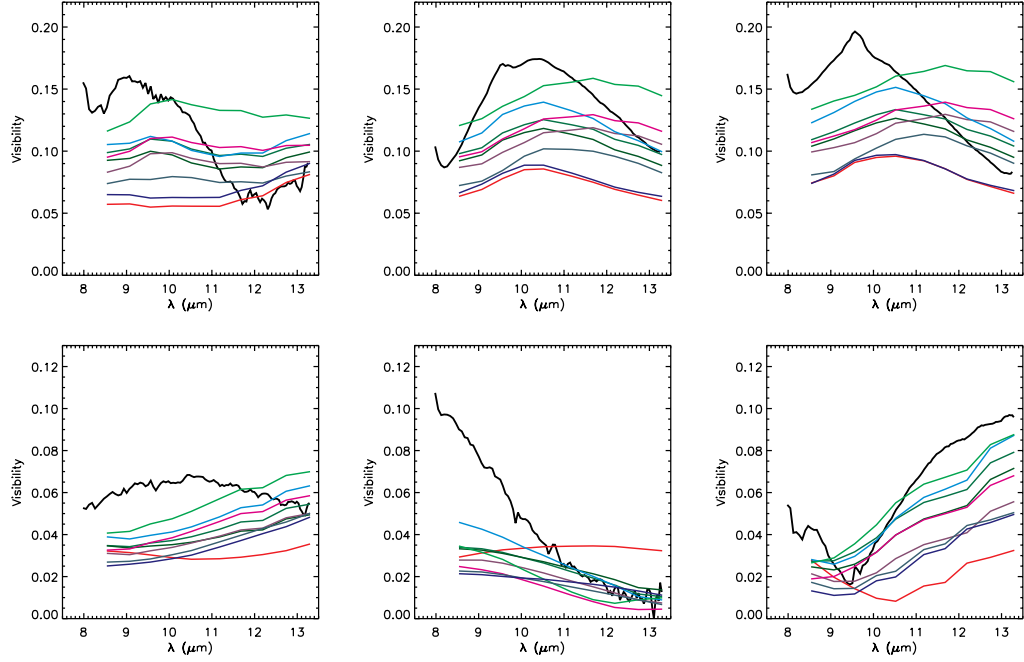


Figure 4.11 – Comparison of different radiative transfer models to the MIDI visibilities. Model parameters are listed in Table 4.4 and colour-coded lines are as the same as in Figure 4.12. From top-left and clockwise the baselines are Saku_1 to Saku_6.

4.3.2 Fitting accuracy

For the estimation of the goodness of fit in our models, we use the statistical quantity *reduced* χ^2 defined below as:

$$\chi^2 = \sum_{i=1}^N \frac{(V_{obs,i}^2 - V_{mod,i}^2)^2}{\sigma_{V_{obs,i}^2}^2}, \quad (4.1)$$

where N is the number of wavelengths, $\sigma_{V_{obs}^2}$ is the observed visibility errors, V_{obs}^2 is the observed visibility amplitude and V_{mod}^2 the modeled one, and the *reduced* χ^2 is equal to

$$\chi_{reduced}^2 = \frac{\chi^2}{N - p - 1}, \quad (4.2)$$

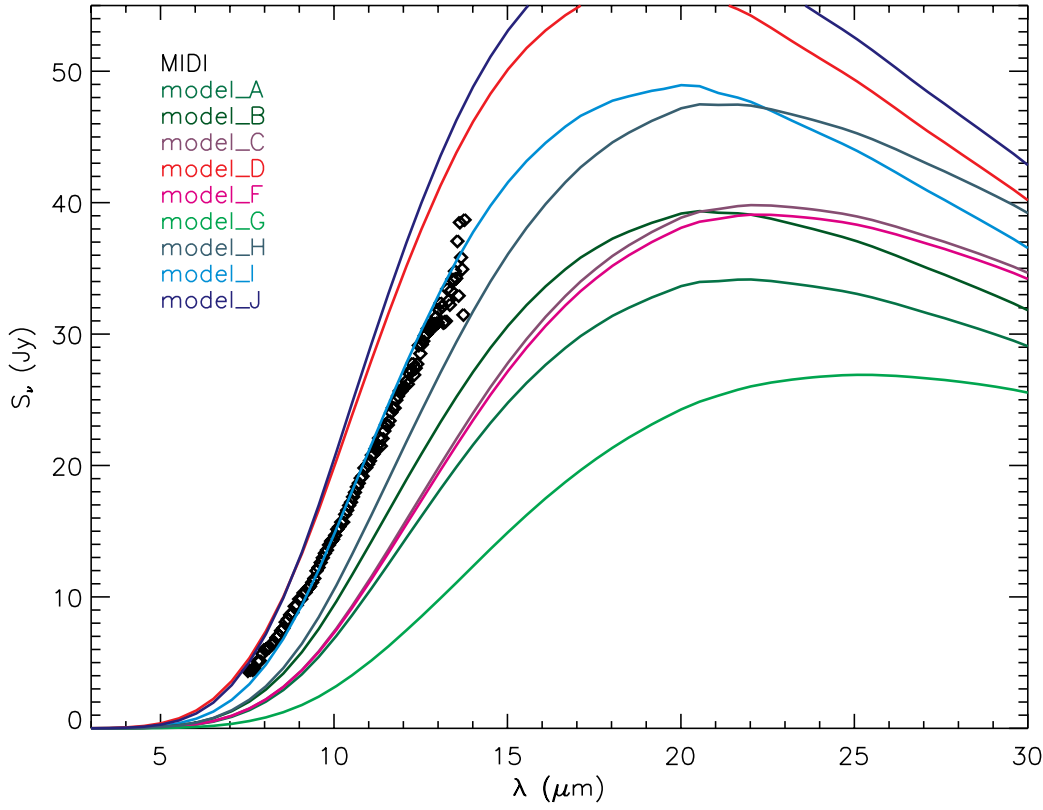


Figure 4.12 – Comparison of different radiative transfer models to the MIDI spectrum. Model parameters are listed in Table 4.4.

where p is the number of fitting parameters. If the modelled and observational data agree well, then χ^2 approaches unity. As such, a “good fit” is achieved when the reduced chi-square statistic approaches unity. Assuming that all modelled visibilities are ideal, then the reduced χ^2 for each baseline should be unity. Here, we introduce for the six baselines what we call *total* χ^2 as

$$\chi_{total}^2 = \sum_{j=1}^6 \chi_{reduced,j}^2, \quad (4.3)$$

for baselines j , and we require it to be equal to 6 for a good fit to all six baselines.

From Figure 4.11 it is not clear which model from those presented for comparison in Table 4.4 fits the observed visibilities better, yet `model_I` gave

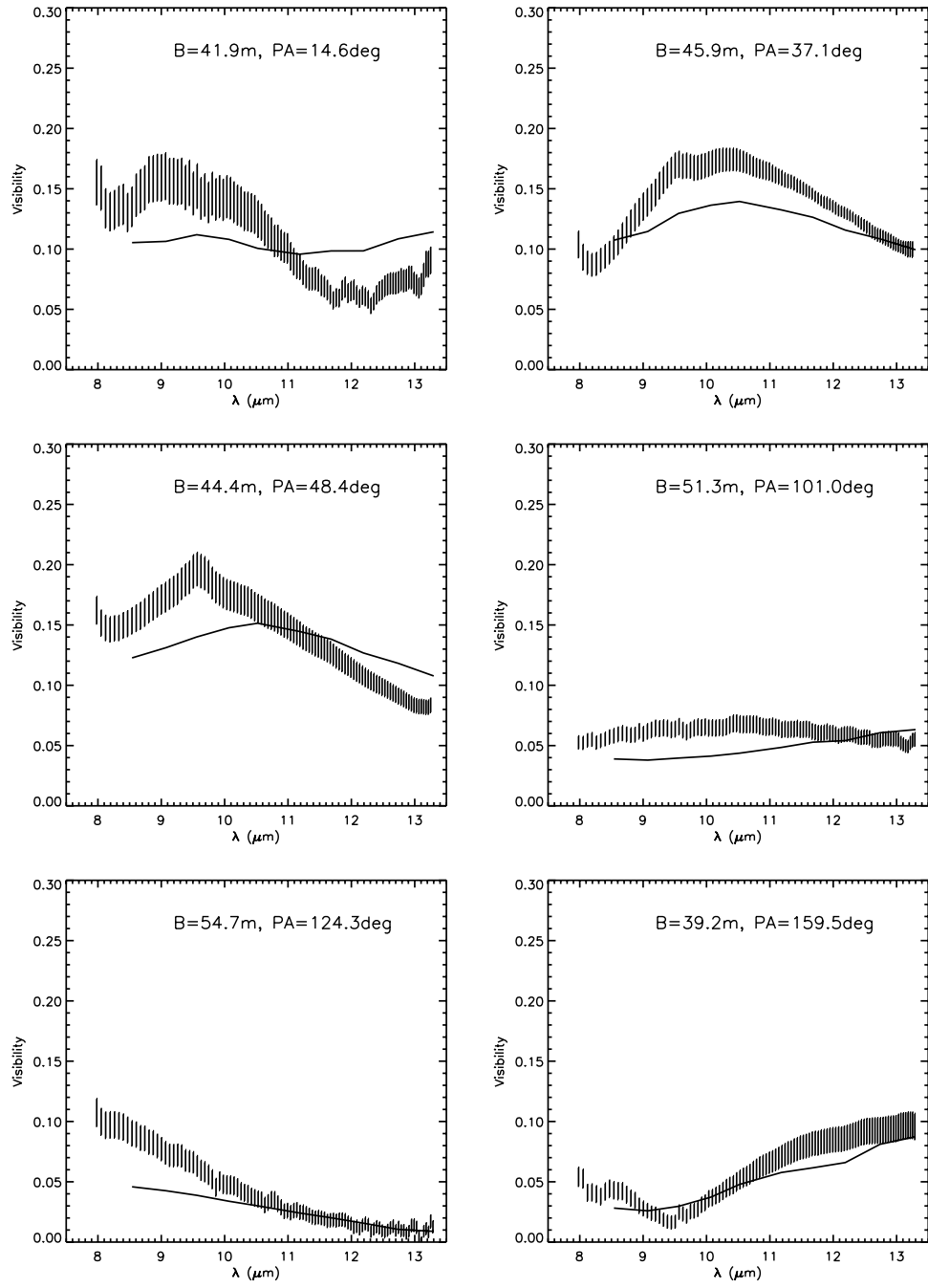


Figure 4.13 – Best fit visibilities of a disc around V4334 Sgr compared to those observed by MIDI (grid).

the lowest total χ^2 value¹³. Furthermore, `model_I` is the best fit to the MIDI spectrum (Figure 4.12).

None of the models presented here managed to fit the wave-like pattern seen in the visibility signal, i.e. the “peaks” and “troughs” at position angles 14.6, 37.1 and 48.4 degrees in Figure 4.13. For the sake of clarity, `model_I` is presented separately in Figure 4.13. Due to the spread of the visibility fits, we preferred to present all possible models in Table 4.4 as opposed to the one stated in Chesneau et al. (2009), which adopted a wider parameter range.

Since that spectrum was simulated better with a lower temperature than the one given in Hajduk et al. (2005), we believe that the disc is not illuminated only by the “naked” star itself. It is most probably illuminated by stellar radiation “filtered” through a dense region of gas. In any case, we did not expect the region between the star and the disc to be empty, as it is the case in our models. Carbonaceous gaseous features have been detected within the N-band by SPITZER (Fig. 4.4). MIDI’s dispersive element does not have sufficient resolution to reveal the same features.

The reconstructed images of the best fit at 8, 10.5 and 13 μ m are shown in Figure 4.14. One will notice the bright background inner rim in all images. This is due to the specific inclination of the disc along our line-of-sight. The high optical depth at 8 μ m masks the inner most region of the disc. The warm dust in the inner region is more apparent at 13 μ m where the optical depth is lower.

The position angle of the disc measured anticlockwise from the north is 130°. For projected baselines between 14.6 and 48.4°, nearly perpendicular to the position angle of the structure, the simulated disc appears to be too big (or else very dense), while for projected baselines near the equatorial plane, there seems to be a good fit to the disc’s size, but it does not follow the exact wave-like pattern of the object.

¹³This is further explained in Section 4.5

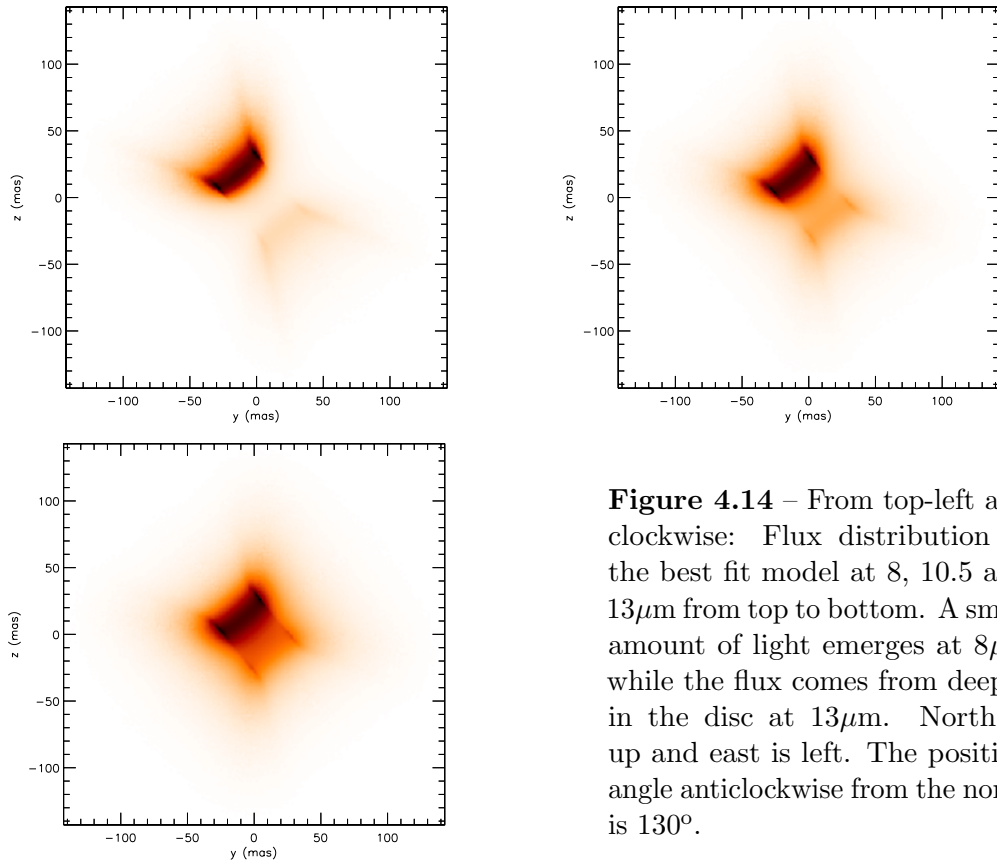


Figure 4.14 – From top-left and clockwise: Flux distribution of the best fit model at 8, 10.5 and $13\mu\text{m}$ from top to bottom. A small amount of light emerges at $8\mu\text{m}$ while the flux comes from deeper in the disc at $13\mu\text{m}$. North is up and east is left. The position angle anticlockwise from the north is 130° .

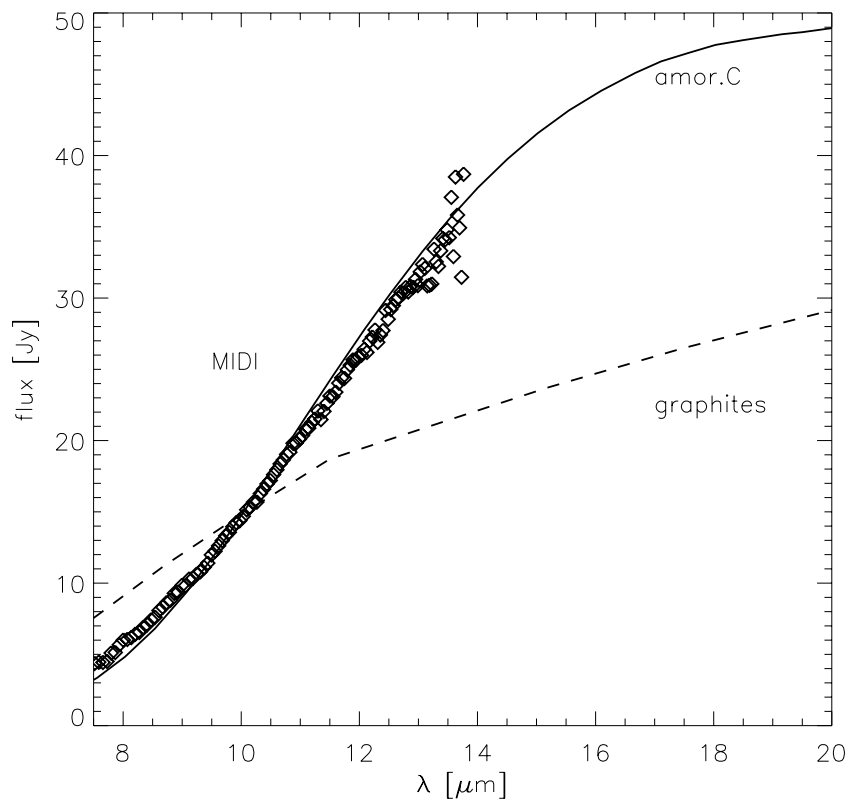


Figure 4.15 – Model spectrum with amorphous (solid) and graphitic (dashed) carbon dust. `model.I` parameters were used in both simulations.

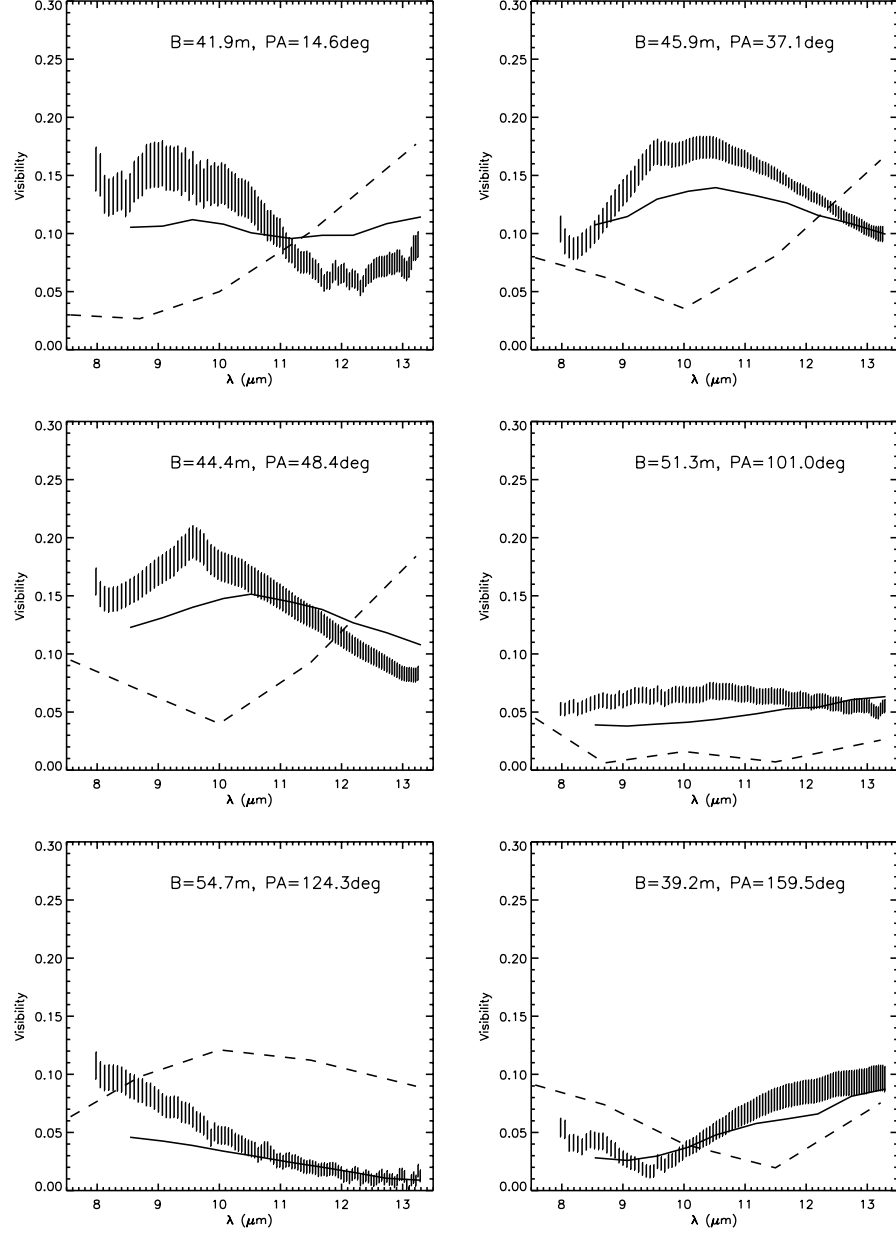


Figure 4.16 – Model visibilities with amorphous (solid) and graphitic (dashed) carbon dust. `model_I` parameters were used in both simulations.

4.4 Sakurai's planetary nebula

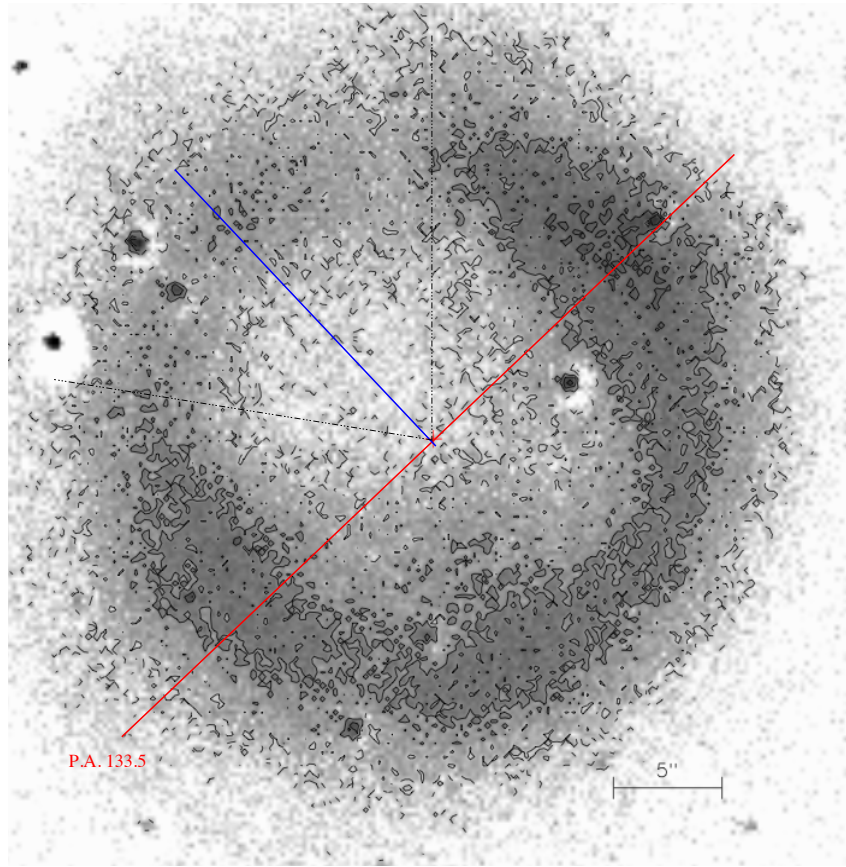


Figure 4.17 – A contour plot of a close-up of the Sakurai's nebula in continuum subtracted [O III] filter at 4 different levels between 30 – 200 of peak intensity (arcsinh distribution). The levels are indicative of the peak pixel value. The pixel scale is $0.2''$. The image was recorded in 2002 after the outbursting star was embedded in a dusty cloud, therefore the star is invisible. The red line represents the planetary nebula's position angle ($\sim 130^\circ \pm 5^\circ$) passing through the position of the star (known coordinates) and the brightest areas of the PN. The blue line indicates the direction ($\sim 45^\circ$) at which the nebula is fainter and it is almost perpendicular to the position angle. North is up and East is left. The bar at the bottom is scaled to $5''$.

An image of the planetary nebula of the Sakurai's object was acquired in October 2002 with the instrument FORS1/VLT, taken with the [O III] filter and it is the same image presented by Hajduk et al. (2005). The nebular structure appears to be spherical but weak in emission. After close inspection of the nebula by enhancing the dynamic range of the image (Figure 4.17), thus

tuning the contrast between the weak and brightest areas of the nebula, some interesting aspects came into focus.

The initial study was meant to inspect the flux distribution of the nebula and to estimate its position angle, which is defined as the line that passes through the brightest areas of the nebula and was found to be 130 ± 5 degrees. As it can be seen in Figure 4.17, the North-West and the South-East areas of the nebula are the more luminous, with the first being brighter than the latter¹⁴. On the other hand, a void is present in the northern part of the nebula and another one at $\sim 50^\circ$ to the East, while the faintest part of the nebula is at $\sim 45^\circ$. The origin of those holes is not fully understood.

Duerbeck & Benetti (1996) published two frames of Sakurai's planetary nebula taken in 1996 with the ESO 0.9m Dutch telescope. Their [O III] frame is not conclusive as the background was not subtracted, but their background-subtracted H α frame (Figure 4.18) presents a brighter area of the planetary nebula almost at the same position of the [O III] FORS1 frame (Figure 4.17). The [O III] WFPC2/HST image presented by Bond & Pollacco (2002) is a combination of multiple exposures spanning from 1996 to 1999. Unfortunately, it has a very low signal-to-noise ratio and nothing can be said about the nebula, except for the confirmation of its sphericity. The image presented in this thesis allows the best presentation of the asymmetry detected in the nebula.

4.5 Discussion

The wave-like visibility spectra are probably the second or third lobe of the visibility pattern and could also be modelled by a circular ring¹⁵ (Figures 4.13 and 4.9). It is thus possible MIDI detected a ring, that belongs to the inner rims of the disc-like structure. Since the star is hidden behind the structure, what should be seen, if the object was resolved by a single telescope, would be an inclined, flared disc, whose front inner rim is hidden from the observer as it is more opaque, thus darker, and the opposite inner rim is much brighter, due

¹⁴[O III] emission requires high electron temperatures and environments with densities lower than 10^5 cm^{-3} to avoid collisional de-excitation. Here the density is approximately 10^2 cm^{-3}

¹⁵Data at shorter spatial frequencies are required to optimise the fit.

to the reflection of stellar radiation.

As mentioned earlier in Section 4.2.2 polyyne and hydrocarbon features were detected in absorption by Spitzer (Figure 4.4). The flux levels of those features detected have dropped by a factor of two within three years, while the peak of the SED has shifted by approximately $6\mu\text{m}$ towards the mid-infrared. Extrapolating to the current year, the peak of the SED should be around $32\mu\text{m}$. The decrease of the black-body-like spectrum is further confirmed by last year’s WISE broadband photometry. The HeI emission line at $34\mu\text{m}$ has risen after April 2005 and is consistent in all spectra ever since. Near-infrared emission has significantly dropped since 1997 indicating the cessation of hot dust production associated with a mass-loss event.



Figure 4.18 – A frame of $\text{H}\alpha$ emission taken in 1996 by Duerbeck & Benetti (1996, their Fig.2). Increased $\text{H}\alpha$ emission in the north-west area of the nebula is prominent and it seems to match the brightest area in the $[\text{O III}]$ frame shown in Figure 4.17. The artefact in the centre of the nebula is due to the subtraction of the central star from the image.

If the mass-loss event had stopped and the dusty structure was expanding radially, as suggested by Käufel et al. (2003) and Evans et al. (2006), then the disc would be: (a) large enough and (b) transparent enough to be resolved by the VLT. Our observations showed that the disc was still too small to be resolved by an 8.2-m telescope. The cooling of the dusty structure combined with radial expansion should allow a detection of the object in the near future.

The fit has also revealed another interesting facet of Sakurai’s Object: the coinciding position angles of the disc-like structure and the planetary nebula. The major axis of the dusty structure is positioned at $130 \pm 10^\circ$ North-East (Fig. 4.19) and it is almost identical to the designated orientation of the old planetary nebula along the asymmetric $[\text{O III}]$ emission areas ($130 \pm 5^\circ$).

There are of course certain position angles that fit specific baselines better, e.g. the fit to baseline **Saku_4** reaches reduced χ^2 unity near or at 60, 70, 90 and 100°. We selected a position angle for good fits for both the visibilities and the spectrum. Kerber et al. (2002) introduced a similar positioning. The planetary nebula of Sakurai’s Object is not the only one known to exhibit such an alignment. The disc in V605 Aql and its surrounding spherical planetary nebula Abell 58 have similar properties (Hinkle et al. 2008; Clayton et al. 2006; Clayton & De Marco 1997).

The placement of the two position angles is not coincidental. The mechanism that produced the asymmetry in the old planetary nebula should have survived that evolutionary stage to be able to produce the inclined dusty structure after the VLTP event.

Theoretical work has shown that binarity can cause effects like this (Mohamed & Podsiadlowski 2011; Mastrodemos & Morris 1999). For this particular case, the main problem would be that a companion should have survived the initial evolution of V4334 Sgr from the AGB to the PN phase and the subsequent VLTP event. It is possible it was either a subdwarf or a jovian-like planet at a distance of approximately 5–10 AU from V4334 Sgr in order to affect the expansion of the original PN. After the VLTP event, a companion could spiral in towards the primary, increase the angular momentum of the system and thus shape the dusty ejecta into a disc-like structure (Nordhaus & Blackman 2006). Stellar cannibalism could also explain the chemical abundances in V4334 Sgr and why they differ from typical post-AGB stars (F.Herwig, priv. communication; also Herwig et al. (2011)).

If the companion was far enough to avoid a common envelope phase (more than 5 AU) it would be able to affect the stellar wind from the primary during its AGB phase and initiate an asymmetry on the equatorial plane of the system. Depending on the companion’s mass and orbit, the initial asymmetry might be more or less prominent on the expanding nebula. Assuming that the companion survived the first planetary nebula phase, if not with some minor implications such as element enrichment or orbital shrinkage, then it will certainly affect the new mass ejection in a way similar to the first interaction.

Had the secondary been another star, it should have been detected spec-

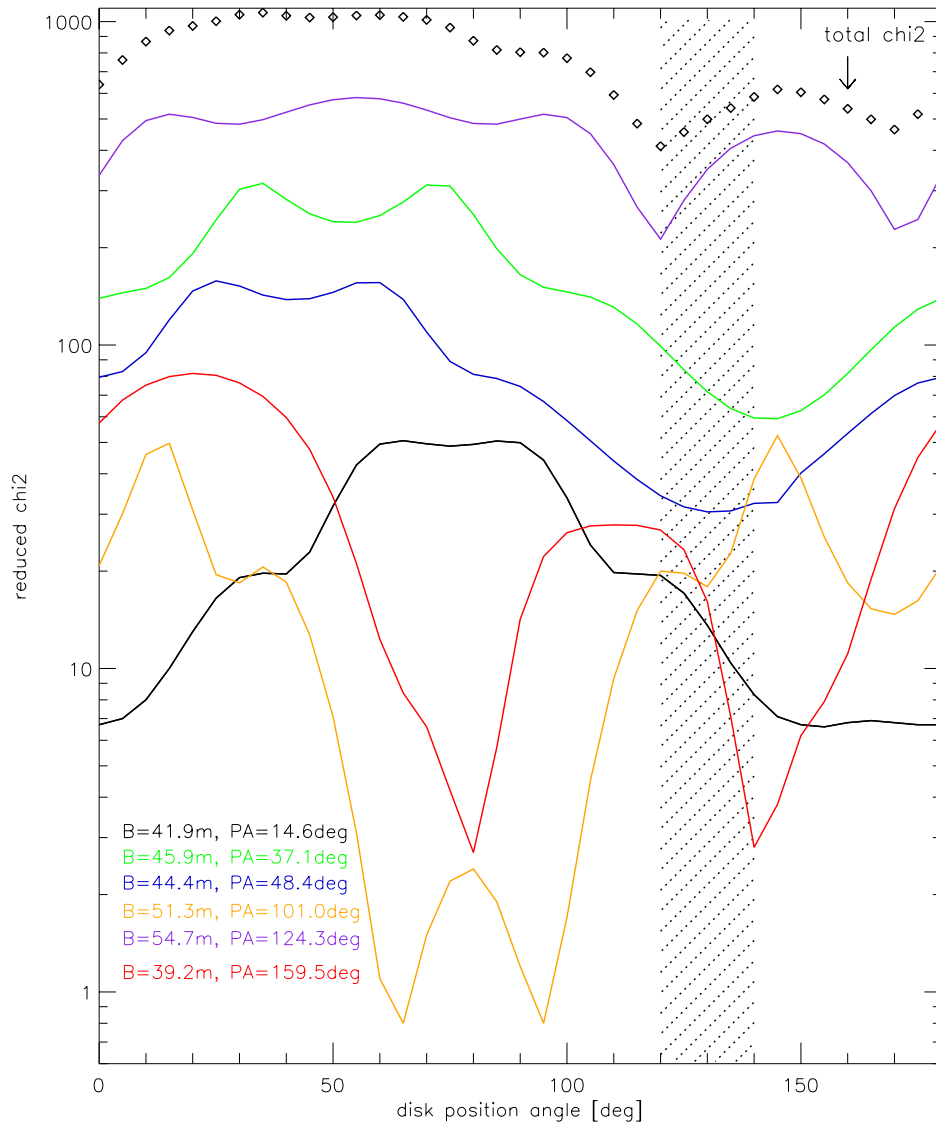


Figure 4.19 – Optimal selection for the disc’s position angle with respect to the North. We computed the reduced χ^2 goodness-of-fit for each baseline (color-coded lines; see legend) using `model_I` and rotating the disc from 0 to 180 degrees. The shaded area represents the extent of the asymmetry detected in the old PN. We overplot the total χ^2 for comparison.

troscopically just after the event. Since Sakurai's Object is still hidden inside dust, the binarity hypothesis stands to be confirmed. If Sakurai's object follows the evolution track presented by Hajduk et al. (2005), then in less than 100 years the star will increase its temperature again and the UV radiation will dissociate the dust surrounding it. At that time, it will also ionise all the gas that it ejected after the very late thermal pulse, thus forming a new planetary nebula.

The passive disc model failed to reproduce the exact shape of the observed visibility spectra due to the complexity of the detected structure. However imperfect the fitting, our findings disprove the idea of a spherically expanding shell that was accepted so far, due to the differential phase signal (Fig. 4.6).

In our model, the SED is fitted well, but the visibilities show significant residuals. This implies that in reality a more complex model is needed here. A denser *uv*-plane coverage (more than the six baselines given here) would be needed to allow further determination of asymmetries. However, the object is now too faint and near the detection limit of MIDI¹⁶. Furthermore, the instrument will be decommissioned by the time Sakurai's Object is observable again in 2014.

¹⁶Limiting flux for the UTs is 0.5 Jy at 12 μ m but the correlated flux is currently 0.3 Jy.

The young nebula M2-9

The contents of this chapter have been included in part in Lykou et al. (2011). The VLTI data has been reduced and analysed by O. Chesneau. The main text was written by the author. Input by the co-authors will be clearly indicated in this chapter.

5.1 The nebula

M2-9 is one of the best-studied examples of elongated and axisymmetric bipolar planetary nebulae with a tightly pinched waist and symmetric lobes. The lobes of the nebula extend up to $22''$ at each side of the bright central core. Schwarz et al. (1997) found that the nebula has polar knots extending up to $52''$ from the central source (core). The core is dominated by $H\alpha$ emission in the visual due to scattering by dust near the core, as well as free-free emission in the

radio regime (diameter $\lesssim 3''$).

5.1.1 Orbital period

Corradi et al. (2011) and Doyle et al. (2000) studied the evolution of the nebula in the $H\alpha + [\text{N II}]$ and $[\text{O III}]$ images taken between 1952 and 2010. They confirmed that the nebula’s shape is changing within the bipolar structure (van den Bergh 1974). As witnessed especially in the $[\text{O III}]$ images, a “beam” of highly-excited oxygen gas appears to revolve, like a lighthouse beam, around the bipolar lobes over time (Fig. 5.1). Corradi et al. (2011) found an orbital period of 92 ± 5 years, or 85 ± 2 years if the orbit is eccentric ($0.05 \leq e \leq 0.15$). This effect can be created by orbital motion and is the best evidence that the core engulfs a binary system. In addition to that, the high-excitation, that is $[\text{O III}]$, lines seen in M2-9 suggest that the illuminating source is a hot and compact star (Doyle et al. 2000; Schwarz et al. 1997; Lim & Kwok 2000; Livio & Soker 2001), *not* to be confused with the primary star whose ejecta now constitute the nebula. In such a scenario, dust originating from the primary will settle in the binary system’s orbital plane in the form of a disc, torus or spiral (see Section 1.5).

5.1.2 Distance of M2-9

The distance of M2-9 is uncertain. Many authors quote a distance of 1000 pc in the absence of a tight constraint (Hora & Latter 1994; Livio & Soker 2001; Smith & Gehrz 2005). Schwarz et al. (1997) proposed a much closer distance of 640 ± 100 pc, based on expansion parallax measurements of the outer lobes. Here, we derive a larger distance, confirmed by Corradi et al. (2011) who reanalysed the data of Schwarz et al. (1997). For all the literature mass estimates described below, the assumed distance¹ was different from the one presented here.

¹All mass estimates with an assumed distance of 1 kpc (except for Lenzuni et al. 1989, 2.37 kpc)

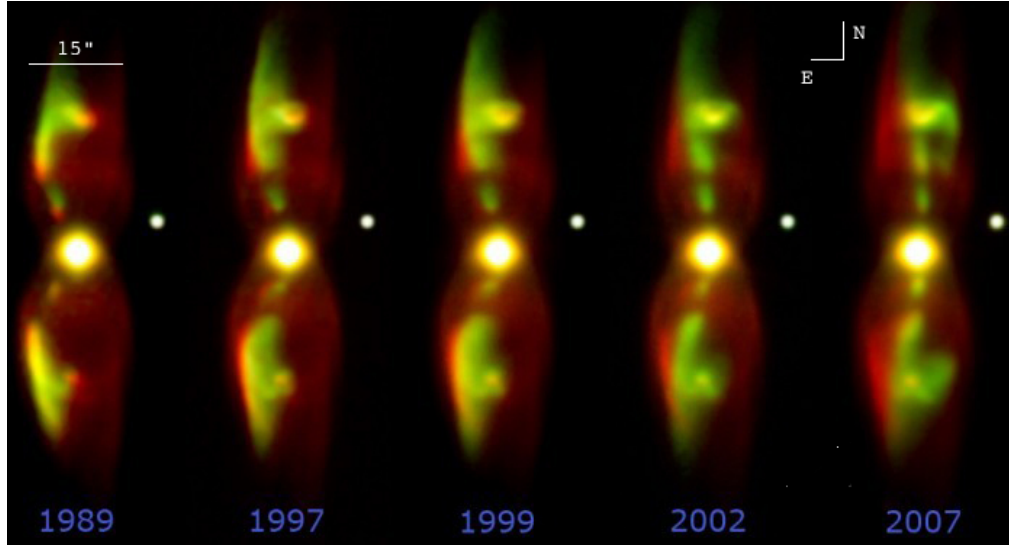


Figure 5.1 – The evolution of the symbiotic nebula M2-9 from 1989 till 2007. The moving “lighthouse beam” is clearly indicated in green ([O III]). The $H\alpha + [N \text{ II}]$ background images are in red. North is up and east is left. The bright star on the right of each exposure is a field star. *Image credit: R. Corradi, M. Santander-Garcia & B. Balick www.apod.nasa.gov/apod/ap070618.html and Doyle et al. (2000); Corradi et al. (2011)*

5.1.3 Mass of the ejecta

Bachiller et al. (1990) mentioned a total amount of molecular gas in the nebula higher than $10^{-3} M_{\odot}$. Feibelman (1984) gave a gaseous mass of $0.21 M_{\odot}$ and mass of dust $2.1 \times 10^{-3} M_{\odot}$ for the entire nebula, but Lenzuni et al. (1989) estimated a higher total dust mass by IRAS observations ($\sim 5.4 \times 10^{-3} M_{\odot}$).

The core of M2-9 was resolved using millimetric interferometry (Plateau de Bure, $5'' \times 3''$ beam), showing that the molecular gas is distributed in a ring-like structure extended about $6''$ east-west. A kinematical age ~ 2100 years was derived from the expansion of the CO gas in the nebula (Zweigle et al. 1997).

Observations by Smith & Gehrz (2005) within the last decade showed that in the core the mass of warm gas is $9.2 \times 10^{-4} M_{\odot}$ and that of warm dust $4 \times 10^{-6} M_{\odot}$, while in the lobes the mass of cold gas is $0.78 M_{\odot}$ and that of cool dust is $3.4 \times 10^{-3} M_{\odot}$. The different dust masses are within the range of the uncertainties in dust emissivities.

5.2 Observational data

The circumstellar region of M2-9 is dominated by a diffuse cloud of emission due to dust scattering, as noticed on images from the HST (Figures 5.1 and 5.2). The central star is invisible as it is hidden behind a dusty envelope. To identify the properties of that envelope, we decided to observe it in the near and mid infrared with the VLT and VLTI. For comparison, we also present archived observations of M2-9 with the infrared satellites ISO, Spitzer and AKARI.

5.2.1 VLTI

M2-9 was observed in the N band ($7.5\text{--}13.5\mu\text{m}$) with MIDI (Leinert et al. 2003, 2004), the mid-infrared recombiner of the VLTI with the use of only two Unit Telescopes (UTs). Only four spectrally dispersed ($R=30$) visibility measurements could be obtained, due to bad weather conditions.

The observations of M2-9 with MIDI were performed in April, June and August 2007 and March 2008 in the so-called `SCI_PHOT` mode, meaning that the photometry of each telescope is recorded simultaneously to the fringes. The visibility errors, including the internal ones and the ones from the calibrator diameter uncertainty, range from 5% to 10%. The accuracy of the absolute flux calibration is about 10–13%. For the flux calibration, HD 163917 ($F_{12\mu\text{m}} = 16.54$ Jy) was used. The log of the observation is given in Table 5.1. Both MIDI data reduction packages (MIA and EWS) were used to analyse the data.

Table 5.1 – VLTI observing log for M2-9

OB	Date	Base	Mode	Projected baseline	
				Length [m]	PA [°]
M2-9_1	2007-04-11	U2–U3	SCI_PHOT/PRISM	40.2	107.3
M2-9_2	2007-06-28	U2–U3	SCI_PHOT/PRISM	47.3	126.0
M2-9_3	2007-08-28	U2–U3	SCI_PHOT/PRISM	39.7	44.0
M2-9_4	2008-03-28	U3–U4	SCI_PHOT/PRISM	45.1	39.0

Calibrators; angular sizes in milliarcseconds (mas): HD 116870 K5III $2.44 \pm 0.12\text{mas}$,
 HD 163917 G9III $2.75 \pm 0.11\text{mas}$, HD 167618 M3.5III $11.33 \pm 0.1\text{mas}$,
 HD175775 G9III $3.26 \pm 0.23\text{mas}$, HD 152820 K5III $2.57 \pm 0.34\text{mas}$

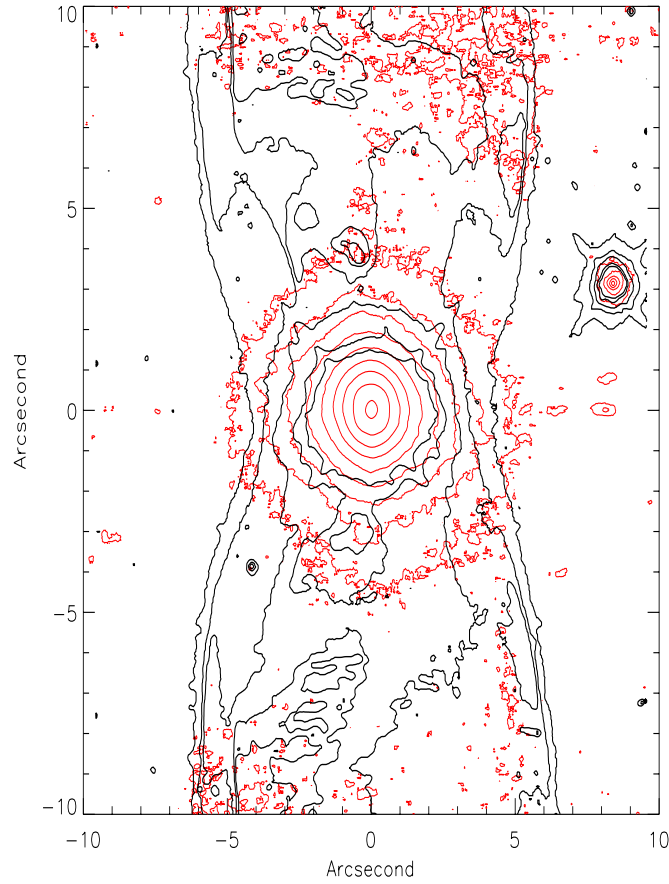


Figure 5.2 – Composition of HST/STIS (black) and NACO/Ks (red) images. North is up and east is on the left. The infrared emission contours follow the lines of the HST scattering in the visible, not only in the core but in a north-west region as well. The unresolved core is less than $0.1''$ in Ks. Contours from the centre to low levels are 95, 10, 2, 0.8, 0.4, 0.2, 0.1, 0.05, 0.025 and 0.015% of the maximum, respectively. Noise appears in the last two lower levels and those reveal the extended nebula as it is evident on the northern and southern part of the image. The diffuse light is increasing smoothly from the 0.05 to the 10% level. *Image and caption provided by O. Chesneau.*

5.2.2 NACO

M2-9 was observed with the near-infrared adaptive optics instrument NACO on the VLT (Lenzen et al. 2003; Rousset et al. 2003) as well, using three broad-band filters centred respectively at $2.18\mu\text{m}$ (Ks), $3.8\mu\text{m}$ (L') and $4.78\mu\text{m}$ (M'). The Ks data were taken during the night of 3 July 2006, and the L' -band and M' -band data on 18 August 2006. These observations were complemented

with close-by PSF calibrations using HD155078 (F5V) in L' and HD156971 (F1III) in M'. We used the S27 (Ks) and L27 (L', M') camera mode to obtain a field of view of $28'' \times 28''$ and a pixel scale of 27.1 mas per pixel.

Data reduction was performed using the NACO/VLT pipeline and self-developed routines in IDL. Jittering was used to remove the sky which forced us to cross-correlate and re-centre all frames. We performed bias subtraction, flat fielding, bad pixel removal and sky subtraction prior to co-adding all dithered exposures with a shift-and-add method to enhance S/N ratio. Chopping-and-nodding was used for the M' observations for sky removal.

Our Ks, L' and M' observations of M2-9 with NACO revealed an unresolved core at diameters less than $0.1''$ (Lykou 2008). Figure 5.2 is a composite image of a Hubble Space Telescope (HST) STIS/CCD image in the visible and our Ks-band image, the latter being an improved near-infrared view of the source compared to Aspin et al. (1988). One can notice a broad near-infrared emission around the core of M2-9 (diameter $< 5''$) and some enhanced emission in the lobes as well ($\sim 10''$ from the core; more prominent at north-west). These are attributed to scattering. Near-infrared photometry gave $m_{L'}=4.12$ and $m_{M'}=2.5$.

5.2.3 ISO

5.2.3.1 ISOCAM

We have reduced and analysed archived² data from ISOCAM (Cesarsky et al. 1996), the Infrared Space Observatory's (ISO) infrared camera. The satellite was mounted with a 60cm Ritchey-Chrétien Cassegrain telescope. Ten exposures have been recorded in 1996 for a range of wavelengths from 3.0 to $14.9\mu\text{m}$ with both short-wave (SW) and long-wave (LW) filters (bandwidths stated in Table 5.2). Each frame is 32×32 pixels with an effective field-of-view $45'' \times 45''$ and the spatial scale of each pixel is $1.5''$.

The standard software CIA was used to reduce and analyse the data (Table 5.2). The cube frames were dark subtracted and deglitched. The

²<http://iso.esac.eso.esa.int/ida/>

Table 5.2 – ISOCAM photometry

λ_{ref} [μm]	$\Delta\lambda$ [μm]	detector	flux [Jy]	σ_{flux} [mJy]
3.0	1.00	SW3	4.6	9.5
3.7	0.55	SW6	7.9	9.6
4.5	0.30	SW7	13.3	9.5
4.5	1.00	LW1	16.1	16.7
6.0	1.00	LW4	27.6	16.7
6.8	0.50	LW5	32.1	16.4
7.7	1.50	LW6	37.2	16.6
9.6	2.20	LW7	34.7	16.7
11.3	1.30	LW8	42.3	16.7
14.9	2.00	LW9	50.6	16.6

faulty ISOCAM column 24 is removed during the calibration. A single exposure was created per cube which was then flat fielded and the photometry was performed with the `flux_sum` method (background fitting).

Photometric errors were consistent for each detector. In ISOCAM the physical detector pixel size is $1''$ and the Airy disc pattern increases with wavelength from $1''$ to $3.5''$ (see J. Blommaert, R. Siebenmorgen, A. Coulais, L. Metcalfe, M.-A. Miville-Deschênes, K. Okumura, S. Ott, A. Pollack, M. Sauvage, & J.-L. Starck 2003, p. 44) thus the core of M2-9 was not resolved by this instrument.

5.2.3.2 SWS

An infrared spectrum has also been retrieved from ISO Short Wavelength Spectrometer (SWS) using short- and long-wavelength gratings (Kessler et al. 1996). The aperture area varies with wavelength range and grating: it is $14'' \times 20''$ for $2.38\text{--}12.0\mu\text{m}$, $14'' \times 27''$ for $12.0\text{--}27.5\mu\text{m}$, $20'' \times 27''$ for $27.5\text{--}29.0\mu\text{m}$ and $20'' \times 33''$ for $29.0\text{--}45.2\mu\text{m}$ (see Figure 5.9).

5.2.4 SPITZER

Calibrated data were extracted from the Spitzer Space Telescope Archive. M2-9 has been observed with both the InfraRed Array Camera (IRAC) and

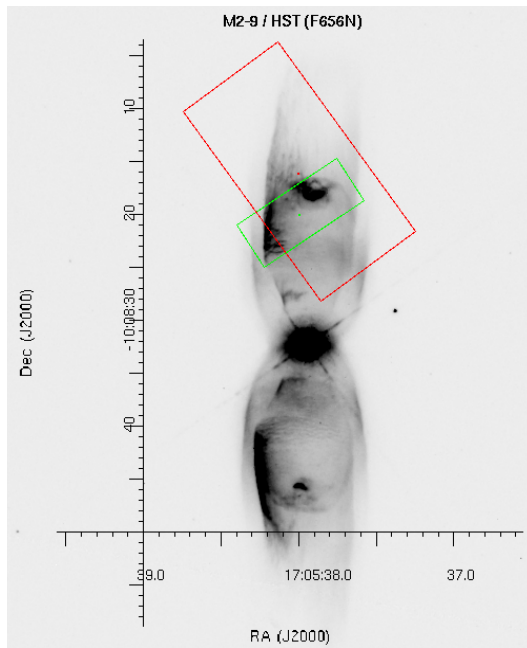


Figure 5.3 – Positioning of the Spitzer/IRS slits over a F656N exposure of M2-9 (Hubble Space Telescope Legacy Archive). Both slits were centred on top of the northern lobe, the Short-High (green; $4.7'' \times 11.3''$) at a $PA=131.2^\circ$ and the Long-High (red; $11.1'' \times 22.3''$) at a $PA=46.1^\circ$. North is up, east is left. The underlying $H\alpha$ image comes from 1996. By the time that Spitzer observed M2-9, the underlying structure of M2-9 was rather different, and the nebular structure inside the green aperture had changed.

the InfraRed Spectrograph (IRS). Unfortunately, the core's strong infrared emission has saturated IRAC rendering those observations useless.

High-resolution spectra (Figure 5.4) by IRS (Houck et al. 2004) revealed important information on the nebular dusty and gaseous chemistry. According to the astrometric information stored in the data, the two slits were positioned over the northern lobe and avoided the core (Figure 5.3): Short-High slit ($9.9\text{--}19.6\mu\text{m}$) is $4.7'' \times 11.3''$ at $PA=131.2^\circ$ and Long-High slit ($18.7\text{--}37.2\mu\text{m}$) is $11.1'' \times 22.3''$ at $PA=46.1^\circ$.

5.2.5 AKARI

We include mid-infrared photometry from the AKARI satellite IRC Point Source Catalogue archive (Murakami et al. 2007; Ishihara et al. 2010). M2-9

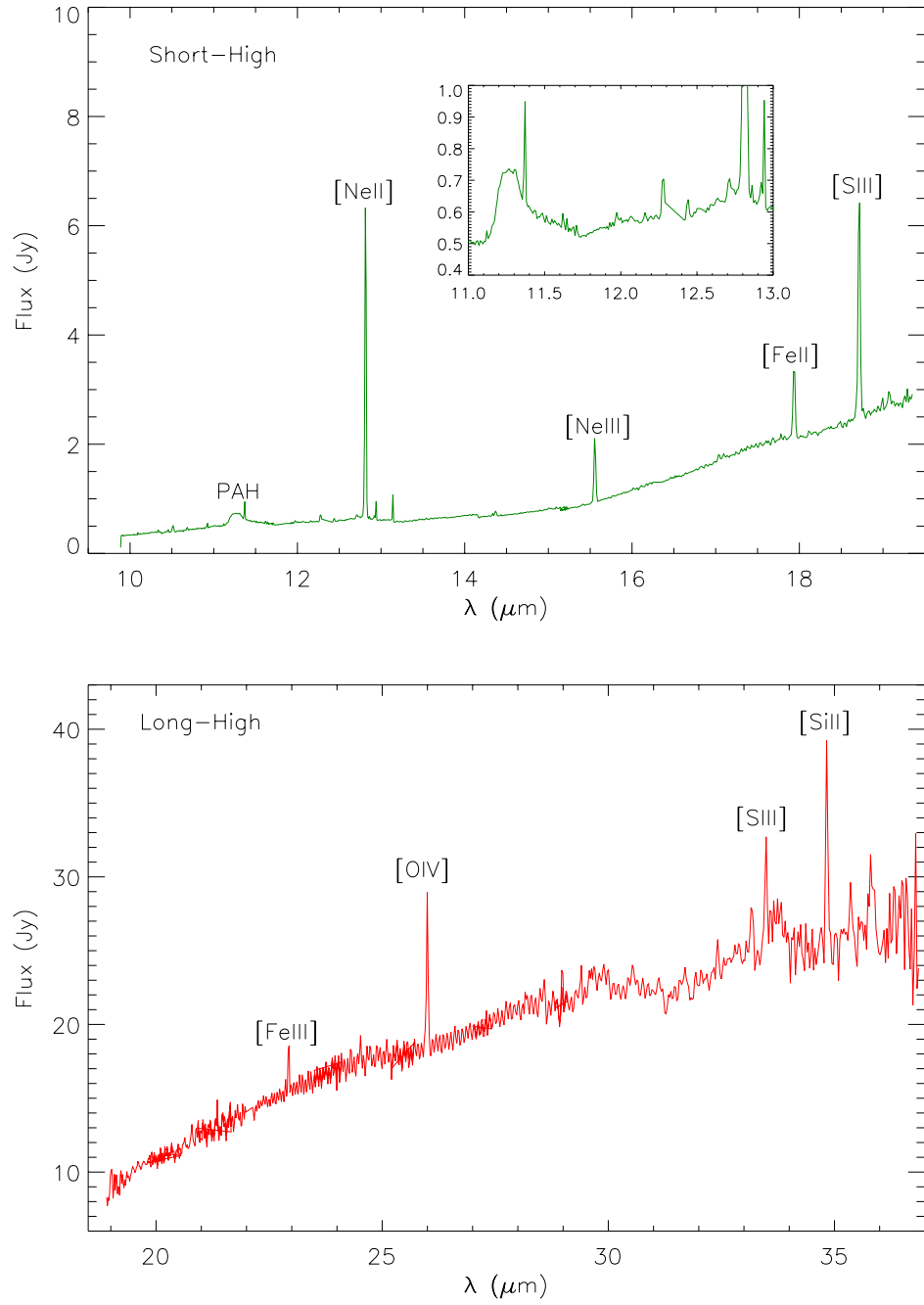


Figure 5.4 – High-resolution spectra of the northern lobe of M2-9 by IRS/SPITZER. Upper curve corresponds to the Short-High slit and lower curve to the Long-High (for slit orientation, see Figure 5.3). The inset in the upper plot is a close-up of the PAH emission features.

has been observed with the InfraRed Camera (Onaka et al. 2007) at two infrared bands, namely S9W (6.7–11.6 μm) and L18W (13.9–25.6 μm) with respective effective wavelengths at 9 and 18 μm (see Figure 5.9 and Table 5.3).

5.3 Observational results

5.3.1 Spectral Energy Distribution

The integrated flux, as detected by MIDI (field-of-view: $\sim 0.4''$ with the UTs), in Figure 5.9 clearly shows a 20% difference between the MIDI and the ISO spectra. Since the rectangular aperture of ISO ($14'' \times 22''$) was positioned over the central area of M2-9 (excluding the largest part of the lobes) and it increased in size for bands larger than 12 μm (including part of the lobes near the central source), it is expected that ISO detected a more extended source than MIDI. The fact that both spectra have similar shape and only slightly different flux levels, indicates that they both detected almost the same compact source.

The photometric points shown on Figure 5.9 are listed in Table 5.3. All available spectra, that is ISO, MIDI and SPITZER, have been dereddened with an extinction of $A_V = 2.5$ taken by Torres-Peimbert & Arrieta (1998) and the Savage & Mathis (1979) interstellar extinction values (Figure 5.5) as

$$F(\lambda)_{\text{dered}} = F(\lambda) \times 10^{A_V/2.5(A_\lambda/E(B-V))}. \quad (5.1)$$

The two Spitzer slits were positioned on top of the northern lobe, but they have probed different parts of the nebula. A more detailed description follows (Figure 5.4).

5.3.1.1 Short-High

The spectrum is very weak compared to the continuum of both MIDI and ISO, which were positioned over the core, but there are many interesting features. There is a broad poly-aromatic hydrocarbons (PAHs, i.e. signature of C-rich chemistry) emission at 11 μm and much fainter broad regions at 12.3 and

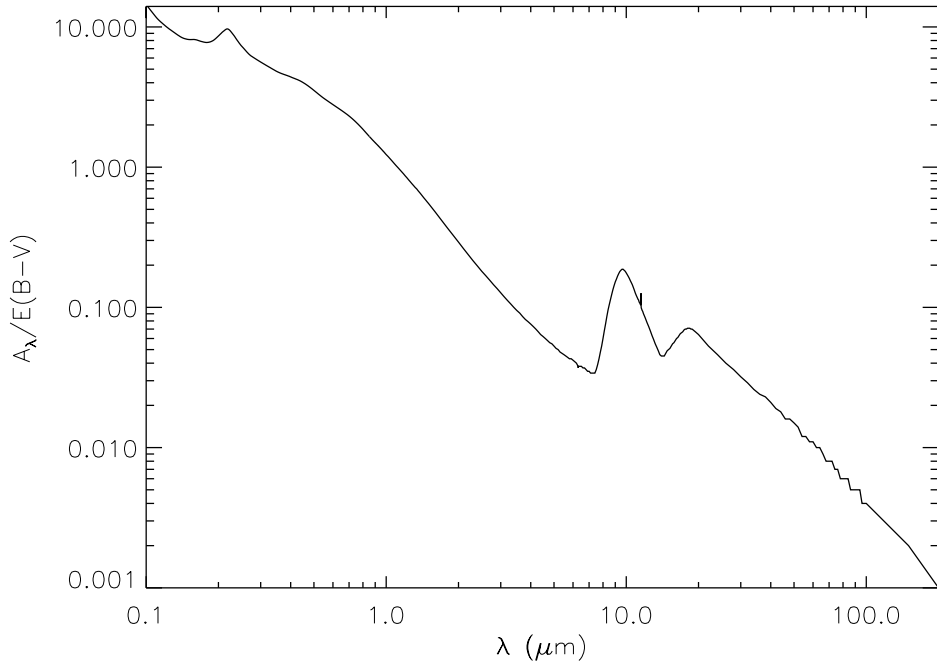


Figure 5.5 – Interstellar extinction by Savage & Mathis (1979). Two peaks associated with extinction by silicate grains are seen in the mid-infrared at 10 and 20 μm .

12.8 μm . [NeII], [NeIII], [FeII] and [SIII] lines are seen at 12.8, 15.6, 17.9 and 18.7 μm respectively. No other PAHs have been detected near the core by ISO, whereas it is unclear whether the 11.4 μm emission at 10% of the continuum of MIDI spectrum originates from PAH (Figure 5.6). This suggests that the 11 μm feature resides in the lobe.

5.3.1.2 Long-High

There is an indication of a broad feature at 33.5 μm (forsterite) but the neighbouring broad shallow absorption from 30 – 34 μm suggests that they may both not be real. Prominent gaseous emission lines are also present: [FeIII] (22.9 μm), [OIV] (25.9 μm), [SIII] (33.48 μm) and [SiII] (34.8 μm).

Table 5.3 – Photometric data points for M2-9 included in Figure 5.9.

λ [μm]	Flux [Jy]	Instrument	Aperture [$''$]	Reference
2.2	0.91	UM-UCSD	11	(1)
3.6	7.03	UM-UCSD	11	(1)
3.8	5.67	NACO	0.4	(2)
4.7	16.3	NACO	0.4	(2)
4.8	15.97	UM-UCSD	11	(1)
8.6	37.01	UM-UCSD	11	(1)
8.8	30.3	TIMMI2	4	(3)
9.0	38.07	AKARI/S9W	9.4	(4)
10.0	47.61	UM-UCSD	11	(1)
10.5	32.8	TIMMI2	4	(3)
10.8	39.64	UM-UCSD	11	(1)
11.3	38.28	UM-UCSD	11	(1)
12.0	50.5	IRAS		(5)
12.8	41.1	TIMMI2	4	(3)
17.9	41.5	TIMMI2	4	(3)
18.0	61.0	UM-UCSD	11	(1)
18.0	73.25	AKARI/L18W	9.4	(4)
24.5	38.1	TIMMI2	4	(3)
25.0	110.2	IRAS		(5)

(1) Cohen & Barlow (1974); (2) Lykou (2008); (3) Smith & Gehrz (2005);

(4) Ishihara et al. (2010); (5) G. Helou & D. W. Walker (1988)

5.3.2 Interferometry

Our VLTI observations of the core of M2-9 reveal the presence of a dusty structure. Visibilities decrease as the P.A. of the projected baselines increases (Fig. 5.7), suggesting a flattened structure. The core is significantly resolved by the 40-50m baselines, with visibilities of the order of 0.1–0.2. Our observations showed that the flattened structure is compact, typically 25×35 mas at $8\mu\text{m}$, and 37×46 mas at $13\mu\text{m}$ (Fig. 5.7). The dusty structure is more elongated along the planetary nebula’s equatorial plane, compared to the direction of the lobes. Therefore, the disc’s geometrical size can be constrained. Thus, MIDI has probed the existence of a flattened structure along the equatorial plane of the nebula.

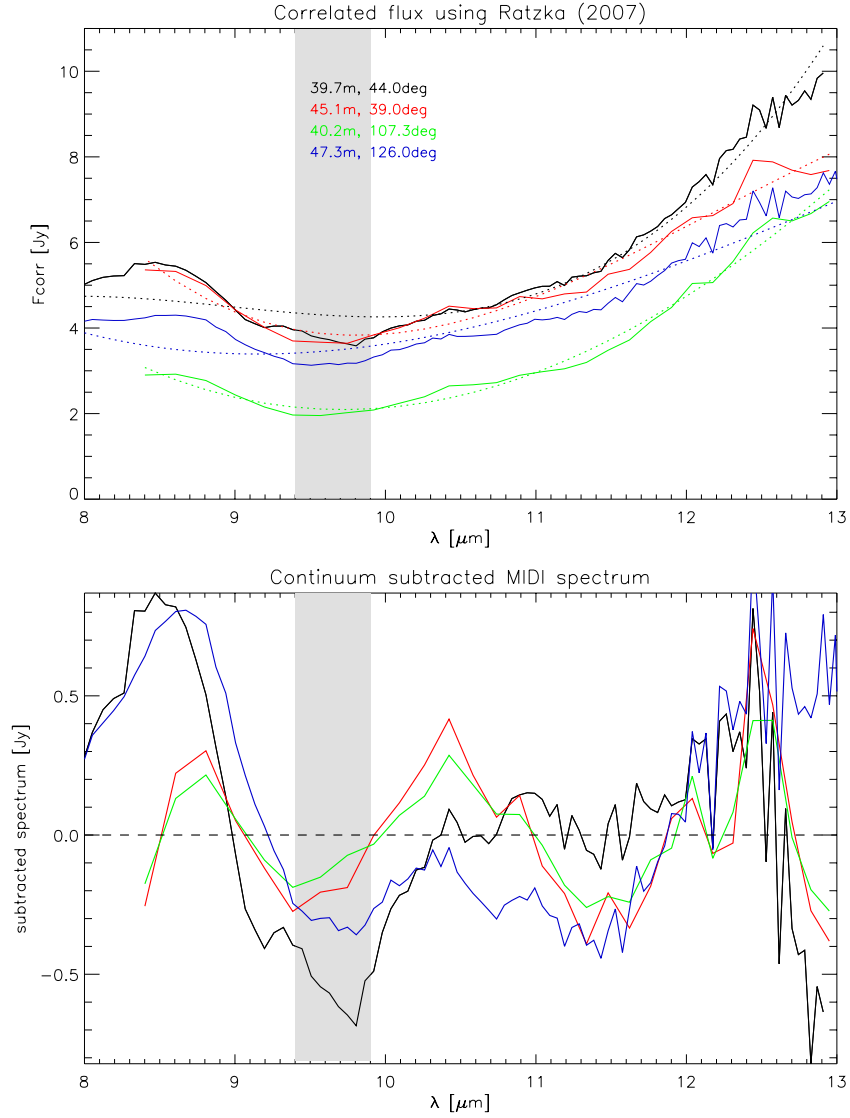


Figure 5.6 – *Top*: Correlated flux of M2-9. Following Ratzka et al. (2007), a polynomial fit was applied to each spectrum (dotted lines) corresponding to the continuum emission. The observed baselines are colour-coded and the reference is given within the figure. *Bottom*: Continuum-subtracted spectrum of M2-9. It is unclear whether the dips at 9.8 and $11.4\mu\text{m}$ correspond to crystalline features as reported by Lykou et al. (2011). The grey shaded areas indicate the region affected by atmospheric absorption from ozone.

5.3.2.1 Correction to Lykou et al. (2011)

Using the suggestion found in Ratzka et al. (2007) we estimated the correlated flux, F_{corr} , for each baseline, as

$$F_{corr} = V(\lambda) \cdot F_{MIDI}, \quad (5.2)$$

where $V(\lambda)$ is the spectrally-dispersed visibility and F_{MIDI} is the MIDI spectrum. Continuum emission is estimating by applying a polynomial fit to the correlated flux. The continuum-subtracted spectrum should reveal fainter emission or absorption features as in Ratzka et al. (2007).

We compare this to the findings of Lykou et al. (2011), where crystalline silicate features were reported at 9.8 and 11.4 μm and were attributed to forsterite (Mg_2SiO_4). As seen in Figure 5.6, it is unclear whether the slight dips seen in the continuum-subtracted spectrum (bottom panel) belong to absorption by forsterites, since the overall flux range is within -0.5 and 0.5 Jy. This might be caused by an oversimplification from the polynomial fits (see difference in levels between 8 and 9 μm in top panel; Figure 5.6).

5.4 Physical parameters of the disc

In this section we present the modelled disc and the constraints introduced by the fitting procedure. MC3D radiative transfer code was used to fit the observational data (see this work, Chapter 3.3).

5.4.1 Dust composition

The dust residing around evolved stars may be oxygen- or carbon-rich (O-, C-rich), or even a combination of both. This is determined by the abundance of each element during the AGB phase.

Cohen et al. (2002) showed that some carbon-rich nebulae, like CPD-56°8032 and NGC 6032, are also rich in silicate grain emission in the far-infrared. These grains must have formed before the transition of the central star to C-rich

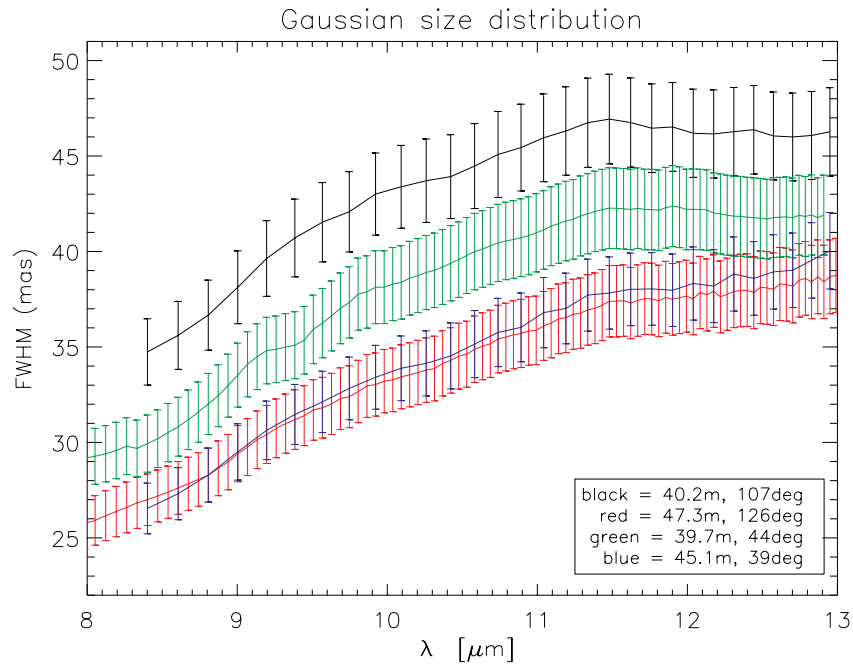


Figure 5.7 – Gaussian size distribution of the disc ($\pm 5\%$) for each baseline (Table 5.1) in N band implementing the dusty structure’s evolution in the mid-infrared.

and the subsequent expulsion of carbonaceous material (e.g. PAHs, SiC). Spectroscopic observations did not reveal any $3.3\mu\text{m}$ PAHs in the core of M2-9 (Smith & McLean 2008), thus the core is not C-rich, but other PAH features are present in the lobes (see Section 5.3.1). Since M2-9 is an O-rich nebula ($C/O < 0.5$, Liu et al. (2001)), thus the dust is expected to be O-rich, one explanation for the existence of PAHs in its lobes is due to the dissociation³ of carbon monoxide from the original, circumstellar envelope (Guzman-Ramirez et al. 2011). The model contained only amorphous silicate dust, since the exact percentage of crystalline silicates that is locked within the disc is unknown.

The dust compound used was that of Draine & Lee (1984) “smooth astronomical silicate”. The database has 1000 wavelengths increasing in a logarithmic scale from 0.001 to $1000\mu\text{m}$. The grain size range is 0.05 – $1\mu\text{m}$ and the preferred distribution was that of Mathis et al. (1977) with a power law index equal to 3.5

³Ionisation by ultraviolet photons can free C and C^+ , which may then bond with hydrogen molecules and create hydrocarbons. Hydrocarbon chains are then converted to PAHs.

(see Eq.[3.12]). For the modelled SED we have used 172 wavelengths between 0.001 and $1000\mu\text{m}$ and for the modelled images we used 17 wavelengths in the N band, namely from 7.97 to $13.1\mu\text{m}$.

5.4.2 Parametric study

We have chosen a certain position angle (P.A.) for the modelled disc with respect to the polar axis of the nebula. According to Phillips & Cuesta (1999), the P.A. of M2-9 polar axis is -2° . We support this estimation from the positions of the two ansae at $\sim 52''$ from the core; the ansae are displaced by $-2 \pm 2^\circ$ East from North from the polar axis (blue line; Figure 5.8 and Schwarz et al. (1997)). Best modelled visibility fits were found at the same position angle (Table 5.5).

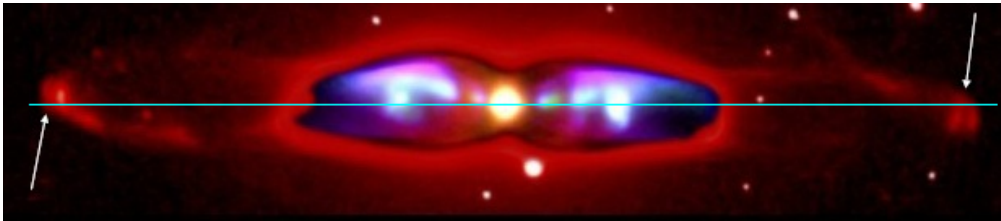


Figure 5.8 – The ansae of M2-9, pointed here by the arrows, extend up to $113''$ from the core (Schwarz et al. 1997). East is up and North is right. The blue line outlines the polar axis, where P.A. $=0^\circ$ Image credit: R. Corradi, M. Santander-Garcia, B. Balick.

Seeing as there has been no *a priori* knowledge of any geometric parameters of the dusty structure, except for its inclination in our line-of-sight ($\sim 74^\circ$), we had to investigate a large number of variables in order to establish a good fit. Those were the following:

1. The **inner radius** of the disc was initially put at 5 AU with 5 AU increments until 35 AU. Even though an approximate size was given by fitting the observed visibility spectra with Gaussian uniform discs, thus estimating their diameters in milliarcseconds and converting those into physical units (Figure 5.7), we preferred to extend our search range.
2. In the absence of any constraints, we set the disc's **outer radius** from 250 to 1000 AU with 250 AU increments. Radii smaller than 500 AU

produced a very dense structure, while values above 500 AU did not reveal any significant difference except for an overabundance of cold dust at wavelengths longer than $20\mu\text{m}$ for a distance longer than 900 AU.

3. The adopted initial value for the **mass of warm dust** ($4 \times 10^{-6} M_{\odot}$) derived by Smith & Gehrz (2005) was too small to recreate the silicate absorption features. We investigated values between 9×10^{-6} and $2.5 \times 10^{-5} M_{\odot}$, but not the ones given for large amount of cold dust that was estimated by Smith & Gehrz (2005) to be approximately $3.4 \times 10^{-3} M_{\odot}$ by fitting the IRAS observations in the far-infrared.
4. The disc's **scale height**, h_0 , was initially set at 5 AU for a thin disc and was increased by 5 AU steps up to 50 AU for a thick disc. The latter was suggested by the low visibilities which indicated a resolved structure, or else a very dense medium. When a better overall fit was found while testing models, the range changed from 35 to 40 AU with steps of 1 AU.
5. We tested values at 0.05 steps for the **flaring**, β , between 0.7 and 1.2. A flaring above 1.0 would produce a large wings in the disc's outer regions, while a flaring below that value would give a bent structure. We settled for a moderate flaring that would fit the MIDI data (Figure 5.10).
6. Parameter α , the **density in the midplane**, had 0.1 increments between 1.5 and 2.5. Eventually it was fixed to a certain value, where silicate absorption was evident at a flux level between the MIDI and ISO spectra.

5.4.3 Large grains and different grain size distributions

Models were tested with larger amorphous silicate dust grains and with different grain size distributions (Eq.[3.12]) having the specifications given in Table 5.4, yet none of those gave any good fit. They all produced a steep emission spike at between 8 and $9\mu\text{m}$ in the SED indifferent to the dust mass and distance, and thus they were immediately rejected.

Table 5.4 – Grain size distributions

# wavelengths	λ range	grain size range	index
500	0.01–200 μm	0.1–1 μm	3.5
1000	0.001–1000 μm	0.5–2 μm	3.5
1000	0.001–1000 μm	0.5–2 μm	2.0
1000	0.001–1000 μm	0.05–1 μm	2.0
1000	0.001–1000 μm	0.05–1 μm	1.5

5.4.4 Fitting results

The reconstruction of the disc’s image was made with the use of MC3D. The models of its spectral energy distribution (SED) and visibility amplitudes have been compared to the MIDI data and the observed SED. After careful examination of all possible parameters, the model with the best fit, is one that resembles the best geometrical shape for a flared disc. The model’s parameters are shown in Table 5.5.

Table 5.5 – Parameters of the best fitted model for M2-9. Our trial and error estimates of the parameters’ uncertainties do not significantly alter the quality of the fit.

Parameters	M2-9
T_{eff} (K)	15 000
Luminosity (L_{\odot})	2500
Distance (kpc)	~ 1.2
Inclination ($^{\circ}$)	74 ± 1
best P.A. ($^{\circ}$)	-2 ± 2
Inner radius (AU)	15 ± 1
Outer radius (AU)	900
α	2.0 ± 0.1
β	0.9 ± 0.1
$h_{100 \text{ AU}}$ (AU)	36 ± 2
ρ_{grain} (g cm^{-3})	2.7
Dust mass (M_{\odot})	$1.5 \times 10^{-5} \pm 5 \times 10^{-6}$

We were able to define a lower and an upper limit to constrain the size of the disc’s structure from a theoretical basis and from our observational data. A projected baseline on the equatorial direction of M2-9 would probe the full size of the disc. In our case, this telescope configuration was not accomplished.

The distance of 640 pc suggested by Schwarz et al. (1997) led us to many difficulties in fitting the observations. Even with scaling down the luminosity and the size of the disc or modifying the dust content, thus the optical depth, no improvement was found in fitting both the SED and the visibilities. Significant geometrical structures should have been detected in the dispersed visibilities for such a nearby source, yet the observed dispersed visibilities are very smooth. None of our models could fit the distance and luminosity assumed so far. Our best fits were found for a larger distance, namely ~ 1200 pc (Table 5.5, Figures 5.9, 5.10 and 5.11). Recent calculations of the nebulae expansion put M2-9 at a distance of 1300 ± 200 pc (Corradi et al. 2011).

The mass of dust, density and geometric parameters used in this model, represented the best fit for the opaque structure detected by MIDI in our line-of-sight (74°). A similar inclination of 73° was also found independently by Solf (2000) for the polar lobes and by Zweigle et al. (1997) for the CO torus.

To fit the near-infrared flux, we have selected a cooler star (15 000 K) as the illuminating source than what was proposed by (30 000 K; Smith & Gehrz 2005). From Figure 5.9 one can notice that the shape of both MIDI and ISO spectra is the same; the only difference is the flux level. The absolute flux calibration for MIDI was 10–15% while for ISO/SWS it ranges from 12–30% depending on the observed band, i.e. $\sim 14\%$ at $14\mu\text{m}$ (Schaeidt et al. 1996). As such, the two spectra could be at similar levels within these uncertainties.

We preferred to fit the ISO spectrum, because our model has a larger aperture than that of MIDI. Our best fit for the MIDI visibilities was found by optimising the model’s total χ^2 (Eqs. [4.1] and [4.3]), taking into account the restricted field-of-view of MIDI. The current fit has a total $\chi^2 = 18.71$ (Figure 5.10).

We preferred to achieve a better fit for the visibilities rather than for the SED. The latter contains a colder component at longer wavelengths, which includes a silicate feature near $18\mu\text{m}$ ($T_{\text{dust}} \leq 150\text{K}$; M.Werner, private communication). MIDI was able to resolve the “warmer” dust component for which we attempted to derive spatial distribution through modelling. A more complex model⁴, for example a disc with two density gradients, might be required to allow a fit for

⁴This is not covered by this radiative transfer code.

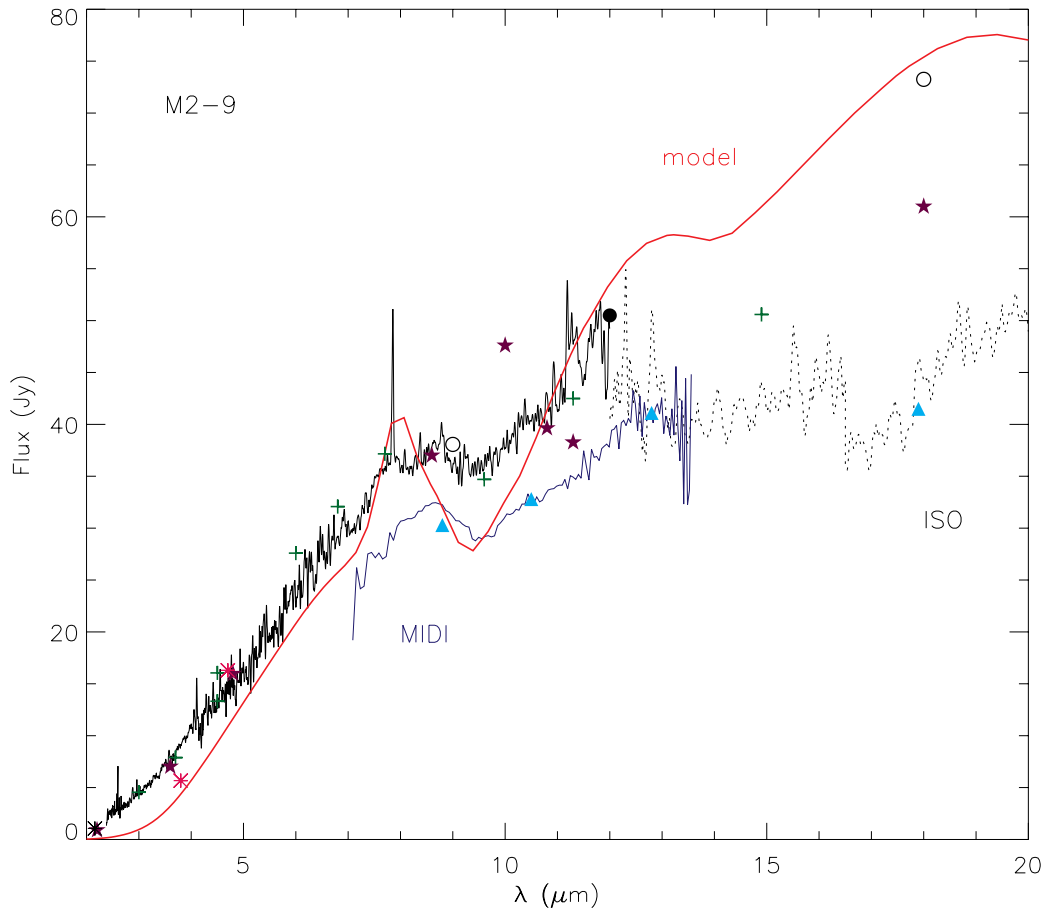


Figure 5.9 – At 1.2 kpc: MIDI spectrum (blue) compared with the ISO spectrum (black – solid: $14'' \times 20''$ aperture, dashes: $14'' \times 27''$ aperture), ISOCAM data (green crosses), AKARI data (open circles), the TIMMI2 photometric measurements of Smith & Gehrz (2005) with an aperture of $4''$ (cyan triangles), IRAS measurements (circles) and Cohen & Barlow (1974) photometry (purple stars, $11''$ beam). The NACO L' and M' band are also included (magenta stars, aperture $0.4''$). Details on M2-9 photometry can be found on Table 5.3. The red line is the best model with the full aperture ($\sim 1''$). All spectra have been dereddened using the Savage & Mathis (1979) law.

the SED as well.

We could not fit our data by decreasing the outer radius, since these modifications increased the silicate absorption feature and lowered the visibilities, suggesting either a denser or a larger, resolved structure (without altering the shape of the spectrum that was due to colder dust). Expanding the outer radius imposed a new problem: more cold dust must be deposited in the disc, thus

the predicted flux of the model exceeds actual measured levels at wavelengths longer than $12\mu\text{m}$. For our best fit, the disc's optical depth in the N band is $\tau_{10\mu\text{m}} = 4.6$. The fit is sensitive to parameters α , β and h_0 , as small changes in those values significantly altered the disc's opacity. The model in use does not include a puffed-up inner rim.

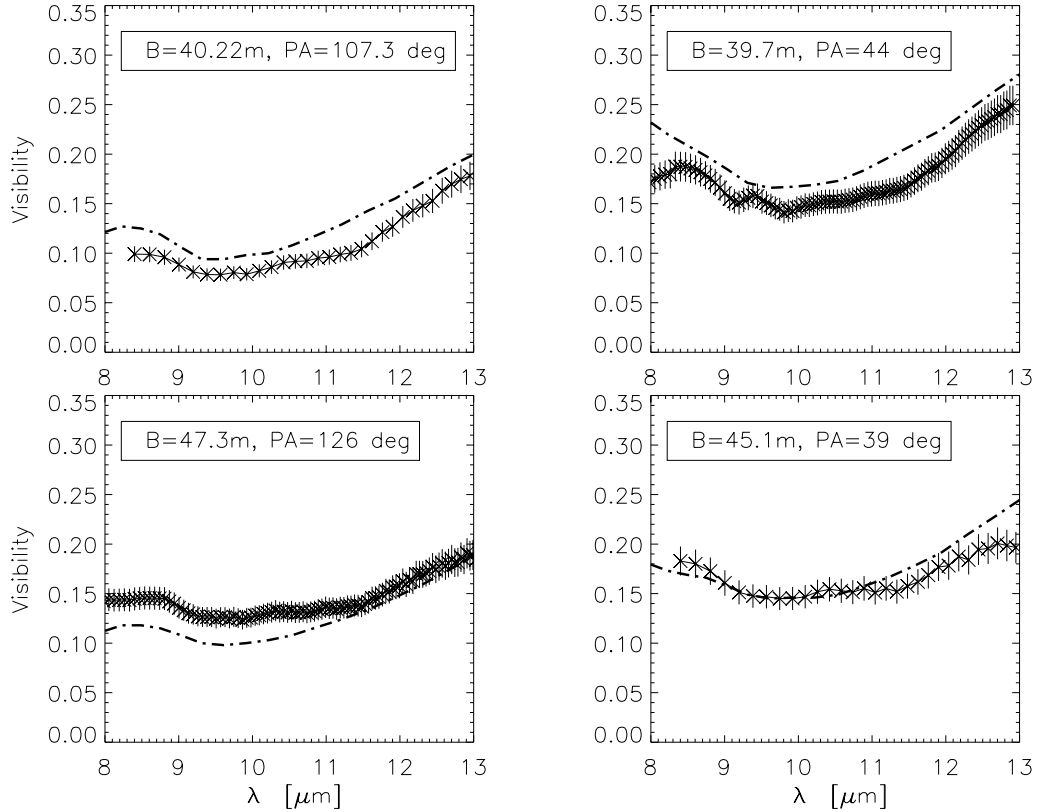


Figure 5.10 – MIDI visibilities, compared with the best model (dashed-dotted lines, see Table 5.5). The visibility curves are for the baselines M2_9-1 to M2_9-4 from top to bottom and left to right (Table 5.1).

A single illuminating source is assumed for the dusty disc; in this case the primary. Thus, the contribution from the companion (Section 5.1.1) in both the heating and shaping processes is not included and cannot be reproduced. This drawback may partly explain the difficulty in fitting the spectral energy distribution. The binary interactions lead us to consider a different disc geometry.

Due to the limited number of baselines, our selection of geometric parameters

was restricted. We have found an acceptable disc model to fit the observational data, which implies a general agreement in terms of emission and spatial distribution of the bulk of the dust in the core of the system. Despite this, it is also true that the source is complex, probably engulfing a binary, and that the passive disc model is probably not a good description of the reality. This source clearly requires interferometric imaging either with aperture masking instruments⁵ (Tuthill et al. 2006, 2010) or with MATISSE/VLTI (Lopez et al. 2008), both of which offer better *uv*-plane coverage than MIDI/VLTI.

5.5 Where is the companion relative to the dust source?

It has long been believed that M2-9 engulfs a binary system. The lighthouse effect provides indirect, but rather convincing evidence of binarity with a period of ~ 100 years. We estimated orbital periods for the binary by using the observations of 18 years from Doyle et al. (2000). From those, it can be seen that the lighthouse beam covered less than 20% of the perimeter of the lobes within that time scale. We found that the period ranges from 90 to 120 years.

Livio & Soker (2001) have used a typical mass for a white dwarf of $0.6 M_{\odot}$ and $0.8 M_{\odot}$ for a post-AGB star, leading to an orbital separation of 27 AU, assuming a circular orbit. The assumption of circularity is based on the fact that no evident acceleration nor deceleration of the lighthouse's angular velocity has been observed to date (R. Corradi, private communication)⁶.

The VLTI observations of a compact dusty structure impose some constraints, which constrain the interpretation of this system. However, these interferometric observations are also limited in the sense that they do not provide any closure phase, nor absolute astrometry as in radio interferometry. It is therefore not possible to locate precisely the position of the compact dusty structure.

⁵At the time this thesis was written, the European Southern Observatory was planning on implementing aperture masking in the mid-infrared on the instrument VISIR/VLT.

⁶Bearing in mind though, that intensive monitoring of the nebula occurred only in the last 20 years (Doyle et al. 2000)

5.5.1 The inner dusty disc

The diameter of the dusty structure detected by MIDI at the baseline closer to the equatorial plane (M2-9_1; Table 5.1) is approximately 33 mas (Figure 5.7). Extrapolating to a projected baseline at 90° (equatorial plane) we would expect a minimum size of 41 mas. From that we presume that the central cavity must be smaller than this size. Our modelling has shown that a diameter of approximately 30 ± 2 AU (or ~ 25 mas) fits the inner edge of the disc (Table 5.5). Increasing the disc's inner rim did not give a better fit to the MIDI data.

We have used the relation for the dust sublimation radius (R_{sub} in AU) by Tuthill et al. (2001):

$$R_{\text{sub}} = 1.1 \left(\frac{T_{\text{sub}}}{1500\text{K}} \right)^{-2} \sqrt{\frac{L}{1000L_{\odot}}}, \quad (5.3)$$

where L is the stellar luminosity and T_{sub} is the dust sublimation temperature. For a star of $2500 L_{\odot}$ (Table 5.6) the inner rim of the dust disc must reside at a distance larger than 4 AU but within the limits defined by the MIDI observations. Neither an $100 L_{\odot}$ heating source, such as the accretion disc in the case of M2-9, nor the $553 L_{\odot}$ source suggested by Schwarz et al. (1997), can fit the observational data.

Table 5.6 – Dust sublimation radii (in AU) for two stellar luminosities

T_{sub} [K]	R_{sub} [AU]	
	$2500 L_{\odot}$	$100 L_{\odot}$
2000	0.97	0.19
1500	1.74	0.35
1000	3.90	0.78

The binary system should reside within the structure detected by MIDI. By applying simple Keplerian physics (assuming circular orbits), we have used several mass ratios⁷ for the binary components to estimate the corresponding orbital diameters, for periods of 90 and 120 years, in physical units and converted them to angular sizes for a distance of 1.25 kpc (Table 5.7).

⁷Within the Chandrasekhar limit for the WD

Table 5.7 – Binary orbital diameters in AU (also converted in mas for a distance = 1.25 kpc), at two different periods, 120 and 90 years

M_1 (M_\odot)	M_2 (M_\odot)	P = 120 yrs		P = 90 yrs	
		d [AU]	d [mas]	d [AU]	d [mas]
0.6	0.6	52	41.6	42	33.6
0.8	1.0	60	48.0	50	40.0
0.6	1.4	62	49.6	50	40.0
0.8	1.4	64	51.2	52	41.6
1.0	1.2	64	51.2	52	41.6
0.6	1.0	57	45.7	47	37.7
0.6	1.2	60	48.0	49	39.2
1.0	1.0	62	49.2	51	40.6

As seen in Table 5.7 orbital diameters that fit within the extrapolated angular size for the dusty structure of 41 mas range from 42–52 AU. This is larger than our best fit model, where the size of the disc’s inner cavity is 30 AU. We should draw attention though to the fact that the disc’s inner rim is centred on the heating source, which in turn is not positioned on the binary’s centre-of-mass. The companion’s heating capabilities are minimal, since a $100 L_\odot$ luminosity did not fit our modelled disc. Its orbital motion though should allow it to truncate the disc, an effect that can alter the geometry of the disc’s inner edge. The model in use cannot reproduce a partially illuminated disc or a disc with an off-centre illuminating source. We can only surmise that high-angular resolution radio observations could establish the astrometric position of the companion (WD/accretion disc).

5.5.2 The exterior torus

The obtained NACO images are fully dominated by the central source and lack dynamical range in its close vicinity (Figure 5.2). At $\sim 3''$ from the core Zweigle et al. (1997) found that the CO emission is coming from a large ring, whose centre seemed offset by $0.5 \pm 0.3''$ from the compact radio source ($< 0.1''$ and unresolved at 1.3 cm, Bignell 1983). More recent Plateau de Bure data (Castro-Carrizo et al., in preparation) with $0.3''$ angular resolution confirm the presence of an offset, and detect additional CO emission coming from regions at a

distance of $\sim 1''$ from the centre.

Molecular hydrogen spectroscopy has yielded two different velocity components at distances $\lesssim 0.5''$ latitudinally from the central illuminating source: 10.9 km s^{-1} (blue-shifted) and 123.7 km s^{-1} (red-shifted). This points to a H_2 disc-like structure (Smith et al. 2005).

Spiral structures (as expected in a symbiotic type system) can be formed by binary interactions during the ejection of the primary's CO envelope (Edgar et al. 2008), yet this is not clear at this point for the case of M2-9. Spirals would be seen best at a high inclination (pole-on). Our source is edge-on. The differential phases of the disc detected by VLTI are small, lying within a range of $\pm 10^\circ$, i.e. well below some strong signature from dusty rings reported in the literature (Deroo et al. 2007b; Ohnaka et al. 2008).

5.6 The mass of the components and an accretion disc

Spectrophotometry of the core has shown an intrinsic amount of (high-excitation) iron emission lines (FeII and FeIII, Allen & Swings 1972). This gives an electron temperature for the core $\sim 10\,000 \text{ K}$ and an electron density of 10^7 cm^{-3} (similar to Mz3, Smith 2003). As it is mentioned in that work, at such high core densities collisional de-excitation prevails and weak forbidden nitrogen lines in the core are not a surprise. Iron was found in the northern lobe as well (Figure 5.4). Hora & Latter (1994) have also detected iron lines that have a high ionisation potential, proving the presence of a particle beam or supersonic shock interface inside M2-9. $\text{H}\alpha$ emission from the core is optically thick with broad wings due to scattering (Balick 1989; Arrieta & Torres-Peimbert 2003). Polarisation measurements in the optical revealed an elliptical polarisation in the core of M2-9, which was consistent in every observed waveband (namely B, R and I). Aspin & McLean (1984) explain this as scattered continuum from the central ionising source by an extended ionised dusty torus around the core (diameter $\lesssim 4''$). All this indicates that the illuminating source of M2-9 must be a hot and compact star.

The lifetime of a planetary nebula is a $\sim \text{few} \times 10\,000$ years and that of a white dwarf billions of years. Thus, material ejected by what is now the secondary, a white dwarf, is already dissolved in the interstellar medium. We expect that the material that composes M2-9 at the moment, originates from what is now the primary, an evolved giant, either an AGB or a post-AGB star.

According to Akashi & Soker (2008) shaping of the ejecta of a tight-waist PN is possible by an accretion disc around the secondary. An accretion disc could be bright enough and illuminate part of the disc that has been detected by MIDI. We believe that the disc found in the core of M2-9, engulfs an evolved star (post-AGB) and a WD, namely the primary and secondary components of the binary. The first one is the main heating source for the dust at $\sim 2500\,L_\odot$ (Table 5.5), while the second one obtains its luminosity from an accretion disc, although it is the main ionising source for the nebula (lighthouse beam).

The most probable scenario to explain the observations of Schwarz et al. (1997) is that the mass-losing star transfers material onto the secondary at a rate of $\dot{M}_* = 10^{-6}\,M_\odot\,\text{yr}^{-1}$ at supersonic speeds ($5\text{--}10\,\text{km s}^{-1}$) feeding the accretion disc of a white dwarf. A luminosity of $\sim 100\,L_\odot$ was estimated for the ionising source from the radio observations (Purton et al. 1982) and the luminosity relation $L_* = 78_{-16}^{+15} \times S_{6\text{cm}}$ from Zijlstra (1990) for the source's flux density at 6cm.

The following equation by Soker (2004) was used in order to calculate accretion luminosities for the white dwarf:

$$\dot{M}_{\text{acc}} = 3 \times 10^{-7} \left(\frac{M_{\text{WD}}}{0.6\,M_\odot} \right)^2 \left(\frac{v_s}{10\,\text{km s}^{-1}} \right)^{-4} \left(\frac{a}{100\,\text{AU}} \right)^{-2} \left(\frac{\dot{M}_*}{10^{-4}\,M_\odot\text{yr}^{-1}} \right), \quad (5.4)$$

where \dot{M}_{acc} is the mass accretion rate, \dot{M}_* is the mass loss rate of the primary, M_{WD} is the mass of the accreting white dwarf, a is the binary separation and v_s is the wind speed.

Table 5.8 – Accretion luminosities for a range of WD masses and different companion mass outflows.

v_{outflow} (km s ⁻¹)	L_{acc} (L _⊙)				
	0.6 M _⊙	0.8 M _⊙	1.0 M _⊙	1.2 M _⊙	1.4 M _⊙
5	1144	2760	5460	8734	14 740
10	73	174	338	566	914

Table 5.8 displays a range of accretion luminosities estimated by equation

$$L_{\text{acc}} = \frac{G\dot{M}_{\text{acc}}M_{\text{WD}}}{R_{\text{WD}}}, \quad (5.5)$$

for different secondary masses for the above-mentioned accretion rates and velocities, assuming a binary separation of 30 AU and a WD radius of 6000 km, in order to confirm our assumption that the 100 L_⊙ luminosity is due to accretion.

Our findings confirm a WD mass of 0.6–0.8 M_⊙, previously suggested by Livio & Soker (2001) and in accordance to Gesicki & Zijlstra (2007). We can see that the accretion luminosities for a wind velocity ~ 10 km s⁻¹ are not high enough to evaporate dust up to 15 AU (inner rim). The cool primary’s luminosity (2500 L_⊙) is sufficient though.

5.7 Remarks

MIDI has detected the dusty structure in the core of M2-9 for the first time. The structure detected is of a complex nature. It is most probably surrounding the binary, while being truncated by the white dwarf companion. It is not yet obvious how this structure is related to the torus seen in the submm wavelengths by Plateau de Bure Interferometer, although there has to be a certain correlation for their shaping mechanisms. Although the structure can not be modelled completely – its spectral energy distribution in particular – with the available radiative transfer code, an approximation of its geometric structure can be given. Nevertheless, the fits obtained for M2-9 (Fig. 5.10) are better in quality compared to those obtained for Sakurai’s Object (Fig. 4.11

and 4.13). A further discussion and comparison with similar structures can be found in Chapter 7.

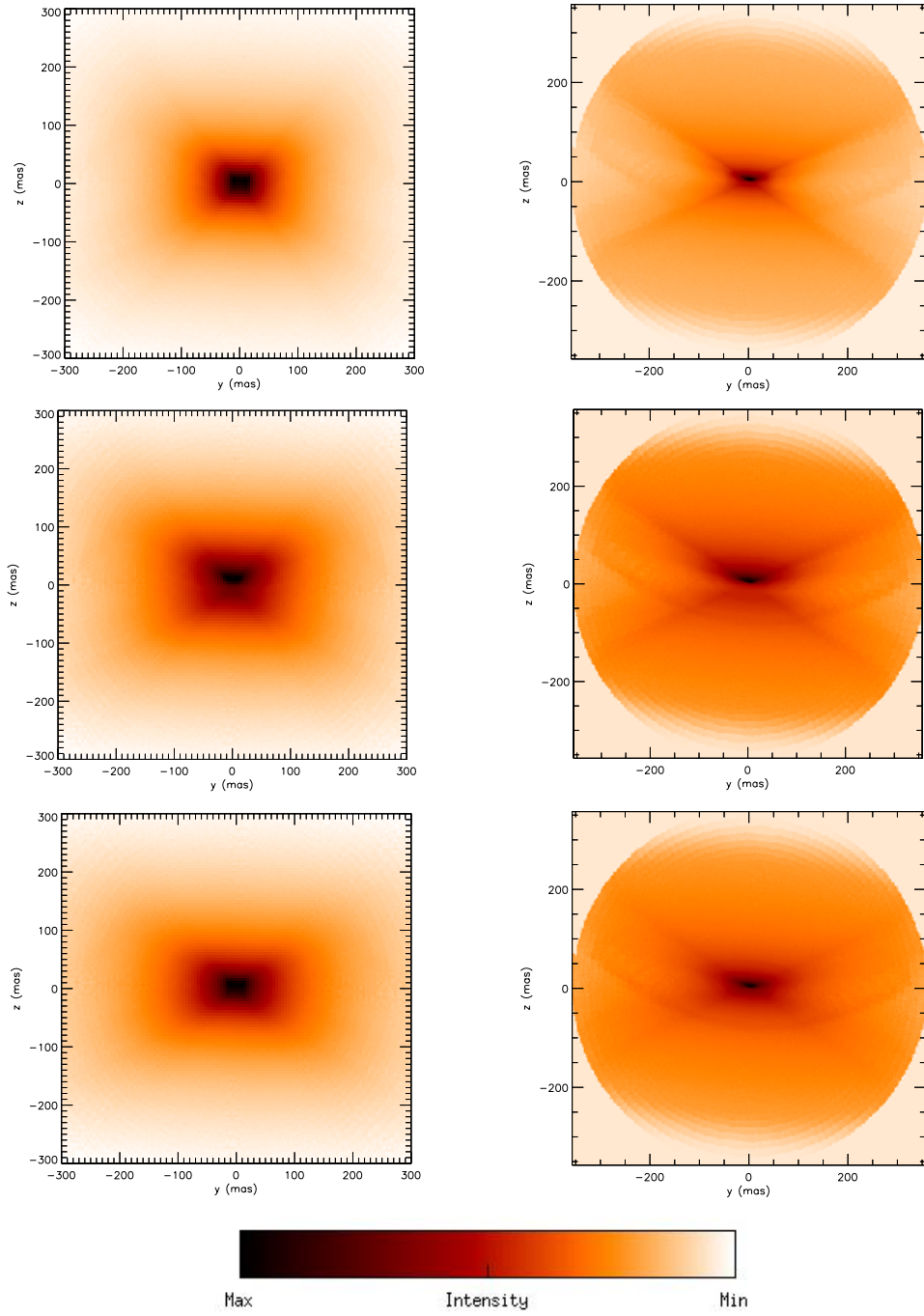


Figure 5.11 – From top to bottom: flux distribution of the model at 8, 10 and 13 μm . Images on the left column belong to M2-9 and the ones on the right to Mz3 (from the work of Lykou 2008; Chesneau et al. 2007). A small amount of light emerges at 8 μm while the flux comes from inner disc parts at 13 μm .

V Hya, a variable carbon star

The Keck aperture masking data were kindly provided to the author, for comparison to this work's data, by P. G. Tuthill.

6.1 History of V Hya

V Hya is a peculiar semi-regular photometric variable star. That is, it has two photometric periods, a short one lasting 529 days ($\Delta m = 1.5\text{mag}$) and a longer one of almost 17 years ($\sim 6,300$ days) when its brightness is reduced by 6 magnitudes in the visual (Campbell 1926; Knapp et al. 1999). The latter is most probably better described as an obscuration event, rather than as a secondary photometric period. Figure 6.1 shows its light curve from 1990 to 2013. The epochs of previous interferometric observations have been added for comparison. The last visual minimum ($V \sim 13.5\text{mag}$) was in 1994 and the next

one occurs in 2012–2013.

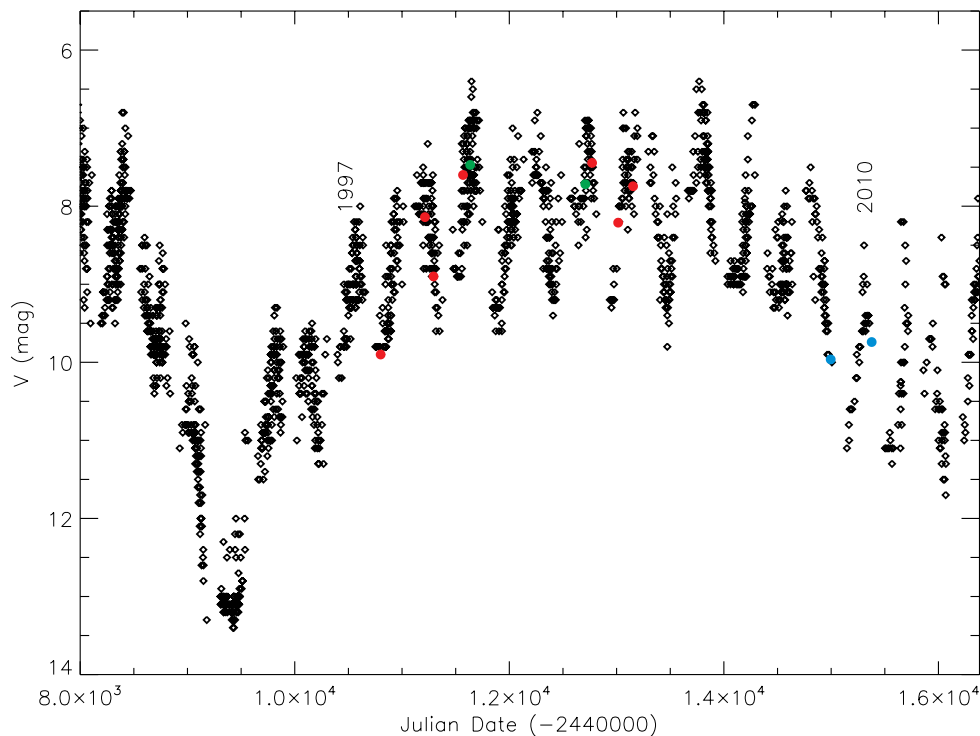


Figure 6.1 – V Hya light curve from April 1990 to April 2013 provided by AAVSO. Observing periods (1997–2010) are indicated by: red dots for Keck aperture masking experiment, green for IOTA interferometer and cyan blue for NACO/VLT.

In the IRAS infrared colour-colour diagram, the position of V Hya indicates that it is a C-rich AGB star (van der Veen & Habing 1988). As in many C-rich stars, V Hya has a prominent SiC emission feature ($\sim 11.5\mu\text{m}$), but it seems to lack acetylene (C_2H_2) features (Fig. 6.2). Of the stars presented in Figure 6.2, AFGL3068 is a known binary (Morris et al. 2006), V Cyg and S Cep present asymmetries in their CO gas distribution (Castro-Carrizo et al. 2010), CIT6 is a suspected triple star (Schmidt et al. 2002) and R Scl has two photometric periods as V Hya (Whitelock et al. 1997; Sacuto et al. 2011). It seems that there is a correlation between the creation of SiC dust and polyynes, and stellar variability among these stars. Mid-infrared observations with MIDI confirm that the SiC emission feature becomes more prominent as the stellar luminosity

drops during one pulsation cycle, i.e. between phase¹ 0.1 and 0.5 (Zhao-Geisler 2010).

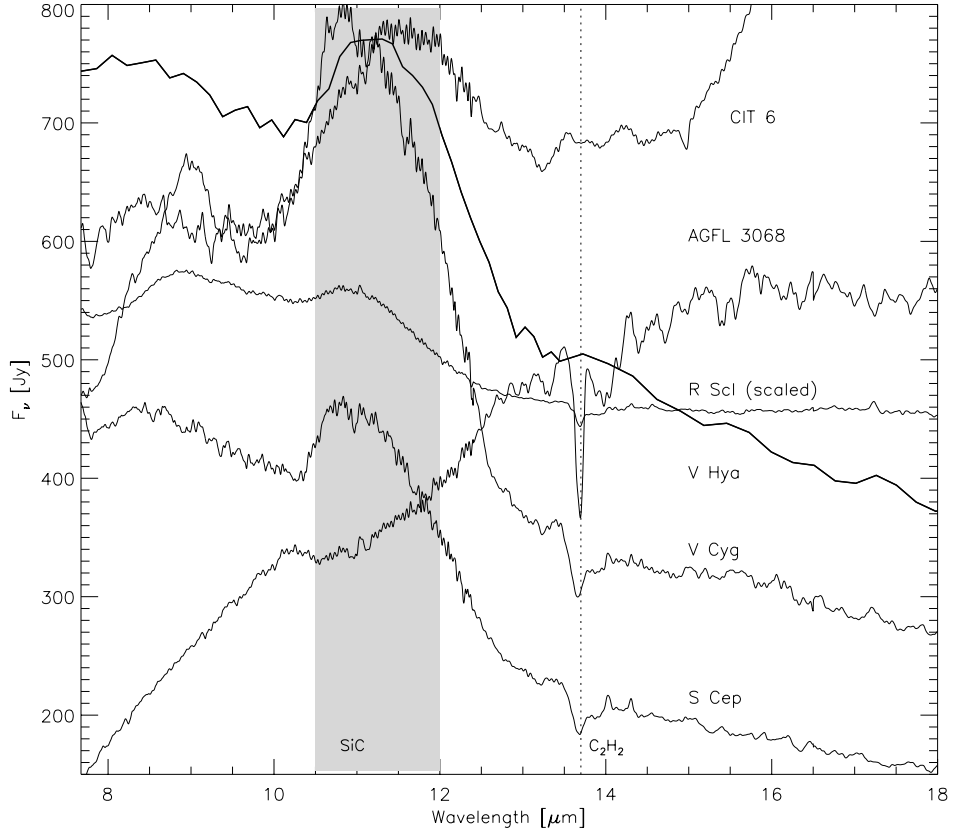


Figure 6.2 – Mid-infrared spectra of C-rich red giants. The shaded area marks the SiC emission feature and the line at $13.7\mu\text{m}$ stands for C_2H_2 absorption. All spectra are from ISO/SWS (Sloan et al. 2003), except for the IRAS low-resolution spectrum of V Hya by Volk & Cohen (1990).

Near-infrared colours gave an effective temperature $T_{\text{eff}} = 2650\text{K}$, a luminosity of $10,000 L_{\odot}$ and a spectral type C6-7,5e (Lambert et al. 1986). Dust continuum observations in the millimetre regime by Dehaes et al. (2007) and comparisons to radiative transfer models for a $T_{\text{eff}} = 2500\text{K}$ star with a ~ 2.5 AU radius and a $T_{\text{dust}} = 700 \pm 200\text{K}$ amorphous carbon dust shell at 44.5 AU from the star, gave a luminosity in the expected Mira range ($9,780 L_{\odot}$) and a mass-loss outflow² of $4.72 \times 10^{-6} M_{\odot}\text{yr}^{-1}$ at a $v_{\text{flow}} = 13.0\text{km s}^{-1}$. This velocity

¹Here phase 0.0 and 1.0 being maximum brightness and 0.5 minimum brightness during one pulsation period.

²Estimated mass loss rates in the literature: 1 to $5 \times 10^{-6} M_{\odot}\text{yr}^{-1}$ (Knapp & Morris 1985;

is consistent with a slow AGB wind.

Table 6.1 presents V Hya broadband photometry from the ultraviolet to the radio regime available in the literature. The disagreement in photometric values of the same waveband is due to the different characteristics of the instruments used and different observing epochs. The spectrum is shown in Figure 6.3.

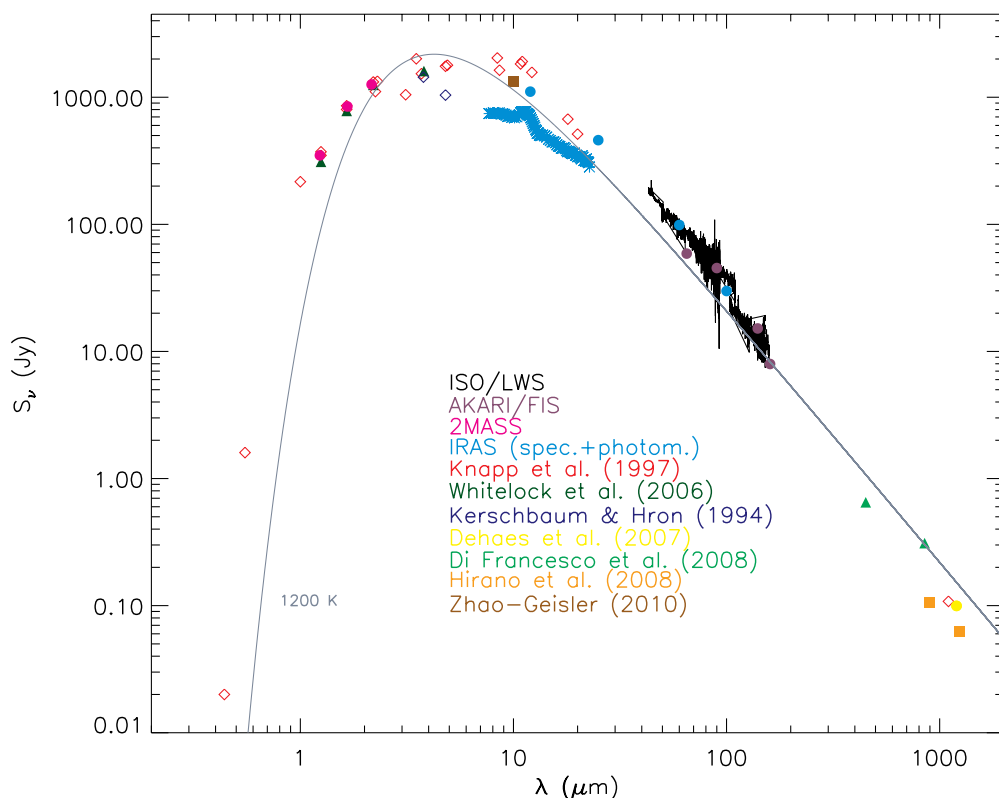


Figure 6.3 – The spectrum of V Hya with observations at different epochs and with different beam sizes. Here we include data from: the photometric catalogues of 2MASS, AKARI and IRAS, the low-resolution spectra of IRAS and ISO, and previous works by Kerschbaum & Hron (1994), Knapp et al. (1997), Whitelock et al. (2006), Dehaes et al. (2007), Zhao-Geisler (2010) (near- and mid-infrared), Hirano et al. (2004) and Di Francesco et al. (2008) (submm). The colour index is listed within the plot. Individual values are given in Table 6.1 and a 1200 K black body is shown for reference.

Even though V Hya is a carbon star, water vapour has been detected by Herschel/HIFI³ (Neufeld et al. 2011). This chemistry could be explained by UV

Zuckerman & Dyck 1986; Tsuji et al. 1988; Kahane et al. 1988; Bujarrabal et al. 1994; Stanek et al. 1995).

³Heterodyne Instrument for the Far-Infrared, <http://herschel.esac.esa.int/>

radiation reaching the inner stellar envelope and dissociating carbon monoxide molecules, thus allowing the formation of water molecules, as found in another carbon star IRC+10216 (Decin et al. 2010).

Table 6.1 – V Hya photometry

λ [μm]	S_ν [Jy]	Ref.	λ [μm]	F_ν [Jy]	Ref.
0.26	0.00023	(1)	4.80	1754.5	(1)
0.32	0.00680	(1)	4.90	1788.3	(1)
0.44	0.02	(1)	8.40	2038.5	(1)
0.55	1.6	(1)	8.60	1632.8	(1)
1.00	216.4	(1)	9.92	1330.0	(4)
1.24	349.0	2MASS	10.80	1827.1	(1)
1.25	372.1	(1)	11.00	1911.6	(1)
1.25	348.6	(1)	12.00	1107.0	IRAS
1.25	310.5	(2)	12.20	1570.9	(1)
1.65	780.9	(2)	18.00	673.1	(1)
1.65	856.60	(1)	20.00	513.0	(1)
1.65	802.0	(1)	25.00	459.6	IRAS
1.66	846.0	2MASS	60.00	98.87	IRAS
2.16	1260.0	2MASS	65.00	58.86	AKARI
2.20	1319.1	(1)	90.00	45.31	AKARI
2.20	1252.0	(2)	100.00	29.89	IRAS
2.25	1107.5	(1)	140.00	15.17	AKARI
2.30	1335.7	(1)	160.00	7.97	AKARI
3.12	1046.9	(1)	450	0.65	(5)
3.50	2008.9	(1)	850	0.31	(5)
3.70	1531.8	(1)	894.9	0.105	(6)
3.78	1440.0	(3)	1100.0	0.108	(1)
3.80	1608.0	(2)	1200.0	0.0995	(7)
4.80	1040.0	(3)	1243.9	0.063	(6)

(1) : Knapp et al. (1997); (2) : Whitelock et al. (2006)

(3) : Kerschbaum & Hron (1994); (4) : Zhao-Geisler (2010)

(5) : Di Francesco et al. (2008); (6) : Hirano et al. (2004)

(7) : Dehaes et al. (2007)

6.1.1 Asymmetries

Past spectropolarimetric studies have shown that the core of V Hya is highly polarised (Kruszewski et al. 1968; Johnson & Jones 1991; Trammell et al. 1994).

The direction of polarisation tends to change with time and is closely related to the 529-d pulsation period. In stellar environments polarised light emerges either due to magnetic fields or due to scattering by dust; the latter is the case for V Hya. These polarimetric studies could not clearly resolve asymmetries in the immediate vicinity of the star, since the resolution of the instruments used could only distinguish the net polarisation (dust scattering and stellar light), unlike recent high-angular resolution polarimetric studies that allow the distinction (Norris et al. 2012).

Previous studies have confirmed the existence of bipolar outflows in the radio (Tsuji et al. 1988; Kahane et al. 1988; Knapp et al. 1997; Hirano et al. 2004), the infrared (Sahai & Wannier 1988; Sahai et al. 2009) and the optical (Lloyd Evans 1991; Sahai et al. 2003). The high-velocity outflows ($\sim 100\text{--}230\text{ km s}^{-1}$) are located along the East-West axis of the star with respect to our line-of-sight. These are inconsistent with slow AGB winds (Kahane et al. 1988, 1996; Knapp et al. 1997, 1999) and they are attributed to a jet-like outflow. This outflow has been detected in the mid-infrared as well by Lagadec et al. (2005) and it was found to extend $0.9''$ bilaterally from the central source along the East-West axis. It is most probably the interaction between the slow circumstellar wind with the high-velocity jet. Furthermore, spectral line broadening is inconsistent with slow rotation in AGB stars (Lloyd Evans 1991).

Recent sub-millimetre interferometric observations revealed a CO torus that extends approximately $8''$ (or 3000 AU at 380 pc) from the central source along the North-South axis of V Hya (Hirano et al. 2004). The torus is inclined by 60° with respect to our line-of-sight (Figure 6.4). It has a low-velocity wind of $\pm 8\text{ km s}^{-1}$ in agreement with the values of Knapp et al. (1997) and Sahai et al. (2009).

Sahai et al. (2003) found⁴ an expanding dusty structure (expansion rate $0.065''/\text{yr}$) with a diameter of $0.5''$ (or $\leq 200\text{ AU}$ at 380 pc) in $\text{H}\alpha$ (Figure 6.4). This is the closest look into the vicinity of V Hya so far.

⁴Spectroscopic observations with STIS/HST for two epochs: January and December 2002.

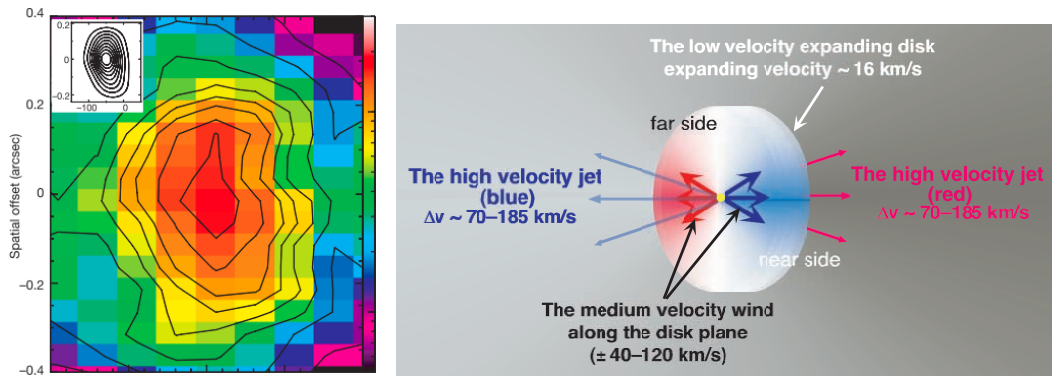


Figure 6.4 – On the *right*, a sketch of the equatorial torus and polar jet of V Hya. Taken by Hirano et al. (2004). The detected velocity difference could belong to different parts of a spiral structure, although this would not be able to be resolved with the instrument in use. The structure detected by Keck and VLT is enclosed within the torus, as is the $0.5''$ equatorial disc detected in $H\alpha$ by Hubble Space Telescope on the *left*. Taken by Sahai et al. (2003).

6.1.2 A suspected companion

The jet, the molecular torus and the dusty structure along with the 17-year obscuration event are indicative of a companion. A companion would explain the collimated polar jet and the equatorial molecular torus (Hirano et al. 2004). Further proof of its existence has been given in the past: broadened absorption lines in the optical, usually extended towards the blue, can be explained by a spin-up of the star by a companion (Kahane et al. 1988; Barnbaum et al. 1995; Lloyd Evans 1991).

Sahai & Wannier (1988) pointed out the possibility of an accretion disc around a companion, which could explain the high-velocity outflow detected at $4.6\mu\text{m}$ (CO $v=1-0$) within a region of $2.5''$. More recent observations in the near- and far ultraviolet, revealed a high ultraviolet excess assigned to either stellar emission from a companion or infall from an accretion disc (Sahai et al. 2008).

From their series of observations commencing in 1991, Lloyd Evans (2000) suggest that the visual spectrum of V Hya resembles mostly that of an accretion disc. A more recent review states that the companion was a main sequence star, now a reborn T Tauri star due to accretion from the primary (Evans 2009).

It appears that V Hya is a system close to transforming into a post-AGB

star (Sahai et al. 2003, 2009; Tsuji et al. 1988). The only available imaging results so far in the near-infrared of the dusty environment around V Hya were made by Lagadec et al. (2007) with NACO/VLT. They did not resolve the circumstellar dusty environment – the central, elongated structure is less than $0.5''$ in size on the East-West axis at $3.74\mu\text{m}$ – although the extended environment ($\sim 2''$) seems spherical in shape. The use of high-angular resolution techniques is required to dissect the dusty structure of V Hya.

6.2 Observations

V Hya was observed at the VLT in aperture masking interferometric mode with the UT4 8.2-m telescope at Cerro Paranal during two nights in June 2009 (run ID : 083.D-0885). Due to a telescope operation software glitch, pupil tracking mode was disabled during the observations of the calibrators and the masks were covered by the telescope’s spiders, rendering the full data set valueless. Fortunately, a second observing run was granted for June 2010 with the same instrument (run ID : 085.D-0396).

Table 6.2 – NACO filters

Name	λ_c [μm]	$\Delta\lambda$ [μm]	Transmission
NB_1.24	1.237	0.015	60%
NB_1.64	1.644	0.018	47%
IB_2.24	2.240	0.06	57%
NB_3.74	3.740	0.02	92%
NB_4.05	4.051	0.02	89%

Taken from NACO ver.89 User’s Manual.

SAM and SAMPol⁵ modes with the `9_hole` mask were employed for these observations (see Section 2.6.1). Four narrow-band and one intermediate-band near-infrared filters were used, namely NB_1.24, NB_1.64, IB_2.24, NB_3.74 and NB_4.05, corresponding to J, H, K, L and M band, respectively (Table 6.2). Two cropped camera apertures (S13, 512×514 pixels and L27, 256×258 pixels) were used in order to obtain dithered exposures. That is, the object was

⁵SAMPol is the NACO/VLT polarimetric aperture masking mode that utilises a Wollaston prism and a half-wave plate as well (Tuthill et al. 2010; Norris et al. 2012)

re-centred within each of the four quadrants of the detector⁶, allowing us to obtain four sets of rapid exposure frames. The dithering direction was clockwise from the upper-left quadrant. This allowed for a fast observing sequence (faster detector readouts) and for an increase in signal-to-noise ratio while eliminating systematic background noise. The observation log is in Table 6.10. We used ν Hya (K0/K1III) as a calibrator.

Two problems should be mentioned about the second night’s observations. A centering misalignment was seen for many of the exposures which is partly due to the rapidly increasing airmass at the time of observation. As such, a different calibrating star had to be observed (δ Crt, K0III). We would like to stress that any results from that night should be considered as lower limits in the angular size estimations (see Table 6.4).

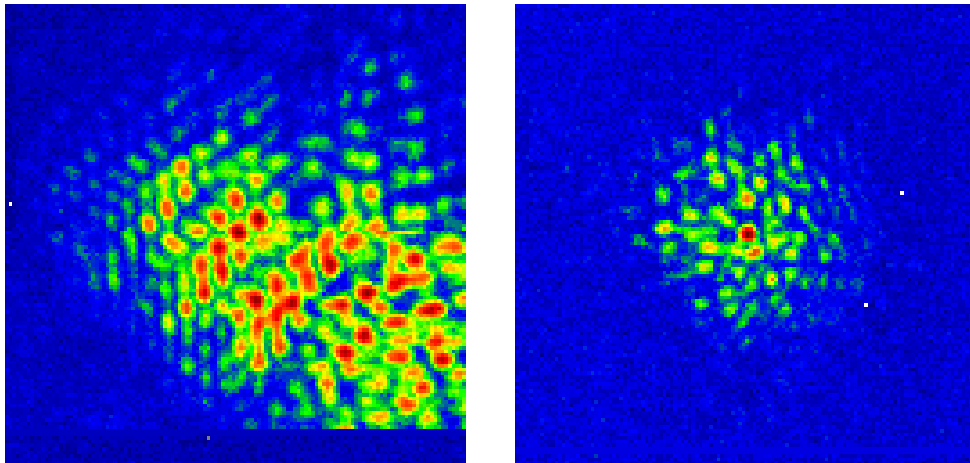


Figure 6.5 – Example of “bad” quality, spurious interferogram (after sky subtraction) due to unsteady AO on the left, compared a “good” exposure seen on the right.

During the first night atmospheric seeing⁷ varied between $1''$ and $3.25''$. Although the night was clear, the strong winds affected the adaptive optics (AO) system (NAOS) of NACO giving coherence time of less than 1 millisecond. This caused offset positioning of the target on the detector when NAOS was not able to lock on a steady target. Losing absolute position forced the re-

⁶CONICA camera is 1024×1028 pixels.

⁷Although DIMM seeing in Table 6.10 is above $2''$, the Guide Probe instrument gave seeing values of approximately $1''$ less than DIMM. The instrument scientist and telescope operator advised us to use those values.

centering of the target in the middle of each run by continuous AO optimisations. Observations in L and M had to be repeated due to bad centering. This delayed the time sequence of the run and resulted in observing the second calibrator at airmass higher than 1.5.

As a result of that, many of the interferograms were spurious (e.g. Figure 6.5) and offset from the required central position on the camera, i.e. the central peaks appear to be located near the camera window edges. Even though a higher S/N cutoff was applied for data rejection during the reduction, the remaining frames produced data with larger error bars (see next Section).

The data were reduced with the pipeline described in Section 2.6.1.1.1. The SAMPol data will be reduced and analysed at a later date with the method described by Norris (2010) to confirm the findings presented in their work (see Table 6.3).

6.3 Stellar diameter

Attempts to estimate the angular size, and thus the physical size, of V Hya have been made before by means of optical interferometry. Due to the source's variability it is expected that values should vary depending on the photometric phase during the epoch of observation.

Millan-Gabet et al. (2003) presented a combination of IOTA⁸ and Keck-I aperture masking results⁹ in the K band ($2.2\mu\text{m}$). They found that the observed visibilities can be explained best by a composite model of a stellar photosphere and a surrounding dust shell, giving a uniform disc diameter of 14.5 ± 0.3 mas and a Gaussian disc diameter of 35 ± 3 mas, respectively.

IOTA results in 2003 showed that the star has a uniform disc diameter of 21.23 ± 2.77 mas in the H band (phase=0.1, B=26-m, Ragland et al. 2006). As mentioned by Ragland et al. (2006), the stellar angular diameter in H band has been previously estimated at 13 mas by the spectral type and $V - K$ colour relation of van Belle (1999). Seeing as V Hya is a variable source, the latter

⁸Infrared Optical Telescope Array, <http://tdc-www.harvard.edu/IOTA/>

⁹The observations were carried during the first trimester of 2000; Figure 6.1

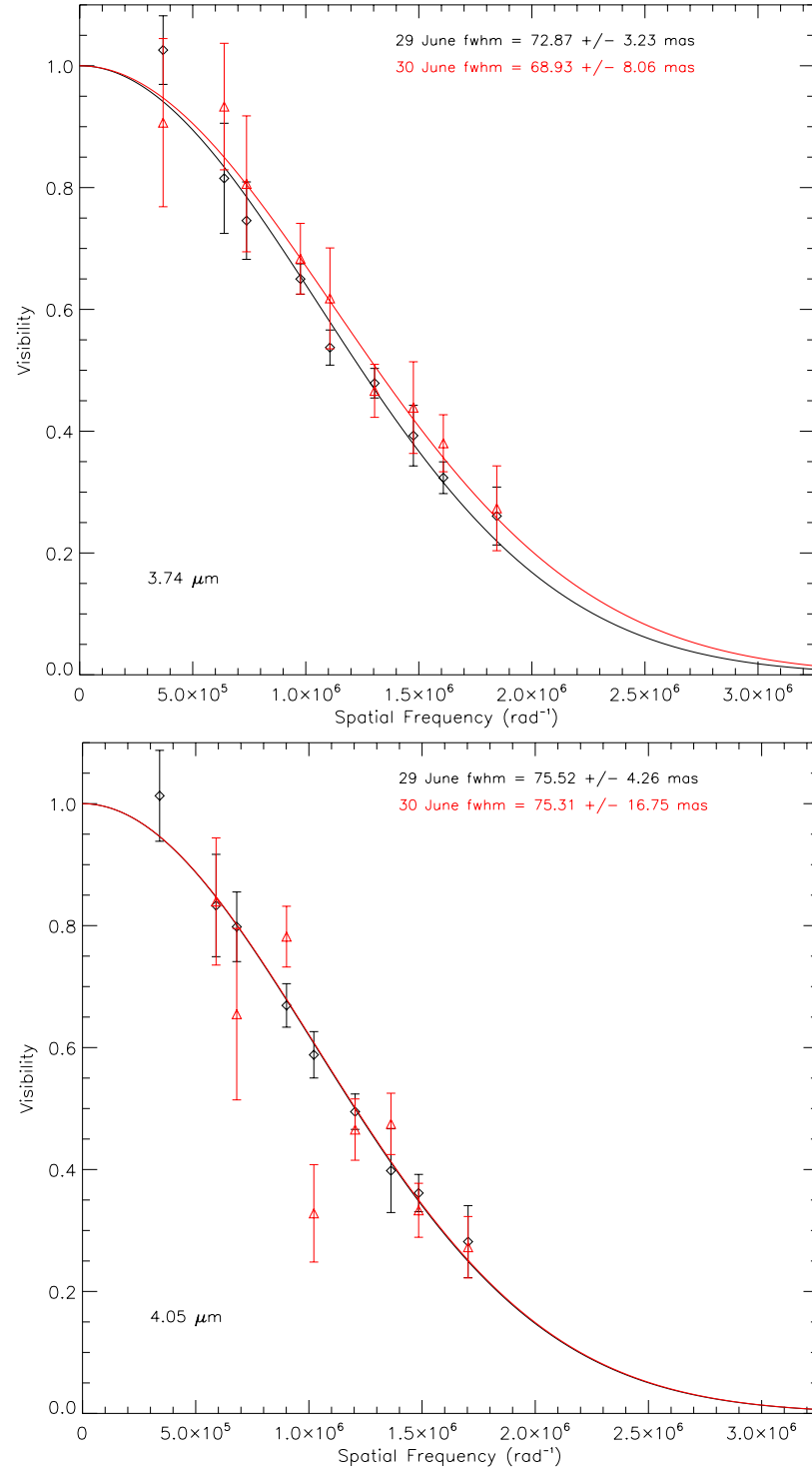


Figure 6.6 – Gaussian model fits (Table 6.4) for SAM data at 3.74 (top panel) and 4.05 μm (bottom panel) azimuthally-averaged data for the first (black) and second (red) night of observations. The second night's data have a larger spread due to the spurious interferograms recorded on that night.

Table 6.3 – Diameters of V Hya from interferometric observations in the literature.

Date	Instrument	Band	θ [mas]	Type	Ref.
Jan 00	Keck-I	K	35 ± 3	dust shell	(1)
Feb/Apr 00	IOTA	K	14.5 ± 0.3	star	(1)
Mar 03	IOTA	H	21.23 ± 2.77	star	(2)
Apr 07 – Mar 08	MIDI	N	19.3 ± 3.5	star	(3)
Apr 07 – Mar 08	MIDI	N	105 ± 4	dust shell	(3)
29 Jun 10	SAMPol	1.24	11.7 ± 2.5	dust shell	(4)
29 Jun 10	SAMPol	1.64	13.3 ± 2.1	dust shell	(4)
29 Jun 10	SAMPol	2.24	21.9 ± 0.4	dust shell	(4)

(1) Millan-Gabet et al. (2003); (2) Ragland et al. (2006);

(3) Zhao-Geisler (2010); (4) Norris (2010)

estimation could be an approximation.

Tables 6.3 and 6.4 summarise the angular diameters in the near and mid infrared found in the literature and estimated in this work, respectively. A “dust shell” nomination signifies a Gaussian distribution fit, while a “star” nomination stands for a Uniform disc fit, except for Zhao-Geisler (2010) where it stands for a Fully Limb-Darkened Disc combined with a Gaussian distribution fit. For the full set of angular sizes in the N -band derived with said model, we refer the reader to the work of Zhao-Geisler (2010) and their Figures 5.24 and 5.30.

We attempted to fit said model to our aperture masking data, but all attempts failed to reproduce reliable fits. Good fits were given only for Gaussian distribution models. This could be explained by two points:

First, a different structure was detected with MIDI. The VLTI’s longer baselines allowed the detection of a structure at small spatial scales compared to the more extended structure detected by a single 8-m telescope. Second, the two experiments differed also in projected baseline coverage, again indicating that they probed different structures.

Figure 6.6 presents the azimuthally averaged data over a bin of 0.5 metres for both wavelengths and nights of observation. The error bars presented here are either equal to the standard deviation of the visibility scatter when more than two points lie within a bin, or equal to the mean of the visibility errors when there are two or less points within the bin. The visibilities from second

night's observations have a larger spread due to the spurious interferograms recorded on that night.

The data and best fits are scaled to visibility equal to one. This compensates for the lack of data at lower spatial frequencies¹⁰. All the parametric fits made in this work utilised the Levenberg-Marquardt least-squares minimisation procedure via **MPFIT** by Craig B. Markwardt¹¹. **MPFIT** will scale the Gaussian distribution by multiplying with a parameter (here A , e.g. $\exp(-3.57 \theta^2 x^2) \cdot A$, where θ is the angular size and x is the spatial frequency). By submitting two initial parameters, i.e. a minimum angular size and A , the algorithm will search for the best fit to the data by re-calibrating the given parameters.

Table 6.4 shows the fitted full-width-half-maxima of the fitted distributions with azimuthal-averaging. Our results show that the fitting gave similar angular sizes, within error bars¹², for both nights. The Gaussian distribution fits are just estimates of the approximate sizes of the source under the assumption of spherical symmetry, i.e. variation in source morphology with respect to the azimuth is not taken into account.

Table 6.4 – Diameters of V Hya from SAM.

Date	θ [mas]
$3.74\mu\text{m}$	
29 Jun 10	72.87 ± 3.23
30 Jun 10	68.93 ± 8.06
$4.05\mu\text{m}$	
29 Jun 10	75.52 ± 4.26
30 Jun 10	75.31 ± 16.75

¹⁰There is no baseline equal to zero. The length of the shortest available baseline is approximately 0.5-m

¹¹<http://cow.physics.wisc.edu/~craigm/idl/idl.html>

¹²The larger error in an azimuthally-averaged fitted diameter is due to the larger errors in the individual values.

6.3.1 Physical sizes

An estimate of the physical stellar radius can be given by the period-mass-radius relation¹³ of Wood (1990):

$$\log R = \frac{2.07 + \log P + 0.9 \log M}{1.94}, \quad (6.1)$$

where the radius, R , and the mass, M , are in solar units and the pulsation period, P , is in days. Our calculations for a full and half a pulsation cycle are listed in Table 6.5.

Table 6.5 – Physical stellar radii of V Hya

Mass (M_{\odot})	Radius (AU)	
	$P_0=529$ d	$P=P_0/2$
1.0	1.37	0.96
1.5	1.66	1.16
2.0	1.89	1.33
3.0	2.29	1.60
4.0	2.62	1.83

The results can be compared to observed angular sizes by Keck and IOTA in the H-band, where the stellar photosphere dominates. For the adopted distance of 380 pc and noting that the Keck observations in 1997 (~ 10.4 mas) occurred at the pulsation cycle’s minimum (see Figure 6.1), while those of Keck and IOTA in 1999 and 2003 (~ 14.4 and 21.23 mas), occurred at the pulsation cycle’s maximum, we find that the physical sizes are 3.95, 5.46 and 8.06 AU, respectively. There seems to be a large difference between the expected stellar radius and that estimated from the interferometric observations. This discrepancy can be explained either by accounting for an expanding, dusty envelope around the central star, or by inferring that the relation of Wood (1990) does not apply here.

Apart from the data presented in Table 6.3, the central continuum source varies in size in other wavelengths as well. Between February and May 2003, Hirano et al. (2004) report that the central source, with a size of less than

¹³This was estimated for the Large Magellanic Cloud.

1'', is unresolved in both sub-mm bands with SMA¹⁴. Sahai et al. (2003) estimated angular sizes of 120 mas in January 2002 (phase=0.42) and 81 mas in December 2002 (phase=0.05), from the continuum emission in their STIS/HST observations¹⁵.

It is worth noting that the angular size estimations via fitting Uniform and Gaussian disc models to azimuthally averaged data, is an over-simplified approach to finding the stellar and dusty structure's dimensions. In actuality the complexity of V Hya cannot be explained with simple, one-dimensional flux distributions.

6.4 Near-infrared interferometric imaging

The main asset of the aperture masking technique is the production of diffraction limited imaging. Although the previously mentioned approximations are sufficient for the stellar component in J and H bands, the complexity of the surrounding dusty structure at longer wavelengths can be explored better by imaging.

6.4.1 NACO/VLT

BSMEM was used to reconstruct images from the bispectra (see Section 2.4). Table 6.6 state the parameters used and the statistical stability of the resulting images from each dither of the full camera frame. Those images that did not converge are not presented here. In more detail: *FWHM* is the size of the initial Gaussian used in image reconstruction, *pixsize* is the reconstructed image's pixel size in milliarcseconds, χ^2 for the best fit to the original data found for the last iteration¹⁶ and θ_{array} is the array resolution, that can be compared to the resolution limits of Table 2.1. All reconstructed images are 32×32 pixels.

As mentioned previously, dithers 37–44 (Table 6.6) were observed at high airmass during the second night and the results should be considered as size

¹⁴Submillimeter Array, Hawaii, USA

¹⁵Our SAM/NACO observations were performed at phase=0.23.

¹⁶The maximum number of iterations is 200.

limits due to larger atmospheric distortion. Also in Table 6.6 the reader will notice that in more than one occasions the fits appear to be overestimating ($\chi^2 < 1$) or underestimating ($\chi^2 > 1$) the errors. For that, we suggest the comparison in the future with a different image reconstruction software.

Figure 6.7 shows the averaged, reconstructed dithers from Table 6.6 in each respective wavelength, namely dithers 09–12 for $3.74\mu\text{m}$ (top image) and 13–15 for $4.05\mu\text{m}$ (bottom image).

An oblate structure with a horn-like feature North between 2–10% of the peak flux can be seen in both colours. The structure’s size is comparable to those found by Keck aperture masking¹⁷ (within 200 mas) and definitely better resolved than that presented by Sahai et al. (2003).

At $3.74\mu\text{m}$ ($4.05\mu\text{m}$) the structure is extended approximately 120 mas (140 mas) North and 70 mas (90 mas) South from the central peak, and it is ~ 95 mas (100 mas) in size along the East-West axis. The North-South

¹⁷Paper in preparation; new data obtained in February 2013.

Table 6.6 – Image reconstruction parameters for SAM data.

# dither	λ [μm]	FWHM [mas]	pixsize [mas]	θ_{array} [mas]	# iterations	χ^2
09	3.74	100	18.63	55.90	31	1.05
10	3.74	158	0.92
11	3.74	164	0.95
12	3.74	200	0.90
37	3.74	177	1.01
38	3.74	89	0.92
39	3.74	200	1.33
40	3.74	200	0.66
13	4.05	120	20.18	60.55	35	1.00
14	4.05	22	0.91
15	4.05	200	0.86
16	4.05	118	1.03
41	4.05	200	0.64
42	4.05	36	1.08
43	4.05	50	0.95
44	4.05	200	0.63

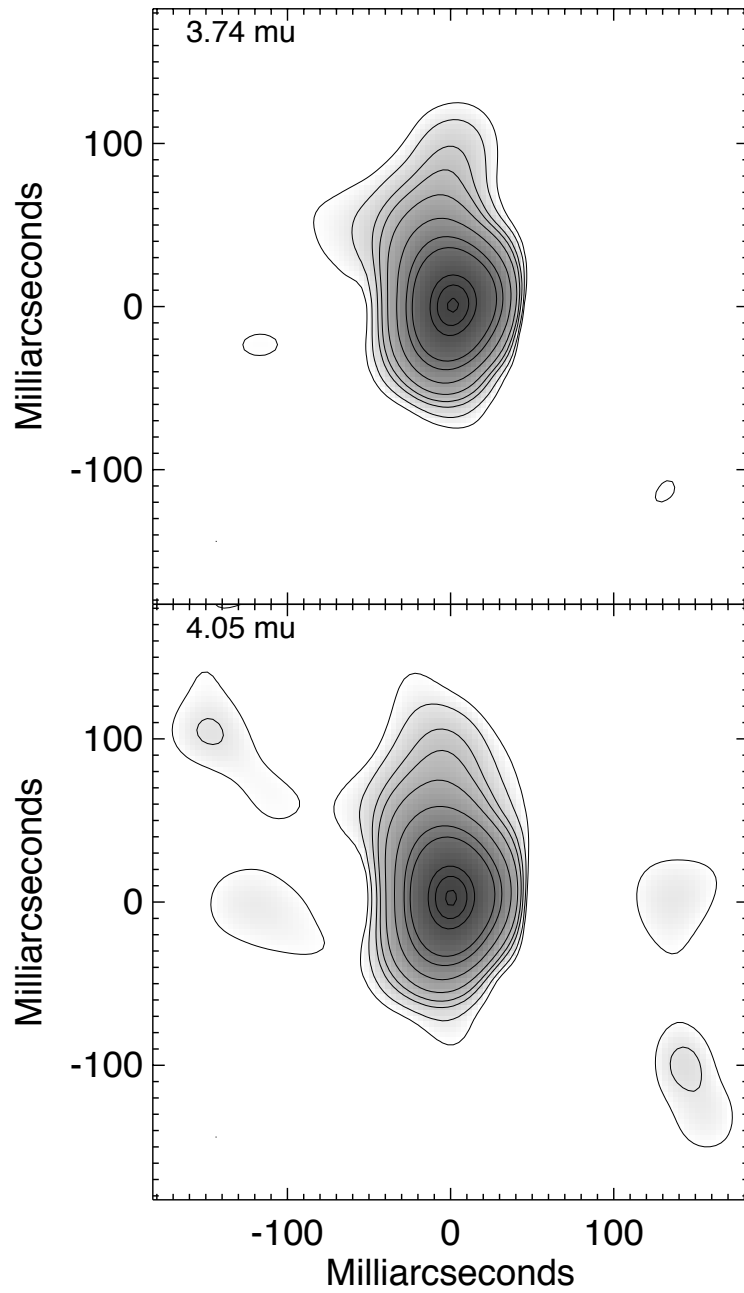


Figure 6.7 – The circumstellar environment of V Hya at 3.74 and $4.05\mu\text{m}$ as seen by SAM/NACO. Images are averaged over all reconstructed dithers (1st night data, Table 6.6) in their respective filters. North is up and East is left. Contour levels are 0.5, 1, 2, 3, 5, 10, 20, 30, 70, 85 and 98% of the peak flux. The dusty structures in both images are elongated more toward the North than the South. Lowest believable contour is 2% of the peak.

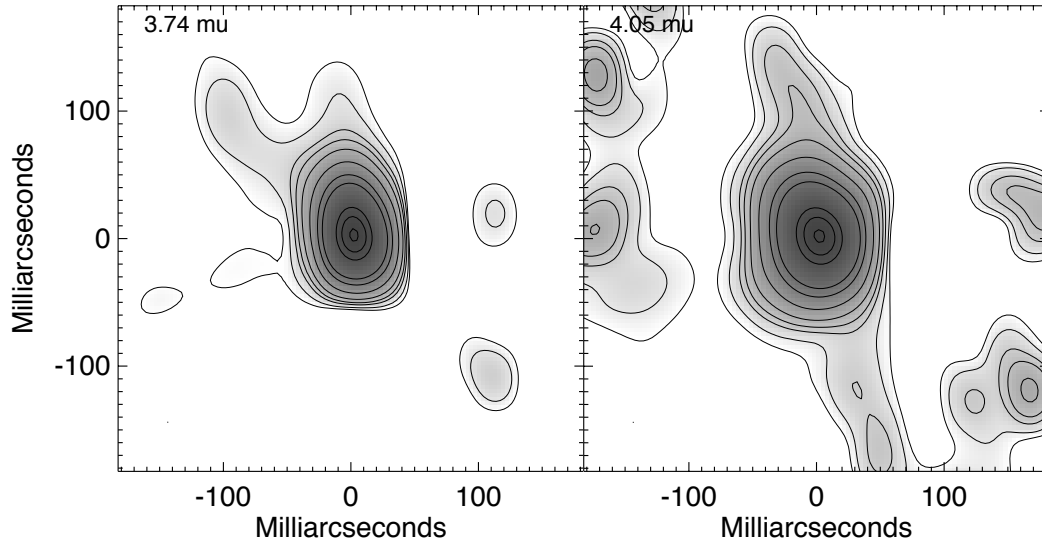


Figure 6.8 – Same as Figure 6.7 but for the second night of observations. Only the reconstructions that converged (Table 6.6) were used in these images. A significant noise pattern is present, due to the spurious data. Lowest believable contour is 5% of the peak.

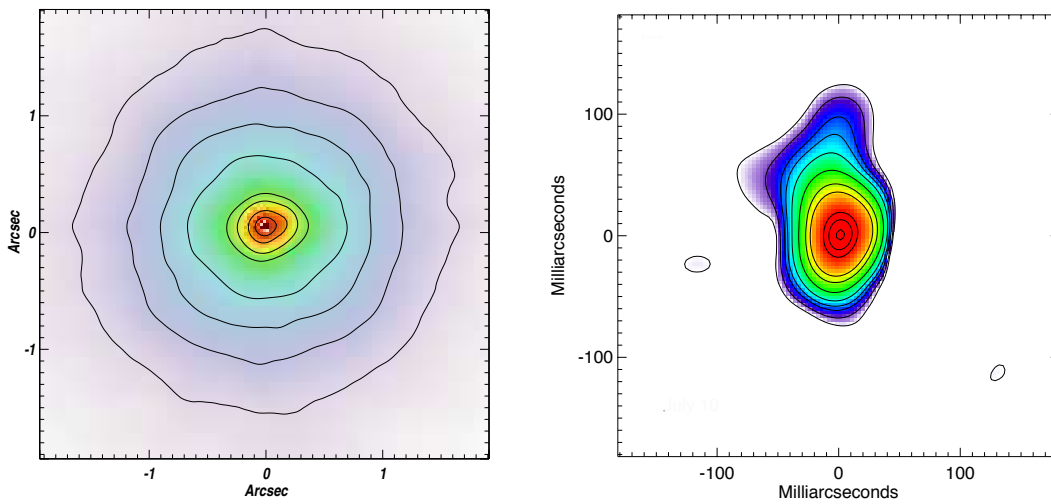


Figure 6.9 – On the left is a full aperture view of V Hya at $3.74\mu\text{m}$ by Lagadec et al. (2007) compared to the masked aperture output on the right (same as in Figure 6.7).

Table 6.7 – Dusty envelope of V Hya (in physical units for a distance of 380pc).

area	$3.74\mu\text{m}$	$4.05\mu\text{m}$
$\geq 2\%$ of peak flux	$100 \times 160 \text{ mas}$ ($38.0 \times 60.8 \text{ AU}$)	$90 \times 75 \text{ mas}$ ($34.2 \times 28.5 \text{ AU}$)
$\geq 70\%$ of peak flux	$25 \times 35 \text{ mas}$ ($9.5 \times 13.3 \text{ AU}$)	$20 \times 35 \text{ mas}$ ($7.6 \times 13.3 \text{ AU}$)

orientation is consistent with the position of the edge-on disc¹⁸ seen by Sahai et al. (2003). An additional clump is seen at lower levels ($\leq 2\%$) North-East from the central source within a position angle of $30\text{--}60^\circ$ in both wavelengths.

NACO in aperture masking mode offers a significantly better view of the dusty environment around V Hya compared to simple imaging mode. This is evident in Figure 6.9 where one will notice that the unresolved central component of V Hya is approximately 200 mas at $3.74\mu\text{m}$ while the surrounding cloud has a roughly spherical, $3''$ in radius, shape (Lagadec et al. 2007). On the other hand a much closer view to the core of V Hya is enabled once the aperture is masked. The central source at both wavelengths is confined within an area of roughly $25 \times 35 \text{ mas}$ (Table 6.7), as opposed to the $0.2''$ given by simple NACO imaging mode. This area is somewhat larger than its respective size in H band from photospheric emission ($\leq 15 \text{ mas}$ in diameter or else $\leq 2.85 \text{ AU}$ in radius at 380pc; Table 6.3), which is expected from the limited spatial scales given by the current aperture mask experiment even at as high a resolution as $0.5\lambda/D$.

6.4.2 Keck

V Hya has been observed with the Keck¹⁹ 10-metre telescopes over six epochs from 1997 to 2004. We present some of the near-infrared imaging results of Keck aperture masking experiment (Figures 6.11 and 6.10) kindly provided by P. G. Tuthill for comparison to the SAM/NACO data²⁰.

From the images at $3.08\mu\text{m}$ it is obvious that the dusty structure has

¹⁸V Hya torus is known to be inclined to our line-of-sight, but this is not yet determined for the dusty disc.

¹⁹Hawaii, U.S.A.

²⁰The complete dataset will be presented in a future paper.

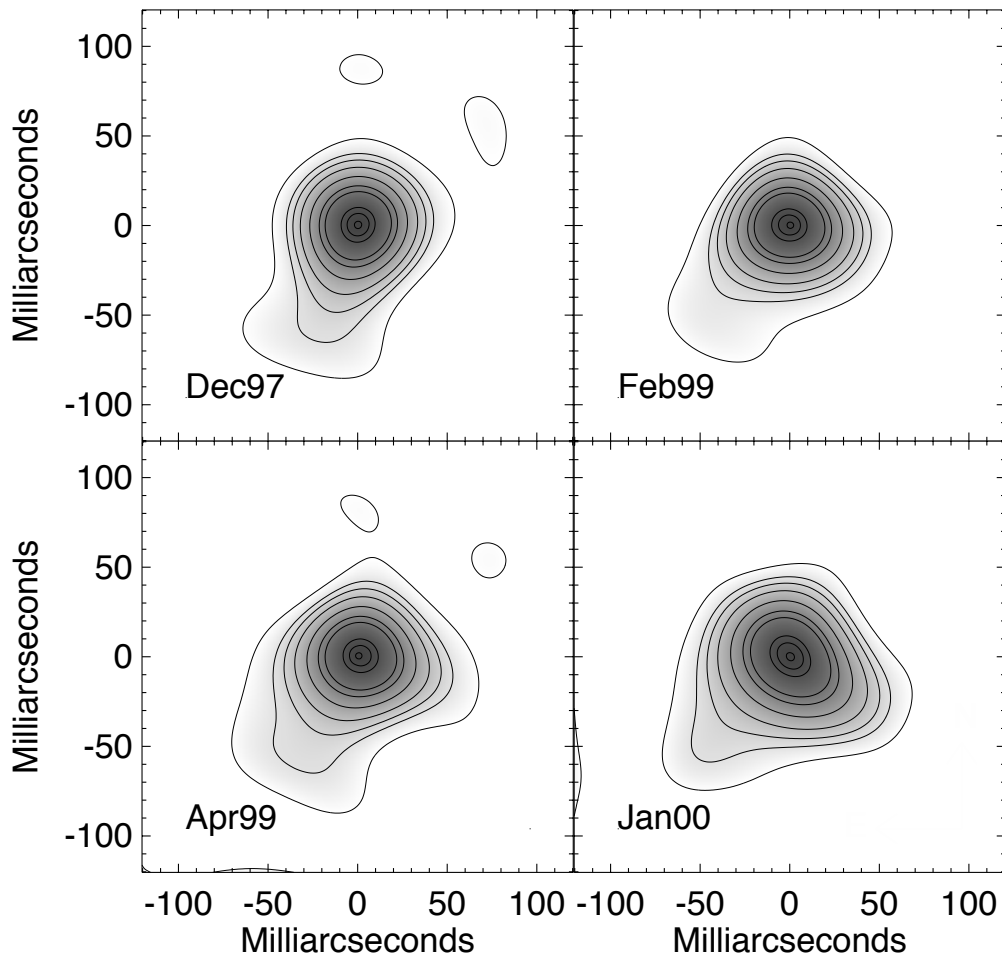


Figure 6.10 – Keck aperture masking over four epochs from December 1997 until January 2000 at $3.08\mu\text{m}$. Contour levels are 1, 2, 3, 5, 7, 10, 30, 70, 85 and 99% of the peak flux. North is up and East is left.

changed significantly within a span of three years especially at levels lower than 30% of the peak flux, while the central source ($\geq 70\%$ of the peak flux) is always within an area of 20×20 mas.

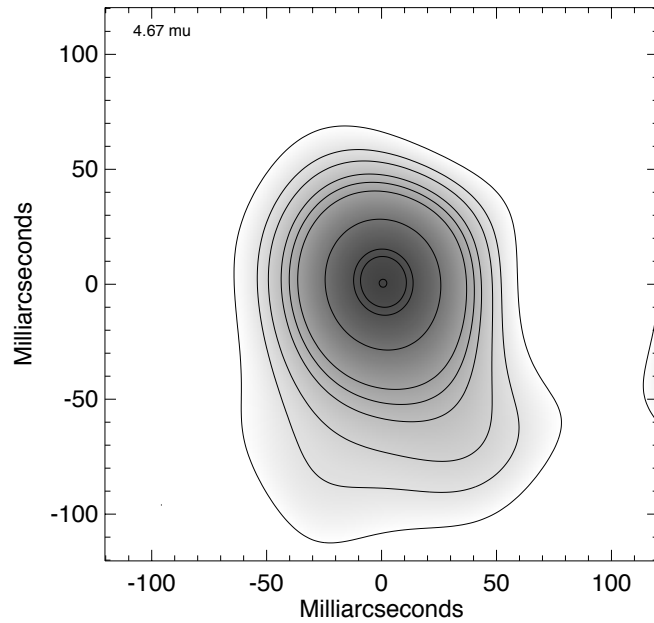


Figure 6.11 – Keck aperture masking in April 2004 at $4.67\mu\text{m}$. Contour levels are 1, 2, 3, 5, 7, 10, 30, 70, 80 and 99% of the peak flux. North is up and East is left.

6.5 An evolving dusty structure

The variability of V Hya’s environment has been monitored in the last 30 years both kinematically and interferometrically. Zhao-Geisler (2010) reported a significant asymmetry between 2007 and 2008 with MIDI/VLTI ($8\text{--}13\mu\text{m}$) based on data with a restricted uv coverage ($45^\circ \leq \text{P.A.} \leq 80^\circ$). Nevertheless, a strong decrease in diameter is mentioned from short to longer wavelengths within the N-band. Observations during 1995 in the mid-infrared (namely 9.78 and $11.65\mu\text{m}$) by Lagadec et al. (2005) revealed an enhanced emissive region towards the South-West in both bands and a hot dust component offset by $0.9''$ on the East-West axis. Sahai et al. (2003) found a transiting emission “blob” ($0.065''/\text{yr}$) offset by $0.2''$ from the central pixel extending South-West²¹. The molecular toroid of $20''$ in size is found to be aligned with a dusty disc (dust scattering in $\text{H}\alpha$) $0.5''$ in size expanding at a low velocity ($10\text{--}15\text{ km s}^{-1}$, Sahai et al. 2003).

²¹Knapp et al. (1997) mentioned a “tilted expanding disc”.

The results presented here are the first successful attempt in imaging the circumstellar environment of V Hya, first with Keck and then with the VLT. Unfortunately, the lack of observations at the same wavelengths does not allow the direct comparison of the structure. Nevertheless it is evident that the environment changes within the near-infrared regime (Figures 6.7, 6.9, 6.10 and 6.11).

Table 6.8 – V Hya binary orbital semimajor axis a for the two photometric periods. Values are projected in angular sizes for an adopted distance of 380pc.

M ₁ (M _⊙)	M ₂ (M _⊙)	6,300 days		529 days	
		(AU)	(mas)	(AU)	(mas)
0.8	0.6	7.49	19.71	1.44	3.78
0.8	0.8	7.84	20.63	1.50	3.94
0.8	1.0	8.15	21.44	1.56	4.10
0.8	1.5	8.84	23.26	1.69	4.44
1.0	1.0	8.45	22.23	1.62	4.27
1.0	1.5	9.10	23.95	1.75	4.59
1.0	2.0	9.67	25.45	1.86	4.88
1.0	2.5	10.18	26.79	1.95	5.14
1.5	1.5	9.67	25.45	1.86	4.88
1.5	2.0	10.18	26.79	1.95	5.14
1.5	2.5	10.64	28.01	2.04	5.37
2.0	2.5	11.07	29.13	2.12	5.59

6.5.1 What lies within the structure

We calculate expected angular sizes of a binary system for V Hya. Since the star is carbon-rich, we expect that its initial mass ranges between 1–2 M_⊙. We have selected a mass range of 0.6–2.5 M_⊙ for the companion, which may be a main sequence star (Evans 2009). Such a companion is not expected to ionise the surrounding medium, unless it is paired with an accretion disc (Sahai & Wannier 1988; Sahai et al. 2009), though Luttermoser & Brown (1992) suggest that the 3.6-cm emission (hot plasma) is probably due to shock excitation and related to the pulsation phase. A red giant companion is improbable since it would have been detected in the infrared already.

The binary orbital semi-major axis a , where $a = \sqrt[3]{G(M_1 + M_2)P^2/4\pi^2}$

for the two photometric periods, are given in Table 6.8 and they are converted to angular sizes for an adopted distance of 380pc. Knapp et al. (1999) give a separation of ~ 23 AU for a “*dust cloud attached to a binary companion*” assuming that its orbital period of 6160-d and the system’s mass is $1 M_{\odot}$, and “*the transit time of an orbiting body is then about 2200-d and its diameter at least several $\times 10^{13}$ cm*”, or else larger than 0.67 AU (or $147 R_{\odot}$). Nevertheless, the latter size is somewhat too large to belong to a Solar-type main sequence star.

If the binary’s orbital period is equal to the 529-d photometric period, then we see that the binary separations range from 1.4–2.1 AU indicating that the system could be going through a common envelope phase (Barnbaum et al. 1995). In that case though, the projected binary sizes in the sky are not compatible with the stellar angular sizes measured with the IOTA interferometric array (Table 6.3). This suggests that the binary period is similar to the longer photometric period, i.e. ~ 17 years.

Taking into account that the photosphere of V Hya is 22 mas or less (Table 6.3) and considering the estimated angular separations of a binary system from Table 6.8, it leads us to assume that the companion is within 50 mas (19 AU) from the red giant, thus it should be detectable even with a diametrically large single telescope but with constant monitoring of the source with aperture masking.

The companion is known to emit in the ultraviolet (Lloyd Evans 2000) and the primary’s photospheric emission is more prominent in J and H. At longer near-infrared wavelengths thermal re-emission from the primary’s dusty surroundings is more dominant.

According to Knapp et al. (1999) the 17-yr obscuration event can be caused by an eclipsing binary. Since the companion is not visible, this leads us to assume that the obscuration event is most probably caused by a transiting dusty blob, one that: (i) either surrounds the companion due to mass transfer from the primary, or (ii) the central dense portion of a spiral arm that orbits the binary (e.g, Figure 6.12 and Edgar et al. (2008)).

NACO/VLT interferometry was not able to differentiate the dusty blob at the given spatial frequencies (Figure 6.13). Further monitoring with an

imaging interferometer with baselines between 10 and 20 metres and with better resolving capabilities²² is needed to allow the determination of the astrometric positions of the dusty blob.

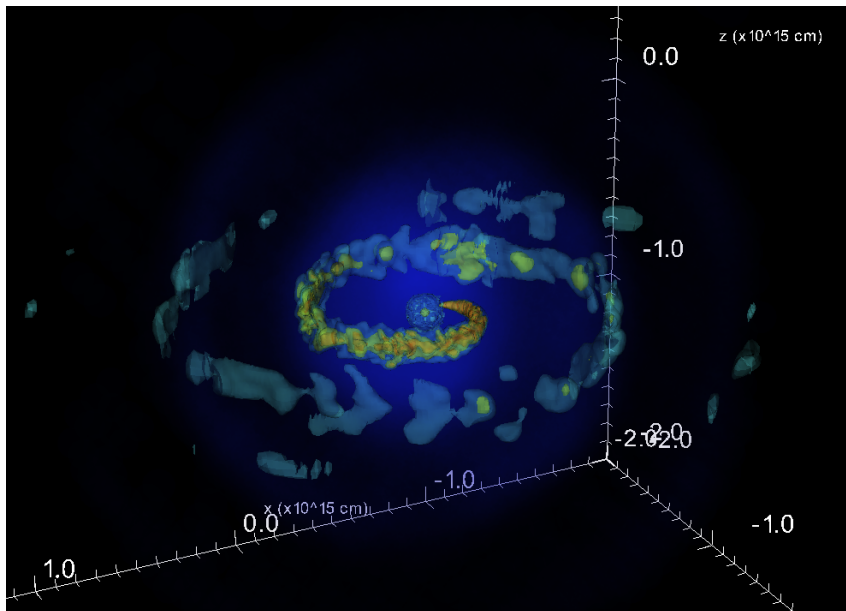


Figure 6.12 – Temperature distribution of ejecta formed into a spiral from the interaction of a binary companion. The scale is 100 AU (Jason Nordhaus, private communication).

6.5.2 Similarities with other stars

V Hya is not the only AGB star that presents a complex structure both in the infrared – the clumpy, evolving core and the disc-like structure – and radio regimes – the molecular torus and the bipolar jets. Yet at approximately $1.5''$ from the core, the dusty envelope appears to be round (Figure 6.9). Other stars with similar properties are:

- π^1 Gru has molecular structures similar to V Hya; that is a bipolar outflow and an equatorial disc (Chiu et al. 2006; Sacuto et al. 2008).
- IRC+10216 has overall spherical shells, but an $0.4''$ expanding clumpy structure as well (Leão et al. 2006).

²²PIONIER/VLTI near-infrared instrument

- The O-rich red giants TX Cam and R Cas were found to have molecular spiral structures at ~ 7 and $8''$ from the central continuum source, respectively (Castro-Carrizo et al. 2010).
- AFGL3068 has an Archimedes spiral formed by the ejecta of the primary star (Mauron & Huggins 2006). Both binary components have been detected at low resolution with Keck telescope (Morris et al. 2006).
- Mira, a known binary system, where Mira B, the companion, accretes the ejecta of Mira A. The bridge of ejecta transfer is seen both in the infrared and X-rays, while a spiral structure created by the primary's ejecta, is surmised to surround the binary (Ireland et al. 2007; Sokoloski & Bildsten 2010).

With the introduction of the ALMA interferometer and the recent advances in imaging with CHARA and VLTI interferometers, close-up observations on the molecular structure of V Hya within $1''$ from the core and the dusty structures around TX Cam and R Cas are advisable.

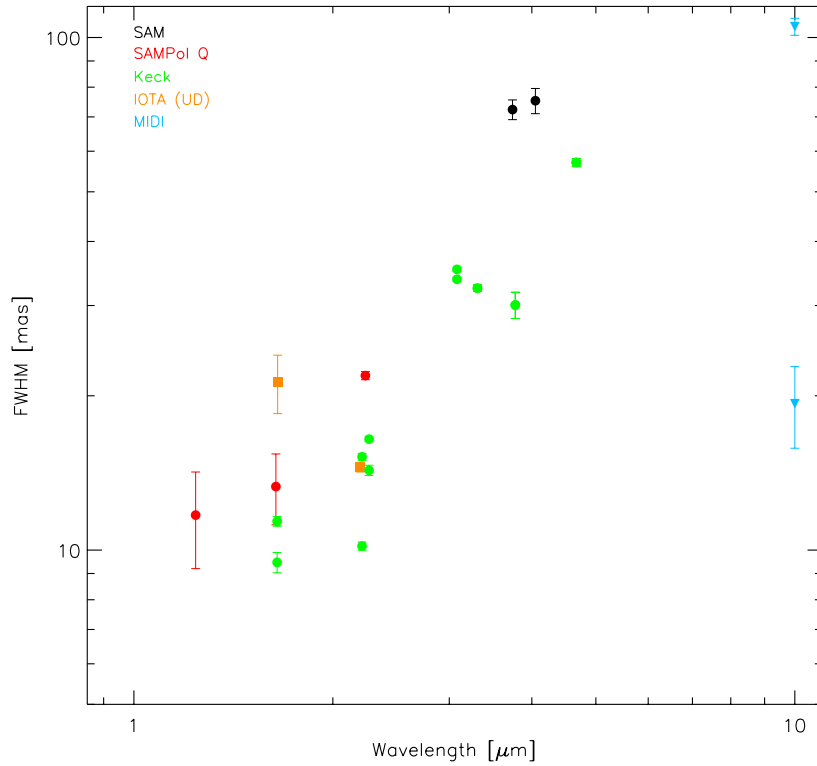


Table 6.9 – Angular sizes (Gaussian) in mas from the Keck aperture masking experiment.

Date	1.647 μ m	2.214 μ m	2.269 μ m	3.082 μ m	3.310 μ m	3.776 μ m	4.670 μ m
Dec 97	9.46 \pm 0.43	10.18 \pm 0.19	—	33.75 \pm 0.29	—	—	—
Feb 99	11.38 \pm 0.25	15.20 \pm 0.24	—	35.29 \pm 0.32	—	—	—
	15.30 \pm 0.26	—	14.31 \pm 0.33	35.59 \pm 0.35	—	—	—
	13.44 \pm 0.25	—	—	32.71 \pm 0.31	—	—	—
Apr 99	—	—	16.46 \pm 0.17	36.95 \pm 0.26	—	—	—
Jan 00	—	—	17.95 \pm 0.23	42.19 \pm 0.31	—	—	—
Jan 04	—	—	—	—	—	30.07 \pm 1.77	57.04 \pm 1.01
May 04	11.28 \pm 0.10	—	17.98 \pm 0.15	39.78 \pm 0.15	32.43 \pm 0.47	—	—

Table 6.10 – Observation log of V Hya

Date	Mode ¹	Mask	Camera	λ [μm]	#pixels ¹	Pix. Scale [mas/pix]	#frames	t_{int} [sec]	Seeing ² [$''$]	Airmass ³
29/6/2010	SAMPol	9H	S13	1.24	512	13.22	4×50	2.50	2.45	1.18
29/6/2010	SAMPol	9H	S13	1.64	512	13.22	4×200	0.50	2.03	1.22
29/6/2010	SAMPol	9H	S13	2.24	512	13.22	4×200	0.11	2.55	1.25
29/6/2010	SAM	9H	L27	3.74	256	27.12	4×800	0.02	2.62	1.30
29/6/2010	SAM	9H	L27	4.05	256	27.12	4×800	0.02	2.84	1.31
30/6/2010	SAM	9H	L27	3.74	256	27.12	4×800	0.02	2.62	1.30
30/6/2010	SAM	9H	L27	4.05	256	27.12	4×800	0.02	2.84	1.31

Calibrators: 1st night: ν Hya; 2nd night: δ Crt

¹ A larger camera window is needed in SAMPol to compensate for the projected offset of the two polarisations.

² DIMM seeing

³ Airmass at the beginning of observing sequence.

CHAPTER 7

Conclusions

Portions of this chapter have been included in Lykou et al. (2011) and Chesneau et al. (2009). The contributions of the co-authors in those publications have been clearly indicated here. The remaining material was written by the author.

7.1 Results

In this work we presented the discovery of dusty structures around evolved stars, from the AGB to the VLTP evolutionary phase, with the use of interferometric techniques. In more detail:

7.1.1 A disc-like structure in Sakurai's Object

A very dense and inclined disc-like structure has been found around Sakurai's Object. Its size, resolved by MIDI/VLTI in 2007, was estimated to be 25–40 mas at $8\mu\text{m}$ and 50–60 mas at $13.5\mu\text{m}$. With the use of radiative transfer models, which reproduced the geometric shape and chemical composition of a disc, we find that the disc-like structure's radius is 65–500 AU (at 3.5kpc) and it contains $6(\pm 1) \times 10^{-5} M_{\odot}$ of amorphous carbon. The structure's large scale height ($h_{100\text{AU}} \sim 50\text{ AU}$; Table 4.4) acts as a barrier towards our view to the central illuminating source.

Our finding is in disagreement with previous statements about an expanding, dusty, circumstellar envelope (Käufl et al. 2003; Evans et al. 2006). The structure's opacity and the continuous decline of the source's temperature, as seen from its spectral energy distribution over the years (Figure 4.4), leads us to believe that this is due to the continuous dust growth within the structure.

Furthermore, we find that the orientation of the structure's major axis ($130 \pm 10^\circ$) is well aligned with an asymmetry we detected in the old planetary nebula ($130 \pm 5^\circ$; Figure 4.17); a fact that makes us believe that the shaping mechanism which originally modified the symmetry of the old planetary nebula might have persevered to create the new asymmetry within the dusty structure.

The shaping mechanism as such, could be a binary companion, but the opacity of the disc does not allow us a direct view towards the star and thus the confirmation of this hypothesis. There have also not been any previous studies to confirm binarity prior to the discovery of Sakurai's Object in 1996. Another example of a fast evolving star where a VLTP has occurred and that is surrounded by a disc is V605 Aql (Clayton et al. 2006; Hinkle et al. 2008).

7.1.2 The disc in M2-9

We present the discovery of a complex dusty disc inside the elongated bipolar planetary nebula M2-9, with the use of infrared interferometry, for which we have derived geometrical constraints and chemical composition. Our findings show that the disc is much smaller than the extended structure around the

nebula’s core (Castro-Carrizo et al. 2012) with an inner rim of 15 AU assuming a distance of 1.2kpc, and is primarily composed of silicates (Table 5.5). This suggests that the dusty material is derived from the AGB envelope of the primary and has survived its evolution onwards. The disc is also aligned with the equatorial axis of the nebula. It is probable that the dust is heated by the primary, an evolving star ($0.6\text{--}1.4M_{\odot}$), but it is also partially heated and truncated by the accretion disc of the secondary, a white dwarf ($0.6\text{--}1M_{\odot}$; see Tables 5.7 and 5.8).

The distance derived from the model fitting (1.2 ± 0.1 kpc) is in disagreement with previous estimations by Schwarz et al. (1997, 650pc). The latter distance failed to reproduce the modelled spectral energy distributions or visibilities. A recent study of the M2-9 nebula itself confirmed our results (1.3 kpc, Corradi et al. 2011).

M2-9 is yet another example of an object with silicate chemistry within the disc, suggesting that the material was ejected during the oxygen-rich phase of the primary star. Nevertheless, there are PAHs in the lobes of the nebula (Figures 5.3 and 5.4), at a much lower percentage, most probably formed after the dissociation of carbon monoxide from the original circumstellar envelope.

7.1.2.1 Comparison to the disc in Mz3

There are some similarities between the disc found in M2-9 and that of its spectroscopic twin, Mz3 (Chesneau et al. 2007; Lykou 2008). As Nathan Smith has stated in Lykou et al. (2011): “...*In the work of Smith (2003) it is shown that the optical to infrared SED of Mz3 required two components; a hot star and a cool star. M2-9 has a very similar SED in the optical to that of Mz3, thus it is probable that it has similar components...*”. Mz3 is also known to have an X-ray jet (Kastner et al. 2003) which further confirms the existence of a binary system at its centre, although it is not visible through its dusty disc.

Both discs have been resolved with high-angular resolution techniques and their composition is similar (amorphous silicates). An attempt to find crystalline silicates using the method presented in Ratzka et al. (2007) as in Chapter 5 was inconclusive (see Figure 7.1). In addition, the discs are in the

equatorial planes of the planetary nebulae (that is, perpendicular to the bipolar ejecta) and at similar inclination from the rotation axis ($\sim 74^\circ$). The mass stored in the disc of M2-9 is approximately 1.6 times more than that in Mz3. The structure inside M2-9 is slightly larger in terms of size (Figure 5.11).

7.1.3 An evolving structure around V Hya

We have successfully resolved the dusty structure around V Hya in the near infrared at a resolution better than the diffraction limit of VLT (see Tables 2.1 and 6.7). The increased resolving capabilities of the telescope are also justified by a comparison to the simple imaging mode results by NACO (Lagadec et al. 2007), that showed a central structure of approximately 300 mas with a wider, spherical envelope extending up to $3''$ in diameter.

The size of the red giant is smaller than 20 mas in H -band – where the stellar photospheric emission dominates – as has been found by IOTA (Ragland et al. 2006) and Keck observations (Table 6.9 by P. G. Tuthill). Our imaging results have revealed a disc five times smaller than the one reported by Sahai et al. (2009): in L -band its size is 100×160 mas and in M -band it is 90×75 mas at 2% of the peak flux, while the majority of the flux lies within an unresolved core of approximately 25×35 mas. While the shortest aperture masking baseline we have used corresponds to an angular scale of roughly 0.5 seconds of arc — and hence larger structures would be resolved out on our baselines — it is most likely that the red giant resides within the small core we see in our images.

The oblate structure (Figure 6.7) is aligned to the North-South axis in our line of sight, an orientation similar to that of an expanding dusty disc found previously by Sahai et al. (2003). Clumpy structures at lower flux levels can also be seen at both 3.74 and $4.05\mu\text{m}$ comparable to those observed with Keck telescope by P. G. Tuthill between 1997 and 2004 (Figures 6.10 and 6.11). It appears that the position of those clumps changes with time, as if they are associated with an orbital motion.

We believe that the 17-year pulsation cycle is caused either by a companion, or by a dusty blob near said companion, that we estimate to orbit within a 50 mas separation (Section 6.5.1). Given the fact that the red giant dominates

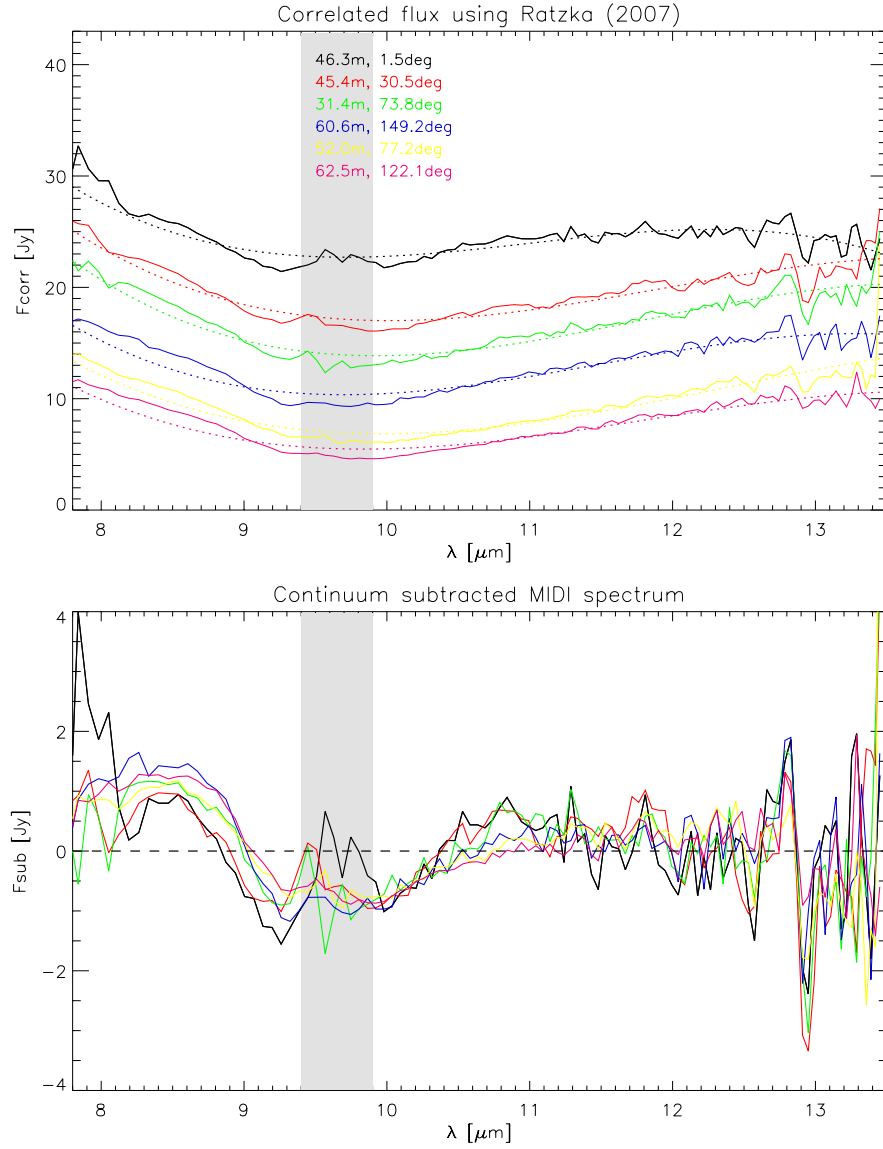


Figure 7.1 – *Top*: MIDI correlated flux for Mz3. Data taken from Chesneau et al. (2007). The dotted lines are polynomial fits to each spectrum. *Bottom*: Continuum-subtracted spectrum of for Mz3. The sharp, downward feature belongs to the bright $12.8\mu\text{m}$ [NeII] nebular emission line. The noise increase at $9.7\mu\text{m}$ corresponds to the narrow ozone feature. No signature of crystalline silicate features can be seen in these spectra. The color-coded observed baselines are indicated within the legend in the top panel. The grey shaded areas indicate the region affected by atmospheric absorption from ozone.

the emission in the near-infrared, but strong emission lines dominate in the visual, the companion must be a fainter star and not a jovian planet (Evans

2009, and references therein).

In the case that the clumpy structures detected in V Hya by the VLT and Keck are in fact the origin of a rotating, spiral structure, we could expect a scenario similar to AFGL3068. This source is a striking example of a spiral formed by a binary: a red giant and a companion at 100 AU (Morris et al. 2006; Maunon & Huggins 2006).

7.2 Past research on dusty structures

In Appendix A we present a list of evolved stars that possess both bipolar nebulae and dusty equatorial structures. There are more sources with equatorial structures available in the literature, but for most of them bipolarity has not been detected yet. We have searched the available literature for sources with bi/multi-polar nebula and equatorial waists, that have or are suspected to have binary central stars. Although binaries have been detected in round and elliptical pre-planetary and planetary nebula (see the work of Miszalski et al. 2009a,b; de Marco 2009; Ciardullo et al. 1999; Bond & Livio 1990, and references therein), these objects do not show any further asymmetries such as jets, arcs or equatorial structures.

Out of the 118 sources listed in Appendix A, 49 are confirmed binaries. Taking into account that most of said binaries have a bipolar outflow and a disc, it is inferred that the remaining sources with similar characteristics may engulf binaries¹. This direct correlation suggests that the detection of a bipolar nebula should indicate the existence of a large (few \times 1000 AU, e.g. M2-9 molecular torus) or a small (few \times 100 AU, e.g. M2-9 dusty disc) dense equatorial structure, and vice versa. Such binary companions are difficult to identify due to the optical thickness of their dusty equatorial waists. In most of the sources, those waists are known as torii (molecular, dusty or both), but as in the case of M2-9 and Mz3, these torii might engulf a smaller dusty disc which cannot be resolved with the standard optical methods used. Hence the

¹It is possible that nebulae that appear elliptical or round and engulf binaries might in fact be bipolar in shape, although due to their projection in our line-of-sight it is not easy to confirm that fact.

use of high-angular resolution instruments, i.e. interferometers.

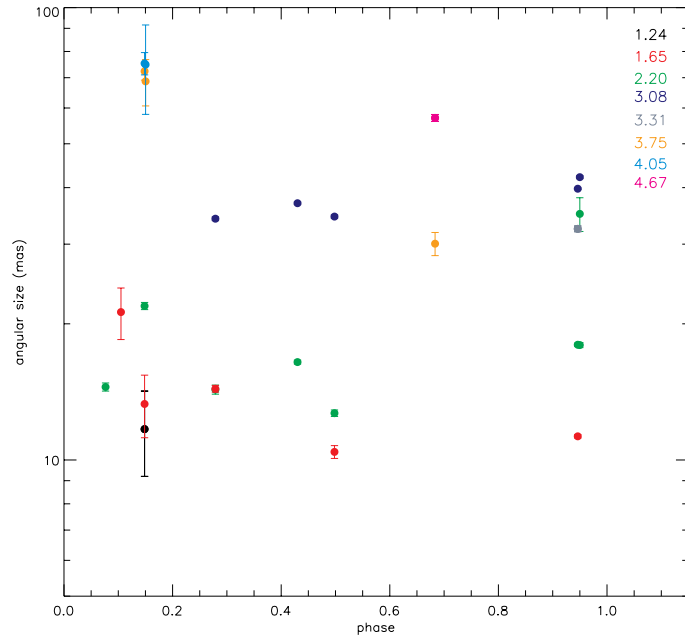


Figure 7.2 – Angular size variations within the 529-d pulsation period over multiple epochs for V Hya within the time period given in Figure 6.1. Data taken from Tables 6.3 and 6.4. The colour-coded respective wavelengths are given in the top-right corner. No direct correlation of size variation can be derived due to the sparse sampling, but it can be inferred from the $1.65\mu\text{m}$ data that the source’s size declines toward visual minimum and increases toward visual maximum.

7.3 Evolution of dusty structures

Our findings revealed three different types of dusty structures in three different evolutionary stages. A pure disc can be identified as a structure whose scale height is much smaller than its outer radius, and it is expected to be in Keplerian rotation. Such discs are well known for post-AGB stars (e.g. Red Rectangle, Osterbart et al. 1997). An example of a young planetary nebula was the disc found in Mz3 (Lykou 2008). The structures that we find in this work can not be described as pure discs, but as complex. The objects we observed are young and in the process of currently losing mass, so their structures are expected to change significantly until said mass loss stops. The structures in these stars

should become the discs we see after the post-AGB stage.

Table 7.1 – Dusty structures at different evolutionary stages

star	π^1 Gru ⁽¹⁾	V Hya	AFGL3068 ⁽²⁾	M2–9
size [†] [mas]		100×160 [3.74] 90×75 [4.05]		25×35 [8] 37×46 [13]
size [AU]	200 – 3300	38×60.8 [3.74] 34.2×28.5 [4.05]	100 – 12900	15 – 900
height [AU]	130	?	?	36
M_{dust} [M_{\odot}]	?	?	?	1.5×10^{-5}
chemistry	O \geq C	C	C	O
structure	torus	spiral?	spiral	unstable disc
companion	MS	?	RG?	WD
period	25 yr	17 yr	830 yr	100 yr
stage	AGB	AGB	AGB	post-AGB
star	Mz3	CPD–56°8032 ⁽³⁾	M2–29	V4334 Sgr ⁽⁴⁾
size [†] [mas]	10×20 [8] 20×40 [13]			25×40 [8] 50×60 [13]
size [AU]	9 – 500	97 – 3000	20 – 250	65 – 500
height [AU]	17	12		50
M_{dust} [M_{\odot}]	9×10^{-6}	3×10^{-4}	10^{-6}	6.5×10^{-5}
chemistry	O	C	O	C
structure	disc	disc-like	disc?	disc-like
companion	?	?	?	?
period	?	?	18 yr	?
stage	young PN	young PN	PN	VLTP

[†] : respective wavelength [μm] of observation

?: indicates a unverified state.

(1) Chiu et al. (2006); (2) Maunon & Huggins (2006)

(3) Chesneau et al. (2006); (4) Gesicki et al. (2010)

V Hya is a mass-losing AGB star with a distant companion, a CO torus. Here we present the detection of a compact, rotating structure that lies within the molecular torus and possibly follows the 17-yr period of an obscuration event seen in its visual lightcurve.

M2-9 is a combination of a red giant (primary) with an accreting WD (secondary) and an orbital period of 100 years. The primary star is the dominant heating source of a disc-like structure. The structure is unstable as it is truncated by the orbiting secondary, which in turn is responsible for ionising the gaseous nebula.

Mz3 is a young planetary nebulae with an unidentified companion, but with an X-ray jet indicating the presence of an accretion disc. It has a flat-like (pure) disc with an inner rim close to its main heating source.

Sakurai's Object is a born-again star with an old, roundish planetary nebula. The star experienced a new mass-loss event in late 1997 and has been embedded in a dust cloud ever since. We find that this dust cloud has transformed into a disc-like structure. It is also aligned with a bilateral pattern found in the nebula. It is possible that an accretion disc formed during the star's past and survived long enough to initiate the VLTP event² (Herwig et al. 2011), and assist in the shaping of a new disc from the newly ejected carbon-rich material. A similar phenomenon has been detected in the recurrent nova RS Oph, where a circumbinary disc has survived the heat blast and the bipolar shocks produced by the nova event (O'Brien et al. 2006; Evans et al. 2007). It is possible that a preexisting disc in Sakurai's Object is now embedded within the structure detected here. The inclined, bipolar outflow of RS Oph, is also an example of what might be the status of Sakurai's Object planetary nebula, where a rather faint region exists perpendicular to the density enhancement and the dusty structure.

Orbital motion plays a significant role in the creation of discs. Pure discs tend to form mostly in RV Tau type stars with orbital periods less than one year. In V Hya and M2-9 the structures are still forming, compared to Mz3 where it the disc seems to have stabilised. These dusty structures are expected to evolve along with the transition of the primaries towards post-AGB and PN stages, respectively. The structures might be: (i) destroyed by ultraviolet radiation, i.e. truncation of the inner edges, evaporation of gas trapped within the structures and thus re-positioning of the dusty material, annihilation of a large portion of dust, and/or (ii) reformed by the orbital motion of the binary system.

It is not clear whether there is an evolutionary sequence that connects the type of structures found here together. More examples of transition objects for stages between those shown here are needed. The examples we list in Table 7.1 are still inconclusive about a direct correlation between evolutionary stages and

²Enriching the stellar surface with heavier materials.

dusty structures, since more than one parameters are involved in the process of disc creation. A better defined sample is required to trace how these structures evolve compared to what we found in this work.

7.4 Conclusions

An evolved star is expected to have a symmetric mass-loss wind, but as it can be seen from the many examples that exist in the literature, the final ejecta are not always symmetric. As it has been mentioned before, the interaction of two winds during the AGB and the post-AGB phase, as well as stellar rotation, magnetic fields, binary companions, are responsible for the shaping of the nebulae around the stars. Stellar rotation alone can not account for disc creation, since as the red giant is losing mass its angular momentum is reduced as well, thus the ejecta can not be confined around the stellar equator. On the same principle, magnetic fields around a single star can not confine the ejecta. The increasing mass-loss and decrease of rotational velocities would break the dynamos needed. The existence of a binary companion though is enough to spin-up the primary and to allow the ejected material to settle on the binary's orbital plane.

In any case, it is not known yet at which exact epoch and under which conditions those asymmetries occur or even how they evolve. Continuous observing of many objects would be a solution to those problems, but the timescales in many cases are hundreds to thousands of years. Thus, observations of objects with similar characteristics but different ages, might be a more eloquent approach. This is the main reason we decided to observe an AGB star (V Hya), a symbiotic star (M2-9), a young planetary nebula (Mz3)³ and a star that passed through a VLTP stage (Sakurai's Object).

During the last decade it has been widely accepted that bipolar (or multipolar) nebulae are shaped by binaries: the shaping of an evolved star's ejecta by the orbiting companion⁴. In most cases, bipolar shapes are accompanied

³Previous work by Lykou (2008)

⁴This has been the dominant theme in the last two conferences dedicated to this field of research, Asymmetric Planetary Nebulae IV and V conferences, in 2007 and 2010 respectively.

by jets and dusty equatorial waists in the forms of discs, tori, spirals or rings. This leads us to the conclusion that the dusty structures are a by-product of binarity.

The examples presented in Appendix A show that dusty and molecular structures exist from the AGB till the VLTP phase of evolution. These structures have to survive and evolve in hostile environments (strong stellar UV radiation fields) for long periods of time (e.g. Mz3 and M2-9). For instance, in symbiotic binaries with periods between 10–1000 years, there is enough time for heavier material to settle in equatorial structures and survive the binary’s evolution.

It is possible that the dusty structures assist in the ejection of jets by setting a density barrier that channels gas perpendicularly to the orbital plane of a binary (Mastrodemos & Morris 1998, 1999). The gas deposits in those structures can be later photo-evaporated as shown by Gesicki et al. (2010), and dust is left to coagulate into larger grains and settle in more flat-like structures as shown by van Winckel (2003); van Winckel et al. (2009). Since we see dusty structures in highly-evolved sources, their long lifetime suggests that they are related to long-lived shaping mechanisms (e.g. Sakurai’s Object disc and planetary nebula asymmetry).

Nevertheless, the dusty structures are not always *stationary* and *flat*, but they might evolve along with their originating stars: (i) V Hya has a rotating, oblate dusty structure, which is also surrounded by a molecular torus; our modelling failed to reproduce exactly (ii) the complex structure of M2-9, since it is not flat-like as is the one in Mz3, and a companion that truncates the disc-like structure cannot be simulated with the radiative transfer code in hand, and (iii) the newly ejected disc-like structure in Sakurai’s Object, due to the visibility signal (second or third lobe) in three out of the six baselines. As such, we would like to see radiative transfer codes with the option of a binary companion, a molecular envelope and a multi-density gradient law, i.e. an interior and an exterior disc.

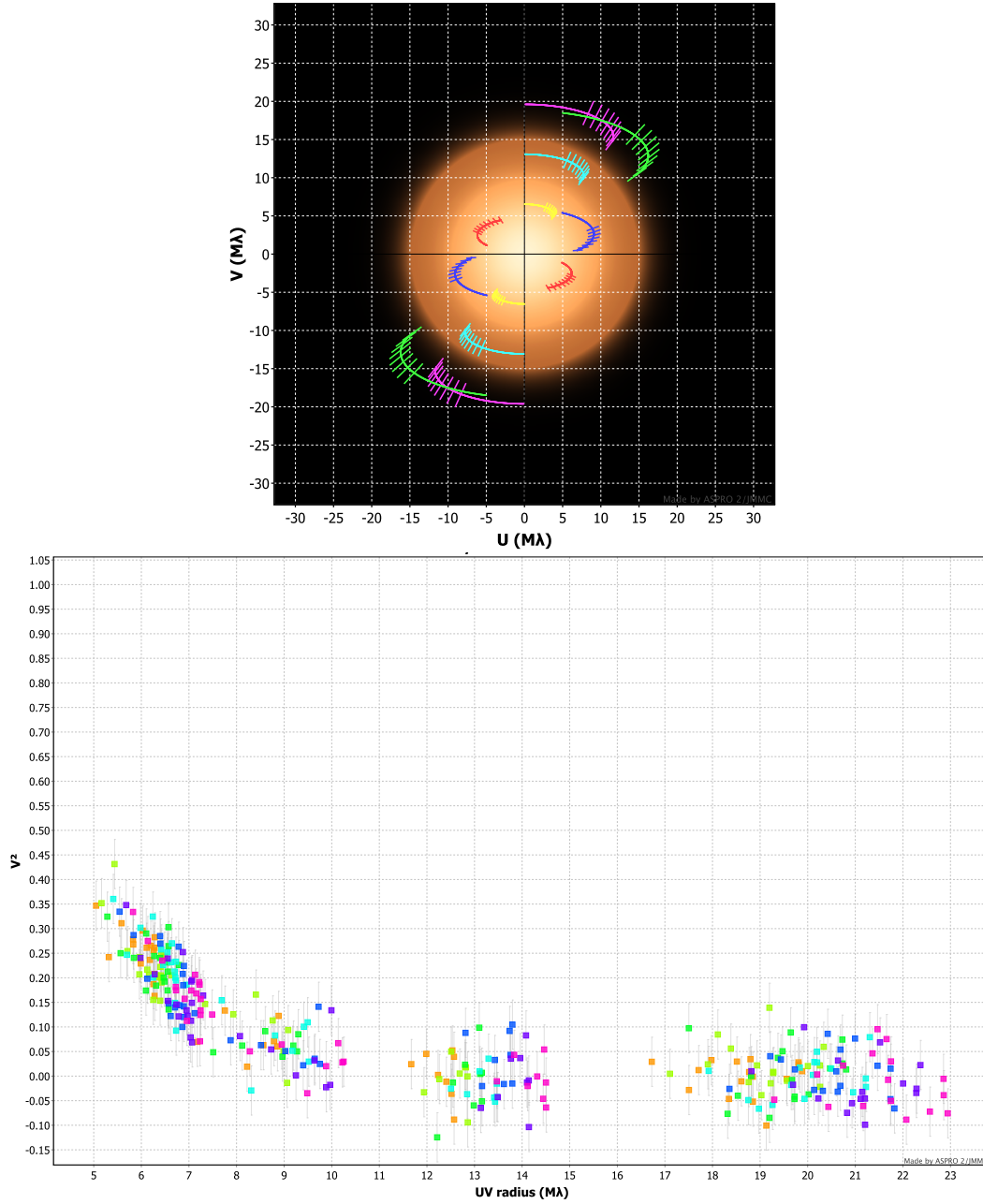


Figure 7.3 – Expected uv coverage (top) and V^2 amplitude (bottom) in H band for V Hya with PIONIER/VLTI and six baselines between 11 – 36-m with the ATs. The squared visibility amplitude of a 15-mas Gaussian distribution is plotted for comparison to the uv coverage. Each colour corresponds to a different wavelength sampled within the H band (1.52–1.81 μ m). The simulating code ASPRO2 adds some reasonable estimate of the noise to mimic real observations, hence the spread of the V^2 amplitude at a given uv radius and the negative values in the plot.

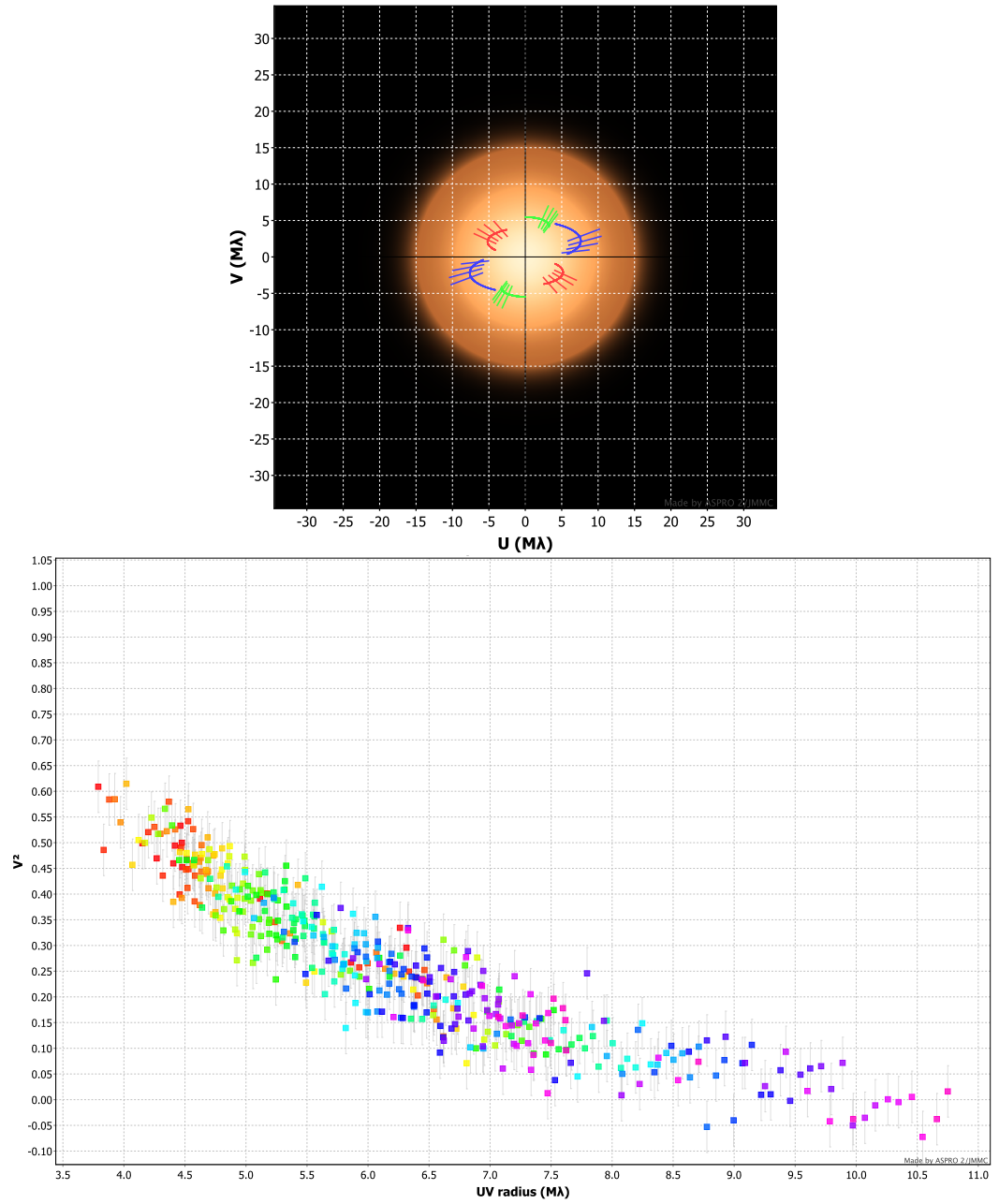


Figure 7.4 – Same as Figure 7.3 but for H and K bands (low-JHK; $1.48\text{--}2.52\mu\text{m}$) with AMBER/VLTI and three baselines between 11 – 16-m.

7.5 Future work

7.5.1 The future of V Hya

7.5.1.1 Visual to near-infrared

SAMPol initial stellar diameter results in J, H and K for Stokes Q were first presented by Norris (2010) with the use of a toy model of a uniform disc for a star and a Gaussian disc surrounding shell. The full data set shall be analysed by incorporating radiative transfer modelling for Stokes Q parameter and subsequent image reconstruction of the polarising medium. In a future paper we will present our findings from SAM/NACO and those of the Keck aperture masking experiment (Lykou et al., in preparation).

Considering that the visual magnitude is already fading as the 17-yr cycle minimum is approached (Figure 6.1), we recently obtained integral field spectroscopy data with the WiFES instrument in Mt. Stromlo, Australia, in blue and red. We intend to estimate the velocity of the bipolar outflow during the obscuration event and assuming that V Hya is an object in transition to the post-AGB phase, we would like to compare the C_2 isotopic ratios to those found in C-rich AGB and post-AGB stars. The dataset has been reduced⁵ but not analysed yet.

We have re-visited the star using aperture masking in May and December 2012 and in February 2013, while it is already in the visual minimum. The full data set has not been analysed yet. Thus, we are still studying the cycle-to-cycle variation of the star and its circumstellar environment (e.g. Figure 7.2). We also plan to re-observe V Hya with AMBER/VLTI and/or PIONIER/VLTI⁶ in H and K bands with baselines smaller than 15-m (IOTA resolved the red giant with baselines from 16 to 26-m; Millan-Gabet et al. 2003). These imaging interferometers should allow us to image V Hya for the first time in the near-infrared and to detect the companion. The star as well as its surrounding environment can be easily sampled with both PIONIER and AMBER (see

⁵Observations and data reduction by L. Guzman-Ramirez, JBCA.

⁶4-telescope interferometer, Precision Integrated-Optics Near-infrared Imaging Experiment, <http://ipag.obs.ujf-grenoble.fr/twiki/bin/view/Ipag/Projets/Pionier/>

Figures 7.3 and 7.4).

7.5.1.2 Far-infrared to millimetre

V Hya has been observed by the Herschel space telescope in both imaging and spectroscopic modes as part of a large program for the detection of mass-loss in evolved stars (Groenewegen et al. 2011). Herschel observations should fill the gap between the mid-infrared and millimetre regime. Castro-Carrizo et al. (2010) announced the presentation of CO millimetre interferometric observations with IRAM in the near future.

After studying the results by Herschel and IRAM, we will suggest to observe the star with ALMA at CO transitions ($J=2-1, 3-2, 4-3$) in order to map the velocity structure of excited molecular gas in the vicinity of V Hya. Recent work by Maercker et al. (2012, R Scl) has shown that ALMA is able to detect spiral structures in AGB stars.

7.5.2 The current evolution of Sakurai's Object

Given the rapid evolution of Sakurai's Object within the last two decades (see Figure 4.4) we expect that within this century we should be able to re-observe the star in the visual. In the meantime, since ground observations⁷ at wavelengths above $20\mu\text{m}$ are limited due to low atmospheric transmittance, we must rely on observations by space telescopes to allow us to study the evolution of the dusty structure over time. The source has been observed with Spitzer telescope's MIPS instrument in 2005 and 2008 with detections at 24 and $70\mu\text{m}$. The author will investigate that data in the near future. It is not confirmed yet, whether AKARI satellite has observed Sakurai's Object in imaging mode as well.

⁷The only available mid-infrared imaging instrument in the Southern Hemisphere is VISIR on the VLT with a maximum wavelength limit at $19.5\mu\text{m}$ (pixel size 75 mas)

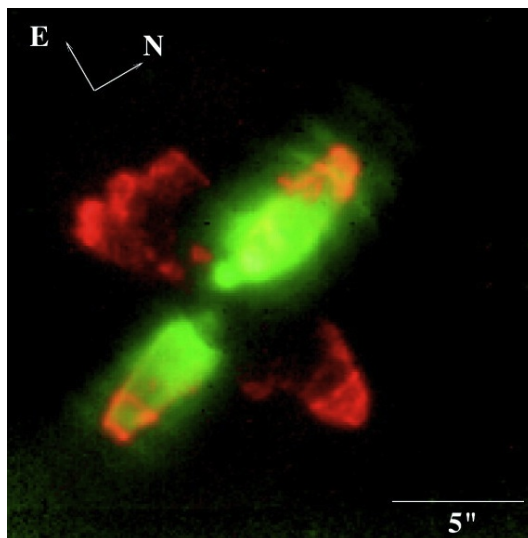


Figure 7.5 – AFGL2688 at $2.15\mu\text{m}$ imaged by the HST. *Reproduction by Sahai et al. (1998)*

7.5.3 Other sources

The European Space Observatory is planning to install an aperture masking mode on the VLT Imager and Spectrometer for mid Infrared (VISIR⁸) which operates between 8 and $20\mu\text{m}$. In that case, it would be interesting to inspect other evolved stars for the identification of discs, such as AFGL2688, a pre-planetary nebula with a rotating bipolar structure (Fig. 7.5), and CPD–56°8032, a young planetary nebula with a disc-like structure (Chesneau et al. 2006) and a peculiar lightcurve (Cohen et al. 2002, Fig.10).

In order to constrain further the geometric parameters of the disc-like structure, M2-9 should be re-observed at a future time with MIDI/VLTI⁹ in different baseline configurations and compare it again to the torus observed by IRAM (Castro-Carrizo et al. 2012).

New imaging infrared interferometric instruments, such as PIONIER (4-beam recombiner) on the VLTI, MIRC (6-beam recombiner) on CHARA interferometer and the Magdalena Ridge Observatory (currently under construction) will offer significant advances in imaging dusty structures around other evolved stars, such as the red giants TX Cam and R Cas that apparently have molecular spiral structures (Castro-Carrizo et al. 2010), and other sources from the list given in Appendix A, to allow statistical analysis for the correlation between

⁸<http://www.eso.org/sci/facilities/paranal/instruments/visir/>

⁹The source is too faint in the near-infrared to use AMBER/VLTI.

late-type stellar evolution and discs.

APPENDIX A

Evolved stars with dusty structures

In this section we present a list of evolved stars found in the literature, in all evolutionary stages spanning from the AGB to the VLTP¹. The objects selected exhibit both bipolar (or multipolar) outflows and equatorial waists in the form of gaseous/dusty torii or spirals or circumbinary discs. The binary properties, such as type of companion and orbital period, are also listed, as well as byproducts of binarity such as accretion discs and jets. A question mark (?) indicates that the binary nature of the central source is not verified yet, and a blank space in the *companion* column followed by a known orbital period designates that the type of companion is not known yet. A larger number of sources with dusty structures can be found in the literature, but these either are not confirmed to have bipolar nebulae or do not show any such shape asymmetries in the first place. Thus, these sources are not listed here.

¹Sakurai's Object and V605 Aql have been added for comparison since their current surrounding nebula are round.

Table A.1 – Examples of evolved objects that do (or are suspected to) engulf binaries

Name	Companion	P _{orb}	Shape†	Structure	Reference
<u>AGB stars</u>					
Mira	WD	1100d	Com	accretion	Ireland et al. (2007)
V Hya	MS?	17yr	Bp	torus/spiral?	this work
R Aqr	WD	44yr	Bp	accretion	Gromadzki, M. & Mikolajewska, J. (2009)
π^1 Gru	MS	$\leq 25\text{yr?}$	Bp	torus	Sacuto et al. (2008)
AFGL3068	RG?	830yr	p-o	spiral	Mauron & Huggins (2006)
CIT 6	3-ple?	600d	Bp	spiral	Dinh-V.-Trung & Lim (2009)
R Cas	?		p-o	spiral	Castro-Carrizo et al. (2010)
TX Cam	?		p-o	spiral	Castro-Carrizo et al. (2010)
CH Cyg	WD	15yr	Bp	jet/accretion	Mikolajewska et al. (2010)
AG Dra	WD	541d	?	jet	Mikolajewska (2002)
MWC 560	RG?		Bp	disc/accretion	Arrieta et al. (2005)
<u>Post-AGBs</u>					
RV Tau	MS	79d	none	disc	de Ruyter et al. (2005)

Continued on next page...

Table A.1 – Examples of evolved objects that do (or are suspected to) engulf binaries

Name	Companion	P _{orb}	Shape†	Structure	Reference
Red Rectangle	yes	318d	Bp	torus	Van Winckel et al. (2002)
M2-9	WD	100yr	Bp	disc	this work
AFGL2688	?		Mp	jets/disc	Weintraub et al. (2000)
He 3-1475			Bp	jet	Huggins (2007)
OH231.8+4.2	MS	≤200yr	Com	flat ≤ 10 ⁴ AU	Etoka et al. (2008)
AFGL2688	?		Mp	torus ≤ 4500 AU	Cox et al. (2000)
He 2-104	WD		Bp	accretion	Corradi & Schwarz (1993a)
Roberts 22	?		Bp	waist	Lagadec et al. (2011a)
08544-4431	507.8d		Bp?	disc	Deroo et al. (2007a)
HR 4049		430d	Bp?	jet/disc	Menut, J.-L. et al. (2009)
06034+1354		60.26d	Bp	torus	de Ruyter et al. (2006)
06072+0953		135.5d			de Ruyter et al. (2006)
06108+2743		50.1d			de Ruyter et al. (2006)
06160-1701		113.9d			de Ruyter et al. (2006)
06472-3713		410.4d			van Winckel et al. (2009)
09256-6324			Bp	torus	de Ruyter et al. (2006)
11385-5517			Bp	spiral/disc	de Ruyter et al. (2006)
12067-4508			Bp	torus	de Ruyter et al. (2006)

Continued on next page...

Table A.1 – Examples of evolved objects that do (or are suspected to) engulf binaries

Name	Companion	P _{orb}	Shape†	Structure	Reference
12185–4856		595d			de Ruyter et al. (2006)
12222–4652		913.8d	Bp	torus	van Winckel et al. (2009)
14524–6838		1493d			van Winckel et al. (2009)
15469–5311		389.9d	Bp	torus	van Winckel et al. (2009)
17243–4348			Bp	torus	de Ruyter et al. (2006)
17534+2603		288.4d	Bp	torus	de Ruyter et al. (2006)
18281+2149		1230d			de Ruyter et al. (2006)
19125+0343		519.6d	Bp	torus	van Winckel et al. (2009)
19157–0247		119.5d	Bp	torus	van Winckel et al. (2009)
20117+1634			Bp	torus	de Ruyter et al. (2006)
22327–1731		259d			de Ruyter et al. (2006)
BD39+4926		775d			de Ruyter et al. (2006)
TW Cam		85.6d			de Ruyter et al. (2006)
U Mon		2597d			de Ruyter et al. (2006)
12538–2611	?		Bp	torus	Siódmiak et al. (2008)
13416–6243	?		Bp	torus	Siódmiak et al. (2008)
13428–6232	?		Bp	torus	Siódmiak et al. (2008)
15039–4806	?		Bp	torus	Siódmiak et al. (2008)

Continued on next page...

Table A.1 – Examples of evolved objects that do (or are suspected to) engulf binaries

Name	Companion	P _{orb}	Shape†	Structure	Reference
15553-5320	?		Bp	torus	Siódmiak et al. (2008)
17163-3907	?		Bp	torus	Siódmiak et al. (2008)
17279-1119	?		Bp	torus	Siódmiak et al. (2008)
17516-2525	?		Bp	torus	Siódmiak et al. (2008)
18135-1456	?		Bp	torus	Siódmiak et al. (2008)
19306+1407	?		Bp	torus	Siódmiak et al. (2008)
20547+0247	?		Bp	torus	Siódmiak et al. (2008)
22036+5360	?		Bp	torus	Siódmiak et al. (2008)
<i>Pre-Planetary nebulae</i>					
AFGL 618			Bp	torus	Siódmiak et al. (2008)
M 1-92	MS		Bp	disc/jet	Murakawa et al. (2010)
M 2-56			Bp	torus	Siódmiak et al. (2008)
W43A	?		Bp	jets	Lagadec et al. (2011b)
16279-4757	?		Bp	torus	Lagadec et al. (2011b)
16594-4656	?		Bp	torus	Lagadec et al. (2011b)
17106-3046	?		Bp	disc	Lagadec et al. (2011b)

Continued on next page...

Table A.1 – Examples of evolved objects that do (or are suspected to) engulf binaries

Name	Companion	P _{orb}	Shape‡	Structure	Reference
17150–3224	?		Bp+arcs!	torus	Kwok et al. (1998)
17311–4924	?		Bp	torus	Lagadec et al. (2011b)
17347–3139	?		Bp	torus	Lagadec et al. (2011b)
17441–2411	?		Mp	disc~1000 AU	Volk et al. (2007)
18276–1431	?		Bp	torus	Lagadec et al. (2011b)
19016–2330	?		Bp	torus	Lagadec et al. (2011b)
19386+0155			Bp	torus	Lagadec et al. (2011b)
19475+3119	?		Qp	torus ~ 10 ⁴ AU	Hsu & Lee (2011)
<i>Planetary nebulae</i>					
Hen 2–113			Bp	torus?	Lagadec et al. (2011b)
Me 1–1	MS?		Bp	rings	Pereira et al. (2008)
Helix	?		Com	disc	Chu et al. (2009)
GLMP 621	RG		Bp	jets	Riera et al. (2003)
NGC7027			Mp	torus	Huang et al. (2010)
MyCn 18	WD		Bp	accretion	Corradi & Schwarz (1993a)
NGC2346	MS	16d	Bp		de Marco (2009)

Continued on next page...

Table A.1 – Examples of evolved objects that do (or are suspected to) engulf binaries

Name	Companion	P _{orb}	Shape†	Structure	Reference
M 2-29	3-ple	18yr+23d	Bp	jet, disc	Hajduk et al. (2008)
ETHOS 1		0.535d	Bp	jets/accretion?	Miszalski et al. (2011b)
K 1-2		0.676d	Bp	jets	Bond & Ciardullo (1989)
He 2-36	WD		Bp	?	Corradi & Schwarz (1993b)
He 2-47	merger/sub*?		Mp	ring~1.2''	Sahai (2000)
M 1-37	merger/sub*?		Mp	ring~1''	Sahai (2000)
Hen 2-161	Yes		Bp	torus	Sahai et al. (2011)
M 2-19		0.67d	Bp	torus?	Miszalski et al. (2009a)
H 2-19		0.24d	Bp	torus?	Miszalski et al. (2009a)
K 6-34		0.20d	Bp	jet/torus?	Miszalski et al. (2009a)
Sp 1		2.91d	Bp	torus	Miszalski et al. (2009a)
NGC6337		0.17d	Bp	jet/torus?	Miszalski et al. (2009a)
A41		0.23d	Bp	torus	Miszalski et al. (2009a)
A70	Ba		Bp	rings	Miszalski et al. (2011a)
NGC6778		0.15d	Bp	torus	Miszalski et al. (2011c)
16333-4807	?		Bp	jet	Lagadec et al. (2011b)
CPD-56°8032	?		Mp	disc	Chesneau et al. (2006)
Hen 2-86	?		Bp	torus	Sahai et al. (2011)

Continued on next page...

Table A.1 – Examples of evolved objects that do (or are suspected to) engulf binaries

Name	Companion	P _{orb}	Shape†	Structure	Reference
Hen 2–320	?		Bp	torus	Sahai et al. (2011)
PNG 348.8-04.1	?		Bp	torus	Sahai et al. (2011)
Hen 2–180	?		Bp	torus	Sahai et al. (2011)
M 2–14	?		Bp	torus	Sahai et al. (2011)
Hb 12	?		Bp	torus	Sahai et al. (2011)
NGC6881	?		Bp	torus	Sahai et al. (2011)
K 3–67	?		Bp	torus	Sahai et al. (2011)
K 5–4	?		Bp	torus	Sahai et al. (2011)
Th 3–4	?		Bp	torus	Sahai et al. (2011)
PNG 356.9-04.4	?		Bp	?	Sahai et al. (2011)
Hen 2–447	?		Mp	torus	Sahai et al. (2011)
H 1–19	?		Mp	torus	Sahai et al. (2011)
H 1–46	?		Mp	torus	Sahai et al. (2011)
Hen 2–41	?		Bp	torus	Sahai et al. (2011)
Th 3–12	?		Bp	torus	Guzman-Ramirez et al. (2011)
H 1–43	?		Mp	torus	Guzman-Ramirez et al. (2011)
H 2–27	?		Bp	torus	Guzman-Ramirez et al. (2011)
15103–5754	?		Bp	torus	Lagadec et al. (2011b)

Continued on next page...

Table A.1 – Examples of evolved objects that do (or are suspected to) engulf binaries

Name	Companion	P _{orb}	Shape [‡]	Structure	Reference
15445-5449	?		Bp	torus	Lagadec et al. (2011b)
16342-3814	?		Bp	torus	Lagadec et al. (2011b)
<u><i>VLT</i></u>					
V4334 Sgr	merger/sub*?	—	R	disc ≤ 800 AU	this work
V605 Aql	merger?	—	R	torus	Lau et al. (2011)

[‡] Com : complex; Bp : bipolar; Mp : multipolar; Qp : quadrupolar; p-o : pole-on; R : round

Many of the objects listed are also known symbiotic binaries, i.e. a Mira-type star and a MS or WD companion.

APPENDIX B

MIDI data reduction

In this section, an example of the data reduction process followed with MIDI's reduction package MIA of incoherent analysis is shown. The full MIA manual can be found online¹. The set of data used is given in Table B.1. The calibrator was observed right after the science target to ensure similar atmospheric and instrumental conditions.

A graphical user interface (GUI) allows the user to select the data to be reduced. A typical structure of the data, as shown on the GUI, includes a list of the recorded FITS files, which are:

- Acquisition frames, where the instrument locates the target;
- Fringe tracking frames, where the instrument locates the interferometric fringes within the OPD;

¹<http://home.strw.leidenuniv.nl/~jaffe/ews/MIA+EWS-Manual/index.html>
http://www.eso.org/sci/facilities/paranal/instruments/midi/doc/VLT-MAN-ESO-15820-4039_v87.pdf

Table B.1 – An example for a science target and a calibrator

info	V4334 Sgr	HD169916
Date	2007-06-29	2007-06-29
Time	03:35:28	03:58:27
Proj. baseline [m]	45.93	46.42
Position angle [deg]	37.11	35.03
Good/Bad scans [%]	94/5.5	94/5.5
Wavelength “Binning” [pixel]	width: 3, step: 3, range: [35,139]	

For the significance of the “binning” values, see main text.

- Interferometric fringes, recorded for channel/telescope 1;
- Interferometric fringes, recorded for channel/telescope 2;
- Photometric frames, recorded for channel/telescope 1;
- Photometric frames, recorded for channel/telescope 2.

Background subtraction is the next step in data reduction. The sky background is removed from the photometric frames (in `HIGH_SENS` mode are recorded after the fringe signal) using chopping in the telescope’s secondary mirror. It is preferred to use the photometric channels for thermal background subtraction. First, bad pixels are removed in the y -direction via median smoothing and then a 1-D Gaussian fit is applied in the same direction. The centroid and width of the fit are recorded. In the next step, a 2nd order polynomial is fit over all centroids in the x -direction and a 1st order polynomial over all widths. For example, see the blue middle line² (fit to the centroids; x -direction; wavelength) and the blue error bars (fits to the widths; y -direction; fringes) in the bottom panel of Figure B.1. This process is performed for each photometric channel³ A and B and the mean of the two fits is overlaid on the interferometric channels to find the fringe signal. The same masks (average of Gaussian fits) will be used to suppress the background from all the frames stored in the data cube. There are four options for mask selection, three depend on fitting the coefficients using the GUI (top panel, Fig.B.1) and the fourth allows you to select your own mask. We chose the default option which gave larger fitted widths, thus

²The top and bottom blue lines are the limits of the widths

³We follow the notations given in most VLTI documents and Ratzka et al. (2007).

selected a bigger portion of the data that might include significant information, but could of course contain additional noise as well.

The two-dimensional windows have the dimensions of the detector subarray corresponding to the chosen dispersive element, i.e. 240×40 for GRISM and 171×41 for PRISM. The fringe signal is the ordinate and the respective wavelength is the abscissa.

Following the background subtraction, as described above, by multiplication of the Gaussian masks with the set of 8000 frames (n_F) of spectrally dispersed interferograms for each interferometric channel (I_1, I_2), the reduction process continues as described in Figure B.2.

Each frame in the data cube is summed (“compressed”) along the y-axis creating one-dimensional arrays and the flux difference between the two interferometric channels is estimated (see also Eq.[2.10] and Fig. B.4). The arrays are then sorted in clumps depending on the number of recorded scans, that is $n_S = 200$ scans per observed set of frames yields $n_f = 40$ arrays per scan.

Wavelength calibration is applied on each scan and the values of the direction of dispersion (x-axis) are modified from pixels to wavelength within the N -band ($8\text{--}13\mu\text{m}$) with a width of 3 pixels and a step of 3 pixels (i.e. the parameter binning given in Table B.1). For PRISM the formula is

$$\lambda = -0.0001539 \cdot (x + 120)^2 + 0.009491 \cdot (x + 120) + 15.451905, \quad (\text{B.1})$$

where x is the pixel number, where the detector’s size is 320 pixels. For instance, the “binning” shown in Table B.1 will correspond to 13.22 and $7.58\mu\text{m}$ for pixels 35 to 139, respectively. The chosen width and step guarantee that no pixel is neglected (pixel increment: 35–38, 38–41, 41–44, ..., 136–139). The pixels are resampled into wavelengths, but the pixel width does not result in a uniform wavelength width (Fig. B.5).

Each scan is then Fourier-transformed (\tilde{I}_ν) into the frequency domain and the interferometric flux is recorded (see also Eq.[2.12] and Fig. B.4),

$$\tilde{I}_{\nu,s} = \frac{1}{n_f} \sum_{f=0}^{n_f-1} I_{int}(f, S) \exp\left(-\frac{2\pi}{n_f} \nu f\right), \quad (\text{B.2})$$

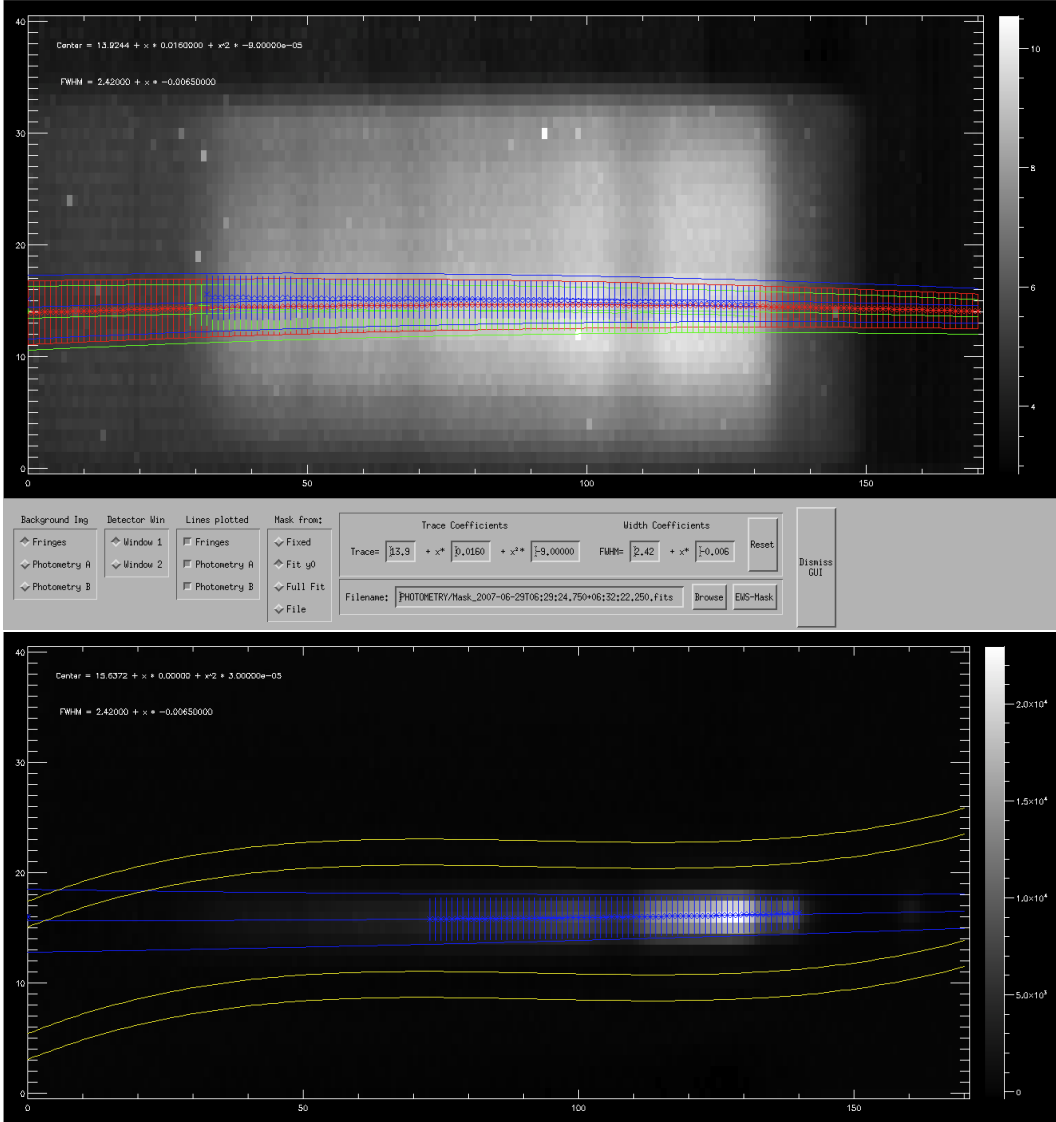


Figure B.1 – Application of a mask for PRISM in MIA (171×41 pixels). *Top:* The Gaussian masks are for: fringes in red, photometric channel *A* in green and photometric channel *B* in blue. *Bottom:* Application of the same mask for photometric channel *A*. The yellow lines trace the area from which the sky noise is estimated.

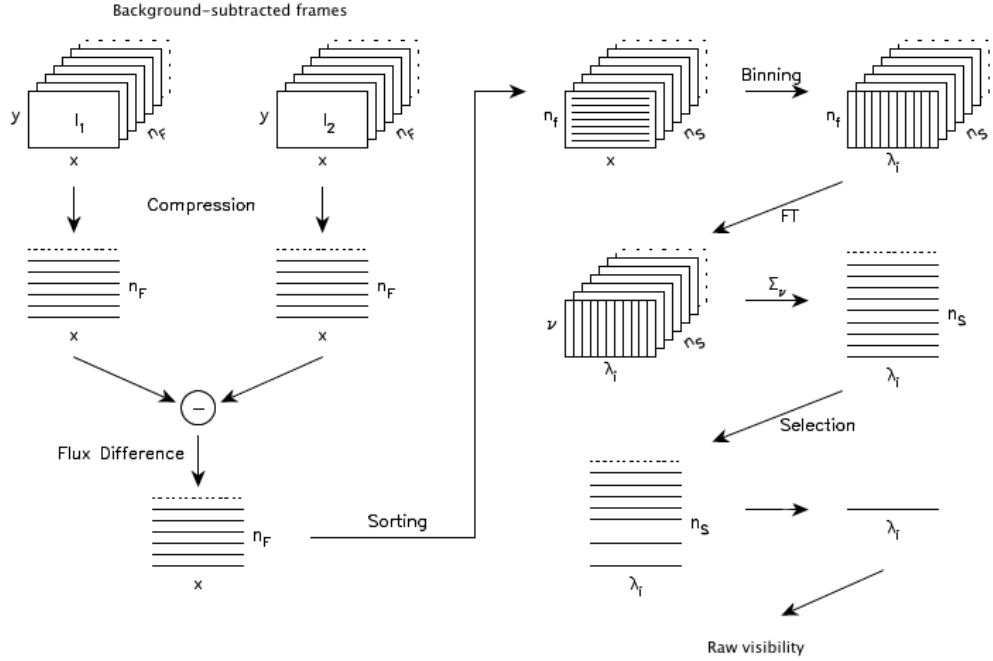


Figure B.2 – MIDI Interactive Analysis flowchart. *Adapted by Ratzka et al. (2007).*

where f and S are the frame and scan number, respectively. Scans that were not recorded at zero OPD are rejected by determining the white-fringe amplitude, i.e. the squared-root of the summed powerspectra⁴ within the frequency range⁵, i.e. wavelength binning selected above (see Fig. B.5). Finally, the raw visibility and the correlated flux, i.e. raw photometry \times visibility (Fig. B.3) are estimated as in Eq.[2.25].

This data reduction process has been followed for data from both the science target (V4334 Sgr) and a calibrator of known diameter (HD169916; 3.75 ± 0.04 mas). The latter is used to derive the instrumental visibility of the VLTI at the given time and setup of observations, which is the raw visibility of the calibrator divided by the visibility of a uniform disc whose size is equal to

⁴Squared-modulus of the interferometric flux's Fourier transform.

⁵Where signal is expected, $OPD/\lambda_{\min} \leq \nu \leq OPD/\lambda_{\max}$.

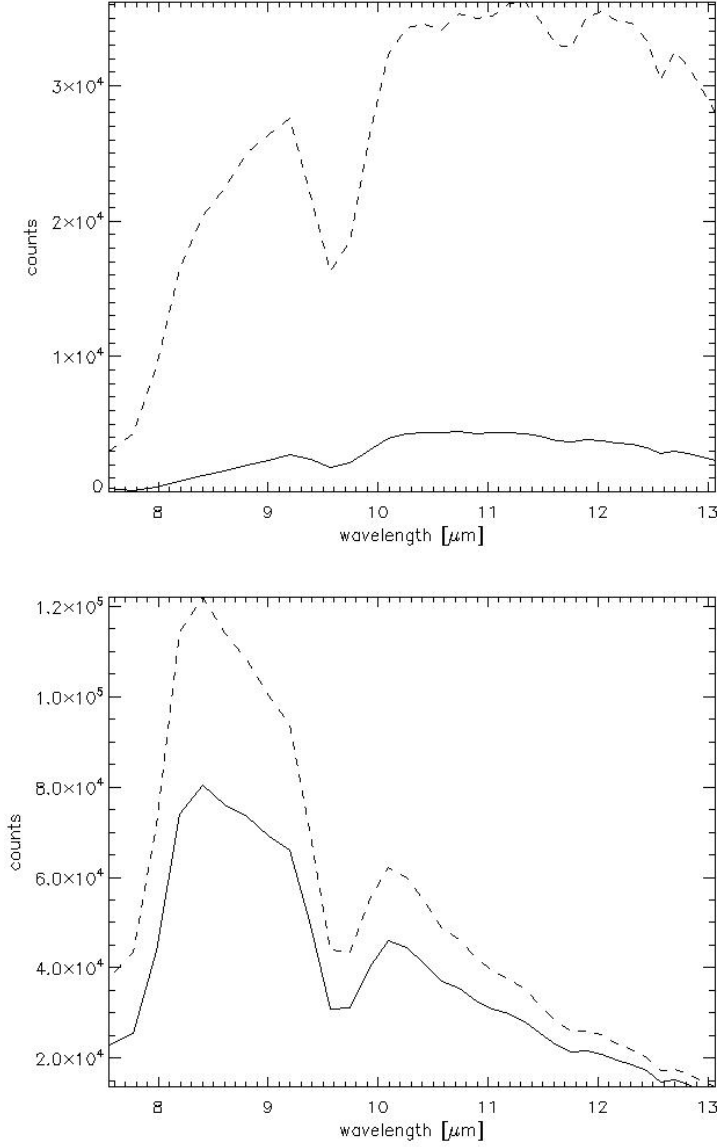


Figure B.3 – Example of MIDI raw photometry (dashed) recorded after the fringes in `HIGH_SENS` mode. The correlated flux, i.e. raw photometry * visibility, will have significantly smaller values (solid). Results for the science target are on the top panel and the calibrator on the bottom.

the calibrator’s diameter (Fig.B.6). The science target’s calibrated visibility is derived by dividing its raw visibility with the instrumental visibility (Fig.B.7). As a last step, we extract the calibrated MIDI spectrum⁶, F_ν (Fig. B.8), which

⁶It is a low resolution spectrum since $R=30$ for PRISM.

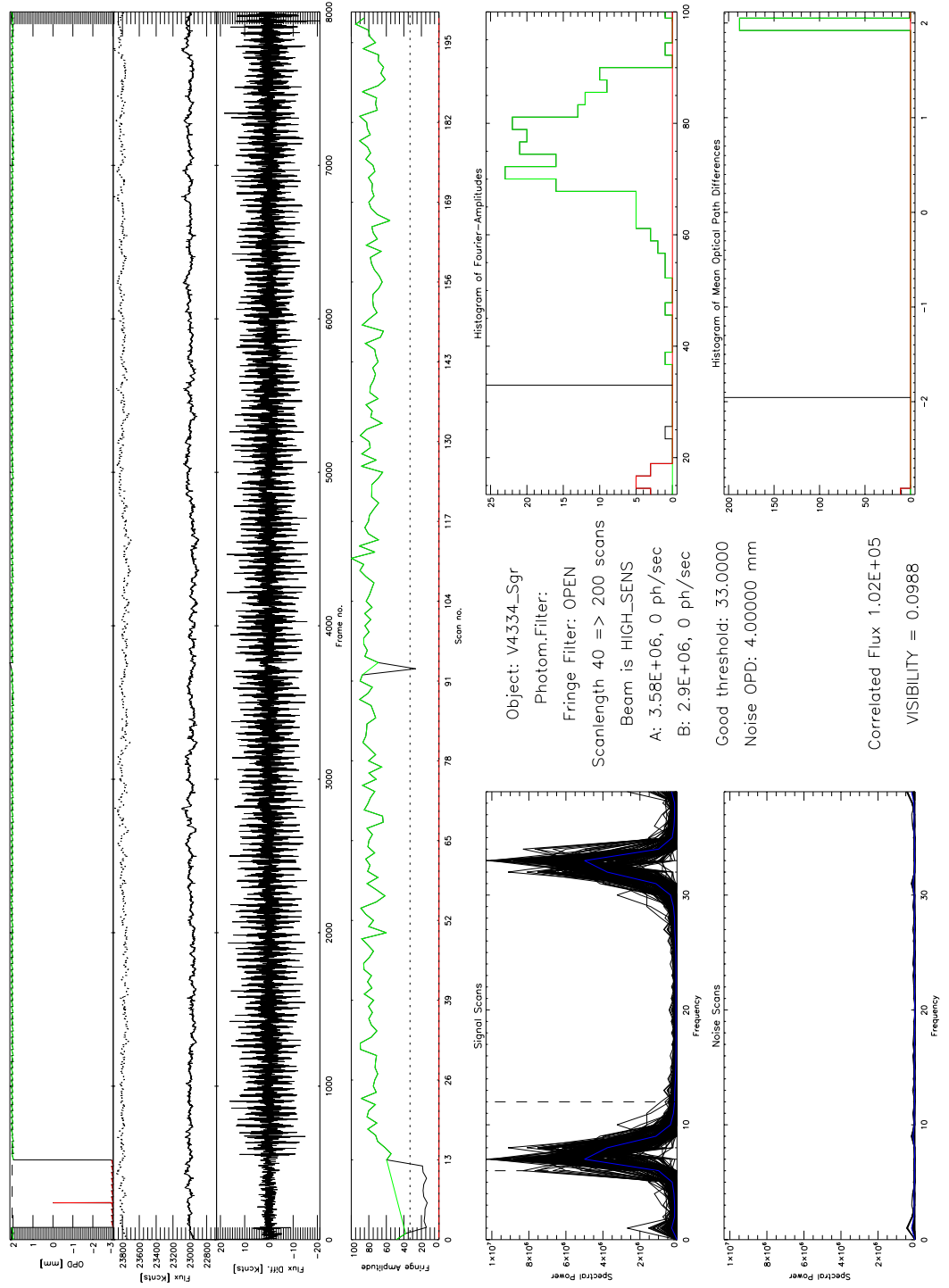


Figure B.4 – MIA graphical user interface. Panels from top to bottom: the first three show the OPD, the raw fluxes of the two beams and their flux difference for $n_F = 8000$ frames. The next one shows the Fourier fringe amplitude for $n_S = 200$ scans (see also Fig. B.2). The bottom two on the left, show the powerspectra of the good and bad scans (see also the blow-up of this panel in Fig. B.5). The remaining panels show statistics on the numbers of signals above a predefined threshold with respect to the Fourier amplitudes and the OPD.

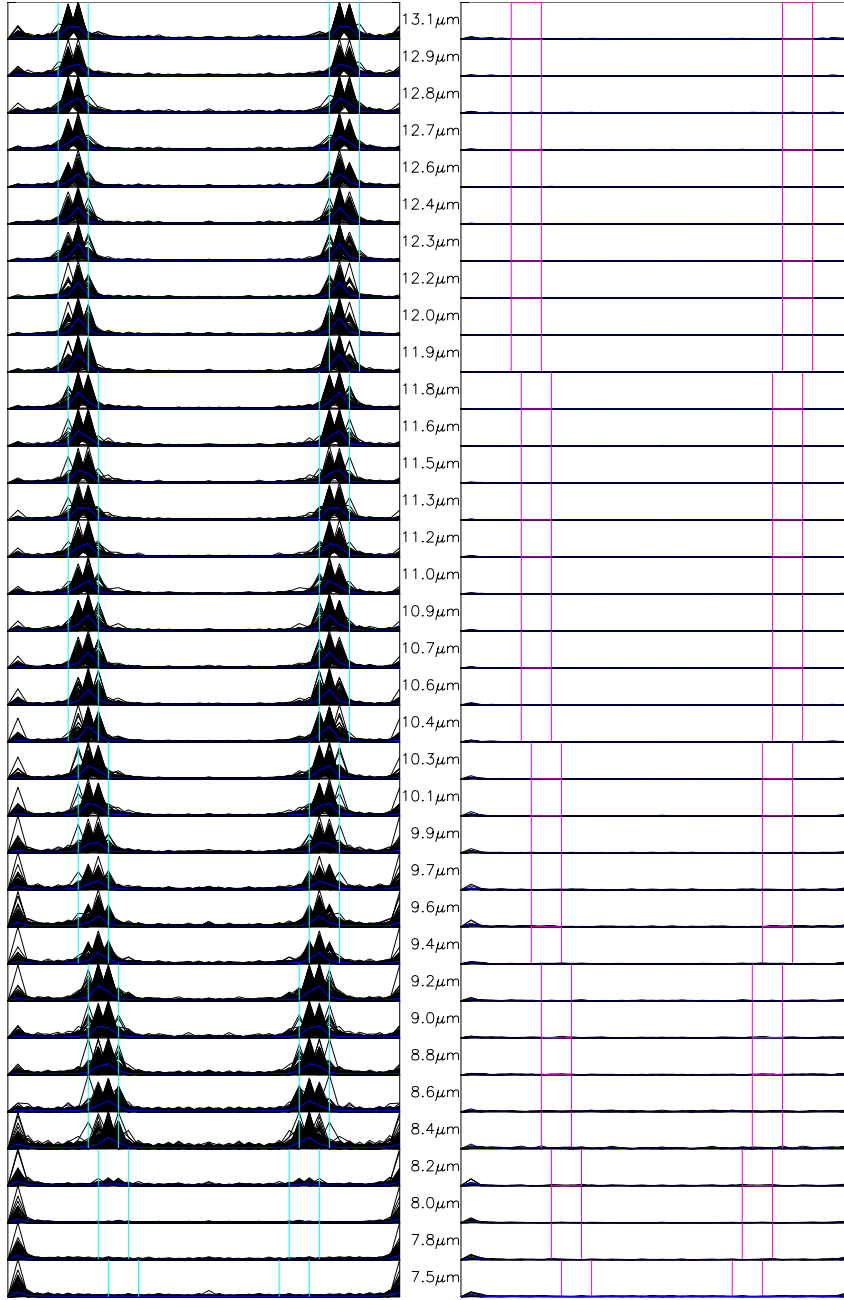


Figure B.5 – Powerspectra (spectral power vs. frequency) for each wavelength for V4334 Sgr (left) and noise levels (right). The blue(pink) lines mark the range of frequencies where good(bad) fringes are expected. The symmetry is a byproduct of the FFT algorithm.

is equal to

$$F_\nu = \frac{F_{\text{raw,SCI}} [\text{counts}]}{F_{\text{raw,CAL}} [\text{counts}]} \cdot F_{\text{ISO,CAL}} [\text{Jy}], \quad (\text{B.3})$$

where $F_{\text{raw,SCI}}$ and $F_{\text{raw,CAL}}$ is the raw photometry for the science target and the calibrator, respectively, and $F_{\text{ISO,CAL}}$ is a template spectrum for the calibrator from ISO.

We derive error bars using the standard deviation of the calibrated visibilities. Following Klotz et al. (2012), if the error was lower than 10% (as in some cases here), we assumed a multiplicative error of 10% as minimum. According to Chesneau (2007) the uncertainties in the **HIGH_SENS** mode lie between 7 and 15% due to the time difference in this mode between photometry and fringe recording. The reader will notice that there has been no mention of the phase (from Eq.[2.24]), only because MIA neglects the phase and uses only the Fourier amplitudes.

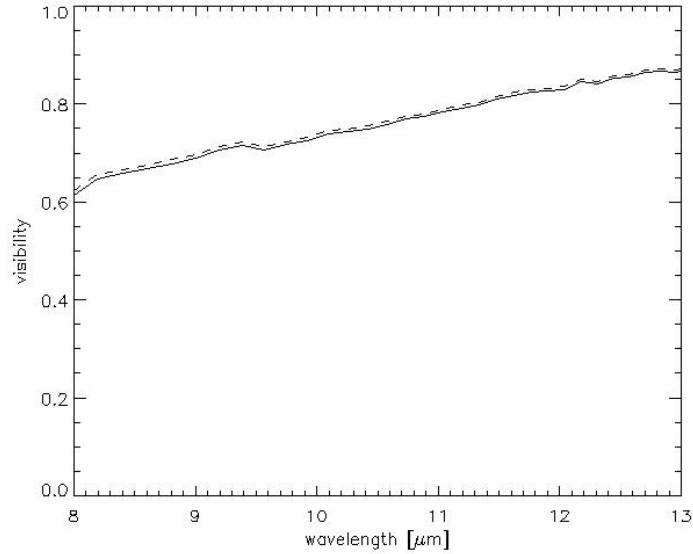


Figure B.6 – The instrumental (dashed) and raw (solid) visibility of HD169916 (Table B.1)

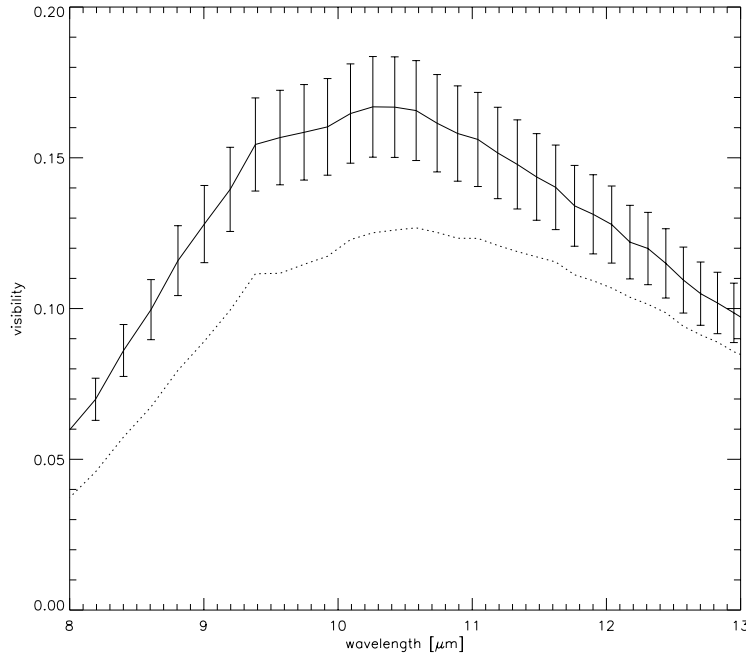


Figure B.7 – Calibrated visibility for V4334 Sgr (Table B.1). The source’s raw visibility is given for reference (dashed).

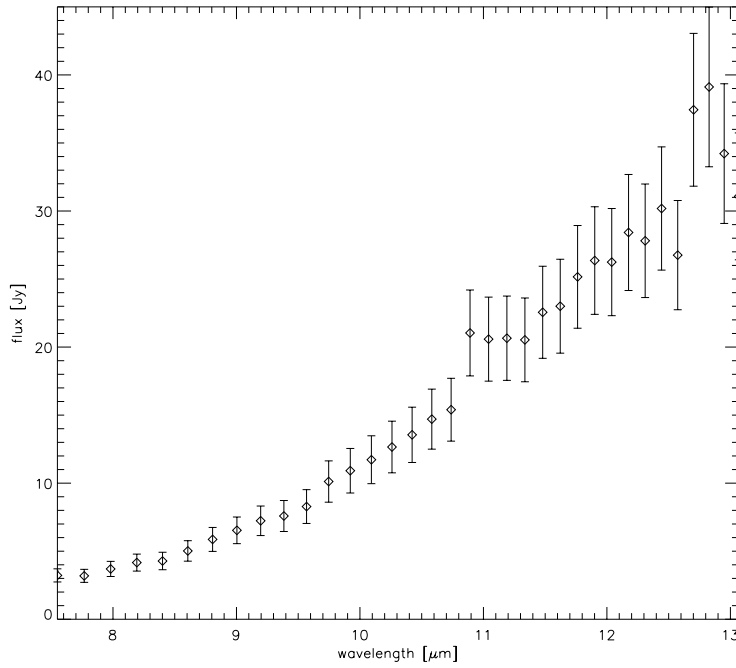


Figure B.8 – Calibrated spectrum for V4334 Sgr. The divergence from the slope in some points beyond $11\mu\text{m}$ is due to uncertainties during flux calibration with the spectrum of HD169916 .

Bibliography

- Akashi, M. & Soker, N. 2008, *New Astronomy*, 13, 157
- Allen, D. A. & Swings, J. P. 1972, *ApJ*, 174, 583
- Amiri, N. 2011, PhD thesis, Ph. D. thesis, University of Leiden (2011). Advisor: E.F. van Dishoeck.
- Applegate, J. H. 1988, *ApJ*, 329, 803
- Arrieta, A. & Torres-Peimbert, S. 2003, *ApJS*, 147, 97
- Arrieta, A., Torres-Peimbert, S., & Georgiev, L. 2005, *ApJ*, 623, 252
- Aspin, C. & McLean, I. S. 1984, *A&A*, 134, 333
- Aspin, C., McLean, I. S., & Smith, M. G. 1988, *A&A*, 196, 227
- Bachiller, R., Martin-Pintado, J., & Bujarrabal, V. 1990, *A&A*, 227, 188
- Baldwin, J. A., Ferland, G. J., Martin, P. G., et al. 1991, *ApJ*, 374, 580
- Balick, B. 1989, *AJ*, 97, 476
- Balick, B. & Frank, A. 2002, *ARA&A*, 40, 439

- Barnbaum, C., Morris, M., & Kahane, C. 1995, *ApJ*, 450, 862
- Bartelt, H. O., Lohmann, A. W., & Wirtitzer, B. 1984, *ApOpt*, 23, 3121
- Bignell, R. C. 1983, in *IAU Symposium*, Vol. 103, *Planetary Nebulae*, ed. D. R. Flower, 69–77
- Bjorkman, J. E. & Wood, K. 2001, *ApJ*, 554, 615
- Blöcker, T., Balega, Y., Hofmann, K.-H., & Weigelt, G. 2001, *A&A*, 369, 142
- Bloecker, T. 1995, *A&A*, 299, 755
- Bond, H. E. & Ciardullo, R. 1989, in *Lecture Notes in Physics*, Berlin Springer Verlag, Vol. 328, *IAU Colloq. 114: White Dwarfs*, ed. G. Wegner, 473
- Bond, H. E. & Livio, M. 1990, *ApJ*, 355, 568
- Bond, H. E. & Pollacco, D. L. 2002, *ApSS*, 279, 31
- Bryan, R. K. & Skilling, J. 1980, *MNRAS*, 191, 69
- Bujarrabal, V., Castro-Carrizo, A., Alcolea, J., & Neri, R. 2005, *A&A*, 441, 1031
- Bujarrabal, V., Fuente, A., & Omont, A. 1994, *A&A*, 285, 247
- Bujarrabal, V., Neri, R., Alcolea, J., & Kahane, C. 2003, *A&A*, 409, 573
- Buscher, D. F. 1994, in *IAU Symposium*, Vol. 158, *Very High Angular Resolution Imaging*, ed. J. G. Robertson & W. J. Tango, 91
- Buscher, D. F. & Haniff, C. A. 1993, *Journal of the Optical Society of America A*, 10, 1882
- Campbell, L. 1926, *Popular Astronomy*, 34, 551
- Castro-Carrizo, A., Neri, R., Bujarrabal, V., et al. 2012, *A&A*, 545, A1
- Castro-Carrizo, A., Quintana-Lacaci, G., Neri, R., et al. 2010, *A&A*, 523, A59
- Cesarsky, C. J., Abergel, A., Agnese, P., et al. 1996, *A&A*, 315, L32

- Chesneau, O. 2007, *New Astronomy Review*, 51, 666
- Chesneau, O., Clayton, G. C., Lykou, F., et al. 2009, *A&A*, 493, L17
- Chesneau, O., Collioud, A., De Marco, O., et al. 2006, *A&A*, 455, 1009
- Chesneau, O., Lykou, F., Balick, B., et al. 2007, *A&A*, 473, L29
- Chiu, P.-J., Hoang, C.-T., Dinh-V-Trung, et al. 2006, *ApJ*, 645, 605
- Chu, Y.-H., Gruendl, R. A., Guerrero, M. A., et al. 2009, *AJ*, 138, 691
- Ciardullo, R., Bond, H. E., Sipior, M. S., et al. 1999, *AJ*, 118, 488
- Clayton, G. C. & De Marco, O. 1997, *AJ*, 114, 2679
- Clayton, G. C., Kerber, F., Pirzkal, N., et al. 2006, *ApJL*, 646, L69
- Cohen, M. & Barlow, M. J. 1974, *ApJ*, 193, 401
- Cohen, M., Barlow, M. J., Liu, X.-W., & Jones, A. F. 2002, *MNRAS*, 332, 879
- Cohen, M., Van Winckel, H., Bond, H. E., & Gull, T. R. 2004, *AJ*, 127, 2362
- Corradi, R. L. M., Balick, B., & Santander-García, M. 2011, *A&A*, 529, A43
- Corradi, R. L. M. & Schwarz, H. E. 1993a, *A&A*, 268, 714
- Corradi, R. L. M. & Schwarz, H. E. 1993b, *A&A*, 273, 247
- Cox, P., Lucas, R., Huggins, P. J., et al. 2000, *A&A*, 353, L25
- de Marco, O. 2009, *PASP*, 121, 316
- de Ruyter, S., van Winckel, H., Dominik, C., Waters, L. B. F. M., & Dejonghe, H. 2005, *A&A*, 435, 161
- de Ruyter, S., van Winckel, H., Maas, T., et al. 2006, *A&A*, 448, 641
- Decin, L., Agúndez, M., Barlow, M. J., et al. 2010, *Nature*, 467, 64
- Dehaes, S., Groenewegen, M. A. T., Decin, L., et al. 2007, *MNRAS*, 377, 931
- Deroo, P., Acke, B., Verhoelst, T., et al. 2007a, *A&A*, 474, L45

- Deroo, P., van Winckel, H., Min, M., et al. 2006, *A&A*, 450, 181
- Deroo, P., van Winckel, H., Verhoelst, T., et al. 2007b, *A&A*, 467, 1093
- Di Francesco, J., Johnstone, D., Kirk, H., MacKenzie, T., & Ledwosinska, E. 2008, *ApJS*, 175, 277
- Dinh-V.-Trung & Lim, J. 2009, *ApJ*, 701, 292
- Doyle, S., Balick, B., Corradi, R. L. M., & Schwarz, H. E. 2000, *AJ*, 119, 1339
- Draine, B. T. & Lee, H. M. 1984, *ApJ*, 285, 89
- Duerbeck, H. W. & Benetti, S. 1996, *ApJL*, 468, L111
- Edgar, R. G., Nordhaus, J., Blackman, E. G., & Frank, A. 2008, *ApJL*, 675, L101
- Etoka, S., Lagadec, E., Zijlstra, A. A., et al. 2008, in *The role of VLBI in the Golden Age for Radio Astronomy*
- Evans, A., Geballe, T. R., Tyne, V. H., et al. 2004, *MNRAS*, 353, L41
- Evans, A., Tyne, V. H., van Loon, J. T., et al. 2006, *MNRAS*, 373, L75
- Evans, A., Woodward, C. E., Helton, L. A., et al. 2007, *ApJL*, 671, L157
- Evans, T. L. 2009, in *American Institute of Physics Conference Series*, Vol. 1094, American Institute of Physics Conference Series, ed. E. Stempels, 963–964
- Eyres, S. P. S. 2002, *ApSS*, 279, 69
- Eyres, S. P. S., Evans, A., Geballe, T. R., Salama, A., & Smalley, B. 1998a, *MNRAS*, 298, L37
- Eyres, S. P. S., Geballe, T. R., Tyne, V. H., et al. 2004, *MNRAS*, 350, L9
- Eyres, S. P. S., Richards, A. M. S., Evans, A., & Bode, M. F. 1998b, *MNRAS*, 297, 905
- Eyres, S. P. S., Smalley, B., Geballe, T. R., et al. 1999, *MNRAS*, 307, L11

- Feibelman, W. A. 1984, *ApJ*, 287, 353
- Ferland, G. J., Porter, R. L., van Hoof, P. A. M., et al. 2013, *ArXiv e-prints*
- Frankowski, A. & Jorissen, A. 2007, *Baltic Astronomy*, 16, 104
- Freeth, T., Bitsakis, Y., Moussas, X., et al. 2006, *Nature*, 444, 587
- Freeth, T., Jones, A., Steele, J. M., & Bitsakis, Y. 2008, *Nature*, 454, 614
- Fried, D. L. 1965, *Journal of the Optical Society of America (1917-1983)*, 55, 1427
- Fried, D. L. 1982, *Journal of the Optical Society of America (1917-1983)*, 72, 52
- G. Helou & D. W. Walker, ed. 1988, *Infrared astronomical satellite (IRAS) catalogs and atlases. Volume 7: The small scale structure catalog, Vol. 7*
- Galvez, M. 2005, *Journal of Physics D Applied Physics*, 38, 3011
- García-Segura, G., López, J. A., & Franco, J. 2005, *ApJ*, 618, 919
- Geballe, T. R., Evans, A., Smalley, B., Tyne, V., & Eyres, S. 2002, *Astrophysics and Space Science*, 279, 39, 10.1023/A:1014683521291
- Gesicki, K. & Zijlstra, A. A. 2007, *A&A*, 467, L29
- Gesicki, K., Zijlstra, A. A., Szyszka, C., et al. 2010, *A&A*, 514, A54
- Gómez, Y. & Rodríguez, L. F. 2001, *ApJL*, 557, L109
- Groenewegen, M. A. T., Waelkens, C., Barlow, M. J., et al. 2011, *A&A*, 526, A162
- Gromadzki, M. & Mikolajewska, J. 2009, *A&A*, 495, 931
- Guzman-Ramirez, L., Zijlstra, A. A., Níchuimín, R., et al. 2011, *MNRAS*, 441
- H. J. Habing & H. Olofsson, ed. 2003, *Asymptotic giant branch stars*
- Habing, H. J. 1996, *ARA&A*, 7, 97

- Hajduk, M., Zijlstra, A. A., & Gesicki, K. 2008, *A&A*, 490, L7
- Hajduk, M., Zijlstra, A. A., Herwig, F., et al. 2005, *Science*, 308, 231
- Haniff, C. A. & Buscher, D. F. 1992, *Journal of the Optical Society of America A*, 9, 203
- Haniff, C. A. & Buscher, D. F. 1998, *A&A*, 334, L5
- Haniff, C. A., Mackay, C. D., Titterton, D. J., Sivia, D., & Baldwin, J. E. 1987, *Nature*, 328, 694
- Hayashi, C. 1966, *ARA&A*, 4, 171
- Heber, U. 1998, in *ESA Special Publication*, Vol. 413, *Ultraviolet Astrophysics Beyond the IUE Final Archive*, ed. W. Wamsteker, R. Gonzalez Riestra, & B. Harris, 195
- Herbig, G. H. & Boyarchuk, A. A. 1968, *ApJ*, 153, 397
- Herschel, W. 1785, *Philosophical Transactions of the Royal Society London*, Series I, 75, 213
- Herwig, F. 2005, *ARA&A*, 43, 435
- Herwig, F., Pignatari, M., Woodward, P. R., et al. 2011, *ApJ*, 727, 89
- Hinkle, K. H., Lebzelter, T., Joyce, R. R., et al. 2008, *A&A*, 479, 817
- Hirano, N., Shinnaga, H., Dinh-V-Trung, et al. 2004, *ApJL*, 616, L43
- Höfner, S. 2008a, *Physica Scripta Volume T*, 133, 014007
- Höfner, S. 2008b, *A&A*, 491, L1
- Höfner, S. 2009, in *Astronomical Society of the Pacific Conference Series*, Vol. 414, *Cosmic Dust - Near and Far*, ed. T. Henning, E. Grün, & J. Steinacker, 3
- Hora, J. L. & Latter, W. B. 1994, *ApJ*, 437, 281
- Houck, J. R., Roellig, T. L., van Cleve, J., et al. 2004, *ApJS*, 154, 18

- Hsu, M.-C. & Lee, C.-F. 2011, ArXiv e-prints
- Huang, Z.-Y., Hasegawa, T. I., Dinh-V-Trung, et al. 2010, ApJ, 722, 273
- Huggins, P. J. 2007, ApJ, 663, 342
- Iben, Jr., I. 1984, ApJ, 277, 333
- Iben, Jr., I. 1985, QJRAS, 26, 1
- Iben, Jr., I. & Renzini, A. 1983, ARA&A, 21, 271
- Iben, Jr., I. & Tutukov, A. V. 1986, ApJ, 311, 753
- Ireland, M. J., Monnier, J. D., Tuthill, P. G., et al. 2007, ApJ, 662, 651
- Ishihara, D., Onaka, T., Kataza, H., et al. 2010, A&A, 514, A1
- Ivezic, Z. & Elitzur, M. 1997, MNRAS, 287, 799
- Ivezic, Z., Nenkova, M., & Elitzur, M. 1999, ArXiv Astrophysics e-prints
- J. Blommaert, R. Siebenmorgen, A. Coulais, L. Metcalfe, M.-A. Miville-Deschênes, K. Okumura, S. Ott, A. Pollack, M. Sauvage, & J.-L. Starck, ed. 2003, ESA Special Publication, Vol. 1262, The ISO Handbook Volume II: CAM - The ISO Camera (v 2.0)
- Johnson, J. J. & Jones, T. J. 1991, AJ, 101, 1735
- Kahane, C., Audinos, P., Barnbaum, C., & Morris, M. 1996, A&A, 314, 871
- Kahane, C., Maizels, C., & Jura, M. 1988, ApJL, 328, L25
- Karttunen, H., Krüger, P., Oja, H., Poutanen, M., & Donner, K. J. 2007, Fundamental Astronomy, 5th edn. (Springer Netherlands)
- Kastner, J. H., Balick, B., Blackman, E. G., et al. 2003, ApJL, 591, L37
- Käufl, H. U., Koller, J., & Kerber, F. 2003, A&A, 406, 981
- Kerber, F., Blommaert, J. A. D. L., Groenewegen, M. A. T., et al. 1999a, A&A, 350, L27

- Kerber, F., Köppen, J., Roth, M., & Trager, S. C. 1999b, *A&A*, 344, L79
- Kerber, F., Pirzkal, N., De Marco, O., et al. 2002, *ApJL*, 581, L39
- Kerschbaum, F. & Hron, J. 1994, *A&AS*, 106, 397
- Kessler, M. F., Steinz, J. A., Anderegg, M. E., et al. 1996, *A&A*, 315, L27
- Klotz, D., Sacuto, S., Kerschbaum, F., et al. 2012, *A&A*, 541, A164
- Knapp, G. R., Dobrovolsky, S. I., Ivezić, Z., et al. 1999, *A&A*, 351, 97
- Knapp, G. R., Jorissen, A., & Young, K. 1997, *A&A*, 326, 318
- Knapp, G. R. & Morris, M. 1985, *ApJ*, 292, 640
- Kruszewski, A., Gehrels, T., & Serkowski, K. 1968, *AJ*, 73, 677
- Kunitomo, M., Ikoma, M., Sato, B., Katsuta, Y., & Ida, S. 2011, in *American Institute of Physics Conference Series*, Vol. 1331, American Institute of Physics Conference Series, ed. S. Schuh, H. Drechsel, & U. Heber, 314–318
- Kwok, S., Su, K. Y. L., & Hrivnak, B. J. 1998, *ApJL*, 501, L117
- Labeyrie, A. 1970, *A&A*, 6, 85
- Labeyrie, A. 1974, *Nouvelle Revue d'Optique*, 5, 141
- Labeyrie, A., Bonneau, D., Stachnik, R. V., & Gezari, D. Y. 1974, *ApJL*, 194, L147
- Lagadec, E., Chesneau, O., Matsuura, M., et al. 2006, *A&A*, 448, 203
- Lagadec, E., Chesneau, O., Zijlstra, A. A., Matsuura, M., & Mékarnia, D. 2007, in *Asymmetrical Planetary Nebulae IV*
- Lagadec, E., Mékarnia, D., de Freitas Pacheco, J. A., & Dougados, C. 2005, *A&A*, 433, 553
- Lagadec, E., Sloan, G. C., Zijlstra, A. A., Maun, N., & Houck, J. R. 2012, *Monthly Notices of the Royal Astronomical Society*, 427, 2588

- Lagadec, E., Verhoelst, T., Mekarnia, D., et al. 2011a, ArXiv e-prints
- Lagadec, E., Verhoelst, T., Mekarnia, D., et al. 2011b, *The Messenger*, 144, 21
- Lagadec, E., Zijlstra, A. A., Sloan, G. C., et al. 2009, *Monthly Notices of the Royal Astronomical Society*, 396, 598
- Lambert, D. L., Gustafsson, B., Eriksson, K., & Hinkle, K. H. 1986, *ApJS*, 62, 373
- Lau, H. H. B., De Marco, O., & Liu, X.-W. 2011, *MNRAS*, 410, 1870
- Lawlor, T. M. & MacDonald, J. 2003, *ApJ*, 583, 913
- Leão, I. C., de Laverny, P., Mékarnia, D., de Medeiros, J. R., & Vandame, B. 2006, *A&A*, 455, 187
- Leinert, C., Graser, U., Przygodda, F., et al. 2003, *ApSS*, 286, 73
- Leinert, C., van Boekel, R., Waters, L. B. F. M., et al. 2004, *A&A*, 423, 537
- Lenzen, R., Hartung, M., Brandner, W., et al. 2003, in *Society of Photo-Optical Instrumentation Engineers (SPIE) Conference Series*, ed. M. Iye & A. F. M. Moorwood, Vol. 4841, 944–952
- Lenzuni, P., Natta, A., & Panagia, N. 1989, *ApJ*, 345, 306
- Lim, J. & Kwok, S. 2000, in *Astronomical Society of the Pacific Conference Series*, Vol. 199, *Asymmetrical Planetary Nebulae II: From Origins to Microstructures*, ed. J. H. Kastner, N. Soker, & S. Rappaport, 259
- Liu, X.-W., Barlow, M. J., Cohen, M., et al. 2001, *MNRAS*, 323, 343
- Livio, M. & Soker, N. 1988, *ApJ*, 329, 764
- Livio, M. & Soker, N. 2001, *ApJ*, 552, 685
- Lloyd Evans, T. 1991, *MNRAS*, 248, 479
- Lloyd Evans, T. 2000, in *IAU Symposium*, Vol. 177, *The Carbon Star Phenomenon*, ed. R. F. Wing, 367

- Lohmann, A. W., Weigelt, G., & Wirtzner, B. 1983, *ApOpt*, 22, 4028
- Lopez, B., Antonelli, P., Wolf, S., et al. 2008, in *Society of Photo-Optical Instrumentation Engineers (SPIE) Conference Series*, Vol. 7013
- Luttermoser, D. G. & Brown, A. 1992, *ApJ*, 384, 634
- Lykou, F. 2008, Master's thesis, University of Manchester, UK
- Lykou, F., Chesneau, O., Zijlstra, A. A., et al. 2011, *A&A*, 527, A105+
- Madappatt, N., de Marco, O., Nordhaus, J., & Wardle, M. 2011, in *American Institute of Physics Conference Series*, Vol. 1331, American Institute of Physics Conference Series, ed. S. Schuh, H. Drechsel, & U. Heber, 319–323
- Maercker, M., Mohamed, S., Vlemmings, W. H. T., et al. 2012, *Nature*, 490, 232
- Mastrodemos, N. & Morris, M. 1998, *ApJ*, 497, 303
- Mastrodemos, N. & Morris, M. 1999, *ApJ*, 523, 357
- Mathis, J. S., Rumpl, W., & Nordsieck, K. H. 1977, *ApJ*, 217, 425
- Matsuura, M., Chesneau, O., Zijlstra, A. A., et al. 2006, *ApJL*, 646, L123
- Mauron, N. & Huggins, P. J. 2000, *A&A*, 359, 707
- Mauron, N. & Huggins, P. J. 2006, *A&A*, 452, 257
- Meng, X. & Yang, W. 2010, *MNRAS*, 401, 1118
- Menut, J.-L., Chesneau, O., Bakker, E., et al. 2009, *A&A*, 496, 133
- Michelson, A. A. 1891, *PASP*, 3, 217
- Michelson, A. A. & Pease, F. G. 1921, *ApJ*, 53, 249
- Mikołajewska, J. 2002, *MNRAS*, 335, L33
- Mikołajewska, J., Balega, Y., Hofmann, K.-H., & Weigelt, G. 2010, *MNRAS*, 403, L21

- Millan-Gabet, R., Pedretti, E., Monnier, J. D., et al. 2003, in Society of Photo-Optical Instrumentation Engineers (SPIE) Conference Series, ed. W. A. Traub, Vol. 4838, 202–209
- Min, M., Dullemond, C. P., Dominik, C., de Koter, A., & Hovenier, J. W. 2009, *A&A*, 497, 155
- Miszalski, B., Acker, A., Moffat, A. F. J., Parker, Q. A., & Udalski, A. 2009a, *A&A*, 496, 813
- Miszalski, B., Acker, A., Parker, Q. A., & Moffat, A. F. J. 2009b, *A&A*, 505, 249
- Miszalski, B., Boffin, H. M. J., Frew, D. J., et al. 2011a, ArXiv e-prints
- Miszalski, B., Corradi, R. L. M., Boffin, H. M. J., et al. 2011b, *MNRAS*, 413, 1264
- Miszalski, B., Jones, D., Rodríguez-Gil, P., et al. 2011c, *A&A*, 531, A158+
- Mohamed, S. & Podsiadlowski, P. 2011, in Astronomical Society of the Pacific Conference Series, Vol. 445, Why Galaxies Care about AGB Stars II: Shining Examples and Common Inhabitants, ed. F. Kerschbaum, T. Lebzelter, & R. F. Wing, 355
- Monnier, J. D. 1999, PhD thesis, UNIVERSITY OF CALIFORNIA, BERKELEY
- Morisset, C. 2006, in IAU Symposium, Vol. 234, Planetary Nebulae in our Galaxy and Beyond, ed. M. J. Barlow & R. H. Méndez, 467–468
- Morris, M., Sahai, R., Matthews, K., et al. 2006, in IAU Symposium, Vol. 234, Planetary Nebulae in our Galaxy and Beyond, ed. M. J. Barlow & R. H. Méndez, 469–470
- Murakami, H., Baba, H., Barthel, P., et al. 2007, *PASJ*, 59, 369
- Murakawa, K., Ueta, T., & Meixner, M. 2010, *A&A*, 510, A30+
- Neufeld, D. A., González-Alfonso, E., Melnick, G., et al. 2011, *ApJL*, 727, L29

- Nordhaus, J. & Blackman, E. G. 2006, MNRAS, 370, 2004
- Norris, B. 2010, Master's thesis, Sydney Institute for Astronomy, University of Sydney
- Norris, B. R. M., Tuthill, P. G., Ireland, M. J., et al. 2012, Nature, 484, 220
- O'Brien, T. J., Bode, M. F., Porcas, R. W., et al. 2006, Nature, 442, 279
- Ohnaka, K., Izumiura, H., Leinert, C., et al. 2008, A&A, 490, 173
- Olofsson, H. 2008, Physica Scripta Volume T, 133, 014028
- Onaka, T., Matsuhara, H., Wada, T., et al. 2007, PASJ, 59, 401
- Osterbart, R., Langer, N., & Weigelt, G. 1997, A&A, 325, 609
- Parker, Q. A., Acker, A., Frew, D. J., et al. 2006, MNRAS, 373, 79
- Pavlenko, Y. V., Geballe, T. R., Evans, A., et al. 2004, A&A, 417, L39
- Pearson, T. J. & Readhead, A. C. S. 1984, ARA&A, 22, 97
- Peraiah, A. 2001, An Introduction to Radiative Transfer (Cambridge University Press)
- Pereira, C. B., Miranda, L. F., Smith, V. V., & Cunha, K. 2008, A&A, 477, 535
- Petrov, R. G. & The AMBER Consortium. 2003, ApSS, 286, 57
- Phillips, J. P. & Cuesta, L. 1999, AJ, 118, 2919
- Pinte, C., Ménard, F., Duchêne, G., & Bastien, P. 2006, A&A, 459, 797
- Purton, C. R., Feldman, P. A., Marsh, K. A., Allen, D. A., & Wright, A. E. 1982, MNRAS, 198, 321
- Raga, A. C., Cantó, J., Esquivel, A., Huggins, P. J., & Maun, N. 2011, in Asymmetric Planetary Nebulae 5 Conference
- Ragland, S., Traub, W. A., Berger, J.-P., et al. 2006, ApJ, 652, 650

- Ratzka, T. 2005, PhD thesis, Max-Planck-Institute for Astronomy, Koenigstuhl 17, 69117 Heidelberg, Germany
- Ratzka, T., Leinert, C., Henning, T., et al. 2007, *A&A*, 471, 173
- Riera, A., García-Lario, P., Manchado, A., et al. 2003, in *Revista Mexicana de Astronomia y Astrofisica Conference Series*, ed. J. Arthur & W. J. Henney, Vol. 15, 82–82
- Robitaille, T. P. 2011, *A&A*, 536, A79
- Roddier, F. 1986, *Optics Communications*, 60, 145
- Rousset, G., Lacombe, F., Puget, P., et al. 2003, in *Society of Photo-Optical Instrumentation Engineers (SPIE) Conference Series*, ed. P. L. Wizinowich & D. Bonaccini, Vol. 4839, 140–149
- Rutten, R. J. 1995, *The Generation and Transportation of Radiation*, 5th edn. (Sterrekundig Instituut Utrecht lecture notes)
- Rutten, R. J. 2003, *Radiative Transfer in Stellar Atmospheres* (Sterrekundig Instituut Utrecht lecture notes)
- Sacuto, S., Aringer, B., Hron, J., et al. 2011, *A&A*, 525, A42
- Sacuto, S., Jorissen, A., Cruzalèbes, P., et al. 2008, *A&A*, 482, 561
- Sahai, R. 2000, *ApJL*, 537, L43
- Sahai, R. & Chronopoulos, C. K. 2010, *ApJL*, 711, L53
- Sahai, R., Findeisen, K., Gil de Paz, A., & Sánchez Contreras, C. 2008, *ApJ*, 689, 1274
- Sahai, R., Hines, D. C., Kastner, J. H., et al. 1998, *ApJL*, 492, L163+
- Sahai, R., Morris, M., Knapp, G. R., Young, K., & Barnbaum, C. 2003, *Nature*, 426, 261
- Sahai, R., Morris, M. R., & Villar, G. G. 2011, *AJ*, 141, 134

- Sahai, R., Sugerman, B. E. K., & Hinkle, K. 2009, *ApJ*, 699, 1015
- Sahai, R. & Wannier, P. G. 1988, *A&A*, 201, L9
- Sánchez Contreras, C., Gil de Paz, A., & Sahai, R. 2004, *ApJ*, 616, 519
- Savage, B. D. & Mathis, J. S. 1979, *ARA&A*, 17, 73
- Schaeidt, S. G., Morris, P. W., Salama, A., et al. 1996, *A&A*, 315, L55
- Schmidt, G. D., Hines, D. C., & Swift, S. 2002, *ApJ*, 576, 429
- Schonberger, D. & Blocker, T. 1993, in *Astronomical Society of the Pacific Conference Series*, Vol. 45, *Luminous High-Latitude Stars*, ed. D. D. Sasselov, 337
- Schönberger, D. & Blöcker, T. 1996, *ApSS*, 245, 201
- Schwarz, H. E., Aspin, C., Corradi, R. L. M., & Reipurth, B. 1997, *A&A*, 319, 267
- Shakura, N. I. & Syunyaev, R. A. 1973, *A&A*, 24, 337
- Siódmiak, N., Meixner, M., Ueta, T., et al. 2008, *ApJ*, 677, 382
- Sloan, G. C., Kraemer, K. E., Price, S. D., & Shipman, R. F. 2003, *ApJS*, 147, 379
- Smith, E. C. D. & McLean, I. S. 2008, *ApJ*, 676, 408
- Smith, N. 2003, *MNRAS*, 342, 383
- Smith, N., Balick, B., & Gehrz, R. D. 2005, *AJ*, 130, 853
- Smith, N. & Gehrz, R. D. 2005, *AJ*, 129, 969
- Soker, N. 1999, *AJ*, 118, 2424
- Soker, N. 2002, *Monthly Notices of the Royal Astronomical Society*, 336, 826
- Soker, N. 2004, *New Astronomy*, 9, 399
- Soker, N. 2004, *MNRAS*, 350, 1366

- Soker, N. 2006, *ApJL*, 645, L57
- Soker, N. 2006, *Publications of the Astronomical Society of the Pacific*, 118, pp. 260
- Soker, N. & Livio, M. 1994, *ApJ*, 421, 219
- Soker, N. & Rappaport, S. 2001, *The Astrophysical Journal*, 557, 256
- Sokoloski, J. L. & Bildsten, L. 2010, *ApJ*, 723, 1188
- Solf, J. 2000, *A&A*, 354, 674
- Speck, A. K. 2012, *Journal of the American Association of Variable Star Observers (JAAVSO)*, 195
- Stanek, K. Z., Knapp, G. R., Young, K., & Phillips, T. G. 1995, *ApJS*, 100, 169
- Torres-Peimbert, S. & Arrieta, A. 1998, in *Revista Mexicana de Astronomia y Astrofisica Conference Series*, Vol. 7, 171
- Trammell, S. R., Dinerstein, H. L., & Goodrich, R. W. 1994, *AJ*, 108, 984
- Traub, W. A. 2000, in *Principles of Long Baseline Stellar Interferometry*, ed. P. R. Lawson, 31
- Tristram, K. R. W. 2007, PhD thesis, Max-Planck-Institut für Astronomie, Königstuhl 17, 69117 Heidelberg, Germany
- Tsuji, T., Unno, W., Kaifu, N., et al. 1988, *ApJL*, 327, L23
- Tuthill, P., Lacour, S., Amico, P., et al. 2010, in *Society of Photo-Optical Instrumentation Engineers (SPIE) Conference Series*, Vol. 7735
- Tuthill, P., Lloyd, J., Ireland, M., et al. 2006, in *Society of Photo-Optical Instrumentation Engineers (SPIE) Conference Series*, Vol. 6272
- Tuthill, P. G. 1994, PhD thesis, , Univ. of Cambridge, (1994)
- Tuthill, P. G., Monnier, J. D., & Danchi, W. C. 2001, *Nature*, 409, 1012

- Tuthill, P. G., Monnier, J. D., Danchi, W. C., & Haniff, C. A. 1998, in Society of Photo-Optical Instrumentation Engineers (SPIE) Conference Series, ed. R. D. Reasenberg, Vol. 3350, 839–846
- Tuthill, P. G., Monnier, J. D., Danchi, W. C., Wishnow, E. H., & Haniff, C. A. 2000, *PASP*, 112, 555
- Tyne, V. H., Evans, A., Geballe, T. R., et al. 2002, *MNRAS*, 334, 875
- van Belle, G. T. 1999, *PASP*, 111, 1515
- van den Bergh, S. 1974, *A&A*, 32, 351
- van der Veen, W. E. C. J. & Habing, H. J. 1988, *A&A*, 194, 125
- van Hoof, P. A. M., Hajduk, M., Zijlstra, A. A., et al. 2007, *A&A*, 471, L9
- van Winckel, H. 2003, *ARA&A*, 41, 391
- Van Winckel, H., Cohen, M., & Gull, T. R. 2002, *A&A*, 390, 147
- van Winckel, H., Lloyd Evans, T., Briquet, M., et al. 2009, *A&A*, 505, 1221
- Vlemmings, W. H. T. 2011, in Asymmetric Planetary Nebulae 5, ed. A. A. Zijlstra, F. Lykou, E. Lagadec, & I. McDonald (Jodrell Bank Centre for Astrophysics), 89
- Volk, K. & Cohen, M. 1990, *AJ*, 100, 485
- Volk, K., Kwok, S., & Hrivnak, B. J. 2007, *ApJ*, 670, 1137
- von der L  he, O. & Ageorges, N. 1997, in NATO ASIC Proc. 501: High angular resolution in astrophysics, ed. A.-M. Lagrange, D. Mourard, & P. Lena, 81
- Waelkens, C., Van Winckel, H., Waters, L. B. F. M., & Bakker, E. J. 1996, *A&A*, 314, L17
- Webbink, R. F. 1984, *ApJ*, 277, 355
- Weigelt, G., Balega, Y., Bloeker, T., et al. 1998, *A&A*, 333, L51
- Weigelt, G. P. 1977, *Optics Communications*, 21, 55

- Weingartner, J. C. & Draine, B. T. 2001, *ApJ*, 548, 296
- Weintraub, D. A., Kastner, J. H., Hines, D. C., & Sahai, R. 2000, *ApJ*, 531, 401
- Whitelock, P. A., Feast, M. W., Marang, F., & Groenewegen, M. A. T. 2006, *MNRAS*, 369, 751
- Whitelock, P. A., Feast, M. W., Marang, F., & Overbeek, M. D. 1997, *MNRAS*, 288, 512
- Wittkowski, M., Boboltz, D. A., Driebe, T., et al. 2008, *A&A*, 479, L21
- Wittkowski, M., Boboltz, D. A., Ohnaka, K., Driebe, T., & Scholz, M. 2007, *A&A*, 470, 191
- Wolf, S. 2003, *Computer Physics Communications*, 150, 99
- Wolf, S., Henning, T., & Stecklum, B. 1999, *A&A*, 349, 839
- Wolf, S. & Hillenbrand, L. A. 2003, *ApJ*, 596, 603
- Wood, K., Wolff, M. J., Bjorkman, J. E., & Whitney, B. 2002, *ApJ*, 564, 887
- Wood, P. R. 1990, in *From Miras to Planetary Nebulae: Which Path for Stellar Evolution?*, ed. M. O. Mennessier & A. Omont, 67–84
- Woodruff, H. C., Ireland, M. J., Tuthill, P. G., et al. 2009, *ApJ*, 691, 1328
- Woodruff, H. C., Tuthill, P. G., Monnier, J. D., et al. 2008, *ApJ*, 673, 418
- Worters, H. L., Rushton, M. T., Eyres, S. P. S., Geballe, T. R., & Evans, A. 2009, *MNRAS*, 393, 108
- Wright, E. L., Eisenhardt, P. R. M., Mainzer, A. K., et al. 2010, *AJ*, 140, 1868
- Young, T. 1802, *Philosophical Transactions of the Royal Society of London*, 92, 12
- Zhao-Geisler, R. 2010, PhD thesis, Ruperto-Carola University of Heidelberg, Germany

Zijlstra, A. A. 1990, *A&A*, 234, 387

Zijlstra, A. A. 2007, *Baltic Astronomy*, 16, 79

Zubko, V. & Elitzur, M. 2000, *ApJL*, 544, L137

Zuckerman, B. & Dyck, H. M. 1986, *ApJ*, 311, 345

Zweigle, J., Neri, R., Bachiller, R., Bujarrabal, V., & Grewing, M. 1997, *A&A*, 324, 624